การคำนวณแบบเฟิร์สพรินซิเพิลของความบกพร่องและรอยต่อบางชนิดในสารกลุ่มเพอรอฟสไกท์ออกไซด์

นายอิทธิพล ฟองแก้ว

วิทยานิพนธ์นี้เป็นส่วนหนึ่งของการศึกษาตามหลักสูตรปริญญาวิทยาศาสตรดุษฎีบัณฑิต
สาขาวิชาฟิสิกส์
มหาวิทยาลัยเทคโนโลยีสุรนารี
ปีการศึกษา 2559

FIRST PRINCIPLES CALCULATIONS OF SELECTED DEFECTS AND INTERFACES OF PEROVSKITE OXIDES

Ittipon Fongkaew

A Thesis Submitted in Partial Fulfillment of the Requirements for the

Degree of Doctor of Philosophy in Physics

Suranaree University of Technology

Academic Year 2016

FIRST PRINCIPLES CALCULATIONS OF SELECTED DEFECTS AND INTERFACES OF PEROVSKITE OXIDES

Suranaree University of Technology has approved this thesis submitted in partial fulfillment of the requirements for the Degree of Doctor of Philosophy.

Thesis Examining Committee

(Asst. Prof. Dr. Worawat Meevasana)
Chairperson

(Prof. Dr. Sukit Limpijumnong)
Member (Thesis Advisor)

U. Pinsook.
(Assoc. Prof. Dr. Udomsilp Pinsook)
Member

Suwit Suthirakun.
(Dr. Suwit Suthirakun)
Member

Rattikorn Yimnirun
(Assoc. Prof. Dr. Rattikorn Yimnirun)
Member

(Prof. Dr. Sukit Limpijumnong)
Vice Rector for Academic Affairs
and Innovation

(Prof. Dr. Santi Maensiri)
Dean of Institute of Science

อิทธิพล ฟองแก้ว : การคำนวณแบบเฟิร์สพรินซิเพิลของความบกพร่องและรอยต่อบางชนิดในสารกลุ่มเพอรอฟสไกท์ออกไซด์ (FIRST PRINCIPLES CALCULATIONS OF SELECTED DEFECTS AND INTERFACES OF PEROVSKITE OXIDES) อาจารย์ที่ปรึกษา : ศาสตราจารย์ ดร.ชูกิจ ลิมปิจำนงค์, 279 หน้า.

ในวิทยานิพนธ์นี้ได้ใช้การคำนวณแบบเฟิสต์พรินซิเพิลคำนวณ โครงสร้างภายในและอัตลักษณ์ของความบกพร่อง หรือสารเจือและเปรียบเทียบกับผลการทดลองที่มี ในวิทยานิพนธ์นี้มุ่งเน้นการคำนวณหาอัตลักษณ์ของสารเจืออยู่สามสิ่งที่มีความสัมพันธ์กับโครงสร้างโดยรอบของสารเจือเป็นอย่างมาก นั่นคือ ความถี่การสั่น การดูดกลืนรังสีเอกซ์ และพลังงานของรังสีเอกซ์ในการกระตุ้นอิเล็กตรอนในอะตอมของ ซึ่งผลการศึกษาที่สำคัญสามารถสรุปได้ดังต่อไปนี้ (1) ได้ทำการศึกษาความเสถียร ตำแหน่ง และความถี่การสั่นของอะตอมไฮโดรเจน (H) ใน $SrTiO_3$ เพอรอฟสไกท์ออกไซด์ ซึ่งได้เสนอสาเหตุของการพบช่วงความถี่การสั่น 3500 ต่อเซนติเมตร เกิดจากการก่อตัวของ H กับความบกพร่องแบบช่องว่างของ Sr $(H\text{-}V_{Sr})^-$ ขณะที่ $2H\text{-}V_{Sr}$ สามารถเกิดขึ้นได้ด้วยกรณี H มีความเข้มข้นสูงซึ่งสามารถอธิบายพีคสัญญาณบริเวนใกล้ 3500 ต่อเซนติเมตรได้และสอดคล้องกับการทดลองในการสังเกตพบช่วงความถี่การสั่น 3500 ต่อเซนติเมตรได้เป็นอย่างดี นอกจากนี้ ยังได้เสนอที่มาของการสังเกตุพบพีคสัญญาณความถี่ที่ 3355 และ 3384 ต่อเซนติเมตรซึ่งเกิดจากการก่อตัวของการก่อตัวของ H กับความบกพร่องแบบช่องว่างของ Ti (2) ได้นำเสนอวิธีการในการศึกษาและระบุตำแหน่งโครงสร้างภายในของการเจือธาตุโลหะและโลหะทรานสิชันในเพอรอฟสไกท์ออกไซด์โดยใช้การวิเคราะห์พลังงานงานการก่อตัวร่วมกับการจำลองสเปกตรัมการดูดกลืนรังสีเอกซ์แบบใกล้ขอบขีดเริ่มของการดูดกลืน ซึ่งผลที่ได้อธิบายและสอดคล้องกับการทดลองเป็นอย่างดี (3) ผลของการผ่อนคลายเชิงโครงสร้าง การเคลื่อนของอะตอมภายใน และการเจืออะตอมรวมถึงความบกพร่องบนผิวที่ส่งผลต่อการเกิดอิเล็กตรอนอิสระใน 2 มิติในรอยต่อของ LAO/STO ในทิศ (001) ได้ถูกศึกษาโดยการจำลองหลายรูปแบบ โดยมุ่งเน้นโมเดลจากความเป็นไปได้ของกระบวนการหลีกเลี่ยงความไม่ต่อเนื่องเชิงขั้วของโครงสร้าง การเกิดหรือไม่เกิดอิเล็กตรอนอิสระใน 2 มิติ ในรอยต่อของ และกระบวนการปรับเปลี่ยนโครงสร้างเชิงอิเล็กโทรนิกส์ ผลของโครงสร้างและความหนาแน่นของอิเล็กตรอนแต่โมเดลได้ถูกวิเคราะห์และนำเสนอ (4) ได้ใช้การวิเคราะห์โดยใช้การทดลองวัดการกระตุ้นอิเล็กตรอนด้วยเอกซเรย์ ของอะตอมเจือและความบกพร่องบนผิวของ LAO ร่วมกับผลการคำนวนพลังงานยึดเหนี่ยว และระดับ

พลังงานยึดของอิเล็กตรอนชั้นในของอะตอม เพื่อใช้ในการอธิบายการเปลี่ยนแปลงสเปกตรัมจากการทดลองวัดการกระตุ้นอิเล็กตรอนด้วยเอกซเรย์ของฟิล์มบาง LAO ที่ถูกเตรียมจากเงื่อนไขที่แตกต่างกัน โดยพบว่าพีคของสเปกตรัมที่วัดได้จาก อะตอมออกซิเจนในชั้น $1s$ ที่สูงจากปริมาณทั่วไป 2 eV ไม่ได้เกิดจาก OH ดังการคาดการณ์ทั่วไป แต่เกิดจากออกซิเจนกลุ่มที่มีความสัมพันธ์กับคาร์บอน และสัมพันธ์กับการเปลี่ยนแปลงของสเปกตรัมที่วัดได้จากอะตอมคาร์บอนในชั้น $1s$.

สาขาวิชาฟิสิกส์ ลายมือชื่อนักศึกษา__________

ปีการศึกษา 2559 ลายมือชื่ออาจารย์ที่ปรึกษา__________

ITTIPON FONGKAEW : FIRST PRINCIPLES CALCULATIONS OF SELECTED DEFECTS AND INTERFACES OF PEROVSKITE OXIDES. THESIS ADVISOR : PROF. SUKIT LIMPIJUMNONG, Ph.D. 279 PP.

KEYWORD: FIRST PRINCIPLES/ PEROVSKITE/INFRARED SPECTROSCOPY/ LOCAL VIBRATIONAL MODE/ X-RAY ABSORPTION

In this thesis, local structure and signatures of defects in different perovskite materials and their interfaces have been calculated using first-principles approaches. They are compared with available experimental results. The main focus is on three types of signatures that are strongly related to the local structures of defects; the vibrational frequencies, the x-ray absorption spectra, and x-ray photoelectron spectroscopy. Important results can be briefly summarized as following. (1) We have studied the stability and local vibration modes of a hydrogen (H) in cubic perovskite $SrTiO_3$. We propose that the cause of the observed 3500 cm^{-1} band is a H in a Sr vacancy (H-V_{Sr})$^{-}$, while the 2H-V_{Sr} complexes which can also form in samples with high H concentrations have the frequencies consistent with the observed hump in agreement with the experimentally observed 3500 cm^{-1} band. In addition, we also propose that the distinct twin peaks at 3355 and 3384 cm^{-1} are associated with the complex defects between H and V_{Ti}. (2) We have been presented method to study and identify local structure of transition metal and metal doped in perovskite by combine formation energy approach with XANES simulation. Our results show good agreement with the measured spectra. (3) Effects of structural relaxation, interdiffusion, and surface termination on 2DEG formation at the LAO/STO (001) interface were investigated by various models of LAO/STO interfaces with the goal of evaluating different possible mechanisms to avoid the polar discontinuity with or without formation of a 2DEG or electronic reconstruction. The resulting electron densities in various models are discussed. (4) We combined an experimental XPS study of the defect termination on LAO surfaces and their desorption under annealing with calculated analysis of the atomic binding energies and the core-level binding energies. These are used to interpret the changes in XPS spectra of an LAO film under different growth and annealing treatments. We find a peak with ~2 eV binding energy shift toward higher binding energy in the O1*s* spectrum cannot be associated with OH as is commonly assumed. Instead it is assigned to carbonaceous species by studying the corresponding changes in the C1*s* spectrum.

School of Physics　　　　Student's Signature________

Academic Year 2016　　　　Advisor's Signature________

ACKNOWLEDGEMENTS

First of all, I am very grateful to my advisor Prof. Dr. Sukit Limpijumnong for his great advisory, support, kind patience, and inspiration. I would like to thank Prof. Dr. Walter R. L. Lambrecht for his kindness accepting me into his group for a year to learn, great advices, be encouraged, and great knowledge. I also would like to thank Assoc. Prof Dr. Jiraroj T-Thienprasert for his kindness advisory, collaboration and fruitful instruction to me as a young student since six year ago. I would like to thank Asst. Prof. Dr. Worawat Meevasana, Assoc. Prof Dr. Rattikorn Yimnirun, Assoc. Prof. Dr. Udomsilp Pinsook and Dr. Suwit Suthirakun for contributing as my advisory committee members. Part of this thesis was performed during my visit at department of Physics, Case Western Reserve University (CWRU). I also want to thank Core Facility for Advanced Research Computing at CWRU and Synchrotron Light Research (SLRI) for computational resource. I am deeply grateful to Development and Promotion of Science and technology Talents project (DPST) for funding support and opportunity for my education life. I also appreciate friendship from Thai students in Cleveland when I was in the states. Importantly, my study would not be completed without supports and warm advices from the faculties of School of Physics, Suranaree University of Technology. I also thank to all of my good friends back in high school, undergrad and especially members in our Condensed Matter Theory research group. Most importantly, without great support from my dad, mom, brother and my girlfriend, I probably stuck in somewhere on my way to accomplish the degree, thank you all.

Ittipon Fongkaew

CONTENTS

Page

CHAPTER

CONTENTS (Continued)

Page

CONTENTS (Continued)

CONTENTS (Continued)

CONTENTS (Continued)

LIST OF TABLES

LIST OF TABLES (Continued)

LIST OF TABLES (Continued)

Table **Page**

LIST OF FIGURES

Figure **Page**

LIST OF FIGURES (Continued)

LIST OF FIGURES (Continued)

LIST OF FIGURES (Continued)

LIST OF FIGURES (Continued)

LIST OF FIGURES (Continue)

Figure **Page**

LIST OF FIGURES (Continued)

Figure **Page**

LIST OF FIGURES (Continued)

Figure **Page**

LIST OF FIGURES (Continued)

Figure **Page**

LIST OF FIGURES (Continued)

LIST OF ABBREVIATIONS

DFT	Density Functional Theory
LDA	Local Density Approximation
GGA	Generalized Gradient Approximation
SP	Schrodinger-Poisson
FP-LMTO	Full-Potential Linearized Muffin-tin Orbital Method
RXES	Resonance X-ray Emission Spectroscopy
BC	Bond Center
AB	Anti-bonding
LAO	$LaAlO_3$
STO	$SrTiO_3$
2DEG	Two Dimension Electron Gas
IR	Infrared
XAS	X-ray Absorption Spectroscopy
XPS	X-ray Photoemission Spectroscopy
PBE	Perdew, Burke, and Ernzerhof functional
MD	Molecular Dynamics
KS	Kohn-Sham
HSE	Heyd Scuseria Ernzerhof
VASP	Vienna Ab-initio Simulation Package
PAW	Projector Augmented Wave
PS	Pseudo

LIST OF ABBREVIATIONS (Continued)

NEB	Nudged Elastic Band
EPR	Electron Paramagnetic Resonance
MEP	Minimum Energy Path
PEB	Plain Elastic Band
LVM	Local Vibrational Mode
XANES	X-ray Absorption Near-Edge Spectroscopy
DOS	Density Of State
FEFF	Effective Scattering Amplitude
IUPAC	International Union of Pure and Applied Chemistry
FE	Ferroelectric
AFD	Anti-Ferrodistortive
VBM	Valence Band Maximum
CMB	Conduction Band Minimum
VB	Valence Band
CB	Conduction Band
PDOS	Partial Density Of State
WK	Weber and Kapphan
OE	Octahedral Edge
CF	Cube Face
OA	Off Axis
LES	Low Energy Surface
TM	Tarun and McCluskey

LIST OF ABBREVIATIONS (Continued)

EXAFS	X-ray Absorption Fine Structure
BT	$BaTiO_3$
BNT	$Bi_{0.5}Na_{0.5}TiO_3$
T_c	Curie Temperature
LAO/STO	$LaAlO_3$-$SrTiO_3$ Interfaces
AFM	Atomic Force Microscopy
MEIS	Medium-Energy Ion Scattering
CL-BE	Core-Level Binding Energy
PLD	Pulsed Laser Deposition
AFRL	Air Force Research Laboratory
UHV	Ultra High Vacuum
LUMO	Lowest Unoccupied Molecular Orbital
HOMO	Highest Occupied Molecular Orbital
EELS	Energy Electron Loss Spectroscopy

CHAPTER I

INTRODUCTION

1.1 Overview

Recent advanced computation and measurement techniques make it possible to investigate local atomic structures and properties of real materials in details. The "first principles calculations" or "ab initio calculations" based on quantum mechanical calculations of the electronic structures and density functional theory (DFT) allow one to model materials without taking any information from the measurements except the fundamental information about each element, i.e., the number of protons and electrons. Hence, the approach is highly unbiased. However, in most cases the system composes of a very large number of atoms; leading to an even larger number of electrons. Consequently, one cannot solve the set of Schrödinger equations of these systems because of two main practical reasons.

(1) The interactions between electrons as well as electrons-nuclei are complicated. (2) The number of electrons in the systems is too large. To reduce the complication of the interactions in the systems, some approximations have been introduced. The complicated many-body interactions between electrons can be approximated by simplifying the exchange-correlation term in the potential. The most commonly used approximations are based on density functional theory (Kohn and Sham, 1965) with the local density approximation (LDA) (Ceperley and Alder, 1980) or generalized gradient approximation (GGA) (Perdew *et al.*, 1996). Based on these

approximations, the complicated many-body problem is reduced into a solvable set of equations. The solutions of the set of equations lead to the ground state electronic wave functions as well as many other properties; including the total energy of the system. In the past, because the computational resources were very limited and the computational techniques were not well optimized, the calculations were capable of only small systems such as perfect crystals of a small number of atoms in the unit cell. With today advanced computer systems and highly developed computations techniques at various levels of approximations, the systems to be studied can be reasonably large. One can create unit cell that is sufficiently large containing a defect or an impurity inside to imitate their behaviors under diluted limits, e.g. (Limpijumnong and Van de Walle, 2004; Limpijumnong *et al.*, 2006; Li *et al.*, 2011). This opens up the opportunity to computationally study real materials that are not perfect; allowing direct comparison with experiments. In additional to the core part of the computational techniques, there are additional computational algorithms and modules focusing on generating the measurable properties based on the computed electronic structures and local atomic structures. For examples, (1) the computational codes called FEFF (Chasse *et al.*, 2002; Rehr *et al.*, 2009) can generate the x-ray absorption spectrum associated with a given structural model of the materials, (2) the computational codes called nextnano3 (Trellakis *et al.*, 2006) can simulate Schrodinger-Poisson (SP) equation for the transport properties based on electronic structures from density functional calculation of a given material system, (3) the additional module in the ABINIT codes (Gonze, 2005) that can be used to generate photon spectra, and (4) the additional module of FP-LMTO codes that can be used to calculate the resonance x-ray emission spectroscopy (RXES) and x-ray photoelectron spectroscopy (XPS) (Preston *et al.*, 2008).

While the advanced computational techniques can be used to study a wide range of material systems, this work is focus on the ABO_3-perovskite crystalline compounds that have high potential for electronic, optoelectronic and other advanced technological applications. This class of material has interesting properties in various aspects, such as ferroelectricity (Bednorz and Müller, 1984), piezoelectricity (Wang *et al.*, 2007) and semiconductivity (Frederikse *et al.*, 1964). Recently, the discovery of high mobility 2D electron gas at interfaces between perovskite (e.g., $SrTiO_3$) and other oxides (Ohtomo and Hwang, 2004) further opens up new opportunities in oxide electronics. These properties lead to many important applications of perovskite oxides, such as optical wave-guides, laser frequency doubling, high capacity computer memory cells, superconductivity, and etc. (Orlando Auciello, 1998; Mete *et al.*, 2003; Janotti *et al.*, 2012).

Similar to other semiconductor materials, the physical properties of perovskite oxides are affected by both intentional and unintentional defects. The computational study of defects and interfaces in tetrahedral-bonded (four-fold coordination) semiconductors such as Si, Ge, GaAs, CdSe, GaN, AlN, InN, ZnO, and etc, is very well developed and extensive (see for e.g., Stampfl and Van de Walle, 1999; Van de Walle *et al.*, 2001; Van de Walle and Neugebauer, 2004; Northrup and Zhang, 1993; Mattila and Nieminen, 1996; Janotti and Van de Walle, 2007; Du *et al.*, 2005; T-Thienprasert *et al.*, 2012). However, to our knowledge, computation study of defects and interfaces in perovskite oxides is quite limited. To aid the engineering process of this class of materials to the same success as those group-V, III-V and II-VI semiconductors, it is important that the computational framework for this class of materials is well established. Although, it seems straightforward to apply the framework of the four-fold coordination semiconductors to this class of materials, there are two major differences. (1) Perovskite oxides are ternary compounds which mean their growth conditions involve much more complicated conditions in the chemical potential space. In binary compounds, for instance GaN, the extreme growth conditions can be either Ga-rich or N-rich and other growth conditions can be varied in between the two. But for perovskite oxides, for instance $SrTiO_3$, there are three chemical potentials involved and the thermodynamically stable growth condition is defined in this three dimension space of the chemical potentials. (2) In the perovskite structure, the coordination of the cations and the empty space in the crystal are very different from the well-known diamond-like structures (wurtzite and zincblende). This is very important to understand the defects and interfaces. For example, the common sites for an interstitial atom such as bond center (BC), antibonding (AB), octahedral and tetrahedral opening sites are no longer the same.

In this thesis, we plan to select some interesting defect and interface systems of perovskite oxides that can be used as examples to establish the framework for standard computational study of defects and interface in this class of materials. Not only the new knowledge on the selected systems will be obtained, but we also hope that the procedure used will set an example that can be applied to study other defects and interfaces in this class of materials.

For defects and impurities, we choose to study hydrogen, selected native defects and cation impurities such as Mn in $SrTiO_3$ and Ca in $BaTiO_3$ and $(Bi_{1/2}Na_{1/2})TiO_3$.

For interface, we choose to study 2D electron gas in $SrTiO_3/LaAlO_3$ system. These choices of the systems are based on following reasons.

Hydrogen, selected native defects and cation impurities in $SrTiO_3$: Hydrogen is known to greatly impact materials' electronic properties and is very difficult to avoid incorporation during growth due to its high diffusivity and availability. In oxides, hydrogen has been suspected to exist as interstitial defects, substitutional defects as well as defect complexes with other impurities and native defects. Each form of H has unique effect on the conductivity of the host material. Therefore, it is very important that the correct form of H is identified. Because H can exist in different forms, H in $SrTiO_3$ is a good example system to study possible defects in perovskite structure. For oxides, cation-doping is generally used to intentionally dope the material to gain desired conductivity needed. For $BaTiO_3$, metal and transition-metal atoms has been proposed as doping elements. Calcium (Ca) doping can effectively improve the temperature characteristic of capacitance (TCC) for the $BaTiO_3$ or $(Bi_{1/2}Na_{1/2})TiO_3$ system (Yuan *et al.*, 2010), the nonlinear optical and electro-optic coefficient, which is important properties to designing nonlinear optical device can be dramatically enhanced by doping Fe (Zhang *et al.*, 2007). Other cation impurities such as Zr or Sn in $BaTiO_3$ or Ca, Pb, and Ba in $SrTiO_3$ crystals can change their relaxor ferroelectric behaviors (Maiti *et al.*, 2008); (Moura *et al.*, 2008; Wei and Yao, 2007; Bednorz and Müller, 1986; Lemanov *et al.*, 1996). To enhance the stability against chemical reduction, a metal element with a lower valence state, e.g., Mg^{2+}, Ni^{2+}, and Mn^{3+}, can be used to dope into perovskite oxides as an acceptor dopant (Moriwake, 2004; Jia *et al.*, 1994). Two-dimension electron gas in $SrTiO_3//LaAlO_3$ system: Intrinsic point or native point defects such as O vacancies and other vacancy related defects are believed to play an important role in electrical conductivity and in detaining dielectric property of perovskite oxides (Scharfschwerdt *et al.*, 1996). Oxygen vacancies or some kind of cation intermixing are believed to be the cause of carriers with a density varying in a wide range, e.g., from 0.5 *e*/Å up to three orders of magnitude more in the interface between two band insulators $LaAlO_3$ (LAO) and $SrTiO_3$ (STO) perovskites (Eckstein, 2007; Li *et al.*, 2011) leading to a 2D electron gas. There are variety of models proposed to explain the origin of this interesting carriers at the interface. Recently, Li *et al.* (Li *et al.*, 2011) showed, based on density functional calculations, that oxygen vacancies are preferentially formed on the LAO surface. These surface oxygen vacancies provide the carriers that lead to the two-dimensional electron gas at the interface. This work demonstrates that the band profile at the interface is mainly determined by the concentration of the surface oxygen vacancies consistent with available experimental results. A. Janotti *et al.* (Janotti *et al.*, 2012) introduced a model to explain the high electron density of 3.3×10^{14} cm^{-2} (0.5 electrons per unit cell) by assuming that the carriers are originated from somewhere other than the ideal interface. The sources can be oxygen vacancies or Sr-La intermixing at the interface. They proposed that if the exposed AlO_2 (LAO top of surface) surface is passivated, the electron transfer is suppressed and a 2DEG can in principle be observed. Based on their work, the role of the free surface LAO is very interesting and require further investigations.

Although, perovskite oxides have been investigated theoretically and experimentally for many years, there are many outstanding issues that need to be investigated theoretically. This is especially true for the investigation in the view of perovskite oxides as semiconductors where the electronic properties of defects and interfaces are studied in details. Some perovskite oxides systems have been studied by first principles calculations. However, most of the works are on structural stability of pure materials and works on defects or impurities are limited. Because doping in perovskite oxides has been of great interests and experimental results are widely available with limited theoretical explanations. Learning from other oxides, metal ions as an impurity can occupy on the cation sites (in this case, A-site or B-site) or act as an interstitial depending on the equilibrium growth conditions, their ionic radii and charges. The metal impurities can also form complex defects with other native defects and other widely available impurities such as vacancies and hydrogen. Examples of possible complexes are cation impurity on Ti-site with oxygen vacancies and simultaneous substitution at both *A*-site atom and Ti site with self-compensation ions (Eror and Balachandran, 1982; Witek *et al.*, 1984) and cation impurity – hydrogen complexes (Weber *et al.*, 1986; Tarun and McCluskey, 2011).

Consequently, in order to gain more fundamental understanding in perovskite oxides. In this thesis, we propose to perform first principle calculations to investigate properties of native point defects and impurities in selected perovskite oxide systems that are of current interests, have technological implications, and can set standard to study other similar systems. If needed, formation of defect complexes between native defects and between native defects and dopants will be investigated. To confirm the predicted local structure models and electronic structure model measurable spectra and some parameter such as infrared spectra, x-ray absorption spectra, x-ray photoelectron spectra, carrier densities and mobility that can be directly compared with IR, XAS, XPS measurements and crystal growth processes, will be performed. The obtained local structure models of defects will provide crucial knowledge for controlling electronic and optical properties of each perovskite oxide and will pave the way toward the successful engineering design to utilize the material for electronic applications.

1.2 Research Objectives

1. To study the electronic and optic properties of selected defects and dopants in $SrTiO_3$, $BaTiO_3$ and $(Bi_{1/2}Na_{1/2})TiO_3$ perovskite oxides.

2. To study potential defects that is the cause of the recent observed 2DEG in $SrTiO_3$//$LaAlO_3$ interfaces.

For the selected systems under study, their local structures, electronic structures, energies, or optical properties that can be used to compare with experiments will be studied.

1.3 Scope and Limitation of the Study

1.3.1 Scope of the study

This thesis will cover a theoretical study of selected perovskite oxides based on first principles density functional theory. Systems that have impact on technological applications but not yet thoroughly investigated by first principles calculations will be selected. At this point, we have identified a few potential systems, including defects and impurities in $BaTiO_3$, $SrTiO_3$, and $(Bi_{1/2}Na_{1/2})TiO_3$. In addition the $SrTiO_3$//$LaAlO_3$ interfaces that are experimentally observed to give 2DEG will be studied with the focus on the role of defect on LAO surfaces. For selected systems, depending on the available data in the literatures and current interests, potential point defects will be selected and studied. The formation of such native defects, impurities, and related complexes, when needed, will be investigated. Their energetic, electronic and optical properties will be calculated. If there are experimental characterization results available, some of the properties will be simulated for direct comparisons.

1.3.2 Limitations of the study

The calculations will be employed at the DFT levels with LDA and/or GGA (PBE) exchange correlations. DFT calculations are known to provide good and consistent total energy results and accurate mechanical properties. However, the electronic band gaps are known to be underestimated due to the simplification employed (replace the many-body interactions with density functional interactions). Important defects signatures that can lead to their identifications in actual experiments will be simulated. Depending on defect, the signatures can be IR absorption characteristics, X-ray absorption characteristics, X-ray photoelectron spectroscopy, and etc. For defect calculations, the supercell size of around 120 – 200 atoms, which is widely accepted to be sufficient to study the diluted limit of defects, is the limit of our computational resource for the DFT-level calculations.

CHAPTER II

THEORETICAL APPROACHES

2.1 First Principles Calculations in Materials

First principles or ab initio method means investigation without using empirical assumption or parameters (Kresse and Furthmüller, 1996). In order to calculate the properties of solids or clusters by first principles, the systems are treated as electrons and nuclei and their behaviors can be described by quantum mechanics, such as the many-body non-relativistic Schrödinger equation with Hamiltonian H below.

$$H = -\sum_{I}\frac{\hbar^2}{2M_I}\nabla_I^2 - \sum_{i}\frac{\hbar^2}{2m_e}\nabla_i^2 - \frac{1}{4\pi\varepsilon_0}\sum_{i,I}\frac{Z_I e^2}{|\vec{r}_i - \vec{R}_I|} + \frac{1}{2}\frac{1}{4\pi\varepsilon_0}\sum_{i\neq j}\frac{e^2}{|\vec{r}_i - \vec{r}_j|} + \frac{1}{2}\frac{1}{4\pi\varepsilon_0}\sum_{I\neq J}\frac{Z_I Z_J e^2}{|\vec{R}_I - \vec{R}_J|} \quad (2.1)$$

Where $\hbar$ is Plank's constant, ε_0 is the vacuum permittivity, M_I are the mass of nuclei, m_e is the mass of electron, Z_I are atomic numbers, $\vec{R}_I$ and $\vec{r}_i$ are the position of nuclei and electrons correspondingly.

The first and second term are the kinetic energy terms of nuclei and electron, the third, fourth and fifth terms are the Coulomb potentials for interaction of electron-nucleus, electron-electron and nucleus-nucleus, respectively. However, quantum behavior of nuclei is insignificant in most cases, since nuclear mass M_I is much larger than electron mass m_e (Martin, 2004). In most first principles method, such as Hatree-Fock theory or Density Functional theory, nuclei are treated classically and electrons are described by quantum mechanics.

2.2 Born-Oppenheimer Approximation

It is more convenient to ignore the motion of nuclei (the first term in equation (2.1)), as nuclear mass M_I is much larger than electron mass m_e. This results in the approximation called Born-Oppenheimer or adiabatic approximation (Martin, 2004; Harrison, 2003). With this approximation, the Hamiltonian becomes;

$$\begin{aligned} H &= -\sum_I \frac{\hbar^2}{2M_I}\nabla_I^2 - \sum_i \frac{\hbar^2}{2m_e}\nabla_i^2 - \frac{1}{4\pi\varepsilon_0}\sum_{i,I}\frac{Z_I e^2}{|\vec{r}_i - \vec{R}_I|} + \frac{1}{2}\frac{1}{4\pi\varepsilon_0}\sum_{i\neq j}\frac{e^2}{|\vec{r}_i - \vec{r}_j|} + \frac{1}{2}\frac{1}{4\pi\varepsilon_0}\sum_{I\neq J}\frac{Z_I Z_J e^2}{|\vec{R}_I - \vec{R}_J|} \quad (2.2) \\ &= T + V_{ext} + V_{int} + E_I \end{aligned}$$

Or $H = H_e + E_I$, where T, V_{ext}, V_{int} and E_I are the second to fifth term in Equation (2.1) or the first to fourth terms in equation (2.2); H_e includes the first three terms related to interaction on electrons, and E_I is simply reduced to the classical Coulomb potential of nuclei.

States of electron are possibly to be determined by H_e with the nuclei at certain positions $\vec{R}_I$. If the wave functions Ψ of electrons are obtained, the energy of the system can be determined as

$$E = \langle\Psi|H_e|\Psi\rangle + E_I \quad (2.3)$$

Many useful quantities can be derived from the system energy. For example, the force (by electron) on a nucleus at $\vec{R}_I$ can be obtained via Hellmann-Feynman theorem, and the force on the nucleus at $\vec{R}_I$ due to other nuclei can be calculated classically (Martin, 2004; Feynman, 1939). Therefore, the force on the nucleus at $\vec{R}_I$ is

$$F = -\langle \Psi | \frac{\partial H_e}{\partial R_I} | \Psi \rangle - \frac{\partial E_I}{\partial R_I} \tag{2.4}$$

The force obtained can be used for optimization of the systems or dynamics calculations such as ab initio molecular dynamics (ab initio MD).

2.3 Density Functional Theory (DFT)

The problem of first principles calculation for solids or cluster of atom is reduced to a Schrödinger equation of many electrons, as shown below.

$$H_e = -\sum_i \frac{\hbar}{2m_e} \quad {}_i \quad \frac{1}{4\pi\varepsilon_0}\sum_{i,I}\frac{Z\,e^2}{|\vec{\ }_1 \quad {}_I|} \quad 1 \quad 1 \quad \varepsilon_0 -\sum_{i\neq j}\frac{e^2}{|\vec{\ }_1 \quad \vec{\ }_j|} \quad {}_{xt} + V_{int} \tag{2.5}$$

T is the kinetic term, and V_{ext} is Coulomb potential due to nuclei which is independent to electrons V_{int} is the most problematic term since it depends on the state of electrons, but the state of electrons is to be determined by H_e.

One may apply the independent electron approximation to split the N-electron Schrödinger equation to one-electron Schrödinger equations and to solve the N equations one by one from this with lowest Eigen energy, but it gives no correlation (the third term in equation (2.5)) between electron (Martin, 2004). Since electrons are indistinguishable, and electrons are Fermions which follow Pauli exclusive principle. It requires the wave function $\Psi(\vec{\ }_1, \vec{\ }_2, \ldots \vec{\ }_N$, for $\vec{\ }_1$ $\vec{\ }_j$ and $i \neq j$, and $|\Psi(\vec{\ }_1, \vec{\ }_2, \ldots \vec{\ }_N|$ remains unchanged with exchanging any two coordinates $\vec{\ }_i, \vec{\ }_j$. N-electron wave function may therefore be expressed as determinant (known as Slater determinant) of the N one-electron wave functions in N coordinates as shown below (Martin, 2004; Harrison, 2003).

$$\Psi(\vec{r}_1, \vec{r}_2, \ldots\ldots \vec{r}_N) \quad \sqrt{N!} \begin{vmatrix} \psi_1(\vec{r}_1) & \cdots & \\ \vdots & \ddots & \vdots \\ \psi_N(\vec{r}_1) & \cdots & \end{vmatrix} \tag{2.6}$$

It is Hartree-Fock approximation, if the V_{int} is approximated by self-consisting mean field potential (guess the wave function and electron density to calculate the potential due to average guess electron density, and use the solution or combine it with old guess as new guess). The (average) electron density n(r) is

$$n(r) = \sum_i \left|\psi_i(\vec{r}\,)\right| \tag{2.7}$$

The Hamiltonian H_{HF} under Hartree-Fock approximation is

$$H_{HF} = -\sum_i \frac{\hbar}{2m_e} \quad \frac{1}{4\pi\varepsilon_0} \sum_{i,I} \frac{Z\,e^2}{|\vec{r}_i \quad |} \quad \varepsilon_0 - \int \frac{n(\vec{r}_j)}{|\vec{r}_i \quad \vec{r}_j|} \tag{2.8}$$

In DFT, however, the correlation of electrons is included, at least in principle, and the convenience of independent electron approximation is kept. By the two Hohenburg-Kohn Theorems, the ground state electron density $n_0(r)$ determines the V_{ext} (and therefore the H_e), and there is a universal energy functional $E[n]$ for any V_{ext} that $E[n_0]$ is the global minimum and equal to the ground state energy of H_e. If the form of the energy functional is known, the ground state density $n_0(r)$ and the ground state energy E_0 are obtained, many properties can be derived from them, and the aims of first principles calculation can be achieved.

However, the form of energy functional is not known, so approximation is applied in DFT calculations. The energy (only consider the many-electron system) in functional form is

$$E[n_0]=T[n_0]+V_{ext}[n_0]+V_{int}[n_0] \tag{2.9}$$

Consider the Kohn-Sham approach, which assumes that there is a many-body system without interaction equivalent to the original many-body interacting system which gives the same energy E and the same electron density n. The original potential ($V_{ext}+V_{int}$) is only replaced by an effectives potential (V_{KS}) in formula, but the "electrons" in the new system act independently. The formula of Kohn-Sham Hamiltonian H_{KS} is H_{HF} added by the exchange and correlation term E_{XC}.

$$H_{KS} = -\sum_i \frac{\hbar}{2m_e} \quad \frac{1}{4\pi\varepsilon_0}\sum_{i,I}\frac{Z e^2}{|\vec{r}_i \quad \vec{r}_I|} \quad \varepsilon_0 \quad -\int\frac{n(\vec{r}_j}{|\vec{r}_i \quad \vec{r}_j|} \quad -_{XC} \tag{2.10}$$

And the ground state energy is:

$$E[n_0]=T[n_0]-\frac{1}{2}\frac{1}{4\pi\varepsilon_0}\sum_I\int\frac{n_0(\vec{}}{|\vec{r}_i \quad \vec{r}_I|} \quad \frac{1}{\pi\varepsilon_0}\int\frac{n_0(\vec{r}_i}{|\vec{r}_i \quad \vec{r}_j|} \quad \vec{r}_j \quad -_{XC}[n_0] \tag{2.11}$$

Since it is non-interacting system in Kohn-Sham approach, the N-electron wave function is a determinant of N by N single electron wave functions as equation (2.6), but it is not the independent electron approximation in DFT. The electron density n can also be expressed by N one-electron wave function ψ_i as equation (2.7). By applying variational principle to the energy functional in equation (2.11), the N-electron Schrödinger equation can be separate into one-electron Schrödinger like equation (Kohn-Sham equation) as show in equation (2.12) below (Harrison, 2003; Jones and Gunnarsson, 1989).

$$\left(-\frac{\hbar}{2m_e} \quad \frac{1}{4\pi\varepsilon_0}\sum_{I}\frac{Z\,e^{2}}{|\vec{r}_i \quad -_I|} \quad -\frac{1}{4\pi\varepsilon_0}\int\frac{n\,(\vec{\ }}{|\vec{\ } \quad \vec{r}_j|} \quad \partial n \quad)\psi_i(\vec{r}) \quad \varepsilon_i\psi_i(\vec{r}) \qquad (2.12)$$

The exchange and correlation term E_{XC} in equation (2.12) is not known in general, but it can be approximated by different approaches such as Local density approximation (LDA), Generalized Gradient approximation (GGA), Perdew-Burke-Ernzerhof (PBE) and Hybrid functional Heyd-Scuseria-Ernzerhof (HSE) which is a class of approximations to the exchange–correlation energy functional in density functional theory (DFT) that incorporate a portion of exact exchange from Hartree–Fock theory with exchange and correlation from other sources (ab initio or empirical). DFT can be extending to spin-polarized systems, with consideration of both electron density and spin density. By self-consistent process, as show in Figure 2.1, the energy functional $E[n]$ is minimized with the set of one-electron wave function ψ_i obtained from equation (2.12) to solve the many-electron system. The total ground state energy of N electrons (non spin-polarized) is

$$E=2\sum_{i=1}^{N/2}\varepsilon_i-\frac{1}{2}\frac{1}{4\pi\varepsilon_0}\int\frac{n_0(\vec{r}_i \quad \vec{\ }}{|\vec{r}_i \quad \vec{r}_j|} \quad \vec{r}_j \quad E_{XC}[\ ] \quad \partial n \quad n(\vec{r}) \qquad (2.13)$$

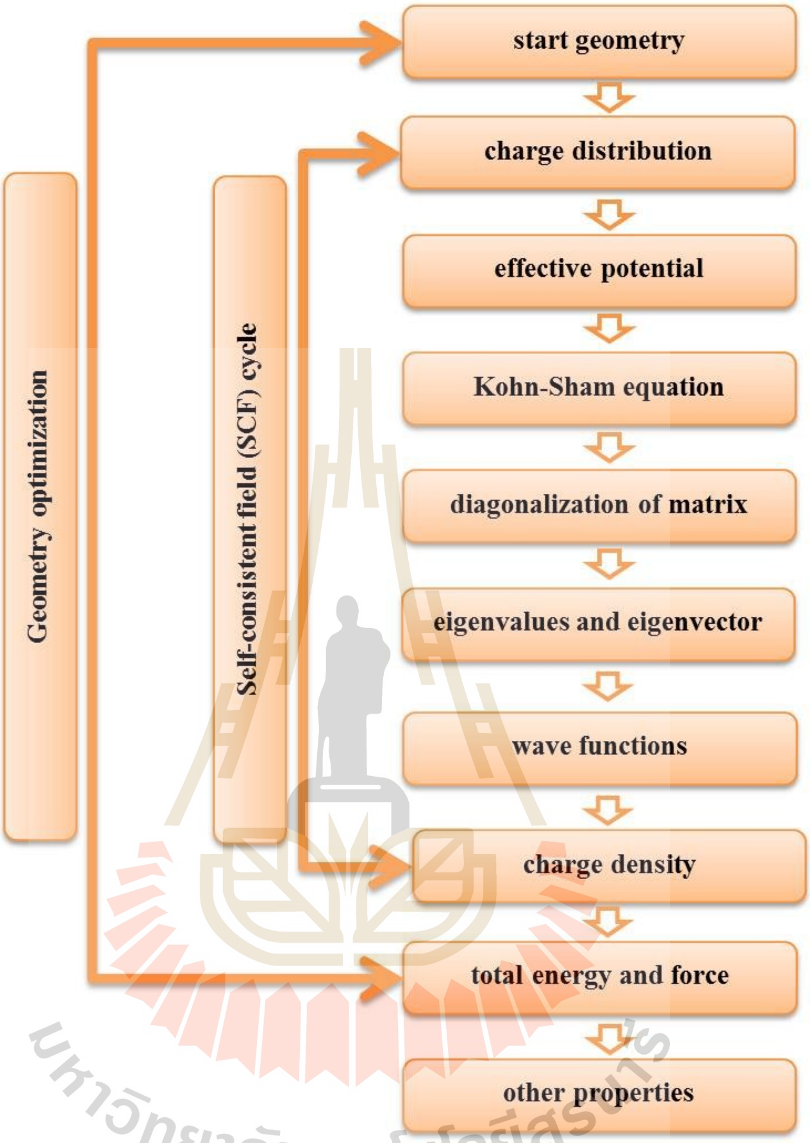

Figure 2.1 Scheme of typical electronic calculation. The outer cycle represents the geometry optimization or other manipulation of geometry. The inner cycle is the self-consistency procedure to solve the Kohn-Sham equation.(Martin, 2004; A J Freeman and Wimmer, 1995).

2.4 Basis, Pseudo-potential and Projector Augmented Wave method

The wave functions of electrons are not analytical functions, except very few simple systems, such as a hydrogen atom. During computation, wave function can be denoted as digits for each grid point in the space (or in reciprocal space) being considered or decomposed in different sets of basis, like plane wave basis, atomic orbital basis or Gaussian basis. Plane wave basis is implemented in VASP, the code for all first principle calculations in this project. More issue about plane wave basis is shown in the following in this session.

In a crystal, the (one electron) wave function ψ_k, by Bloch Theorem, is

$$\psi_k(\vec{r}) = u_k(\vec{r})e^{i\vec{k}\cdot\vec{r}} \tag{2.14}$$

Where $u_k(\vec{r})$ is periodic with period equals to the lattice vector $\vec{R}$. Expressing u_k in Fourier series, it becomes equation (2.15) below.

$$\psi_k(\vec{r}) = \sum_m c_m e^{i(\vec{k}+\vec{G}_m)\cdot\vec{r}} \tag{2.15}$$

Where $\vec{G}_m$ is the reciprocal lattice vector.

It automatically spans in plane wave basis. In computation, it includes only finite terms with $|\vec{k}+\vec{G}_m| < q$, and q is the cutoff wave number. Cutoff energy E_{cutoff} is defined as $\frac{\hbar^2}{2m_e}q^2$ which is more commonly shown in DFT calculations with plane wave basis (Gonze, 2005; Van de Walle *et al.*, 2001).

Using plane wave basis set has some advantages, compared to other basis sets like those localized basis sets, for example, atomic orbital or Gaussian-type basis. It is complete orthonormal basis set to span any periodic functions. The accuracy can be simply controlled by cutoff energy E_{cutoff} or cutoff wave number q, as it converges as $q \rightarrow \infty$, and it is easy to formulate. For example, performing Fourier transforms between real space and reciprocal space or calculating matrix elements of different observables (Ohno *et al.*, 2012; Springborg, 2000). It is easy to calculate 3-dimension periodic systems (bulk crystalline solid). However, it also induces some disadvantages. The boundary condition of simulation box is restricted to 3-dimentional periodic. To simulate systems of low-dimensional, such as surfaces (LAO//STO surface and interfaces in Chapter IX), huge box or unit cell of simulation with vacuum region is required to reduce the interaction between different periods that results in significant increase of computational demand. Huge simulation box can also increase the basis size for the same cutoff, since the different between $\vec{G}_m$ in equation (2.15) decreases with size. Most electrons behave localized around nuclei, but plane waves are extending in space, so it requires a large set of plane waves (high cutoff energy) to span the wave functions.

The core electrons of atoms are of less interesting for most purposes of studies, since they hardly change in different situation, such as in chemical reactions. It should improve the speed of calculating, if only valence electrons are considered, with core electrons ignored.

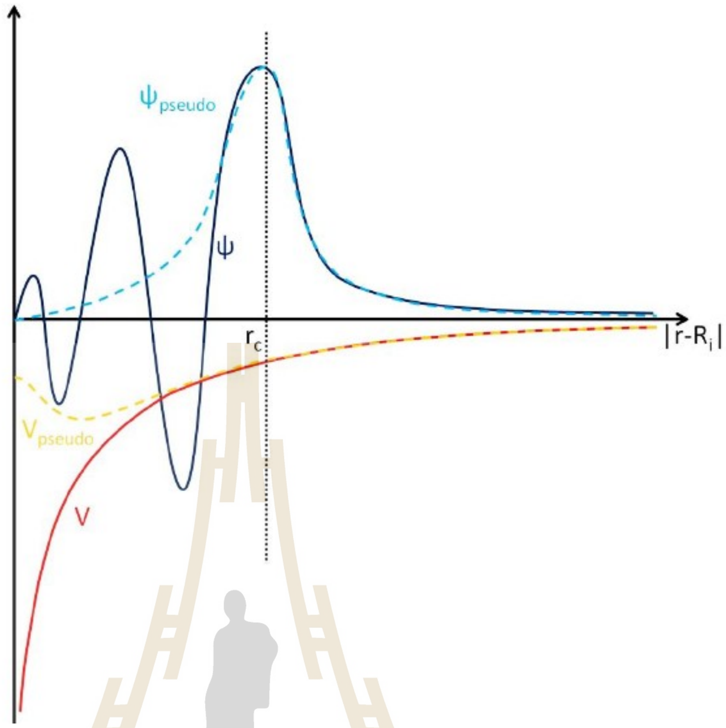

Figure 2.2 The pseudowavefunction (blue dash line) and the true wave function (blue solid line), and the corresponding pseudopotential (orange dash line) and true potential (red solid line) from an atom at R_i. The cut off radius is r_c.

Pseudopotential method is developed to increase the efficiency of computation by reducing the number of electrons and the size of basis, therefore especially important for plane wave basis. In pseudopotential approximation, the Kohn-Sham effective potential (last three terms in left side of equation (2.12)) is further replaced by an effective potential (called psuedopotential) that keep wave functions of valence electron outside a certain cutoff radius r_c from a nucleus, like Figure 2.2, but the core electrons and the singularity of Coulomb potential are removed from the effective systems. It restricts to keep the norm of wave function within cutoff radius in the approach of norm-conserve psuedopotential. The ultrasoft-psuedopotential, faster but less accurate in general, aims to mostly smoothen the wave functions within the cutoff region, leading to reduce the number of plane wave to span waves functions. Correction of relativistic effect can also be induced in the psuedopotential (Martin, 2004; A J Freeman and Wimmer, 1995).

By generalizing pseudopotential and projector augmented wave (PAW) method (Blöchl, 1994; Kresse and Joubert, 1999) are developed to improve the accuracy, and keep the efficiency. PAW is also employed in VASP code for the calculation of almost work in this thesis.

Blöchl (Blöchl, 1994) proposed the projector augmented wave method and started that “The physically relevant wave functions in this Hilbert space exhibit strong oscillation, which make numerical treatment cumbersome. Therefore, we transform the wave functions of this Hilbert space into new, so-called pseudo (PS) Hilbert space.” This is basic idea of PAW method. A linear transformation τ is used to transform pseudo wave functions ($\tilde{\imath}$) to wave function in all-electron method (ψ).

The transformation τ is chosen to be some local atom-center contribution $\tilde{}$ within augmentation region Ω_R but unchanged elsewhere, so,

$$\tau = I + \sum_{R} \tilde{} \tag{2.16}$$

Similar to pseudopotential, $\tilde{}$ are chosen that transform some ($\tilde{\imath}$), which are smoothen in Ω_R, to some (ψ_n), which usually are the valence atomic orbitals of an isolated atom orthogonal to core state. Core electrons are treated in a similar way, but the wave functions of core electron are not changed in the self-consistent process in calculation (Kresse and Joubert, 1999). Most calculations are done with pseudo wave functions and pseudo operator in pseudo Hilbert space, so the efficiency is close to ultrasoft pseudopotential method. The result can be projected back to Hilbert space of all-electron method, so the results are consistent to all-electron calculations with frozen core approximation.

2.5 Periodicity of the Crystal

In order to apply DFT to a real crystal, the KS equations should be solved for all the particles present in the system. Since there are too many particles in a real solid (roughly 10^{24} electrons and ions per cm^3), this will be computationally impossible. Therefore one should look for other possible approximations to solve the problem. Crystal structures are built up from a unit cell which is periodically repeated. To reduce the number of particles in a calculation, it is enough to consider only the unit cell of the crystal. It consists of atoms, whose arrangement defines the crystal’s symmetry, and its repetition in three dimensions in space generates a crystal structure. The unit cell is characterized by lattice parameters. To predict the property of a crystal it is enough to solve the Kohn-Sham equation for a small unit cell of a real solid.

2.6 Brillouin Zone Sampling and Other Techniques

For periodic system, summation of the Eigen value ε_i in equation (2.13) is replaced by integration of $\varepsilon_{k,i}$ for the k over the Brillion zone for all occupied band (equation (2.17)), and in formalism, should be done by calculating the total energy period (unit cell).

$$2\sum_{i=1}^{N/2}\varepsilon_i \rightarrow \int_k \varepsilon_{k,i}\,dk \tag{2.17}$$

In computation, the Eigen values can be obtained at finite number of k-points, and interpolation may be done between discrete k-points. However, some problems rise then. For example, the choice of k-points may affect the efficiency and accuracy of calculation. If there are partial occupied bands, such as those in metals, the integration has to stop at Fermi-level. It may also cause numerical instability and difficultly in converging, since the occupation of the states around Fermi-level might change rapidly during iteration to search the ground state.

There are many ways to sample the k-point. Monkhorst and Pack (Monkhorst and Pack, 1976) suggested a $q_1 \times q_2 \times q_3$ Monkhorst-Pack mesh point given by

$$\vec{k} = u_1\vec{G}_1 + u_2\vec{G}_2 + u_3\vec{G}_3 \tag{2.18}$$

Where $\vec{G}_1$, $\vec{G}_2$, $\vec{G}_3$ are the reciprocal lattice vectors, and

$$u_i = \frac{2r\text{-}q_i\text{-}1}{2q_i},\ r=1, 2, \ldots.\ q_i,\quad \text{where } i=1, 2, 3 \tag{2.19}$$

This gives and unbiased sampling in the Brillouin zone, and the mesh is symmetric. Some points would be equivalent, for the lattice with symmetry. The even Monkhorst-Pack mesh point is more efficient than odd Monkhorst-Pack mesh point, in general(Ohno *et al.*, 2012; Martin, 2004). For example, both of the mesh of 3×3×1 and 4×4×1 for square lattice can be reduced to only three inequivalent k-point, but 4×4×1 is certainly denser than 3×3×1. It should be notice that even Monkhort-Pack meshes do not include gamma point (0,0,0) in Brillouin zone, but it is necessary to include gamma point for some geometry, such as hexagonal lattice. Therefore, the choice of k-points should be concerned, although sometimes it is not mentioned in report.

To improve the numerical stability, especially in metallic systems, smearing of the states can be applied. Fractional occupations of states occur with smearing, so that density of states is smoothened and the occupations of states around Fermi-level change continuously during iteration. Many schemes of smearing are possible. For example, Fermi smearing produces the smearing such that occupation of states follows Fermi distribution. Fermi-Dirac function:

$$f\left(\frac{\varepsilon_{\mathrm{i,k}}-\varepsilon}{\sigma}\right)=\frac{1}{\exp\left(\frac{\varepsilon_{\mathrm{i,k}}-\varepsilon}{\sigma}\right)+1} \qquad (2.20)$$

and

$$f\left(\frac{\varepsilon_{\mathrm{i,k}}-\varepsilon}{\sigma}\right)=\frac{1}{2}\left(1-erf\left[\frac{\varepsilon_{\mathrm{i,k}}-\varepsilon}{\sigma}\right]\right) \qquad (2.21)$$

Gaussian smearing are applied in this thesis for metal and semiconductor, respectively. The degree of smearing is related to the σ parameter called smearing width. Occupation of states above Fermi-level depends on the scheme of smearing, but there should be more occupation above Fermi-level for larger smearing width in general. As DFT is derived for a system ground state, occupation above Fermi-level would produce error. For accurate calculation, a dense mesh of k-point and a small width of smearing should be used.

CHAPTER III

CALCULATION METHOD FOR DEFECTS IN SEMICONDUCTORS, INTERFACES AND SURFACES

In this chapter, the methodologies need for investigating selected defect in semiconductor and interfaces of semiconductor structure (in chapter V to IX) are described. First principles calculations enable us to investigate their behaviors and properties. Base on first principle calculations, one can investigate several properties, e.g. local geometry of defect, electronic structure of defect, defect infrared spectroscopy signature, x-ray absorption characteristics and x-ray photoelectro spectroscopy. The defect formation energy can also be obtained. The formation energy can be used to estimate the defect concentration. For the calculations, we use a plane-wave pseudopotential cade called "Vienna Ab-initio Simulation Package (VASP)" (Kresse and Furthmüller, 1996; Kresse and Furthmüller, 1996).

3.1 Defect Concentration

For creation of defects and impurities in a crystal normally costs energy. One of the main quantities in the study of point defects is the Gibbs free energy. In thermodynamic equilibrium the concentration c of an impurity in a crystal is given by the expression (Van de Walle and Neugebauer, 2004; Kohan *et al.*, 2000).

$$c = N\exp(-\Delta G / k_B T) \tag{3.1}$$

Where N is the number of equivalent possibilities, with the same energies, in which the defect can be incorporated (per unit volume). ΔG is the change in the Gibbs free energy of the system, k_B is Boltzmann's constant, and T is the temperature.

The change in Gibbs free energy of the system is given by

$$\Delta G = \Delta E + P\Delta V - T\Delta S \tag{3.2}$$

Where ΔE is the change in the total energy (contains chemical potential terms), P is the pressure, ΔV is the change in the volume when an impurity is introduced into the system, and ΔS is the change in vibrational entropy of the system. The change in the volume is negligible for most crystalline solids at moderate temperatures and atmospheric pressure. Moreover for different defects, the change in vibrational entropy is usually very small. Therefore the Gibbs free energy of the system is equal to the formation energy ($\Delta E = E_f$) of the system. Hence equation (3.1) can be written as

$$c = N\exp(-E_f / k_B T) \tag{3.3}$$

According to this equation, defects with high formation energies will occur in low concentrations. Since the growth of a semiconductor is close enough to the equilibrium condition, it allow the use of the equation (3.3). This brings up the prominence of the formation energy of defects in crystals. Though thermodynamics provides the driving force for the formation of the defects, it should be noted that the number of defects also depends on the thermal history of the host material i.e. on the kinetics of the growth process. In the following, the derivation of the formation energy is discussed.

3.2 Formation Energy

Density functional theory calculations in the supercell geometry are used as a standard method to study defects and impurities in semiconductor materials. As discussed in chapter II, using appropriate exchange correlation energy functional provides a description of the many-body electronic ground state energy of a system.

Since the purpose of this thesis is to investigate the electronic properties of an isolated defect in an infinite crystal, performing calculations needs a large supercell containing a defect which provides a low concentration of defects in a crystal. The larger the supercell size, the smaller the interactions between defects and impurities in neighboring supercells, and the better the results will be compared to a single, isolated impurity. Moreover, relaxation of several layers of atoms around the impurity is also included inside the supercell.

Equation (3.3) shows that the concentration of point defects and impurities depends on their formation energies. The formation energy of a defect or impurity D in the charge state q is defined as

$$E_f[D^q] = E_{tot}(D^q) - E_{tot}(bulk) + \sum \Delta n_X \mu_X + q(E_F + E_{VBM} + \Delta V) \qquad (3.4)$$

where $E_{tot}(D^q)$ is the calculated total energy of a supercell containing a defect D in charge state q, $E_{tot}(bulk)$ is the calculated total energy of a defect-free supercell (bulk), n_X is the number of atoms x being added to a defect-free supercell to create a defect D, μ_X is the atomic chemical potential of atoms species x, E_F is the electron chemical potential, also known as Fermi energy, of the system referenced to the valence band maximum (E_{VBM}), which we choose to be the top of the valence band of the primitive defect-free unit cell. In semiconductor, the Fermi energy can be varied from the valence band maximum (VBM) to the conduction band minimum (CBM) depending on the carrier in the material. Sometimes, it can be estimated by assuming a sample is charge neutral. However, it is often more practical to study the defect formation energies of defects as a function of the Fermi energy. As the Fermi energy sweeps though the energy levels associated with defects, electrons move from an external reservoir into the system to occupy this level. In this picture, the stable charge state, i.e., charge state q that gives the minimum defect energy $E_{tot}(D^q)$, changes as the Fermi level is varied such that the defect levels can be identified with kink in a graph of defect energy for the stable charge state versus E_F. However, In the defect containing supercell, the position of band edges (CBM, VBM) is affected by the defect, which brings different reference energies for the defect containing and the perfect crystal. In order to assume that we use the same reference energy level for the calculations with and without the defect, another term (denote as ΔV) should be added to the formation energy for charge defect. This is schematically shown in Figure 3.1. A widely applied practice to determine ΔV is to consider the total electrostatic potential at some point, or region, far from the defect and to align it with the potential in the same region in the undoped supercell (Van de Walle and Neugebauer, 2004).

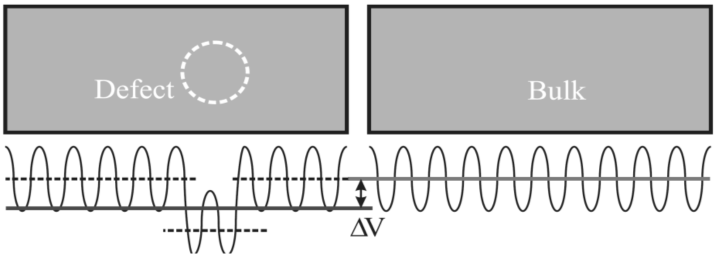

Figure 3.1 Schematic representation of the ΔV value.

For example, consider an oxygen vacancy as a native defect in an oxide material. The formation energy or the energy needed for an oxygen vacancy to form in a supercell is schematically shown in Figure 3.2. According to the definition, the formation energy is the difference between the total energy of the oxide with an oxygen vacancy and the initial pure oxide. Since an oxygen atom is removed from the system and is moved into a "reservoir" of oxygen atoms (e.g. a gas of O_2 molecules), the total energy of an oxygen atom in the reservoir ($\mu_{\mathrm{O}} = E[\mathrm{O}_2]/2$) should be also added to the formation energy expression. If the system is electrically charged, then an extra term should be considered. Here the oxygen vacancy gives away one electron and has a positive charge state, so the energy of an electron in its reservoir (chemical potential of the electron) is added to the formation energy expression. As mentioned before, defects can occur in multiple charge states, and the formation energy is different for each of them. The stable charge state for an impurity at a given Fermi level is the one which has the lowest formation energy.

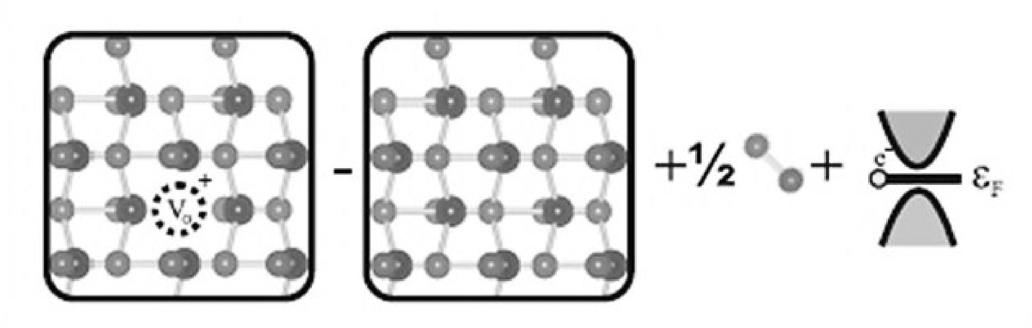

Figure 3.2 Schematic illustration of the formation energy of an oxygen vacancy in a crystal.

3.3 Chemical Potentials

As it is mentioned previously, the chemical potentials represent the energy of the reservoirs with which atoms are being exchanged. The chemical potentials highly depend on the experimental growth conditions, and should be considered as variables in the expression of the formation energy.

For example, to align the energy levels between the supercell containing defect and without defect (bulk), a deep core level of an atom is used as a reference point. For the bulk, the reference atom can be any atom because they are all equivalent. For a defect cell, such atom is chosen at the atom that is the most bulk-like, i.e., the atom that is the most far away from the defect center. The upper limits for the chemical potentials for a ternary system such as perovskite ABO_3, μ_A, μ_B, and μ_O are the energies per atom of the metallic A, metallic B and gaseous O_2, which are set to zero in this study. To grow ABO_3 crystal in thermal equilibrium, it is required that

$$\mu_{\mathrm{ABO_3}} = \mu_{\mathrm{A}} + \mu_{\mathrm{B}} + 3\mu_{\mathrm{O}} \tag{3.5}$$

However, A and B atoms can form compound with oxygen atom to form their oxide phases, such as AO, AO_2, A_2O_3, BO, BO_2, and B_2O_3. Therefore, the chemical potentials of A and B have to be further limited by considering these oxide phases. Accordingly, not only equation (3.5) but also the following equations are needed to be satisfied:

$$\begin{aligned}
&\mu_{\mathrm{AO}} \geq \mu_{\mathrm{A}} + \mu_{\mathrm{O}}, \\
&\mu_{\mathrm{AO_2}} \geq \mu_{\mathrm{A}} + 2\mu_{\mathrm{O}}, \\
&\mu_{\mathrm{BO}} \geq \mu_{\mathrm{B}} + \mu_{\mathrm{O}}, \\
&\mu_{\mathrm{BO_2}} \geq \mu_{\mathrm{B}} + 2\mu_{\mathrm{O}} \text{ and} \\
&\mu_{\mathrm{B_2O_3}} \geq 2\mu_{\mathrm{B}} + 3\mu_{\mathrm{O}}.
\end{aligned} \tag{3.6}$$

To illustrate the range of possible chemical potentials for ABO_3 growth, a triangular phase diagram is used (see Figure 3.3). The triangular phase diagram is actually the plane defined by equation (3.5) with the chemical potentials normalized (divided by $\mu_{\mathrm{ABO_3}}$, except the chemical potential of O divided by $3\mu_{\mathrm{ABO_3}}$) to make the sum equal to one. Then, equation (3.5) can be rewritten as

$$1 = \mu'_{\mathrm{A}} + \mu'_{\mathrm{B}} + \mu'_{\mathrm{O}} \tag{3.7}$$

The triangular phase of μ'_{A}, μ'_{B} and μ'_{O} is showed for the case of $BaTiO_3$ in Figure 3.3.

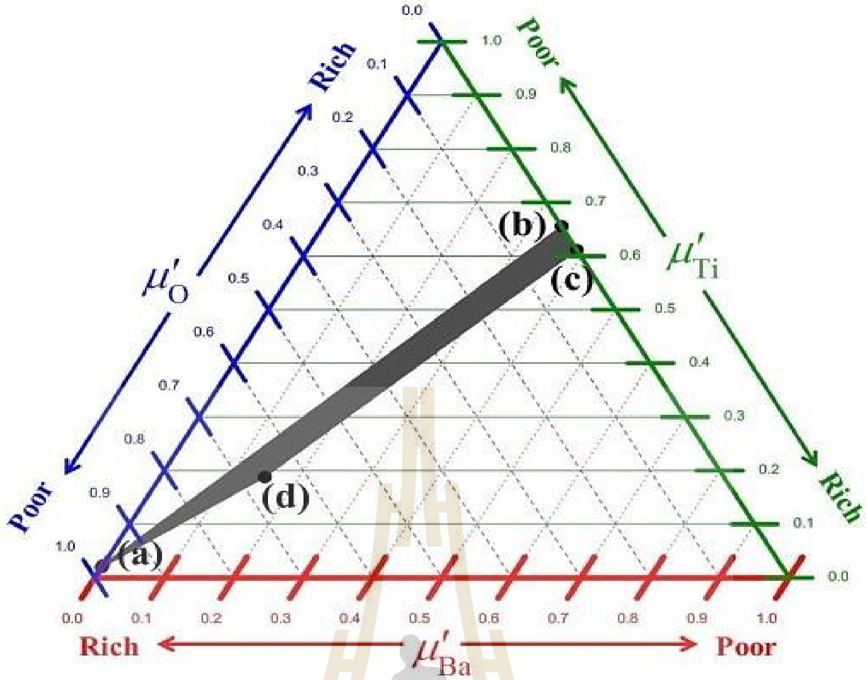

Figure 3.3 Triangular phase diagram representing the chemical potentials of Ba, Ti, and O for $BaTiO_3$ growth, according to equation (3.7).

In Figure 3.3, the black points and the shaded area on the diagram satisfied equation (3.6). To grow $BaTiO_3$ under thermal equilibrium, the chemical potentials of Ba, Ti, and O could be any values, which lie within the shade area. Outside the shaded area, one of the oxide phases would be formed instead of $BaTiO_3$. At point "a", the chemical potentials of Ba and Ti reach the maximum values and that of O reaches the minimum values, i.e., Ba-rich, Ti-rich and O-poor growth condition. At points "b", Ti reaches its lowest possible value while O reaches the maximum value, i.e., Ti-poor and O-rich growth conditions. At points "c", Ba reaches the minimum value and O reaches the maximum value, i.e., Ba-poor and O-rich growth condition. These three extreme points ("a", "b", and "c") will be used for calculating the formation energies of defects in ABO_3 in a similar manner as two extreme cases generally used for binary compounds (for instant, Zn-rich and O-rich conditions in ZnO). A defect with low energy is more likely to form than the higher ones (Northrup and Zhang, 1993). The formation energies can be used in the detailed balance to create the approximation of the defect concentrations. The defects with low formation energies are the ones that are likely exist and to aid experimental identification the obtained local defect structures will be further used for calculating XAS, local vibrational mode and other properties.

3.4 Other Methods and Techniques

In this section, other calculation technique are combined with first principle calculations to compare with experiment result, such as the nudged elastic band (NEB) method, local vibration mode calculation, X-ray absorption spectrum simulation, and core level binding energy calculation (to compare with XPS) will be presented.

3.4.1 The nudged elastic band

Point defect may be mobile, depending on many factors, e.g., local bond strength, size of the diffusion atoms, and temperature. The diffusion properties of defect are essential to understand their incorporation during growth processing. In experiment, the dynamics of point defect can be studied by several techniques, for e.g., the electron paramagnetic resonance (EPR) and positron annihilation measurement. The migration barriers are estimated based on the observations of the temperature at which defects become mobile. Therefore, the calculations of defect migration barriers are important. A method to find lowest energy path and the saddle point for a migration barrier of an atom between the initial structure and final structure, called “nudged elastic band (NEB)” method (Henkelman *et al.*, 2000; Henkelman and Jónsson, 2000) is use in this thesis. The NEB method works by optimizing a number of intermediate images along the reaction path. Each image is optimized to the lowest possible energy while maintaining equal spacing to its neighboring images. This constrained optimization is done by adding spring forces along the band between images and by projecting out the component of the force due to the potential perpendicular to the band. The object function of system consist of N images can be constructed as

$$S^{PEB}(\mathrm{R}_1,\ldots,\mathrm{R}_{N-1}) = \sum_{i=0}^{N} V(\mathrm{R}_i) + \sum_{i=0}^{N} \frac{Nk}{2}(\mathrm{R}_i,\ldots,\mathrm{R}_{i-1})^2 \qquad (3.8)$$

Where R_i is the reaction coordinate where some subset of the coordinates in the system is used to define a progress variable. $V(\mathrm{R}_i)$ is a potential function and k is the spring constant. One could imagine minimizing this object function to find a minimum energy path (MEP) with respect to the intermediate images while fixing the end point images. This method is referred as “plain elastic band (PEB)” where the force acting on image i is

$$\mathrm{F}_i = -\nabla V(\mathrm{R}_i) + \mathrm{F}_i^s \qquad (3.9)$$

where

$$\mathrm{F}_i^s = k_{i+1}(\mathrm{R}_{i+1} - \mathrm{R}_i) - k_i(\mathrm{R}_i - \mathrm{R}_{i-1}) \qquad (3.10)$$

The PEB method has its own fundamental problems. One problem is the corner cutting problem. This problem is resulted from a component of the spring force, which tends to pull images off the MEP. Another is the sliding down problem which result from component of the true force $\nabla V(\mathrm{R}_i)$ in the direction of path (Berne *et al.*, 1998). In the NEB method, these problems are solved by projecting out the perpendicular component of the spring force and the parallel component of the true force when minimizing of an elastic band. Therefore, the force acting on image *i* become

$$\mathrm{F}_i^0 = -\nabla V(\mathrm{R}_i)\big|_\perp + \mathrm{F}_i^s \cdot \hat{\tau}_\parallel \hat{\tau}_\parallel \qquad (3.11)$$

Where $\hat{\tau}_\parallel$ is the unit tangent to the path and $\nabla V(\mathrm{R}_i)\big|_\perp = \nabla V(\mathrm{R}_i) - \nabla V(\mathrm{R}_i) \cdot \hat{\tau}_\parallel \hat{\tau}_\parallel$. This projection of the perpendicular component of $\nabla V(\mathrm{R}_i)$ and the parallel component of the spring force is referred as “nudging”. NEB method is one of the most effective tools to find the MEP. NEB can find the energy barrier rather accurately, especially when sufficient images are included in the chain.

Among all the images only one will be exactly at saddle point, which corresponds to the saddle point along the MEP, thus Climbing Image (CI) NEB (Henkelman and Jónsson, 2000) has been developed. Within the CI-NEB, the image closest to the saddle point is chosen to climb the hill and to approach the saddle point. The image does not feel the elastic force and its dynamics is determined by a force F:

$$F(R_{C-I}) = -\nabla V(\mathrm{R}_i)\big|_\perp + 2\hat{\tau}_\parallel \left[\hat{\tau}_\parallel \cdot \nabla V(\mathrm{R}_i)\right] \qquad (3.12)$$

where the component parallel to the path is now reversed. The climbing image therefore moves toward a minimum in the direction perpendicular to the path, and toward a maximum along the path, which corresponds to move exactly toward a saddle point. The implementation of NEB method in the VASP code allows us to carry out CI-NEB and activation energy barriers for defect diffusions in solids.

3.4.2 Vibration mode frequency

The IR spectroscopy relates to the vibration of the atoms in a crystal. This is because the vibration frequencies of atoms in crystals are in the region of the frequency of IR light. Each crystal has their specific natural vibration modes. This leads to the signature absorption of the IR light at their resonance frequencies, showing up as peaks in the IR absorption spectrum (or Raman spectrum, depending on the symmetry of the vibration modes). The local vibrational mode (LVM) of a defect is its specific signature that can be used to characterize the defect using an IR absorption spectra or IR Raman spectra. The LVM of a defect can be directly calculated by determining a full dynamic matrix of a supercell containing the defect. The so-called frozen-phonon approach (Teweldeberhan and Fahy, 2005) will be used in this thesis. In the approach, each atom in the supercell, after fully relaxed, is displaced one at a time and the force responses on other atoms are recorded to construct the force response matrix. So, when each and every atom in the supercell is slightly shifted in all three axes, one at a time, and the dynamic matrix can be calculated based on the repulsive forces. Within the harmonic approximation, the total energy of a supercell with small displacements of atoms from their equilibrium positions can be written as

$$E = E_0 + \frac{1}{2}\sum_{i,j,\alpha,\beta} \Phi_{\alpha,\beta}(i,j) d_\alpha(i) d_\beta(j) \tag{3.13}$$

where $d_\alpha(i)$ is the displacement of atom i from its equilibrium position in the direction α and $\Phi_{\alpha,\beta}(i,j)$ is the real-space force constant matrix. The small displacement $d_\beta(j)$ of atom j in the direction β induces a force on atom i in the direction α as

$$F_{\alpha}(i) = -\Phi_{\alpha,\beta}(i,j)d_{\beta}(j) \tag{3.14}$$

From the equation (3.14), the real-space force constant matrix $\Phi_{\alpha,\beta}(i,j)$ can be constructed by calculating the forces $F_{\alpha}(i)$ induced by creating a small displacement d_0 ($d_{\beta}(j) = d_0 = 0.01 \times a$ where a is a lattice constant) of each atom j in the supercell in three orthogonal directions, β=1, 2, 3 one atom and one direction at a time. To reduce the anharmonic contribution, each component of the force constant matrix is obtained from two calculations. One with $+d_0$ and displacement and another with $-d_0$ displacement. Once the force constant matrix is obtained, the dynamical matrix,

$$D_{\alpha,\beta}(i,j) = (M_i M_j)^{-1/2}\Phi_{\alpha,\beta}(i,j) \tag{3.15}$$

Where M_i is the mass of atom i, can be readily constructed. After the dynamical matrix is diagonalized, the eigenvalues, and the normalized eigenvectors give rise to the vibrational frequencies and the atomic movements for each particular mode.

For H defects that have LVM much higher than the lattice phonon, their LVM can be rather accurately approximated by calculating a reduced dynamic matrix containing only the defect atom and in some cases also one or a few nearest neighbors (Limpijumnong *et al.*, 2005). In the experiment, the vibrational modes of the crystal can be measured by using an infrared spectrometry (IR) or Raman scattering techniques. Using first-principles calculation, we can calculate the absorption intensities of infrared-active modes that are given by the corresponding oscillator strength (Giannozzi and Baroni, 1994).

$$f(\nu) = \sum_{\alpha}\left|\sum_{i\beta} Z^*_{\alpha\beta}(i)\rho(i|\nu)\right|^2 \tag{3.16}$$

Where $\rho(i|\nu)$ is the normalized vibrational eigenvector of the ν^{th} modes, mode, α and β indicate Cartesian polarizations, and $Z^*_{\alpha\beta}(i)$ is the effective-charge tensor of the i^{th} atom. The effective charges $Z^*_{\alpha\beta}(i)$ is the polarization induced by an atomic displacement and it is a second order derivative of the energy that can be calculated using the Berry's phase approach, which is implemented in the VASP codes. The high oscillator strength modes are the modes that are IR active and would show up in the IR absorption spectroscopy.

3.4.3 X-ray Absorption Spectroscopy (XAS)

The main mechanism that leads to the absorption features in XAS spectrum is the excitation of the core electrons to the empty levels above the Fermi energy. The XAS technique turns out to be a very powerful and widely used. One of the reasons is because it is highly elemental selective due to the fact that the core level of each element is different, making it possible to selectively probe each element (and not any other) by using just certain X-ray energy (Koningsberger and Prins, 1988). In the measurement, the core electrons are excited by the x-ray to the empty levels above the Fermi level. The partial density of the electronic states (that the transition from the core level is allowed) depends strongly on the neighboring arrangements surrounding that absorbing atom and can be calculated by first principles calculations. XAS measurements combining with first principles modeling of the XAS spectrum, especially the near edge region (X-ray absorption near-edge spectroscopy; XANES) are shown to be a very powerful way to identify defects in crystals (Limpijumnong *et al.*, 2006). The XANES spectra are highly sensitive to the empty states of the electronic structures where accurate detailed unoccupied band structures are needed. Most of the first principles codes, especially the VASP codes, can provide the density of states (DOS) with options to map the partial DOS with certain orbital characteristic (s, p, or d) on the absorbing atom. These allow one to simulate the theoretical XANES spectrum that can be directly compared with the experimental results. In this thesis, the XANES spectra of interested defects that can be probed by XAS measurements will be simulated using the states unoccupied electronic techniques according to Limpijumnong *et al.* (Limpijumnong *et al.*, 2007). The X-ray absorbance is given by

$$\mu \propto \sum_f \left| \langle f | D | i \rangle \right|^2 \delta(E_i - E_f + \hbar \tag{3.17}$$

Where $|i\rangle$, $|f\rangle$, E_i and E_f are the initial and final states and their energies, respectively. The photon frequency and dipole operator are ω and D, equation (3.17) is known as Fermi's golden rule. The transitions of the core electron are allowed to only the states with proper symmetry. For *K*-edge absorptions, the initial state is 1*s* state, which has an even symmetry. The dipole-allowed final states have to have an odd symmetry, i.e., atomic *p* states (l = 1). Since the initial state is highly localized on the absorbing atom, only the final states near the core of the absorbing atom is relevant. Therefore, the angular momentum and site projected partial density of empty states near the absorber, with some broadening, can be used as the theoretical XANES spectra for comparing with measurements. Note, however, that this approach does not correctly treat the final states of the transition. In the calculations, the final states are calculated while the core electrons are fully occupied. In the actual experiment, when the transition is taken place, a core electron is already left from the initial state in the core to fill the final state. Therefore a proper treatment of the core shall be done. This is called core-hole correction. The XAS specific software such as FEFF 8.4 can perform this correction and improves results in many cases (Nilsson and Pettersson, 2004) FEFF8.4 code based on the multiple-scattering expansion with the muffin-tin potentials will also be used to simulate the *K*-edge XANES spectrum by importing the relaxed structures from VASP as input coordinates of the selected defects.

3.4.4 Core level binding energy

Core level shifts are shifts in the binding energy of the core electrons that occur due to changes in the local environment of the atoms. The shifts can be used as chemical probes of effects such as adsorption of molecules on a surface. The theoretical prediction and study of these shifts using electron structure calculations is the subject of chapter IX in this thesis. The binding energy of core states can be measured with X-ray Photoelectron Spectroscopy (XPS). The method is site and element specific and is often used to characterize adsorbed molecules and atoms on surfaces with respect to chemical state and structure. The interpretation of experimental spectra is complicated by the complex photoemission process and generally needs support by theoretical calculations. Electron structure calculation using Density Functional Theory (DFT) is an established method for predicting structural and energetic properties of large quantum systems such as surfaces and atoms adsorbed at surfaces. (Bagus *et al.*, 2013)

Density functional theory offers an alternative way to calculate binding energies and chemical shifts that accurately accounts for the final-state effect. The method is based on Slater's transition state formalism for the evaluation of electronic excitation energies (Nyberg *et al.*, 1999). Within a Kohn-Sham DFT formalism, the total energy of a system is an analytic function of the occupation numbers of the KS orbitals:

$$E = E(n_1, n_2, ..., n_N) \tag{3.18}$$

where n_i is the occupation number for the one-electron-like molecular orbital. Assuming a photoemission process where, for instance, a core electron from i = 1st level is ejected, the energies of the initial and final states are $E(1,1,1, ...,1)$ and $E(0,1,1, ...,1)$, respectively.

The core-level binding energy is thus equal to

$$E_B = E(0,1,1, ...,1) - E(1,1,1, ...,1) \tag{3.19}$$

By taking advantage of the analytical dependence of E on n_i, one can write:

$$E(0,1,1,...,1) = E(\frac{1}{2},1,1,...,1) - \frac{1}{2}\frac{\partial E}{\partial n_1} + \frac{1}{2!}(\frac{1}{2})^2\frac{\partial^2 E}{\partial n_1{}^2} - \frac{1}{3!}(\frac{1}{2})^3\frac{\partial^3 E}{\partial n_1{}^3} + ..., \tag{3.20}$$

where the partial derivatives are evaluated at $(\frac{1}{2},1,1,...,1)$. The Taylor expansion of $E(0,1,1,...,1)$ and $(\frac{1}{2},1,1,...,1)$ includes the same terms as that in equation (3.20) but with all the signs positive. By taking the difference of these Taylor series, the even order terms cancel out, leaving

$$E_B = -\frac{\partial E}{\partial n_1} + (\delta n_1)^3 \tag{3.21}$$

The Janak's theorem (Brühwiler *et al.*, 1995) proves that the derivative of the DFT total energy with respect to the occupation number of a KS orbital is equal to the orbital energy:

$$\partial E / \partial n_i = \varepsilon_i \tag{3.21}$$

Where ε_i is the Kohn-Sham energy level. Therefore, by keeping only the first term in equation (3.21), the binding energy E_B can be obtained by computing ε_i at a fractional occupation 1/2. This method has been used to calculate core-level binding energies and chemical shifts of a large number of systems, achieving an impressive accuracy (Gong and Mullins, 2008). In addition, four electrostatic mechanisms have been used in Four electrostatic mechanisms have been used in (Bagus *et al.*, 2013) to explain the shifts in terms of where charge is located relative to the core. (1) Transfer of charge from the substrate atom to the adsorbates, where missing (negative) charge in the valence orbital of the substrate atom causes the core electrons feel a positive potential and gives rise to an increase in binding energy. This has traditionally been seen as the major contribution to the core levels shift (CLS). (2) Electrostatic interaction with adsorbates as a result of their extra charge causes the core electrons to feel a negative potential (~1/bond length), lowering the binding energy. This counteracts the charge transfer effect. In addition, charges at the surface cause polarization of the metal, which further influences E_B. (3) Environmental charge density accumulation from bond formation (wave function overlap) causes a shift in binding energy dependent on the coordination number (nearest neighbor count). Higher coordination gives more closely located charge and thus lower binding energy. And (4) hybridization plays a similar role in moving charge by promoting electrons to orbitals with larger radii, resulting in an increased binding energy.

To complete screening picture (Johansson and Mårtensson, 1980), The CLS can be expressed fully in terms of valence charge properties for a system with a core-ionized metal atom. If the binding energy of the core electron is referenced with respect to the Fermi level, the binding energy is seen as the difference between a pure piece of metal and one where the core electron is excited to the valence. We can thus consider an impurity atom with a core hole and an extra valence charge (can be approximated with an atom of atomic number Z+1 in an environment of Z-atoms). The difference in total energy between this system and the pure metal gives the core binding energy. The reason to use the complete screening picture is that the initial state or electrostatic treatment neglects all contributions arising in the excitation process (Måtensson and Nilsson, 1995). The screening process is very fast, so the electrons have time to relax around the core hole before the emitted electron leaves the system. VASP has a function for creating core holes (excitations). The valence electron density relaxes and screens the created core hole. This is the so called final state approximation or the complete screening picture. It includes final state effects on the binding energy, which are not seen by just looking at the ground state electronic structure without relaxation around core holes. This is the framework that allows the calculations used in this thesis.

CHAPTER IV

PEROVSKITES ABO$_3$ AND STRUCTURE

Today, the name "Perovskite" not only denotes this mineral but also the structural family of compounds with the stoichiometric composition ABO$_3$, where A and B are typically metals and O is oxygen. In particular, B usually stands for a transition metal, which is “an element whose atom has an incomplete d sub-shell, or which can give rise to cations with an incomplete d sub-shell” according to the definition of the International Union of Pure and Applied Chemistry (IUPAC). Consequently, the electronic d states of B play a crucial role in the formation of the valence band and the low-lying conduction-band states of perovskites, we will show in section 4.2.

The purpose of this chapter is twofold: the first section delivers some insight into the crystal structure of perovskites focusing in particular on cubic crystal structures of the materials examined in this work. The structural composition is important because it strongly influences the formation of the electronic structure. This interplay between the crystal and the electronic structure together with various additional aspects of the latter is discussed in the remaining sections of this chapter in the context of model approaches. This will be helpful to better understand and interpret the results of calculations from first principles presented in the following chapters.

4.1 Peroveskite Crystal Structure

The family of perovskite oxides materials is composed of a large number of compounds. The ideal cubic perovskite (space group $Pm\bar{3}m$) structure has ABO_3 stoichiometry and is composed of a 3-dimensional framework of corner-sharing AB_6 octahedral. The structure of an ideal cubic perovskite is illustrated in Figure 4.1. where the A cations are located at the corners of the cube. B cation is located in the center of oxygen cage, where the oxygen ions located at the face-centered position of the cube. The *A*-site cation fills the 12-fold coordination formed by the BO_3 network and is surrounded by 12 equidistant anions (Johnsson and Lemmens, 2007). In the ideal cubic symmetry the A cations form a cubic crystal as is shown in the introduction and in Figure 4.1.

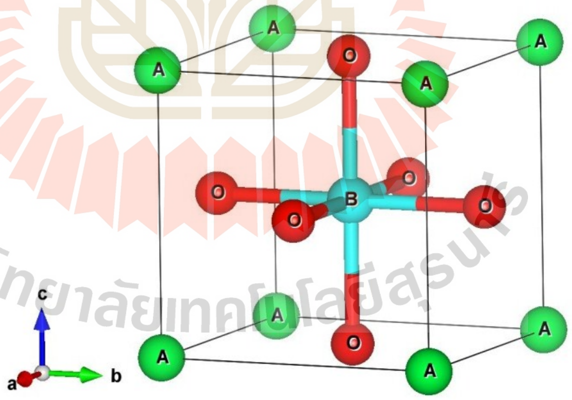

Figure 4.1 Perovskite cubic $Pm\bar{3}m$ structure. B cation sits at the center of the oxygen octahedron O_6 while A cation fills the space between the oxygen octahedral.

We can describe the positions of all atoms in a perovskite crystal by the general formula $\vec{R}=\vec{R}_b+\vec{\delta}_i$. $\vec{R}_b$ runs over the Bravais lattice described by the primitive vectors: $\vec{R}_b=n_1\vec{a}_1+n_2\vec{a}_2+n_3\vec{a}_3$. For a simple cubic lattice, the primitive vectors are

$$\vec{a}_1=\begin{pmatrix} a \\ 0 \\ 0 \end{pmatrix},\ \vec{a}_2=\begin{pmatrix} 0 \\ a \\ 0 \end{pmatrix},\ \vec{a}_3=\begin{pmatrix} 0 \\ 0 \\ a \end{pmatrix} \tag{4.1}$$

$\vec{\delta}_i$ runs over the basis atoms. We can read the positions of the 5 atoms per cubic cell from Figure 4.1.

$$\begin{aligned} &\delta_A :\ 0\ \ 0\ \ 0 \\ &\delta_B :\ \frac{1}{2}a\ \ \frac{1}{2}a\ \ \frac{1}{2}a \\ &\delta_A :\ \frac{1}{2}a\ \ \frac{1}{2}a\ \ 0\ ;\ \frac{1}{2}a\ \ 0\ \ \frac{1}{2}a\ ;\ 0\ \ \frac{1}{2}a\ \ \frac{1}{2}a\ . \end{aligned} \tag{4.2}$$

The O atoms are bound to the B atom by strong covalent bonding: the oxygen p_x and p_y orbitals overlap in the *xy*-plane with the $d_{x^2-y^2}$ orbitals of the B atom. In the *z*-direction, the covalent bonding is accomplished by the overlap between the p_z orbital of O and the $d_{3z^2-r^2}$ orbital of B. Conversely, the bonding involving the A atom is ionic, since the A atom is easy to ionize and will donate enough electrons to satisfy all covalent bonds. The bonding is thus partly covalent (O-B) and ionic (A with the BO_6 octahedral) (Galasso, 2013).

The valence of the B atom, and thus the number of electrons atom A donates, determines the internal charge distribution. When we think the material as built up from layers of BO_2 and AO, these layers can be either both neutral, + and - or vice versa and this can have important consequences as we will see later (in chapter VII and IX). Therefore it is use full to divide the perovskites in the categories $A^{1+}B^{5+}O_3$ (resulting in layers $(AO)^-$ and $(BO_2)^+$), $A^{2+}B^{4+}O3$ (both layers are neutral) and $A^{3+}B^{3+}O_3$ (resulting in $(AO)^+$ and $(BO_2)^-$) (Galasso, 2013).

The ideal cubic perovskite structure is inherently unstable and prone to distortion due to the incompatibility of the ions with the crystal structure, as quantified by the tolerance factor equation (4.3). At low temperature, the perovskites can have different lower-symmetry structures, such as orthorhombic, tetragonal and rhombohedra. The variety of perovskite compositions and structures leads to various functional properties exhibited in the perovskite oxides, such as (anti-) ferroelectricity, piezoelectricity and (anti-) ferromagnetism, which makes perovskites an intensively studied family of functional materials. This cubic perovskite corresponds in most cases to the high temperature paraelectric structure. When the temperature is lowered, these compounds can undergo different types of polar or non-polar structural phase transitions.

For example, $BaTiO_3$ exhibits a sequence of three ferroelectric (FE) phase transitions from cubic to successively: (i) a tetragonal phase ($T_C \simeq 130$ °C) in which the polarization is oriented along the [001] axis (*P4mm*), (ii) an orthorhombic phase ($T_C \simeq 0$ °C) with polarization oriented along [011] (*Pmm2*) and (iii) a rhombohedra phase ($T_C \simeq -80$ °C), with polarization oriented along [111] (*P3m1*). If the center of mass is taken as reference, the transition from cubic to tetragonal phase is characterized by an opposite shift of cations and O atoms, giving rise to a spontaneous polarization. Furthermore, these polar distortions are associated to a small modification of the cell size and shape.

Differently, $SrTiO_3$ has only one phase transition from a paraelectric cubic phase to a non-polar antiferrodistortive (AFD) tetragonal phase (*I4/mcm*) at a temperature $T_C \simeq 100$ K. This AFD phase arises from rotations of oxygen octahedral around the tetragonal axis, such that the total atomic displacements keep the crystal non-polar. Nevertheless, $SrTiO_3$ compound is nearly ferroelectric in the sense that the herald of a ferroelectric phase transition is expected at very low temperature, but is never observed. It was demonstrated that the suppression of the ferroelectric phase transition is due to quantum fluctuations (Müller and Burkard, 1979). Materials presenting such behavior $SrTiO_3$ (Müller and Burkard, 1979), $CaTiO_3$ (Železný *et al.*, 2002), $KTaO_3$ (Perry and McNelly, 1967) are called incipient-ferroelectrics (or quantum ferroelectrics).

The tendency of ABO_3 perovskites to be either ferroelectric or ADF can be estimated from the Goldschmidt tolerance factor:

$$t = \frac{R_\mathrm{A} + R_\mathrm{O}}{\sqrt{2}(R_\mathrm{B} + R_\mathrm{O})} \tag{4.3}$$

where R_A, R_O and R_B are the ionic radii of respectively the A, O and B atoms in the ABO_3 structure. For example, with this scheme, the ideal cubic perovskite $SrTiO_3$ had $t = 1.00$, $R_\mathrm{A} = 1.44$, $R_\mathrm{B} = 0.605$, and $R_\mathrm{O} = 1.40$, but these radii differ somewhat from the Shannon and Prewitt (Shannon, 1976) values, so the formula is best looked upon as a good rule of thumb from which the following generalizations hold:

When $t < 1$ down to 0.75, due to a decreased R_A, the BO_6 octahedral tilt to optimize the A-O bonding, thus creating tetragonal, orthorhombic or trigonal symmetries. Below this t value, the limonite structure results.

When $t > 1$ due to increased R_A or decreased R_B, the stable structure has hexagonal symmetry, with face sharing octahedral, so it is no longer strictly the perovskite structure.

If the ions are not close-packed, decreased R_B can lead to displacement of the B ion from a central point between the O ions, which may be accompanied by displacement also of the A ions relative to the octahedral frame. In the tetragonal Titanates, these asymmetries, due to increased covalency between one oxygen and titanium at the expense of the opposite oxygen where the “bond” becomes ionic, are the principle reason for the pronounced ferroelectricity. The variations due different packing and ionic radii are nicely illustrated in (Johnsson and Lemmens, 2008) from which the following two diagrams below (Figure 4.2):

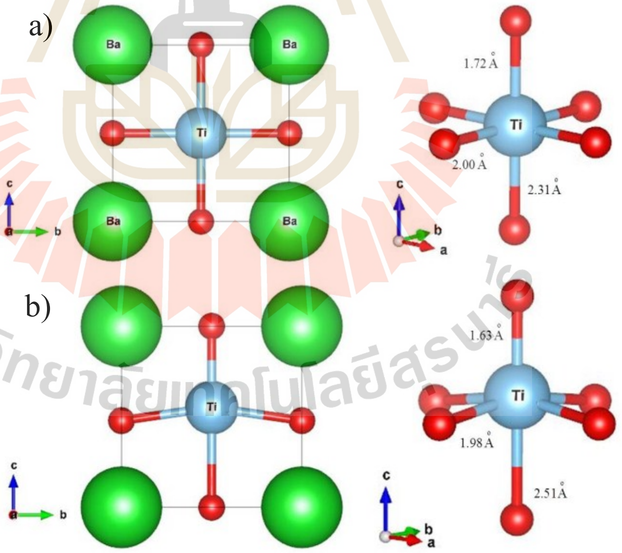

Figure 4.2 (a) Tetragonal $BaTiO_3$. The shifts of Ti and Ba relative to O_6 octahedral around the original Ti position: Ti and Ba both shift by 0.03Å in the same direction. (b) In tetragonal $PbTiO_3$ Ti and Pb are shifted by 0.44 Å(Johnsson and Lemmens, 2008).

4.2 Electronic Band Structure

In this section, we will discuss the electronic band structure properties of our selected perovskites which will be used in the present thesis: cubic-$SrTiO_3$, tetragonal-$BaTiO_3$, tetragonal-$Bi_{0.5}Na_{0.5}TiO_3$ and cubic-LaAlO3 to understand fundamental properties of perovskites and the role of each atomic type are affected on electronic structure.

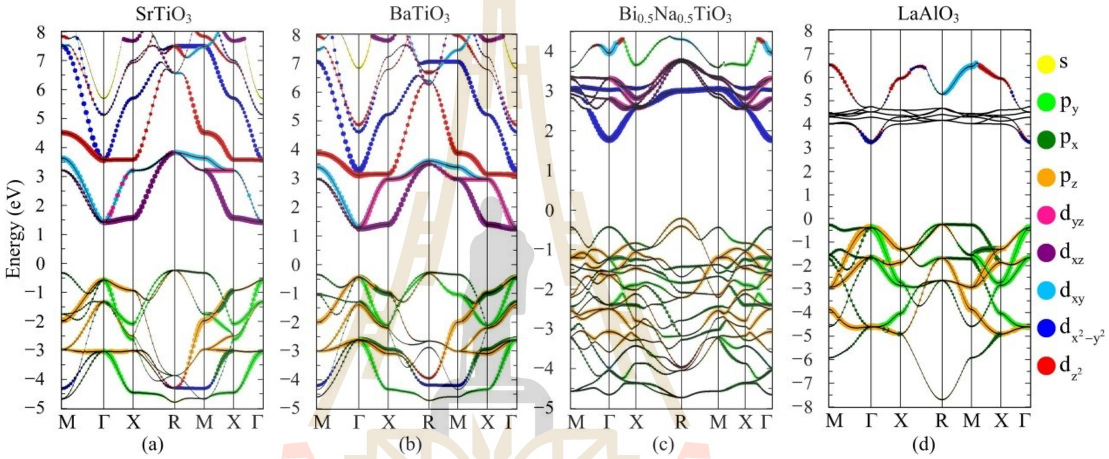

Figure 4.3 Calculated electronic band structure of (a) $SrTiO_3$, (b) $BaTiO_3$, (c) $Bi_{0.5}Na_{0.5}TiO_3$ and (d) $LaAlO_3$ are orbitally resolved into each orbital.

The band structure of selected perovskite compounds in the high symmetry directions in the Brillouin zone calculated using PBE functional are shown in Figure 4.3. The origin of energy was arbitrarily set to be at the valence band maximum (VBM) define as Fermi level (at zero eV), all compounds under study are found to be insulators with an indirect band gap between valence band maximum (VBM) at R point which is dominated by *p* electron orbitals, while conduction band minimum (CMB) at Γ point is dominated by *d* electron orbitals. The band gaps obtained using PBE functional are less than the experimental values due to the well-known problem in the DFT calculations with PBE functional. The partial density of state obtained using PBE is shown in Figure 4.4. For $SrTiO_3$ (see in Figure 4.4(a)), the top of the valence band (VB) which spreads around -4.8 to 0 eV is dominated by O-2*p* states hybridized with Ti-3*d* and Sr-3*d* states. The lower part of conduction band (CB) is mainly composed of Ti-3*d* orbitals hybridized with O-2*p* states and the higher part of the conduction band is mainly derived from Sr-3*d* states. While $BaTiO_3$ (see in Figure 4.4(b)) are quite the same characteristic with STO , the region near the Fermi level, i.e., top of the VB spreads from -4.5 to 0 eV and have O-2*p* like character with very little contribution from Ti-3*d* and Ba-3*d* states. The lower part of the CB is mainly composed of Ti-3*d* orbitals with small contribution from O-2*p* states and the higher part of the conduction band is mainly derived from Ba-3*d* states.

In case of $Bi_{0.5}Na_{0.5}TiO_3$ (see in Figure 4.4(c)), the top of the VB region extends from -5.0 to 0 eV and is dominated by O-2*p* like states hybridized with Ti-3*d* and Bi-6*p* states. The lower part of CB is mainly composed of Ti-3*d* orbitals hybridized with O-2*p* and Bi-6*p* states and the higher part of the conduction band is mainly derived from Na-3*s* and Na-2*p* like orbitals are hybridized with Bi-5*d* states. For $LaAlO_3$ (see in Figure 4.4(d)), the region near the Fermi level, i.e., top of the VB spreads from -7.8 to 0 eV and have O-2*p* and Al-3*p* like character with very less contribution from Al-3*s* and La- 5*p*, 5*d* states. The lower part of the CB is mainly composed of La-5*d* orbitals with small contribution from O-2*p* states.

In summary, from our calculation, the general features of the energy band structure and partial density of state of selected ABO_3 are quite similar. In all compound, the orbital character of the VB is primarily derived from oxygen 2*p* orbitals, with metal-oxygen bonding state at the bottom of the VB and oxygen non-bonding states at the top of VB. The CB has strong metallic *d*-orbital character, originating from the anti-bonding metal-oxygen interaction. CB minima of all four compounds are dominated by *d* states (Ti-3*d* and La-5*d* states).

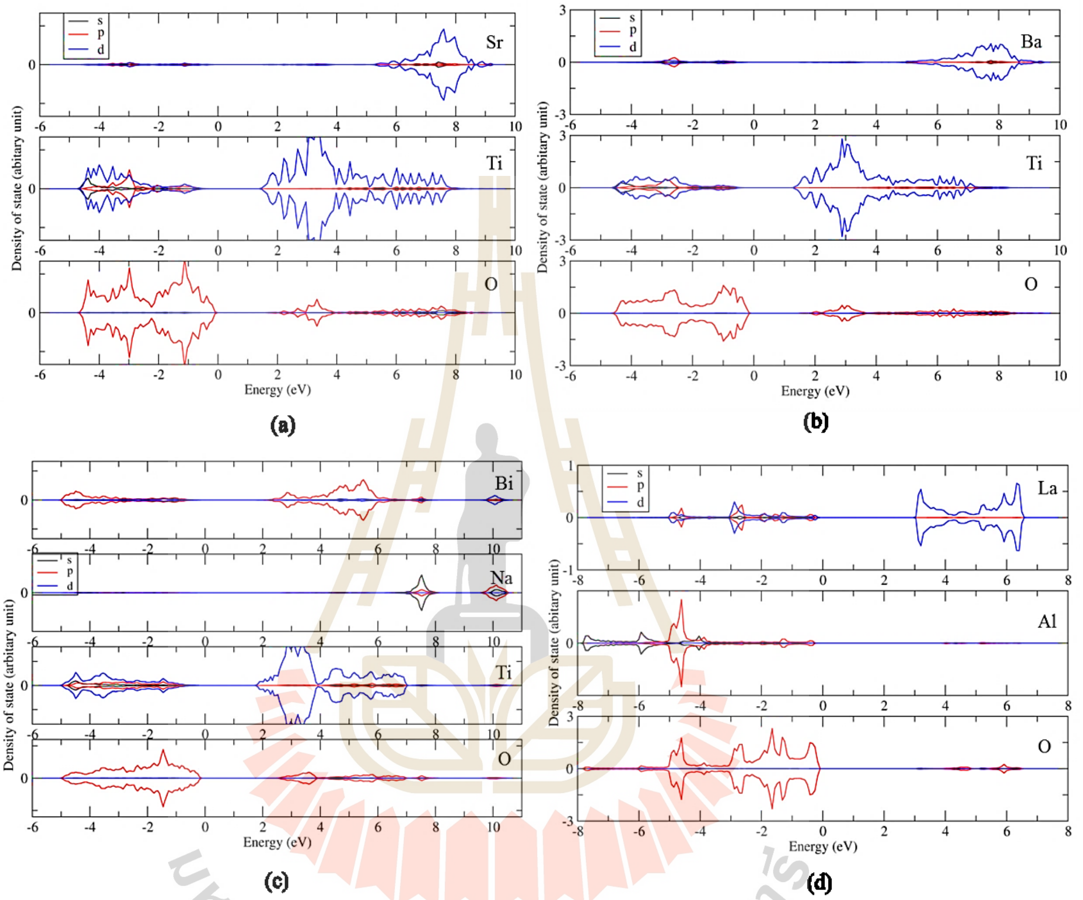

Figure 4.4 Partial density of state (PDOS) for (a) $SrTiO_3$, (b) $BaTiO_3$, (c) $Bi_{0.5}Na_{0.5}TiO_3$, and (d) $LaAlO_3$ are projected orbitals (*s*, *p* and *d* orbital) into each atom.

CHAPTER V

FIRST-PRINCIPLES CALCULATIONS OF HYDROGEN DEFECTS IN $SrTiO_3$ AND IDENTIFICATION BY LOCAL VIBRATION MODE CALCULATIONS

5.1 Introduction

In most oxide materials, hydrogen is known to be an abundant impurity, which can exceedingly affect their electronic properties (Du and Biswas, 2011; Hlaing Oo *et al.,* 2010; Limpijumnong *et al.*, 2009; King *et al.*, 2009). A thorough understanding of local configurations of H is deemed essential for understanding energetics and kinetics of H in oxides. Infrared (IR) spectroscopy has proven to be a powerful tool to experimentally probe H structures. Based on known IR absorption peaks for molecules containing hydroxyl groups, absorption peaks around 3000 cm^{-1} are usually associated to O-H bonds. However, to identify actual local structures responsible for the observed peaks, first principles calculations are generally needed. While many computational studies have been dedicated to the identification of proton sites in the crystal structures with four-fold coordinated O, e.g., zincblende, wurtzite, rutile and bixbyite (Limpijumnong *et al.*, 2009; Li *et al.*, 2008; Van de Walle, 2000) For the perovskite structure, there are computational results on proton sites in some compounds, for example, $BaTiO_3$ (Iwazaki *et al.*, 2010) and $BaZrO_3$ (Sundell *et al.*, 2007). However, the direct calculation details of H site in $SrTiO_3$ are limited which impedes further study of H migration. It is very difficult to understand proton migration mechanisms without knowing its ground state site first. (Sata *et al.*, 1996) Strontium titanate (STO) is an important oxide material due to a rich variety of industrial applications, for examples, in dielectric and optical devices (Rao and Krupanidhi, 1994; Seung-Hee and Ho-Gi, 1992; Kun *et al.*, 2006) and as a substrate for superconducting thin films (Wu *et al.*, 1987). Discovery of high mobility 2D electron gas at interfaces between $SrTiO_3$ and other oxides (Ohtomo and Hwang, 2004) further opened up new opportunities in oxide electronics. $SrTiO_3$ has a cubic perovskite structure at room temperature and exhibits an AFD phase transition to tetragonal at 105 K. (Houde *et al.*, 1987) Several infrared spectroscopy experiments have been performed to study hydrogen in $SrTiO_3$. (Houde *et al.*, 1987; Klauer and Wohlecke, 1992; Weber *et al.*, 1986) Depending on the sample conditions, O-H absorption bands have been observed around 3500 and 3300 cm^{-1}. The band around 3500 cm^{-1} has been studied in detail since 1980 by the group of Weber and Kapphan (WK) using polarized IR absorption spectroscopy (Weber *et al.*, 1986; Kapphan *et al.*, 1980) combined with the applications of uniaxial stress as well as electric field. Polarized Raman scattering measurement was later performed by the same group to confirm the IR results. (Klauer and Wohlecke, 1992) At room temperature they observed a main peak centered at 3495 cm^{-1} accompanied by a small hump consisting of several peaks in the range of 3505–3520 cm^{-1}. The main peak blue shifts to 3510 cm^{-1} at low temperature and subsequently splits into three lines ($\nu_A < \nu_B < \nu_C$ with the spacing of ~2.5 cm^{-1}) as the crystal transforms into the tetragonal phase at temperature below 105 K. Polarizations of the split lines showed that the central line (ν_B) corresponds to dipoles lying in *xy* plane (the plane perpendicular to the tetragonal axis) while the outer lines (ν_A and ν_C) correspond to dipoles that have components both parallel and perpendicular to the tetragonal axis. By selectively applying uniaxial stress or electric field, the modes further split allowing WK to gain additional information on the stress and field dependencies of O-H dipoles in each direction. WK proposed two structural models for the proton in SrTiO3, that is, octahedral edge (OE) and cube face (CF). Both models have various equivalent sites (24 for OE and 12 for CF) in the cubic phase that would split into three unequivalent groups in the tetrahedral phase consistent with the measured results.

Recently, Tarun and McCluskey (Tarun and McCluskey, 2011) observed twin peaks at 3355 and 3384 cm^{-1} and proposed that they are the local vibration modes (LVM) of a Sr vacancy decorated by two protons, that is, 2H-V_{Sr} complex, where the protons also form strong O-H bonds with the O atoms surrounding the V_{Sr}.

For semiconductors with sp^3 (fourfold) coordination, such as Si, Ge, GaAs, or even ZnO, a proton generally prefers to stay along the bonds; allowing the O-H bond to point along one of the sp^3 bonding directions. However, for $SrTiO_3$, a much more ionic compound with little directional bonding, the O-H direction is dictated by the overall Coulombic repulsions (to Ti^{4+} and Sr^{2+}) and attractions (to O^{2-}) with the neighboring atoms. An O-H pointing to a cation such as the CF configuration is usually unstable in a closely packed ionic crystal due to the strong Coulomb repulsion and limited space to relax.

In this chapter, the role of a proton (H^+) in cubic perovskite $SrTiO_3$ and the topology of low-energy proton sites around an O atom are thoroughly studied and the local vibrational mode of the stable site is calculated by using first-principles calculations based on density functional theory (DFT). In addition, the local vibrational modes associated with each structure will be determined in order to compare with the recent experimental results. We will show that the vibrational frequencies observed by Tarun and McCluskey (Tarun and McCluskey, 2011) should be related to the complex defects between H and V_{Ti} or V_{Sr} rather than isolate defects.

5.2 Hydrogen Sites in $SrTiO_3$

Figure 5.1 shows the local structure around an O atom in $SrTiO_3$. In Figure 5.1(a), two conventional unit cells of cubic $SrTiO_3$ are shown to clearly illustrate all neighbors of the middle O atom (all O atoms in the crystal are equivalent by symmetry) with the detail in Figure 5.1(b). Each O atom has two Ti, four Sr, and eight O neighbors. It is known that, in oxides, a proton prefers to bind strongly with an O with a distance of ~1 Å; the region represented by a low energy surface (LES) which has the shape of a distorted sphere centered on the O [in Figure 5.1(b) we show a perfect sphere for an illustration purpose]. On this LES, a proton has a chance to bind strongly with the O atom and the differences in the formation energies of the proton on different points on the surface arise from the interaction with neighbors. The OE site is on the line connecting an O atom to its O neighbor. This is the line defining the octahedral edge in Figure 5.1(a). The CF site is on the cubic face and on the line connecting between an O and its Sr neighbor. There is another high symmetry site on the cubic face [labeled CF′ in Figure 5.1(b)] which is on the line connecting an O atom and the midpoint of two adjacent Sr atoms on the same side of the cube. This site has been identified to be the minimum energy site for a proton in $BaZrO_3$ (Sundell *et al.*, 2007). On the LES, there are eight equivalent sites for OE and four equivalent sites for CF as well as CF′. In a cubic perovskite unit cell, which consists of three O atoms, the numbers of the equivalent sites are three times more, that is, 24 and 12, respectively.

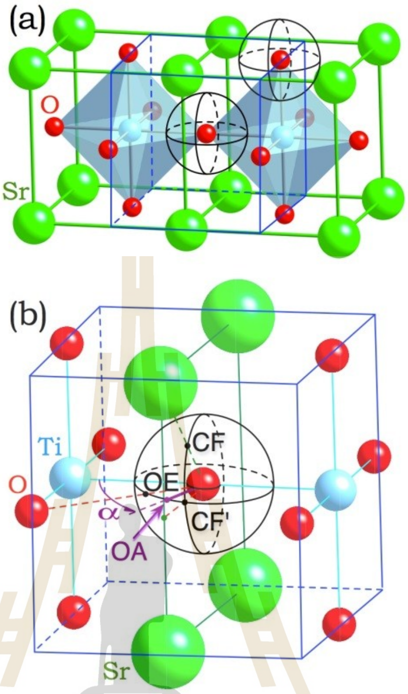

Figure 5.1 Schematic of low energy surface for a proton and four proton sites in $SrTiO_3$.

5.3 Computation Method

In order to study the hydrogen-related defects in cubic $SrTiO_3$, we used first-principles density functional theory within the local density approximation (LDA) based on projector-augmented wave (PAW) method (Kresse and Joubert, 1999) as implemented in VASP code (Kresse and Furthmüller, 1996; Kresse and Hafner, 1994). The cutoff energy for the plane wave basis set was set at 500 eV. The Monkhorst-Pack scheme (Monkhorst and Pack, 1976) was used for the k-space integrations. All atoms in the cell were relaxed until the Hellmann-Feynman forces (Feynman, 1939) on all atoms become less than 10^{-3} eV/Å. The calculated lattice constant of cubic $SrTiO_3$ is 3.873 Å which is in good agreement with the experimental value of 3.905 Å (Lytle, 1964). To study the defects including both native and hydrogen-related defects, a supercell approach was used (Van de Walle and Neugebauer, 2004) In this work, we used 135-atom supercell, which is a 3x3x3 repeating of cubic SrTiO3 primitive cell. The defect formation energy is defined as equation (3.4). To align the energy levels between the supercell containing defect and without defect (bulk), core potentials of atoms being far away from the defect in the defect supercell and those of the same atoms in the defect-free supercell were used. The upper limits for μ_{Sr}, μ_{Ti}, and μ_O are the energies of the metallic Sr, metallic Ti and gaseous O_2, which are set to zero in this study. According method in chapter III, To growth SrTiO3 crystal, it is required that $\mu_{SrTiO_3} = \mu_{Sr} + \mu_{Ti} + 3\mu_O$. However, Sr and Ti atoms prefer to bind with oxygen atom to form their oxide phases, such as SrO, SrO_2, TiO, TiO_2, and $Ti2O_3$. Therefore, the chemical potentials of Sr and Ti have to be refined by considering their oxide phases. For chemical potential of H (μ_H), the energy per H atom of H_2-molecule was used. To illustrate the limits of chemical potentials, a triangular phase diagram will be used to represent the chemical potentials of Sr, Ti and O for $SrTiO_3$ crystal (see Figure 5.2).

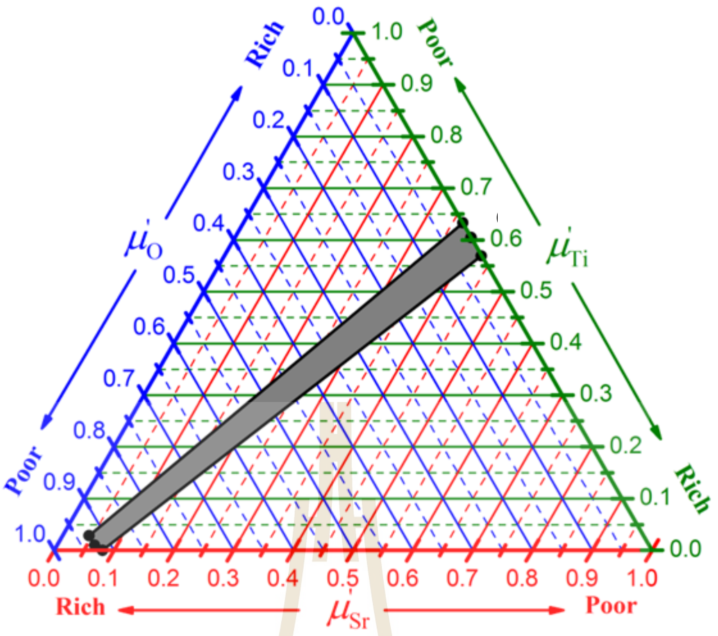

Figure 5.2 Triangular phase diagram for representing the chemical potentials of Sr, Ti, and O. (see text for more details).

In Figure 5.2, the black points and the shaded area on the diagram satisfied equation (3.6) the chemical potentials of Sr, Ti, and O could be any values that lie within the shade area. Sets of chemical potentials along these lines are the result of the limits due to the possible oxide phases. These black points are marked as (a) to (d) in Figure 5.2. The values of the chemical potentials for Sr, Ti, and O associated with the points (a) – (d). For more convenience, the values of chemical potentials for Sr, Ti, and O associated with points (a) – (d) were also listed in Table 5.1. It is clearly seen that at point "a", the chemical potentials of Sr are at their maximum values and that of O is at its minimum value, i.e., Sr-rich, and O-poor. At point "b", the chemical potential of Ti is at its maximum value and O is at its minimum, i.e., Ti-rich and O-poor. At point "c", the chemical potential of Sr is at its minimum value and O is at its maximum value, i.e., Sr-poor and O-rich. And at point "d", the chemical potential of Ti is at its minimum value and O is at its maximum value, i.e., Ti-poor and O-rich. Next, we will consider only these three points ("a", "c", and "d") to represent the formation energies of H-related defects. For hydrogen defect, a half of the total energy of gas phase (H_2) was used as its chemical potential ($\mu_{\mathrm{H}} = E[\mathrm{H}_2]/2$).

The vibrational frequencies of H-related defects were calculated using the same method as described in the Ref. (Limpijumnong *et al.*, 2003). Using this method, we obtained the vibrational frequency including anharmonic part, which is very important for the case of hydrogen. To predict the migration barriers of defects, we used the climbing image nudged elastic band (NEB) method, which is also implemented in VASP code.

Table 5.1 The lists of chemical potentials of Sr, Ti, and O associated with points a, b, c, and d as marked on Figure 5.2.

Points	μ_{Sr} **(eV)**	μ_{Ti} **(eV)**	μ_{O} **(eV)**
a	**-2.43**	**-8.54**	-10.95
b	-2.85	-8.54	-10.81
c	-8.83	**-19.27**	-5.24
d	**-9.59**	-18.51	-5.24

5.4 Hydrogen-Related Formation

To determine the stability and chance of forming these complex defects, the defect formation energy have to be taken into account. The chemical potentials of Sr, Ti, and O were taken from points “a” and “d” for Sr-rich and Sr-poor growth conditions, and from points “a” and “c” for Ti-rich and Ti-poor growth conditions, respectively (see Figure 5.3 and Figure 5.4). In addition, using band structure calculations we found that c-SrTiO$_3$ has an indirect bandgap of ~1.70 eV ($R \rightarrow \Gamma$) and direct bandgap of ~ 2.00 eV. Therefore, in the plot of Figure 5.3 and Figure 5.4 the Fermi-level was extended to 2.00 eV and the vertical dashed line was marked at 1.70 eV for indicating the direct and indirect bandgap, respectively.

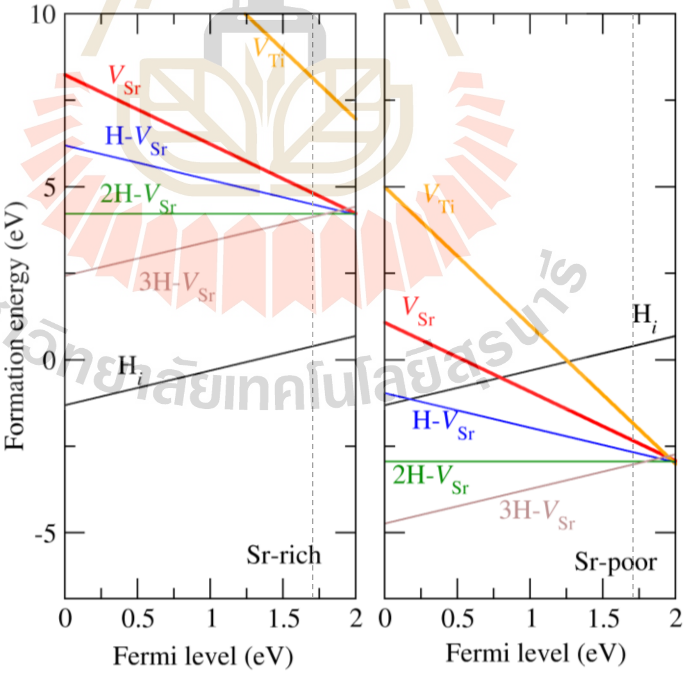

Figure 5.3 Formation energies of defects as a function of Fermi level under Sr-rich (point a) and Sr-poor (point d) growth conditions. The slopes of each line indicate the charge state of each defect.

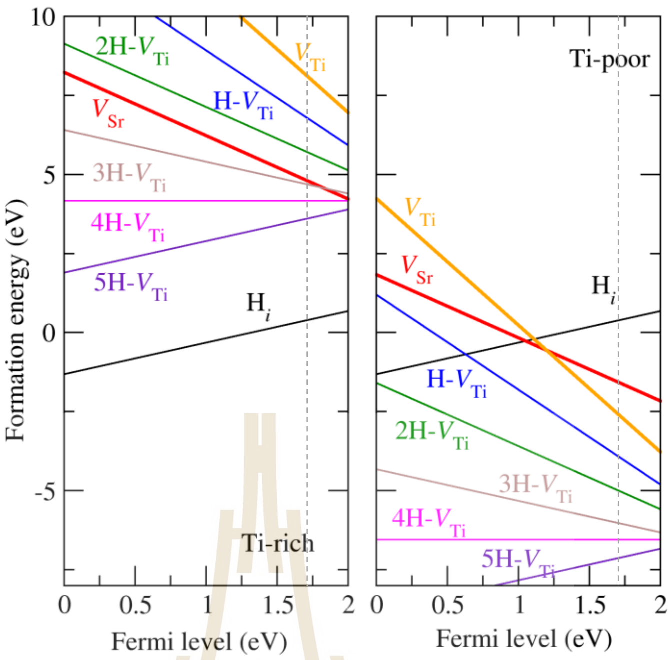

Figure 5.4 Formation energies of defects as a function of Fermi level under Ti-rich (point a) and Ti-poor (point c) growth conditions. The slopes of each line indicate the charge state of each defect.

From formation energies of defects, it is clearly seen that the formation energy of H_i depends only on the μ_H . Therefore, the formation energies of H_i are all the same for both Sr-rich and Sr-poor growth conditions as shown in Figure 5.2. For Hi, we found that it is a single shallow donor. The formation energy of H_i in OE model (H_i^{OE} in Figure 5.1) is 1.31 eV (calculated at VBM), which is lower than that in CF model (H_i^{CF} in Figure 5.1) by ~0.25 eV. This indicated that H_i^{OE} is the most stable configuration and likely form. Relative energies of a proton at OE, CF, and CF' sites are listed in Table 5.2. The effects from the neighboring atoms on the stability of proton on the LES sites can be understood using a simple Coulomb interaction picture.

Table 5.2 Calculated energy, O-H bond length, and stretch frequency for proton in $SrTiO_3$ with and without V_{Sr}. For a proton without V_{Sr}, ΔE is the relative energy referenced to the OA. For the complex defects, ΔE is the binding energy of the last proton according to equations. (1) and (2). Note that the OE, CF, and CF′ configurations are not stable, the proton spontaneously relaxes to OA configuration. Rows highlighted in boldface are the ground state configurations.

Sites	(α,θ)	ΔE(eV)	$d_{O\text{-}H}$ (Å)	ω (cm^{-1})
OE	(45,90)	2.29	-	-
CF	(90,45)	0.25	-	-
CF′	(90,90)	0.01	0.992	3225
OA	(76,90)	0.00	1.011	2745
H-V_{Sr}		-0.84	0.985	3505
2H-V_{Sr}^{a}		-0.81	0.984	3523
2H-V_{Sr}^{b}		-0.79	0.984	3527
2H-V_{Sr}^{c}		-0.75	0.986	3489
2H-V_{Sr}^{d}		-0.64	0.986	3458

A proton prefers to stay close to anions, that is, O ions, and far from cations, that is, Ti and Sr ions. This explains why the site between an O and a Ti nearest neighbor (not labeled) has a high energy. Among the three high symmetry sites, OE is the least favorable site because it is still rather close to Ti. The CF site is also not the most favorable site because the site is rather close to Sr. The CF' is further away from Sr, that is, it is at the middle point between two Sr atoms and also closer to two O atoms; making it more stable than CF by 0.25 eV. However, CF′ is an unstable equilibrium configuration. If we slightly break the symmetry, the proton spontaneously moves away from the CF′ site to the off axis (OA) site. To describe the sites, we use an azimuthal angle (α) as defined in Figure 5.1 and an angle deviated from the z-axis (θ). In Table 5.2, only the angles related to the sites labeled in Figure 5.1 are shown. The equivalent sites can be found by using the crystal symmetries. The global minimum energy site (OA) is significantly deviated from both CF and CF′, that is, by ~30° and ~15°, respectively.

5.5 Binding Energy and Local Vibration Frequency

To fully understand the energy landscape of an interstitial proton in cubic perovskite $SrTiO_3$, we employed the climbing image nudged elastic band method (NEB) (Daniel *et al.*, 2008; Graeme *et al.*, 2000; Graeme and Hannes, 2000; Mills *et al.*, 1995) to calculate the total energy of the proton moving in the paths between important sites. On the basal plane ($\theta = 90°$) we studied the path that starts at the site between an O and a Ti ($\alpha = 0°$) (which is the highest energy point on the LES) passes through the OE and OA, and ends at the CF′ site ($\alpha = 90°$). The formation energy ΔE is calculated relative to the ground state configuration (OA). Along this path (Figure 5.5) the energy drops by over 2 eV as the proton moves from the site between O and Ti to the OA site without any shoulder at the OE site, indicating that the OE site is not even a metastable site. As the proton passes the OA site, the energy increases but by a very small amount, that is, by only 0.01 eV, as the proton moves from OA to CF′. On the Sr plane ($\alpha = 90°$) we calculated a proton that travels on a path from CF′ ($\theta = 90°$) to CF ($\theta = 45°$). Along this path, the energy monotonically increases by ~0.25 eV.

Since CF is at the midpoint between two equivalent CF′ sites, it is a saddle point between minima on the LES.

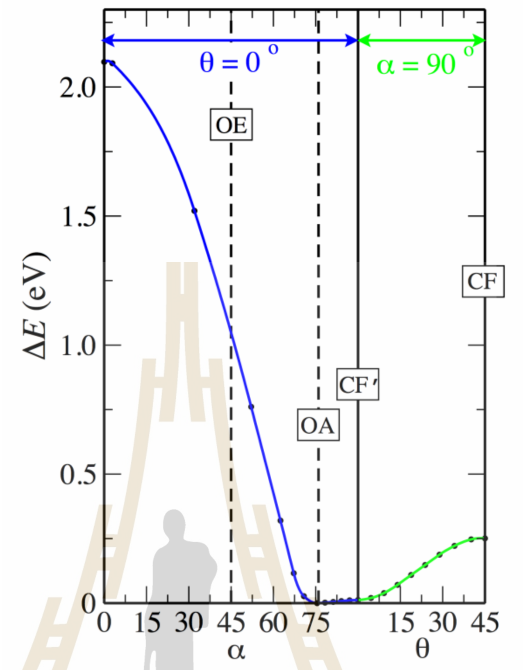

Figure 5.5 Calculated energy of a proton (referenced to the ground state configuration) on paths connection proton sites in Figure 5.1. The azimuthal angle (α) is illustrated in Figure 5.1 and θ is the angle between the O-H bond direction and the *z*-axis. For the first section θ is fixed at 0° and for the second section α is fixed at 90°.

We have also calculated the barrier using NEB for a proton to hop from an OA site on one LES to an adjacent OA on a neighboring LES [two such LES are shown in Figure 5.1(a)] and obtained a much smaller barrier (0.05 eV). Therefore the overall diffusion barrier of a proton in $SrTiO_3$ is set by the hopping between two OA sites in the same LES which is ~0.25 eV. By estimation based on a hopping rate

$\Gamma = \Gamma_0 \exp(-\beta E_a)$ of 1/min, and Γ_0 = 100 THz. This means a proton is very mobile in $SrTiO_3$ even at temperature of ~100 K unless it is trapped by other defects.

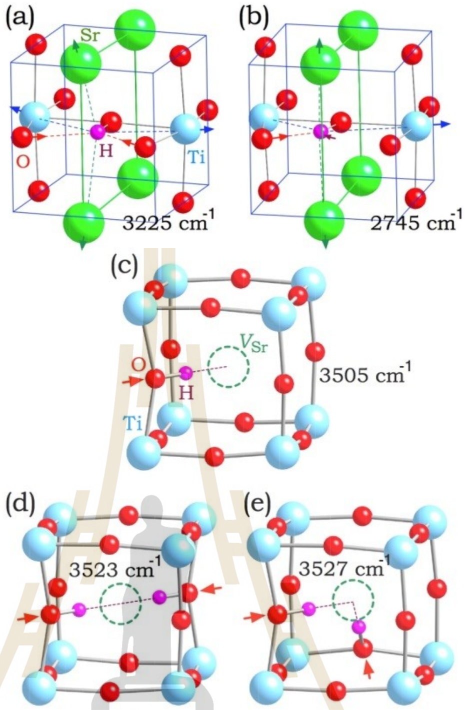

Figure 5.6 Local structures of H^+ (proton) defects in $SrTiO_3$. (a) and (b) Proton at CF′ and OA sites, (c) $(H\text{-}V_{Sr})^-$ complex, and (d) and (e) the two lowest energy $2H\text{-}V_{Sr}$ complexes. The arrows indicate the relaxation directions of the neighboring atoms. The frequencies shown are the calculated O-H stretch modes.

The CF′ and OA configurations are shown in Figure 5.6(a) and Figure 5.6(b). The proton forms a strong bond with an oxygen with the bond lengths of 0.992 and 1.010 Å, respectively. Because of its positive charge, the proton repels cations (Ti^{4+} and Sr^{2+}) and attracts anions (O^{2-}). For the CF′ configuration, the proton is symmetrically placed with respect to the surrounding Ti, Sr, and O ions. This site minimized the Coulomb repulsion between H^+ and Ti^{4+}. Tilting away from the symmetric site (CF′→OA) increases the Coulomb repulsions between H^+ and Ti^{4+} somewhat but decreases the H^+-Sr^{2+} Coulomb repulsions and increases the H^+-O^{2-} Coulomb attractions. The total energy decreases slightly (0.01 eV); rendering OA the lowest energy site. Note, however, that computational details can sometime affect the calculated energy difference in this scale. The O-H vibration frequencies for both OA and CF′ configurations were calculated using the approach described in Ref. (Limpijumnong and Zhang, 2005) including anharmonic contributions which are important for the light H atom. To obtain the systematic errors of our calculations, we calculated the symmetric stretch frequency of a water molecule and obtained the value of 3515 cm^{-1} which is lower than the actual experimental value by 142 cm^{-1}. To correct this systematic error, all values of LVMs presented in this paper are corrected by adding this value. Even after the systematic error correction, we estimate the error bar on our calculated frequencies to be about 100 cm^{-1}. We obtained the vibration frequency of O-H in the ground state configuration (OA) of 2745 cm^{-1}.

From above detailed study we can see that a single proton in pure $SrTiO_3$ cannot explain the experimental observed IR mode around 3500 cm^{-1} for several reasons. (1) The most stable configuration for a proton in $SrTiO_3$ is OA and the previously proposed OE and CF configurations have considerably higher energies and are not even metastable. The OA configuration has an O-H dipole direction inconsistent with the measured polarized IR results. (2) The calculated stretch frequency of the O-H oscillator in the OA configuration is only 2745 cm^{-1} which is much lower than the observed 3500 cm^{-1} value. The difference of ~750 cm^{-1} is much larger than the typical computational error bar (about 100 cm^{-1}). (3) The vibration mode of a single proton in pure $SrTiO_3$ should be quickly broadened to the width of

500 cm^{-1} as the temperature goes from 0 to 100 K as the CF′ configuration being populated. However, the observed 3500 cm^{-1} mode remains rather sharp up to room temperature. (4) The diffusion barrier of a proton is very low such that a proton can diffuse even at room temperature. Thus, most of the interstitial protons should migrate out when the sample is cooled down.

Since a single proton cannot be the cause of the 3500 cm^{-1} mode, the outstanding question is "What O-H configuration could be the cause of it?" The obvious choice is H in cation vacancies. The complex of H and cation vacancies has been found in many oxides (Lavrov *et al.*, 2002). The observed twin peaks at 3355 and 3384 cm^{-1} in $SrTiO_3$ (Tarun and McCluskey, 2011) have been suggested to originate from 2H-V_{Sr} complex. In $SrTiO_3$, there are two possible cation vacancies, V_{Sr} and V_{Ti}. Here we propose that the H in a Sr vacancy (H-V_{Sr}) is the cause of the 3500 cm^{-1} mode, and that the H in a Ti vacancy may explained the twin peaks reported in Ref. (Tarun and McCluskey, 2011).

A (H-V_{Sr})$^{-}$ complex in $SrTiO_3$ has a fully relaxed O-H bond length of 0.985 Å (see Table 5.2) and a calculated O-H vibration frequency of 3505 cm^{-1}, which is in excellent agreement with the experimentally observed mode. A V_{Sr}^{2-} has 12 Oxygen neighbors, all of which are equivalent by the cubic symmetry. A proton can bind to one of these O atoms, forming a (H-V_{Sr})$^{-}$ complex. There are 12 possible O-H oscillators pointing toward the vacancy center as shown in Figure 5.6(c). Similarly, for a given Sr atom of a perfect crystal, there are also 12 possible CF sites for H to form O-H oscillators pointing toward it. It has been shown (Houde *et al.*, 1987) that 12 CF sites in the cubic phase would split into three inequivalent groups in the tetragonal phase with polarization behaviors satisfied the observed mode. Therefore, the $(\text{H-}V_{\text{Sr}})^{-}$ model should also be equally consistent with the observed mode.

Actually, the double negative center V_{Sr}^{2-} could bind up to two protons in a similar way the $\text{V}_{\text{Zn}}^{2-}$ binds protons in ZnO (Lavrov *et al.*, 2002). In the cases that the proton is abundant compared to the vacancy, the $(\text{H-}V_{\text{Sr}})^{-}$ could accept another proton forming a neutral charge $2\text{H-}V_{\text{Sr}}$. There are four inequivalent ways to add the second proton to the existing $(\text{H-}V_{\text{Sr}})^{-}$ complex. The resulted $2\text{H-}V_{\text{Sr}}$ complexes are labeled with a superscript I to IV following the order of decreasing distances between the two O atoms that bind H. The two lowest energy configurations are $2\text{H}-V_{\text{Sr}}^{\text{a}}$ and $2\text{H}-V_{\text{Sr}}^{\text{b}}$ [Figure 5.1(d) and Figure 5.1(e)]. Since there are two O-H oscillators in each $2\text{H-}V_{\text{Sr}}$ complex, we first determined the coupling between the two oscillators by calculating the full dynamic matrix of the complex. Within our calculated force sensitivity (~0.001 eV/Å), we do not find any coupling between the two oscillators and thus obtained two degenerate modes. Small or no coupling is reasonable for this system because the two oscillators are attached to different O and are reasonably far apart. This allows us to separately calculate the frequency of each O-H oscillator including anharmonic effect in a systematic way. The calculated frequencies of all four complexes are shown in Table 5.2. It can be seen that the vibrational frequencies of all seven configurations are nearly linearly correlated with the O-H bond length.

Next, we look into the energetic to evaluate the stability of these complexes. The binding energies between V_{Sr}^{2-} and H_{OA}^{+} and between $(\text{H}-V_{\text{Sr}})^{-}$ and H_{OA}^{+} are defined as

$$\Delta E = E_{\text{tot}}(\text{H}-V_{\text{Sr}}^{-}) + E_{\text{tot}}(\text{bulk}) - E_{\text{tot}}(V_{\text{Sr}}^{2-}) - E_{\text{tot}}(\text{H}_{\text{OA}}^{+}) \qquad (5.1)$$

and

$$\Delta E = E_{\text{tot}}(2\text{H}-V_{\text{Sr}}) + E_{\text{tot}}(\text{bulk}) - E_{\text{tot}}(\text{H}-V_{\text{Sr}}^{-}) - E_{\text{tot}}(\text{H}_{\text{OA}}^{+}) \tag{5.2}$$

where $E_{\text{tot}}(\beta)$ is the total energy of a supercell containing the complex (or impurity) β.

We found that bringing the first H_{OA}^{+} to the V_{Sr}^{2-} is exothermic by 0.84 eV as shown in Table 5.2. Bringing the second H_{OA}^{+} to $(\text{H}-V_{\text{Sr}})^{-}$ to form $2\text{H}-V_{\text{Sr}}$ complexes is also exothermic by 0.81, 0.79, 0.75 and 0.64 eV for the configurations a, b, c and d, respectively. The O-H vibrational frequency for $(\text{H}-V_{\text{Sr}})^{-}$ is in excellent agreement with the observed 3500 cm^{-1} peak and O-H LVMs for $2\text{H}-V_{\text{Sr}}^{\text{a and b}}$ complexes are larger than that for the $(\text{H}-V_{\text{Sr}})^{-}$ complex by ~20 cm^{-1}, which may explain the experimentally observed higher frequency hump.

Recently, Tarun and McCluskey (Tarun and McCluskey, 2011) observed twin peaks at 3355 and 3384 cm^{-1} and proposed that these IR peaks are originated from $2\text{H}-V_{\text{Sr}}^{\text{d}}$. Based on our results, this assignment has some problems. (1) The $2\text{H}-V_{\text{Sr}}^{\text{d}}$ complex is the least stable among all four 2H-V_{Sr} complexes and has higher energy than $2\text{H}-V_{\text{Sr}}^{\text{a}}$ by 0.17 eV; rendering it unstable. (2) The 2H-V_{Sr} complexes have two O-H oscillators spatially well separated and do not couple with each other. Therefore, it cannot give the splitting of ~30 cm^{-1} (our calculations give doubly degenerated modes). (3) The calculated frequencies do not agree with the observed ones. Thus, the observed twin peaks are unlikely due to 2H-V_{Sr} complexes but may be related to nH-V_{Ti} complexes. Therefore, we will investigate the nH-V_{Ti} complexes in next section.

Table 5.3 Summary of vibrational frequencies of H-related defects in c-SrTiO$_3$. The calculated values were included the effect of anharmonic part.

Type of defect	Frequency (cm^{-1})		Corrected Frequency (cm^{-1})
	Calculated	Observed	
H_i^{OE}	2603.01	Main peak at ~3500 cm^{-1} and minor peak ~ 3510-3530 cm^{-1} (Houde *et al.*, 1987; Weber *et al.*, 1986)	2745.34
H_i^{CF}	3082.65		3224.99
$[H\text{-}V_{Sr}]^{-1}$	3362.63		3504.96
$2H\text{-}V_{Sr}^{a}$	3384.56 3376.61		3526.89 3518.94
$2H\text{-}V_{Sr}^{b}$	3392.22 3376.98		3534.55 3519.32
$2H\text{-}V_{Sr}^{c}$	3346.05 3346.29		3488.39 3488.62
$2H\text{-}V_{Sr}^{d}$	3312.49 3318.69		3454.82 3461.03
H_2O molecules	3514.67	3657	3657(Shimanouchi, 1972)

5.6 Hydrogen-Titanium Vacancy Complex

From previous section, we have revealed that H interstitial has a vibrational frequency far lower than 3500 cm^{-1}. We also showed that one or two interstitial H atom(s) could be trapped by V_{Sr} and formed nH-V_{Sr} complexes (n= 1 or 2). In the complexes, H atoms form strong O–H bonds with the O atoms surrounding V_{Sr} in the direction pointing toward the vacancy center. As we obtained the calculated vibrational frequencies of nH-V_{Sr} complexes very close to the observed peaks ~3,500 cm^{-1} by WK consistent oscillator directions, we identified WK's observation to be nH-V_{Sr} complexes; not a single H interstitial. For the double peaks centered at 3355 and 3384 cm^{-1} observed by TM, we previously discussed that they could not arise from *2*H-V_{Sr} complexes as proposed by TM because the frequencies were not in agreement and the complexes could not explain the coupling observed experimentally. In above section, we proposed that the double peaks that TM observed may belong to H and Ti vacancy complexes nH-V_{Ti}, therefore, in this section, we report the binding energies, local structures and the detailed vibrational frequencies of complex defects between H and V_{Ti} based on first-principles density functional calculations. We show that the vibrational frequencies observed observed by TM are consistent with nH-V_{Ti} complexes.

5.6.1 Energetic of complex defects

In this section, we are going to consider the H and Ti vacancy complex defects. To determine the stability and chance of forming these complex defects, the defect formation energy have to be taken into account. The chemical potentials of Sr, Ti, and O were taken from points “a” and “d” for Sr-rich and Sr-poor growth conditions, and from points “a” and “c” for Ti-rich and Ti-poor growth conditions, respectively (see Figure 5.3 and Figure 5.4). From Figure 5.3, we found that V_{Sr} and V_{Ti} are double and quad shallow acceptors, respectively. There is no energy level introduced in the band gap due to V_{Sr} and V_{Ti} defects. Under n-type conditions, V_{Sr} and V_{Ti} are double and quad acceptors, respectively. At low temperature, an interstitial H is always a single donor (or simply a proton) binding strongly to one of the O atoms in STO with the lowest-energy configuration called “OA” However, the interstitial H is not very stable. It can be annealed out of the STO crystals at even below room temperature (~100 K) and it has frequency of only ~2,700 cm^{-1}. Consequently, we proposed that the O-H oscillators observed in many IR experiments, with the frequency ranges of 3,300 – 3,500 cm^{-1}(Houde *et al.*, 1987; Klauer and Wohlecke, 1992; Kapphan *et al.*, 1980; Weber *et al.*, 1986; Tarun and McCluskey, 2011), are more likely associated with H complex defects.

For H and V_{Sr}, V_{Sr} in charge state 2 ($V_{\mathrm{Sr}}{}^{2-}$) could trap a proton H^{+} to form H-V_{Sr} complex defect with a reasonably large binding energy of 0.84 eV. The H-V_{Sr} complexes defect could further bind another proton to form a neutral 2H-V_{Sr} complex defects. In section 5.5, we have studied in detail of the possible configurations and found two most stable 2H-V_{Sr} complexes with the binding energy of the second proton of 0.81 and 0.79 eV, respectively.

The binding energy between a Ti vacancy ($V_{\mathrm{Ti}}{}^{4-}$) and H interstitial, or simply a proton, H^{+} and between (nH-V_{Ti})$^{-4+n}$ and a proton can be defined as

$$\Delta E = E_{\mathrm{tot}}(\mathrm{H}-V_{\mathrm{Ti}})^{3-} + E_{\mathrm{tot}}(\mathrm{bulk}) - E_{\mathrm{tot}}(V_{\mathrm{Ti}}^{4-}) - E_{\mathrm{tot}}(\mathrm{H}^{+}) \tag{5.3}$$

and

$$\Delta E = E_{\mathrm{tot}}([n+1]\mathrm{H}-V_{\mathrm{Ti}})^{-3+n} + E_{\mathrm{tot}}(\mathrm{bulk}) - E_{\mathrm{tot}}(n\mathrm{H}-V_{\mathrm{Ti}})^{-4+n} - E_{\mathrm{tot}}(\mathrm{H}^{+}) \tag{5.4}$$

Equation (5.3) describes the binding energy of the reactions

$$H^{1+} + V_{\mathrm{Ti}}^{4-} \rightarrow (H-V_{\mathrm{Ti}})^{3-} \tag{5.5}$$

which is the energy gain when a proton is bound in a $V_{\mathrm{Ti}}{}^{4-}$. Equation (5.4) is a more general case describing the binding energy of an addition proton to the existing (nH-V_{Ti})$^{-4+n}$ complex (n=0, 1, 2, 3). Note that, equation (5.3) is a specific case of equation (5.4) when n=0.

For H and V_{Ti}, V_{Ti} in charge state 4 ($V_{\mathrm{Ti}}{}^{4-}$), it can trap up to four protons to form a nH-V_{Ti} complex defect. $V_{\mathrm{Ti}}{}^{4-}$ traps the first proton to form (H-V_{Ti})$^{3-}$ with a large binding energy ~1.94 eV. The (H-V_{Ti})$^{3-}$ could trap another proton to form a (2H-V_{Ti})$^{2-}$

complex defect with a binding energy for the second proton of 1.62 eV. In this case, there are two possible ways to add the second proton to form a $(2H\text{-}V_{Ti})^{2-}$ complex defect. (1) The second proton is attached to the O atom on the opposite side of the vacancy from the O atom attached by the first proton. (2) The second proton is attached to one of the four O atoms that are the neighbor of the vacancy and sits next to the O atom attached by the first proton. The two configurations are relaxed at two minimum energy configurations as illustrated in Figure 5.7 (point c and d). To determine the energy barrier between the two configurations, we employed the climbing image nudged elastic band method (NEB).

In Figure 5.7, the highest energy structure (point a) is when the two O–H bonds are pointing directly at each other. To reduce the dipole-dipole interactions, the two O–H bonds are tilted off the equilibrium position into point b, lowering the energy by about 0.05 eV. Without any barrier, the O–H bonds can further tilt into point c, lowering the energy by another 0.05 eV. The structure at point c is the local minimum-energy structure for the first configuration. Next, if we force one of the protons to break its O–H bond and move to form a bond with another O atom, we obtained the *c* to *d* path with a small energy barrier of ~0.1 eV for the proton to move from the first configuration to the lower energy (second) configuration, as shown in Figure 5.7. This rather low energy barrier indicates that protons in the V_{Ti} could move rather freely to find their global minimum energy positions. Therefore, majority of the $(2H\text{-}V_{Ti})^{2-}$ complexes should exist in their lowest energy configuration (point d) at reasonably low temperatures.

The $(2H\text{-}V_{Ti})^{2-}$ complexes could trap another proton to form $(3H\text{-}V_{Ti})^{-}$ complexes There are two possible configurations for the $(3H\text{-}V_{Ti})^{-}$ complexes with the lower energy one shown in Figure 5.8. The (3H-V_{Ti})$^{-}$ complexes could further bind with another proton to form neutral 4H-V_{Ti} complexes. Again, there are two possible configurations for the 4H-V_{Ti} complexes with the lower energy one shown in Figure 5.8. The formation of these complexes can be summarized in the following reaction equations.

$$\begin{aligned}
H^{1+} + V_{Ti}^{4-} &\rightarrow (H - V_{Ti})^{3-} + 1.94 \text{ eV}, \\
H^{1+} + (H - V_{Ti})^{3-} &\rightarrow (2H - V_{Ti})^{2-} + 1.62 \text{ eV}, \\
H^{1+} + (2H - V_{Ti})^{2-} &\rightarrow (3H - V_{Ti})^{-} + 1.51 \text{ eV}, \\
H^{1+} + (3H - V_{Ti})^{1-} &\rightarrow (4H - V_{Ti}) + 1.00 \text{ eV}.
\end{aligned} \tag{5.6}$$

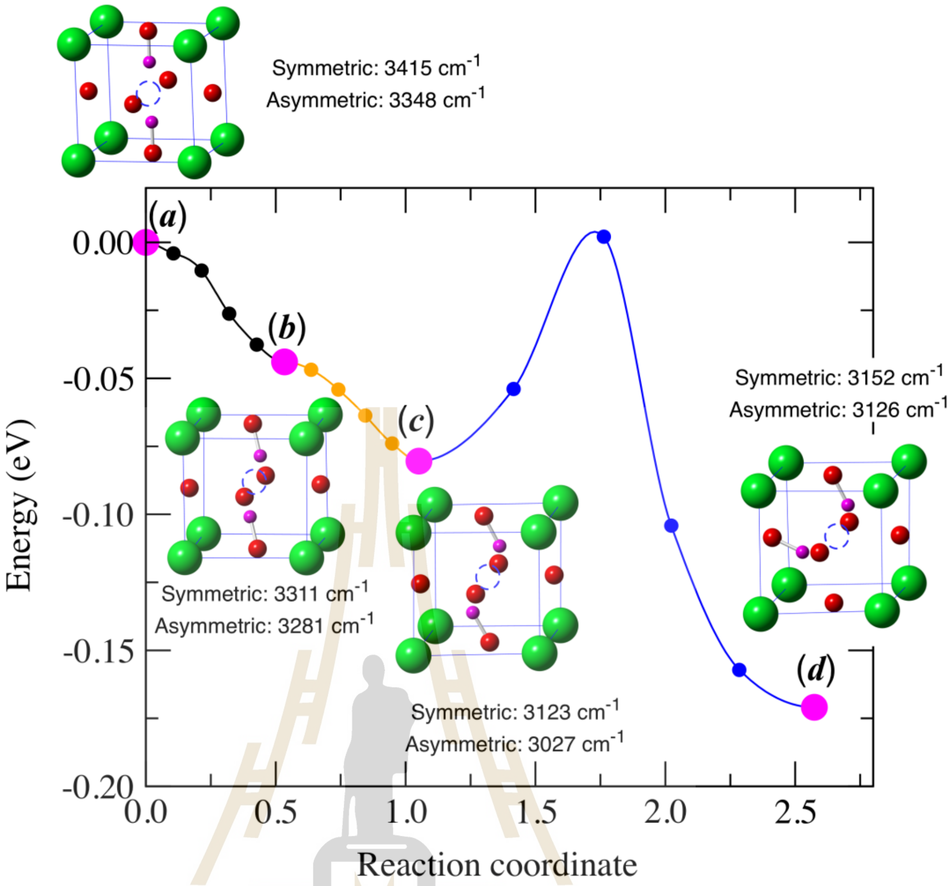

Figure 5.7 Illustration of the energy path relating different configurations of (2H-V_{Ti})$^{2-}$ complexes obtained from the nudged elastic band method. Points (a)–(d) indicate interesting configurations of which the configurations at (c) and (d) are the local minimum and global minimum energy configurations, respectively. The stretch vibrational frequencies are also listed for each configuration.

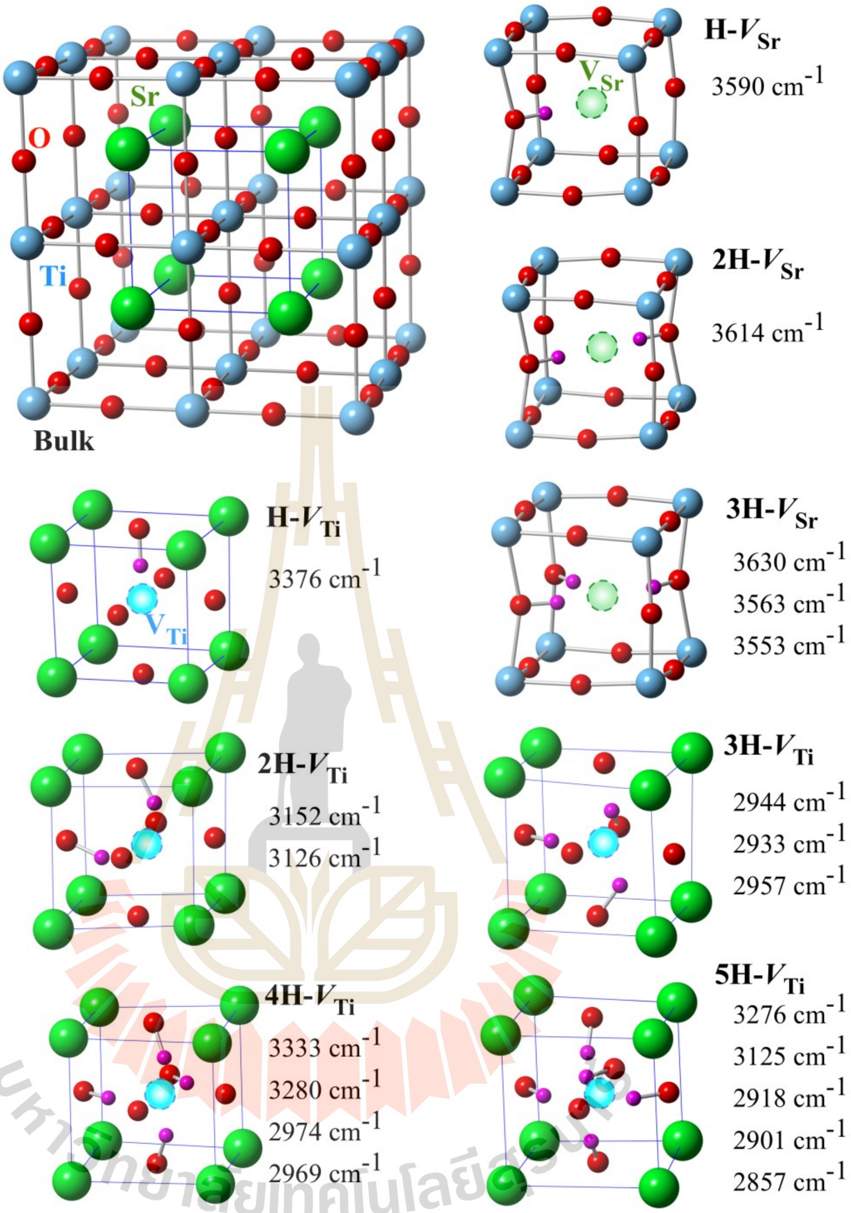

Figure 5.8 The local structures of bulk $SrTiO_3$ and complex defects of H-V_{Sr}, 2H-V_{Sr}, 3H-V_{Sr}, H-V_{Ti}, 2H-V_{Ti}, 3H-V_{Ti}, 4H-V_{Ti}, and 5H-V_{Ti} complexes. Green, blue, red, and pink colors represent the Sr, Ti, O, and H atoms, respectively. The stretch vibrational frequencies for each configuration are also shown.

5.6.2 Local vibrational frequencies of H-V_{Ti} complex defects

The vibrational frequency associated with each defect was determined by calculating the dynamical matrix based on the harmonic approximations as described in Ref. (T-Thienprasert *et al.*, 2010) and chapter III. To test the reliability of the calculations, we first calculated the vibrational modes of a water molecule and obtained the vibrational frequencies of 3712, 3825, and 1533 cm^{-1} for symmetric stretching, asymmetric stretching, and bending modes, respectively. Comparing with the experimental values of 3657, 3756, and 1595 cm^{-1} (Huber, 2013; Shimanouchi, 1972) the computational values contain the error bar of ~70 cm^{-1}.

Next, we calculated the vibration signatures of nH-V_{Ti} complex defects. We found that all nH-V_{Ti} complexes give the vibrational frequency below 3400 cm^{-1} (see Figure 5.8). The (H-V_{Ti})$^{3-}$ complex has the calculated vibrational frequency of 3376 cm^{-1} in a reasonable agreement with the values observed by TM. When a second proton is added to form (2H-V_{Ti})$^{2-}$ complex, the two O–H bonds can vibrate as two oscillators. We found that, unlike the case of 2H-V_{Sr} that the two oscillators have no coupling between them, here there is a coupling between the two oscillators. The reason can be attributed to the closer distance of the two oscillators in the case of the (2H-V_{Ti})$^{2-}$ complex compared to the 2H-V_{Sr} complex. The vibrational frequency of the (2H-V_{Ti})$^{2-}$ complex is split into two values, as shown in Figure 5.8. Interestingly, the two calculated frequencies are differed by 26 cm^{-1}, which is in a good agreement with the splitting of the two peaks of 29 cm^{-1} observed by TM (Tarun and McCluskey, 2011). This is the strongest indication that the observed IR absorption peaks by TM at 3355 and 3384 cm^{-1} should come from (2H-V_{Ti})$^{2-}$ complex rather than 2H-V_{Sr} complex. Note, however, that the absolute values of the calculated vibrational frequencies of the $(2H\text{-}V_{Ti})^{2-}$ complex are only 3152 and 3126 cm^{-1}, somewhat lower than the values observed by TM (by about 7%). In addition to the vibrational frequencies of the lowest energy configuration, those of the higher energy configurations have also been calculated and are shown in Figure 5.7. Beside the vibration frequencies of $(H\text{-}V_{Ti})^{3-}$ and $(2H\text{-}V_{Ti})^{2-}$ complexes, we further calculated the vibration of $(3H\text{-}V_{Ti})^{-}$ and $4H\text{-}V_{Ti}$ complexes in their lowest-energy configurations and showed their vibrational frequencies in Figure 5.8. We found all calculated vibrational frequencies to be in the range of 2900–3400 cm^{-1}.

5.7 Conclusions

In summary, we have studied the stability and local vibration modes of a proton in cubic perovskite $SrTiO_3$ by first-principles calculations. In a perfect crystal, a proton has the lowest formation energy at a site with low symmetry [off-axis site (OA)]. The previously proposed center face (CF) and octahedral edge (OE) sites are 0.25 and 2.29 eV higher in energy than the OA site. While the proton at the OA site forms a short O-H bond similar to a proton in other oxides, its calculated stretch vibration frequency is only 2745 cm^{-1} far lower than the observed absorption band at around 3500 cm^{-1} that was previously assigned to an interstitial proton. Not only the frequency does not match, but the OA configuration has an O-H dipole direction inconsistent with the measured polarized IR results. Moreover, our calculated diffusion barrier of an interstitial proton is only ~0.25 eV; indicating that a proton is very diffusive even at room temperature, and thus is likely to migrate out from the sample during the cooled down. We propose that the cause of the observed 3500 cm^{-1}

band is a proton in a Sr vacancy $(H\text{-}V_{Sr})^{-}$ which has a strong binding energy of 0.84 eV and a calculated O-H vibrational frequency of 3505 cm^{-1} with the dipole orientations in agreement with the experimentally observed 3500 cm^{-1} band. The $2H\text{-}V_{Sr}$ complexes which can also form in samples with high H concentrations have the frequencies consistent with the observed hump ~20 cm^{-1} above the main 3500 band. We also propose that the distinct twin peaks at 3355 and 3384 cm^{-1} observed more recently should originate from complex defects between H and Ti vacancy (nH–V_{Ti} complexes) in $SrTiO_3$. The lowest-energy configurations for nH–V_{Ti} complexes (n=1, 2, 3, and 4) were identified and their vibrational frequencies were calculated. The calculated vibrational frequencies of nH–V_{Ti} complexes are in the range of 2900–3400 cm^{-1}. For the complexes containing more than one O–H oscillator, there is some coupling between the stretch vibration modes. For 2H–V_{Ti} complex, the coupling leads to the split in the two vibration frequencies of 26 cm^{-1}. This combined with study of nH-V_{Sr} complexes in $SrTiO_3$, indicates that the twin IR absorption peaks at 3355 and 3384 cm^{-1} observed by Tarun and McCluskey (Tarun and McCluskey, 2011) are associated with the complex defects between H and V_{Ti} On the other hand, the higher IR absorption peaks at ~3400 cm^{-1}, observed much earlier by Weber and Kapphan, are associated with the complex defects between H and V_{Sr}.

CHAPTER VI

IDENTIFICATION OF Mn SITE IN Mn-DOPED SrTiO$_3$: FIRST PRINCIPLES STUDY

6.1 Introduction

Manganese-doped SrTiO$_3$ (STO) has been widely studied experimentally and theoretically due to its excellent physical properties, including dielectric, electronic and magnetic properties (Dawson *et al.*, 2014; Choudhury *et al.*, 2011; Choudhury *et al.*, 2013; Tkach *et al.*, 2006). Mn atom is known to exist in two oxidation states, i.e., Mn^{2+} and Mn^{4+}. The oxidation state suggests that Mn might incorporate at either Sr^{2+} or Ti^{4+} site. Nevertheless, other factors, such as the mismatch in size with the host atom and coordination number of the local structure, also play roles. Recently, different dielectric and structural properties of Mn-doped STO have been observed in the samples grown under different conditions.(Tkach *et al.*, 2006; Tkach *et al.*, 2004) This suggests that Mn might substitute into different sites in STO. It is expected that when Sr^{2+} (*A*-site) is substituted by a smaller Mn^{2+} ion, Mn should shift off-center from the *A*-site by a significant amount. This could lead to several favorable properties, such as large polarization response, low temperature dielectric relaxation, polar behavior, dilute magnetic, and magnetoelectric multiglass. (Lemanov *et al.*, 2003; Levin *et al.*, 2010; Kleemann *et al.*, 2008) On the other hand, Ti^{4+} (*B*-site) should be nicely fit with Mn^{4+} with a small distortion around Mn^{4+} because their ionic radii are comparable. This is expected to suppress the dielectric permittivity as observed by Tkach and his group (Tkach *et al.*, 2004). However, it remains unclear if the site substitution of Mn can be effectively controlled by limiting the cation composition during growth, i.e., using the compositions $Sr_{1-x}Mn_xTiO_3$ or $SrTi_{1-x}Mn_xO_3$, for on *A*-site and *B*-site, respectively. By using the extended x-ray absorption fine structure (EXAFS) spectroscopy, Levin *et al.* revealed that the samples, which are prepared by solid state reaction with the composition intended for Mn to substitute on *A*-site ($Sr_{1-x}Mn_xTiO_3$) with sintering temperature at 1500 °C under nitrogen or oxygen gas for 5 hours, show some Mn occupying *B*-site (Levin *et al.*, 2010). In addition, some controversies on the key factors responsible for the observed anomalous magnetic and dielectric properties in Mn-doped STO samples have been reported (Kleemann *et al.*, 2008; Valant *et al.*, 2012; Tkach *et al.*, 2010; Yang *et al.*, 2012). This could be attributed to the substitution of Mn at different sites in different samples. Regarding theoretical study, by using first-principles calculations with hybrid functional, Yang *et al.* suggested that Mn substituted for Ti (Mn_{Ti}) can effectively narrow the band gap of STO, but the band gap does not change when Mn substitutes for Sr (Mn_{Sr}). (Yang *et al.*, 2012) This difference in band gap narrowing might be the effect of different band filling between Mn_{Ti} and Mn_{Sr}. They also reported that Ti-site (or *B*-site) is the most energetic preferred site under O-rich conditions. In contrary, another theoretical work based on molecular dynamic simulation combined with *ab-initio* calculations suggested that Mn preferred to substitute for Sr. (Dawson *et al.*, 2014) Therefore, the substitution of Mn on Sr or Ti site under different growth conditions needs to be clarified. In addition, other Mn-related defects, such as Mn interstitial and Mn complex defects, have not been studied in previous works. Here, we employed first-principles calculations, like what previously used to study Mn in $PbTiO_3$ (Boonchun *et al.*, 2007), to investigate Mn-related defects in STO. The most favorable sites of Mn in STO under different growth conditions are examined and the fully relaxed structures were used to simulate the Mn *K*-edge XANES spectra (T-Thienprasert *et al.*, 2011; T-Thienprasert *et al.*, 2013; Limpijumnong *et al.*, 2006) to compare with the available measured Mn *K*-edge XANES spectra from literature (Valant *et al.*, 2012). Valant *et al.* dope Mn into STO by ball milling under different conditions: (1) $(Sr_{1-x}Mn^{2+}_{x})TiO_3$ sample fired at 1500 °C in N_2 atmosphere for 10 h (named $A1500N_2$) and (2) $Sr(Ti_{1-y}Mn^{4+}_{y})O_3$ sample fired at 1150 °C in air for 10 h (named B1150air) and measured their XANES spectra (in Figure 6.1). This result can help us to directly compare the simulation with the experiment to identify the Mn site in each sample.

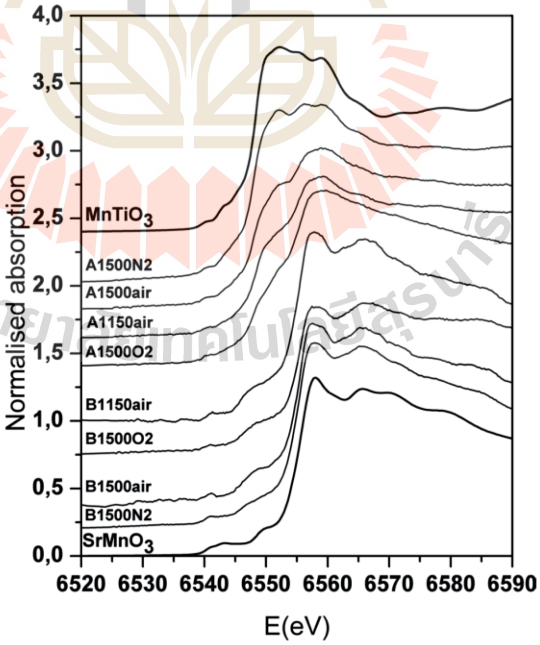

Figure 6.1 Mn *K*-edge XANES spectra of Mn-doped $SrTiO_3$ samples and reference manganese compounds: $MnTiO_3$ and $SrMnO_3$. The spectra have been shifted vertically for clarity. (Valant *et al.*, 2012)

6.2 Method

We utilized first-principles calculations based on spin-polarized density functional theory (DFT) within the generalized gradient approximation (GGA) parameterized by Perdew, Burke, and Ernzerhof (PBE) (Perdew *et al.*, 1996). To describe the electron-ion interactions, the projector-augmented wave (PAW) method as implemented in VASP codes was used (Kresse and Hafner, 1994; Kresse and Joubert, 1999; Kresse and Furthmüller, 1996). The energy cutoff for expanding the plane wave basis set was set at 500 eV. The calculated lattice parameter of STO is 3.952 Å in good agreement with the experimental value.(Lytle, 1964) To study the Mn-related defects in STO, a supercell approach with a 135-atom cell, which is a repetition of the conventional cubic-perovskite unit cell by 3x3x3, was carried out. For *k*-space integrations, we used the Monkhorst-Pack scheme (Monkhorst and Pack, 1976) with a shifted sampling *k*-point mesh of 2x2x2. All atoms in the supercell were allowed to relax until the residual Hellmann-Feynman forces (Feynman, 1939) became less than 10^{-2} eV/Å.

To determine the likelihood of defect formations, we calculated a defect formation energy defined by equation (3.4) and under thermodynamic equilibrium, the following conditions must be satisfied to obtained a homogeneous single crystal STO during growth,

$$\mu_{Sr} + \mu_{Ti} + 3\mu_{O} = E_{tot}(\mathrm{SrTiO_3}). \qquad (6.1)$$

Other undesired phases are the same in previous chapter, such as metallic-Sr, metallic-Ti, O_2 gas as well as other oxide phases, including SrO, SrO_2, TiO, TiO_2, and Ti_2O_3, might also form. To prevent undesired phases, following constraints must be taken into consideration:

$$\begin{aligned}&\mu_{\mathrm{Sr}} < E_{tot}(\text{Sr-metallic}),\ \ \mu_{\mathrm{Sr}} + \mu_{\mathrm{O}} < E_{tot}(\mathrm{SrO}),\ \ \mu_{\mathrm{Sr}} + 2\mu_{\mathrm{O}} < E_{tot}(\mathrm{SrO_2}),\\ &\mu_{\mathrm{Ti}} < E_{tot}(\text{Ti-metallic}),\ \ \mu_{\mathrm{Ti}} + \mu_{\mathrm{O}} < E_{tot}(\mathrm{TiO}),\ \ \mu_{\mathrm{Ti}} + 2\mu_{\mathrm{O}} < E_{tot}(\mathrm{TiO_2}),\\ &2\mu_{\mathrm{Ti}} + 3\mu_{O} < E_{tot}(\mathrm{Ti_2O_3}),\ \ \mu_{\mathrm{O}} < E_{tot}(\mathrm{O_2})/2.\end{aligned} \tag{6.2}$$

Equation (6.1) and equation (6.2) leave us with a set of possible μ_{Sr}, μ_{Ti}, and μ_{O} for STO equilibrium growth; illustrated with the shade area in Figure 6.2. In Figure 6.2, μ_{O} is projected onto the μ_{Sr} and μ_{Ti} plane and all chemical potentials were referenced to their natural phases, i.e., metallic-Sr, metallic-Ti, and O_2 gas are all set to 0. The labels A-D in Figure 6.2 represent the points at the boundary associated with four extreme conditions, i.e., (Sr-rich/O-poor), (Ti-rich/O-poor), (Sr-poor/O-rich), and (Ti-poor/O-rich), respectively. Because the formation energies are functions of chemical potentials, these points representing four extreme conditions and the formation energy at other chemical potentials can then be estimated. When a defect containing Mn, the formation of undesired metallic-Mn as well as Mn-oxide phases should be avoided. To properly investigate the plausible phase precipitate limits for Mn, common natural phases and compound that related with Sr and Ti of Mn, i.e., MnO, MnO_2, Mn_2O_3, Mn_3O_4, $MnTiO_3$ and $SrMnO_3$ were considered and used to define the phase precipitate limits for Mn. The chemical potential of Mn (μ_{Mn}), can be written as:

$$\begin{aligned}&\Delta\mu_{\mathrm{Mn}} = \Delta H(\mathrm{MnO}) - \Delta\mu_{\mathrm{O}},\ \Delta\mu_{\mathrm{Mn}} = \Delta H(\mathrm{MnO_2}) - 2\Delta\mu_{\mathrm{O}},\\ &\Delta\mu_{\mathrm{Mn}} = (\Delta H(\mathrm{Mn_2O_3}) - 3\Delta\mu_{\mathrm{O}})/2,\ \Delta\mu_{\mathrm{Mn}} = (\Delta H(\mathrm{Mn_3O_4}) - 4\Delta\mu_{\mathrm{O}})/3,\\ &\Delta\mu_{\mathrm{Mn}} = \Delta H(\mathrm{MnTiO_3}) - \Delta\mu_{\mathrm{Ti}} - 3\Delta\mu_{\mathrm{O}},\ \Delta\mu_{\mathrm{Mn}} = \Delta H(\mathrm{SrMnO_3}) - \Delta\mu_{\mathrm{Sr}} - 3\Delta\mu_{\mathrm{O}}.\end{aligned} \tag{6.3}$$

Therefore, μ_{Mn} was limited by MnO_2 and metallic-Mn phases for O-rich and O-poor growth conditions, respectively.

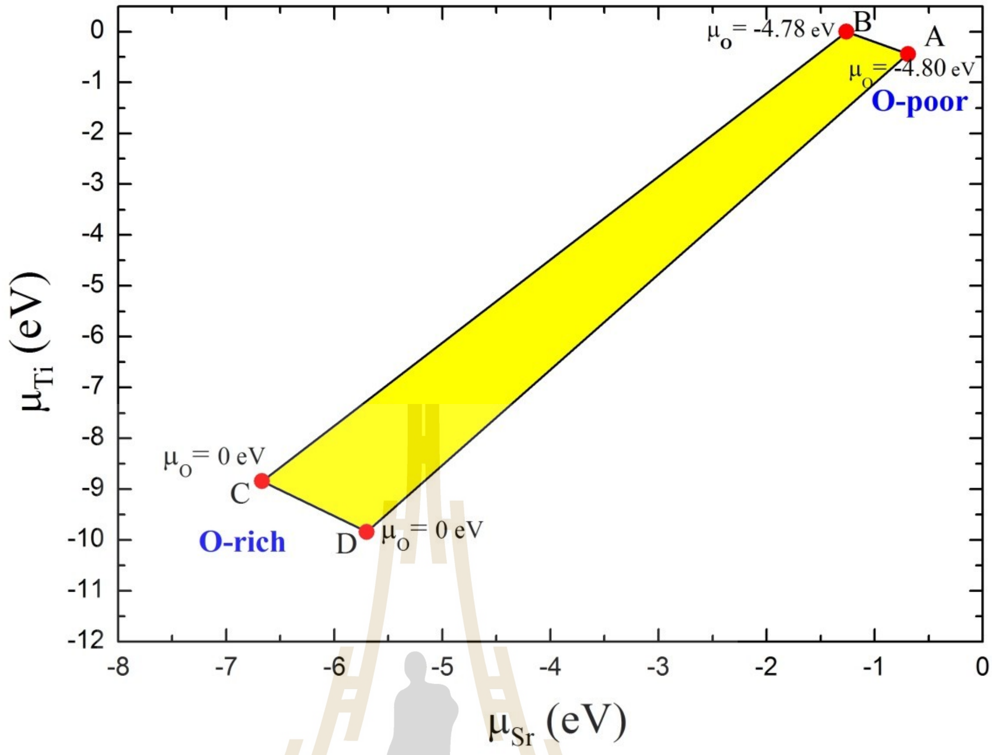

Figure 6.2 Chemical potential domain for thermal equilibrium growth of $SrTiO_3$ crystal. The chemical potentials of Sr and Ti are plotted on the *x* and *y* axes, respectively, while the chemical potential of O is related by the constrain explained in the text. The shaded area represents the allowed chemical potentials satisfied the constraints in equation (6.1) and (6.2).

To simulate XANES spectrum, the fully relaxed local structures of Mn-related defects in STO obtained from VASP codes were used as an input coordinates for FEFF8.2 codes (Rehr *et al.*, 2009) FEFF8.2 is employed to calculate Mn *K*-edge XANES spectrum based on the multiple-scattering expansion within the muffin-tin potentials. The Hedin-Lundqvist was used as the exchange-correlation potential with an imaginary part of 0.5 eV to simulate the experimental broadening. The radii for self-consistent potential and full-multiple scattering calculations were set at 0.55 and 0.80 nm, respectively.

6.3 Formation Energy of Mn in $SrTiO_3$

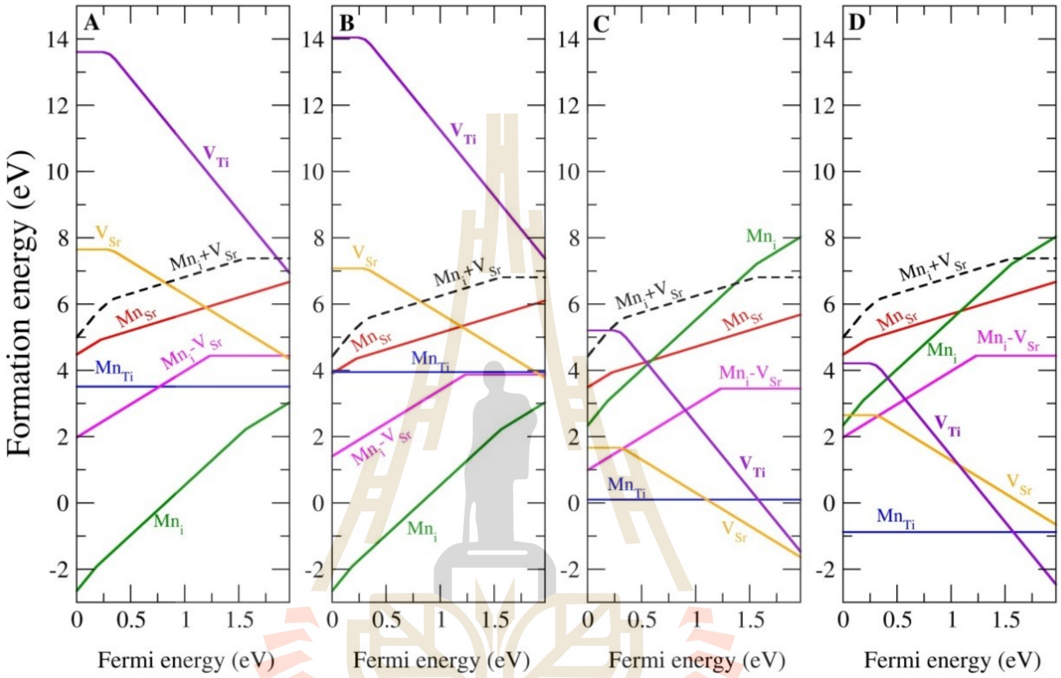

Figure 6.3 Defect formation energies as functions of Fermi energy under different growth conditions, i.e., A, B, C, and D from left to right panels, respectively. The slope of each line indicates the charge state of the defect. The dashed black line represents the sum of the formation energies of Mn_i and V_{Sr} defects.

In Figure 6.3, the formation energies of simple Mn defects, namely, Mn substitution for Sr (Mn_{Sr}), Mn substitution for Ti (Mn_{Ti}), and Mn interstitial (Mn_i), are plotted as a function of Fermi energy under four extreme conditions as described before. In the plot, only the charge state with the lowest energy for each defect at a given Fermi energy is shown. (The charge state of the defect can be determined from the slope of the line.) The Fermi-energy range is extended to the calculated band gap of ~1.98 eV. Note that the calculated band gap is lower than the experimental band gap of 3.25 eV (Van Benthem *et al.*, 2001) due to the well-known DFT problems. Our calculations found that Mn_{Sr} is a donor with defect transition level at $\varepsilon(+2/+1)$ = 0.25 eV, while Mn_{Ti} is a charge neutral for the entire possible Fermi energy range. Mn_i is a donor with two transition levels at $\varepsilon(+4/+3)$ = 0.20 eV and $\varepsilon(+3/+2)$ = 1.57 eV. The local structures of Mn_{Ti}, Mn_{Sr}, and Mn_i defects are illustrated in Figure 6.4 (a) – (c). It appears that Mn substitutes for Sr (or Ti) atom does not lead to a large local structure distortion or large off-center shift. However, for Mn_{Sr}, this is not the lowest energy configuration which will be explained later. The lowest-energy site for interstitial Mn (Mn_i) is at the center of Sr-Sr bond. After inserting the Mn in between two Sr host atoms, the two atoms slightly relax outward. Mn_{Ti} and Mn_i are energetically most favorable (hence, the dominant) defects under both O-rich and O-poor growth conditions, respectively. Note that, the breaking symmetry of Mn on Sr site (shift Mn away from the Sr site) can lower the energy, however, its formation energy remains higher than that of Mn_i and Mn_{Ti} defects. Therefore, Mn_{Sr} cannot be the lowest energy defect at any growth conditions considered. However, experimental results showed that under certain growth conditions, $(Sr_{1-x}Mn_x)TiO_3$ samples (A-site substitution) can be achieved with distinct properties from the usually observed Mn_{Ti}. (Tkach *et al.*, 2004; Valant *et al.*, 2012) In addition, they found that the $(Sr_{1-x}Mn_x)TiO_3$ samples show the co-existence of Mn on *A*-site and *B*-site. Our calculations showed that Mn_{Ti} is likely to exist in most growth conditions and difficult to be avoided, which agree well with the experimental finding. However, Mn_{Sr} has high formation energy and its existence need further explanation as will be explained next.

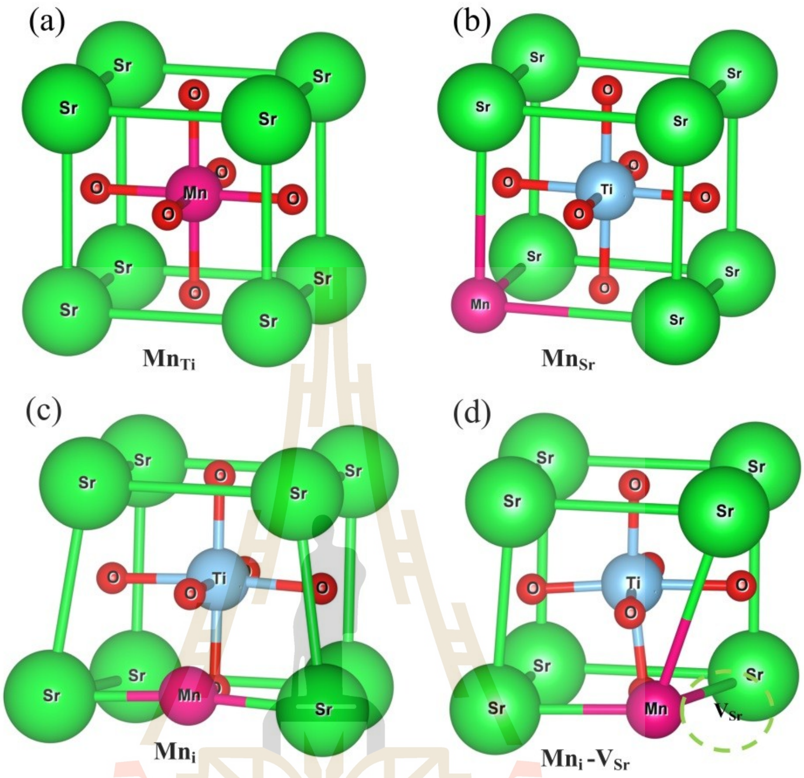

Figure 6.4 The local structures of (a) Mn_{Ti}, (b) Mn_{Sr}, (c) Mn_i, and (d) Mn_i-V_{Sr} complex or off-center Mn_{Sr}.

Interstitial Mn (Mn_i) is a charged defect because Mn is a donor, which can be stable in +4, +3, and +2 charge states. As a charged defect, it can be compensated by an opposite charge native defect; forming a neutral complex. For intrinsic point defects, the potential compensating native point defects are Sr vacancy Sr (V_{Sr}) and Ti vacancy (V_{Ti}), both of which are acceptor.

6.4 Binding Energy of Mn with Vacancy

The calculated the formation energies of V_{Sr} and V_{Ti} are shown in Figure 6.3. The formation energy of V_{Sr} is lower than that of V_{Ti} under several growth conditions. Therefore, V_{Sr} can be the compensating defect in $(\mathrm{Sr}_{1\text{-}x}\mathrm{Mn}_x)\mathrm{TiO}_3$ samples. We investigated the complex defect formation between Mn_i and V_{Sr}, i.e., Mn_i-V_{Sr} complex and found that the complex is a deep donor with two defect transition levels at ε(+2/0) = 1.25 eV. To determine the stability of the complex, we calculated the binding energy defined by

$$E_{bind}(A-B) = E_f(A) + E_f(B) - E_f(A-B) \tag{6.4}$$

where $E_f(A)$ and $E_f(B)$ are the formation energies of the defects A and B, and $E_f(A-B)$ is the formation energy of the A–B complex. If the complex has a large binding energy, it is more likely to form. As shown in Figure 6.3, the dashed line represents the sum of the formation energies of Mn_i and V_{Sr}. The binding energy of Mn_i-V_{sr} complex is the difference between the dashed black line and the magenta (Mn_i-V_{sr}) line. We found that the binding energy of the complex is more than 2.6 eV which is high; indicating that such complex is likely to exist in a high concentration and very stable.

6.5 Local Structures of Mn in SrTiO_3

The local structures of Mn_i-V_{Sr} complex is shown in Figure 6.4(d). The interstitial Mn atom move toward V_{Sr}, but not into the center of it. This structure can also be viewed as a largely distorted $\mathrm{Mn}_{\mathrm{Sr}}$, where Mn atom is largely shifted away from the regular Sr site; resulting in a large off-centering $\mathrm{Mn}_{\mathrm{Sr}}$. This structure is in good agreement with the experimental observation. (Levin *et al.*, 2010; Valant *et al.*, 2012) (In principle, slightly shift Mn off-center during the $\mathrm{Mn_{Sr}}$ calculation should lead to this structure shown in Figure 6.4(d). after relaxation. However, our actual calculation did not give this result, instead we obtained a slightly distorted $\mathrm{Mn_{Sr}}$.)

To directly compare our calculated results with the experiment, we calculated the Mn *K*-edge XANES spectra associated with $\mathrm{Mn_{Sr}}$ (on regular lattice), $\mathrm{Mn_{Ti}}$, and Mn_i-V_{Sr} or off-center $\mathrm{Mn_{Sr}}$ defects. Our calculated results are illustrated in Figure 6.5 along with the experimental Mn *K*-edge XANES spectra obtained from $(\mathrm{Sr}_{1-x}\mathrm{Mn}_x)\mathrm{O}_3$ and $\mathrm{Sr}(\mathrm{Ti}_{1-x}\mathrm{Mn}_x)\mathrm{O}_3$ samples that are experimentally assigned to be associated with Mn substitutions for *A*-site and *B*-site, respectively. (Valant *et al.*, 2012) It is clear that the features of the calculated XANES spectrum of $\mathrm{Mn_{Sr}}$ defect (on regular Sr lattice) is significantly distinct from that of the measured XANES spectrum of $(\mathrm{Sr}_{1-x}\mathrm{Mn}_x)\mathrm{O}_3$ sample. On the other hand, the features of the calculated XANES spectrum of $\mathrm{Mn_i}$-V_{Sr} complex (or off-center $\mathrm{Mn_{Sr}}$) are similar to that of the measured XANES spectrum of $(\mathrm{Sr}_{1-x}\mathrm{Mn}_x)\mathrm{O}_3$ sample. The calculated XANES spectrum of $\mathrm{Mn_{Ti}}$ is in good agreement with the measured XANES spectrum of $\mathrm{Sr}(\mathrm{Ti}_{1-x}\mathrm{Mn}_x)\mathrm{O}_3$ sample. Our XANES calculations confirm the assignment of Mn in $\mathrm{Sr}(\mathrm{Ti}_{1-x}\mathrm{Mn}_x)\mathrm{O}_3$ sample to be $\mathrm{Mn_{Ti}}$ and the assignment of Mn in $(\mathrm{Sr}_{1-x}\mathrm{Mn}_x)\mathrm{O}_3$ sample to be Mn_i-V_{Sr} complex (or off-center $\mathrm{Mn_{Sr}}$).

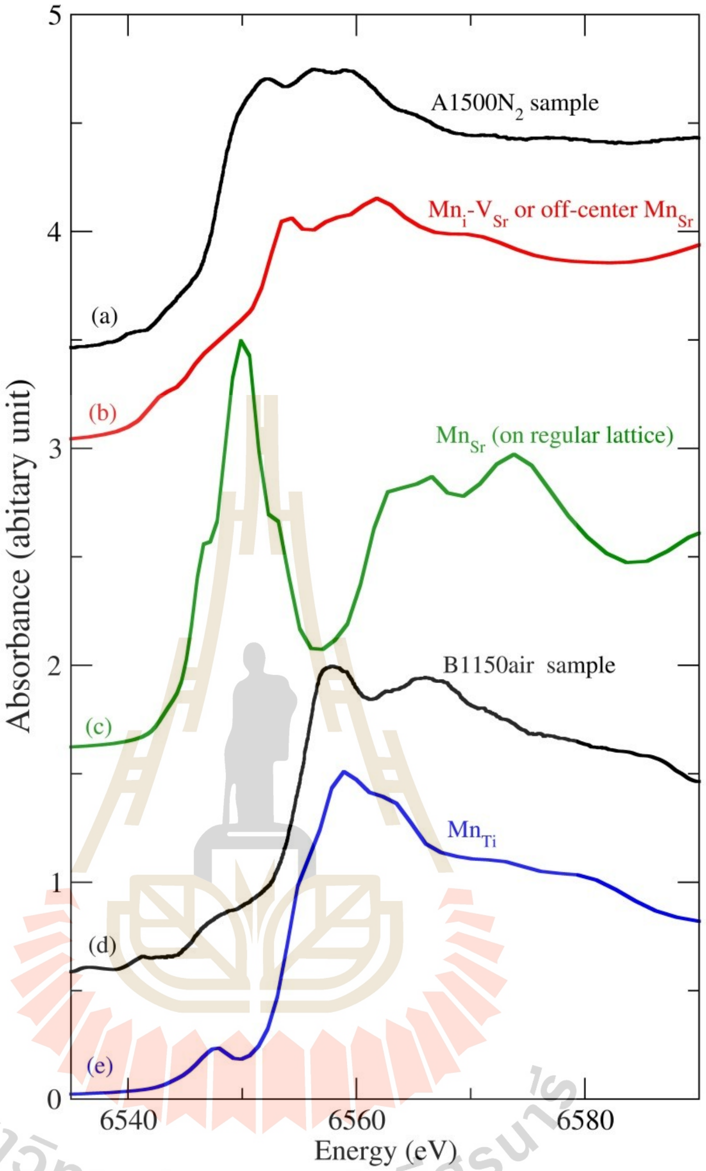

Figure 6.5 Comparison between the calculated and measured Mn *K*-edge XANES spectra. The measured Mn *K*-edge XANES spectra (Valant *et al.*, 2012) of $(Sr_{1-x}Mn_x)TiO_3$ sample ($A1500N_2$) and $Sr(Ti_{1-x}Mn_x)O_3$ sample (B1150air) are marked by (a) and (d). The calculated Mn *K*-edge XANES spectra associated with Mn_i-V_{Sr} (or off-center Mn_{Sr}), Mn_{Sr}, and Mn_{Ti} are labeled by (b), (c), and (e), respectively.

6.6 Conclusions

We use first-principles DFT calculations to investigate Mn-related defects in STO under different growth conditions. We found that Mn_{Ti} is the lowest energy defect under most growth conditions. Therefore, Mn_{Ti} defect can be observed in most of the Mn-doped STO regardless of how the elemental composition is forced, i.e., both $(Sr_{1-x}Mn_x)TiO_3$ and $Sr(Ti_{1-x}Mn_x)O_3$ samples. In addition, our calculations show that a substitutional-vacancy complex Mn_i-V_{Sr}, which has the same chemical composition as Mn_{Sr} but with Mn atom largely shifted off-center, can form in certain growth conditions with reasonably low formation energy. This off-center Mn_{Sr} explains the observed *A*-site substitution in $(Sr_{1-x}Mn_x)TiO_3$ samples. Our calculated XANES spectra associated with Mn_{Ti}, and off-center Mn_{Sr} agree nicely with the measured XANES spectra of $Sr(Ti_{1-x}Mn_x)O_3$ and $(Sr_{1-x}Mn_x)TiO_3$ samples, respectively. This confirms the experimental assignment of Mn substitution for *B*-site and *A*-site with detailed energetic description to support the assignment.

CHAPTER VII

FIRST PRINCIPLES STUDY OF Ca IN $BaTiO_3$ AND $Bi_{0.5}Na_{0.5}TiO_3$

7.1 Introduction

$BaTiO_3$ (henceforth, BT) and $Bi_{0.5}Na_{0.5}TiO_3$ (henceforth, BNT) are currently potential candidates to replace lead-containing ferroelectric materials, which are highly toxic. BT is a ferroelectric material with a tetragonal perovskite structure at room temperature. It has good piezoelectric and ferroelectric properties. However, it has a relatively low Curie temperature at T_c = 120 °C and a phase transition to the rhombohedral phase as the temperature is reduced below 5 °C (Miyake and Ueda, 1948; Merz, 1949). It is necessary to increase the T_c as well as the temperature of the secondary phase transition to make BT practical for real applications (Gao *et al.*, 2007). Adding Bi or other rare-earth elements with smaller ionic radius (Takenaka *et al.*, 1991; Jung *et al.*, 2002) to BT to form compounds, for e.g., $Bi_{0.5}Na_{0.5}TiO_3$ (Yuan *et al.*, 2009), and $Bi_4Ti_3O_{12}$ (Jain *et al.*, 2009), has been reported to increase T_c, improve ferroelectric response and other properties. (Yoshii *et al.*, 2006; Li *et al.*, 2004; Suchuan *et al.*, 2006; Lin *et al.*, 2006; Ge *et al.*, 2010; Gou *et al.*, 2012) BNT, by itself, is also a ferroelectric material. It has Bi^{3+} and Na^{+} ions alternately occupying *A*-site of ABO_3 perovskite structure with rhombohedral symmetry at room temperature. BNT has a rather high Curie temperature of T_c = 320 ^{o}C and a relative large remanent polarization at room temperature. It is expected that a mixture of BT and BNT (BT-BNT) is a ferroelectric material with properties superior to the parent materials. BNT-BT is highly attractive owing to the existence of a rhombohedral (F_α) – tetragonal (F_β) morphotropic phase boundary. Takenaka *et al.* (Takenaka *et al.*, 1991) reported that the BT-BNT at 6% BT composition, i.e., $(Bi_{0.5}Na_{0.5})_{0.94}Ba_{0.06}TiO_3$, has good piezoelectric properties and high dielectric constant. However, the alloy has a stability problem at high temperatures. Yuan *et al.* (Yuan *et al.*, 2010) found that adding a small amount of calcium can effectively improve the temperature characteristic of capacitance (TCC) of the BNT-BT system. However, the role of Ca in BT-BNT system is currently unclear and its preferable site still also unknown. As a cation, Ca is expected to occupy either the *A*-site (Ba, Bi, or Na site) or *B*-site (Ti site). In order to gain a deeper understanding on the role of Ca, the preferable site of Ca in BT-BNT samples has to be identified.

In this chapter, we employed first principles calculations to investigate Ca in BT and BNT. We focused our attentions on the identification of Ca's favorable sites and the resulting electronic properties. The outline of this article is as follows. In section 7.2, the details of our theoretical and computational method are described. In section 7.3, we present a detailed analysis of the possible equilibrium growth conditions of BT and BNT by introducing phase diagrams to show the possible range of chemical potentials of the starting elements. Different growth conditions lead to different form of Ca incorporation. Our main result of the formation energies and electronic properties of Ca substitution for different cation sites in BT and BNT are presented and discussed in section 7.4 and 7.5, respectively. Finally, section 7.6 contains the summary of our work.

7.2 Computational Methods

In this work, we utilized first-principles calculations based on spin-polarized density functional theory (DFT) within the generalized gradient approximation (GGA) with the functional introduced by Perdew, Burke and Ernzerhof (PBE). (Perdew *et al.*, 1996; Perdew *et al.*, 1997) To describe the electron-ion interactions, the projector-augmented wave (PAW) method, (Blöchl, 1994; Kresse and Joubert, 1999) as implemented in VASP code, was used. (Kresse and Hafner, 1993; Kresse and Hafner, 1994; Kresse and Furthmüller, 1996; Kresse and Furthmüller, 1996) The electron wave functions were described using a plane wave basis set with the energy cutoff of 500 eV. This energy cutoff is sufficient to provide a well-converged basis set to describe oxides when using ultrasoft pseudopotentials. (Vanderbilt, 1990) The calculated lattice parameters of tetragonal BT and BNT are in good agreement with the known experimental values as shown in Table 7.1. To study defects in BT and BNT, a supercell approach is used. For BT, we used a 135-atom cell, which is a 3x3x3 repetition of the conventional tetragonal-perovskite unit cell (5 atom/unit cell). For BNT, we used a 120-atom cell, which is a 2x2x3 repetition of the conventional tetragonal-perovskite unit cell (10 atom/unit cell). (Van de Walle and Neugebauer, 2004) For *k*-space integrations, we used the Monkhorst-Pack scheme (Monkhorst and Pack, 1976) with a shifted 2x2x2 *k*-point sampling. The calculated band gap of BT and BNT are smaller than the experimental values due to the well-known DFT problems. The calculated band gaps for BT and BNT at the special *k*-point are 1.68 eV and 2.19 eV whereas the experimental band gaps are 3.2 eV (Wemple, 1970) and 2.94 eV (Parija *et al.*, 2012), respectively. All atoms in the supercell were allowed to relax until the residual Hellmann-Feynman forces (Feynman, 1939) become less than 10^{-2} eV/Å.

Table 7.1 Lattice parameters of tetragonal $BaTiO_3$ and $Bi_{0.5}Na_{0.5}TiO_3$.

Lattice parameters	**Present (Calculation)**	**Experiment**
	$BaTiO_3$	
a **(Å)**	3.979	3.998[a]
c **(Å)**	4.078	4.018[a]
c/a	1.025	1.005[a]
	$Bi_{0.5}Na_{0.5}TiO_3$	
a **(Å)**	5.561	5.519[b]
c **(Å)**	4.089	3.909[b]
c/a	0.728	0.708[b]

[a] Measurement by Electron diffraction density from $BaTiO_3$ sample grown by flux-growth method (Buttner, 1992)

[b] Measurement by Powder neutron diffraction from $Bi_{0.5}Na_{0.5}TiO_3$ sample grown by the flux; powder prepared from ground crystals (Jones, 2000)

7.3 Defect Formation Energies and Crystal Growth Conditions

According description in Chapter III, to use equation (3.3) and (3.4) to determine the abundance of a defect, one needs to know the chemical potentials of all atomic species involved. The actual values of the chemical potentials depend on growth process. However, under suitable choices of thermodynamic equilibrium, the range of possible values of them can be determined by considering the requirements for controllable growth of the crystal. In Chapter III, V, and VI, we already shown the method for considering ternary compound, by the same way, in this chapter we will show, how can we consider chemical potentials for four element compounds. We will be described in this section.

To grow BT and BNT crystal under thermodynamic equilibrium, the following conditions must be satisfied: (Li *et al.*, 2007; Gupta *et al.*, 2007)

$$E_{tot}(\mathrm{BaTiO_3}) = \mu_{Ba} + \mu_{Ti} + 3\mu_O \text{ and } E_{tot}(\mathrm{Bi_{0.5}Na_{0.5}TiO_3}) = \frac{\mu_{Bi}}{2} + \frac{\mu_{Na}}{2} + \mu_{Ti} + 3\mu_O \quad (7.1)$$

where $E_{tot}(\mathrm{BaTiO_3})$ and $E_{tot}(\mathrm{Bi_{0.5}Na_{0.5}TiO_3})$ are the calculated total energy per molecular formula of BT and BNT, respectively, μ_X is the chemical potentials of atom species X referenced to their natural elementary forms. If the sum on the right-hand side of equation (7.1) is larger than the left-hand side, then a rapid and uncontrolled growth of BT or BNT crystal takes place. On the other hand, if the sum on the right-hand side is smaller than the left-hand side, then the crystal disintegrates.

For BT, there are three chemical potentials to be considered. Therefore, the chemical potentials for a given growth condition can be presented as a point in the 3-dimension chemical potential space, where each axis represents each of the three chemical potentials. Equation (7.1) is actually a plane in this 3-dimension space. To make the plane symmetrically intercept the axes at 1, we can define a new set of normalized chemical potentials as follows:

$$\mu'_{\mathrm{Ba}} = \frac{\mu_{\mathrm{Ba}}}{E_{tot}(\mathrm{BaTiO_3})},\ \mu'_{\mathrm{Ti}} = \frac{\mu_{\mathrm{Ti}}}{E_{tot}(\mathrm{BaTiO_3})},\ \text{and } \mu'_{\mathrm{O}} = \frac{3\mu_{\mathrm{O}}}{E_{tot}(\mathrm{BaTiO_3})} \quad (7.2)$$

This transforms the plane equation, equation (7.1), to

$$1 = \mu'_{\mathrm{Ba}} + \mu'_{\mathrm{Ti}} + \mu'_{\mathrm{O}} \quad (7.3)$$

Similarly for BNT,

$$1=\frac{\mu'_{\mathrm{Bi}}}{2}+\frac{\mu'_{\mathrm{Na}}}{2}+\mu'_{\mathrm{Ti}}+\mu'_{\mathrm{O}} \tag{7.4}$$

Where $\mu'_{\mathrm{Bi}}=\frac{\mu_{\mathrm{Bi}}}{E_{tot}(\mathrm{Bi}_{0.5}\mathrm{Na}_{0.5}\mathrm{TiO}_3)}$, $\mu'_{\mathrm{Na}}=\frac{\mu_{\mathrm{Na}}}{E_{tot}(\mathrm{Bi}_{0.5}\mathrm{Na}_{0.5}\mathrm{TiO}_3)}$,

$\mu'_{\mathrm{Ti}}=\frac{\mu_{\mathrm{Ti}}}{E_{tot}(\mathrm{Bi}_{0.5}\mathrm{Na}_{0.5}\mathrm{TiO}_3)}$ and $\mu'_{\mathrm{O}}=\frac{3\mu_{\mathrm{O}}}{E_{tot}(\mathrm{Bi}_{0.5}\mathrm{Na}_{0.5}\mathrm{TiO}_3)}$

Additional limiting conditions have to be placed on the chemical potentials to prevent other low-energy phases of metal oxides, i.e., BaO, BaO_2, Bi_2O_3, Na_2O, TiO, TiO_2, and Ti_2O_3 to form. These conditions can be written as:

$$\left.\begin{aligned}E_{tot}(\mathrm{BaO})&\geq\mu_{\mathrm{Ba}}+\mu_{\mathrm{O}},\\E_{tot}(\mathrm{BaO}_2)&\geq\mu_{\mathrm{Ba}}+2\mu_{\mathrm{O}},\\E_{tot}(\mathrm{TiO})&\geq\mu_{\mathrm{Ti}}+\mu_{\mathrm{O}},\quad\text{for BaTiO}_3\\E_{tot}(\mathrm{TiO}_2)&\geq\mu_{\mathrm{Ti}}+2\mu_{\mathrm{O}},\\E_{tot}(\mathrm{Ti}_2\mathrm{O}_3)&\geq2\mu_{\mathrm{Ti}}+3\mu_{O}.\end{aligned}\right. \tag{7.5}$$

and

$$\left.\begin{aligned}E_{tot}(\mathrm{Bi}_2\mathrm{O}_3)&\geq2\mu_{\mathrm{Bi}}+3\mu_{\mathrm{O}},\\E_{tot}(\mathrm{Na}_2\mathrm{O})&\geq2\mu_{\mathrm{Na}}+\mu_{\mathrm{O}},\\E_{tot}(\mathrm{TiO})&\geq\mu_{\mathrm{Ti}}+\mu_{\mathrm{O}},\quad\text{for Bi}_{0.5}\mathrm{Na}_{0.5}\mathrm{TiO}_3\\E_{tot}(\mathrm{TiO}_2)&\geq\mu_{\mathrm{Ti}}+2\mu_{\mathrm{O}},\\E_{tot}(\mathrm{Ti}_2\mathrm{O}_3)&\geq2\mu_{\mathrm{Ti}}+3\mu_{\mathrm{O}}\end{aligned}\right. \tag{7.6}$$

As a result, the possible chemical potentials of Ba, Na, Bi, and Ti are further limited by their oxide phase according to equation (7.5) and (7.6). To illustrate these limits, a triangular phase diagram can be used to represent the chemical potentials of Ba, Ti and O for BT (see Figure 7.1) and Bi, Na, Ti, and O for BNT crystal (Figure 7.2). In Figure. 1, the black points and the shaded area on the diagram satisfied equation (7.1), (7.2), (7.3), and (7.5). The chemical potentials of Ba, Ti, and O could be any values that lie within the shade area. The black points connected with the black lines represent the solution to equation (7.1) and the extreme points of equation (7.5). Sets of chemical potentials along these lines are the result of the limits due to the possible oxide phases. These black points are marked as (a) to (d) in Figure 7.1. The values of the chemical potentials for Ba, Ti, and O associated with the points (a) – (d) are tabulated in Table 7.2. At point “a”, the chemical potentials of Ba and Ti are at their maximum values and that of O is at its minimum value, i.e., Ba-rich, Ta-rich and O-poor. At point “b”, the chemical potential of Ti is at its minimum value and O is at its maximum, i.e., Ti-poor and O-rich. At point “c”, the chemical potential of Ba is at its minimum value and O is at its maximum value, i.e., Ba-poor and O-rich. Note that points “b” and “c” are not much different. They both have O-rich and metal poor as the values of the chemical potentials of metal varied by only about 1 eV for the two conditions (see Table 7.2). Point “x” represents a condition in the middle of the shaded area. Because these conditions cover the middle region and extrema of the growth conditions, the formation energies of Ca defects in BT will be presented using these conditions.

Table 7.2 Chemical potentials of Ba, Ti, O, and Ca for different growth conditions of BT.

Point	**μ**	μ_{Ba} **(eV)**	μ_{Ti} **(eV)**	μ_{O} **(eV)**	μ_{Ca} **(eV)**
a	μ_a	0	-1.05	-4.97	-0.93
b	μ_b	-5.01	-10.50	0	-5.91
c	μ_c	-6.24	-10.12	0	-5.91
x	μ_x	-3.13	-5.03	-2.62	-2.13

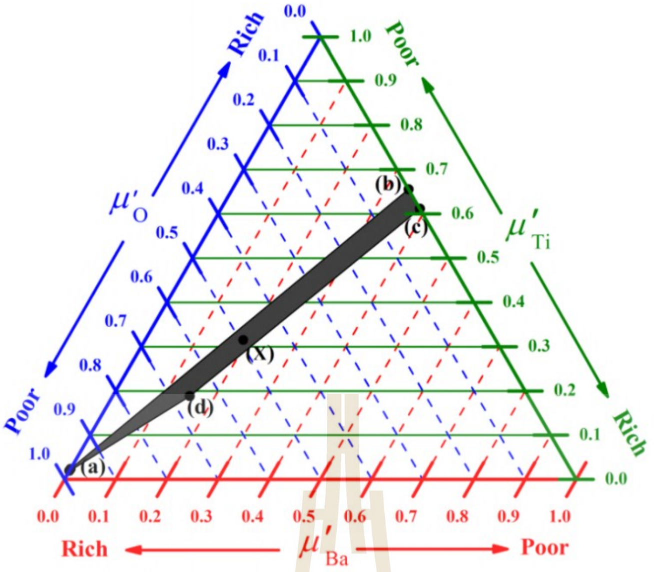

Figure 7.1 Triangular phase diagram for representing the chemical potentials of Ba, Ti, and O according to equation (7.1), (7.2), (7.3), and (7.5) (see text for details).

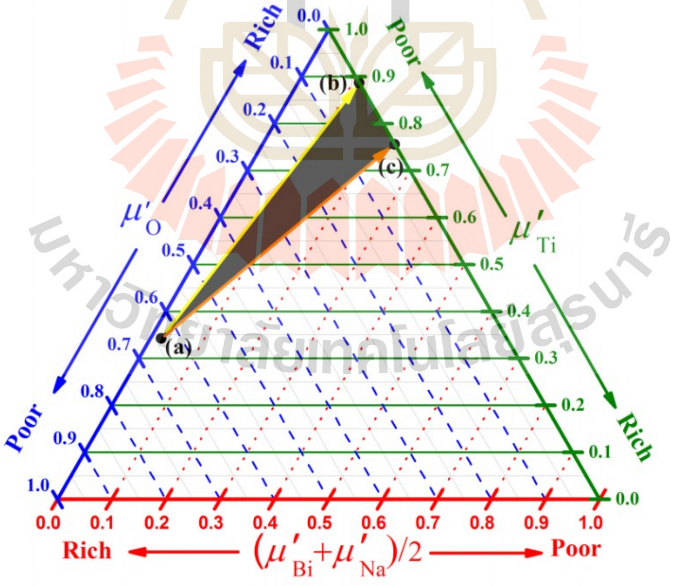

Figure 7.2 Triangular phase diagram for representing the chemical potentials of Bi, Na, Ti, and O according to equation (7.1), (7.2), (7.3), and (7.6) (see text for details).

For BNT, there are four chemical potentials. To show the possible growth conditions of BNT in a 3-dimension chemical potential space, we used the average value of μ'_{Bi} and μ'_{Na}, i.e., $(\mu'_{\mathrm{Bi}} + \mu'_{\mathrm{Na}})/2$ to plot Figure 7.2. The black points and the shaded area on the diagram satisfied equation (7.1), (7.2), (7.3), and (7.6). The chemical potentials of Bi, Na, Ti, and O could be of any value within the shade area. Similar to the case of BT, the black points connected with the black lines represent the solution between equation (7.1) and the extreme points of equation (7.6). Sets of chemical potentials along these lines are the result of the limits due to the possible oxide phases. These black points were marked by letters “a” – “c” in Figure 7.2. Note that only the average of the chemical potentials for Bi and Na is shown in Figure 7.2. To understand the possible growth range for each of them, additional chemical potential plots are needed. The possible chemical potentials for Bi and Na for the conditions along the line “a” to “b” and “a” to “c” in Figure 7.2 are shown in Figure 7.3(i) and Figure 7.3(ii), respectively. In Figure 7.3(i) and Figure 7.3(ii), we marked the chemical potential of O in the plots. At point “a” in Figure. 2, $\mu'_{\mathrm{O}} = 0.64$ and $(\mu'_{\mathrm{Bi}} + \mu'_{\mathrm{Na}})/2 = 0.01$, the line $(\mu'_{\mathrm{Bi}} + \mu'_{\mathrm{Na}})/2 = 0.01$ with the natural phase precipitate limits are shown in Figure 7.3(i) with a label $\mu'_{\mathrm{O}} = 0.64$. At point “b” in Figure 7.2, $\mu'_{\mathrm{O}} = 0$ and $(\mu'_{\mathrm{Bi}} + \mu'_{\mathrm{Na}})/2 = 0.11$, the line $(\mu'_{\mathrm{Bi}} + \mu'_{\mathrm{Na}})/2 = 0.11$ with the natural phase precipitate limits are shown in Figure 7.3(i) with a label $\mu'_{\mathrm{O}} = 0$. The lines for other oxygen chemical potentials in between are also shown. This plot (Figure 7.3(i)) allows us to show the possible range of the chemical potentials of Bi and Na for the conditions along the line “a” to “b” in Figure 7.2. Similarly, Figure 7.3(ii) shows the possible range of Bi and Na chemical potentials for the conditions along the line “a” to “c” in Figure 7.2. These black dots are used to mark the extreme points in Figure 7.3(i) and Figure 7.3(ii) and labeled as $\mathbf{\mu_{A}}$, $\mathbf{\mu_{B1}}$, $\mathbf{\mu_{B2}}$, $\mathbf{\mu_{C1}}$, and $\mathbf{\mu_{C2}}$. Note that for point “b” in Figure 7.2, the chemical potentials of Bi and Na can be varied from condition B1 where Bi is rich and Na is poor to condition B2 where Bi is poorer and Na is richer. Similarly for point “c”, the chemical potentials of Bi and Na can be varied from C1 to C2. For convenience, the values of chemical potentials for Bi, Na and O associated with the black dots are listed in

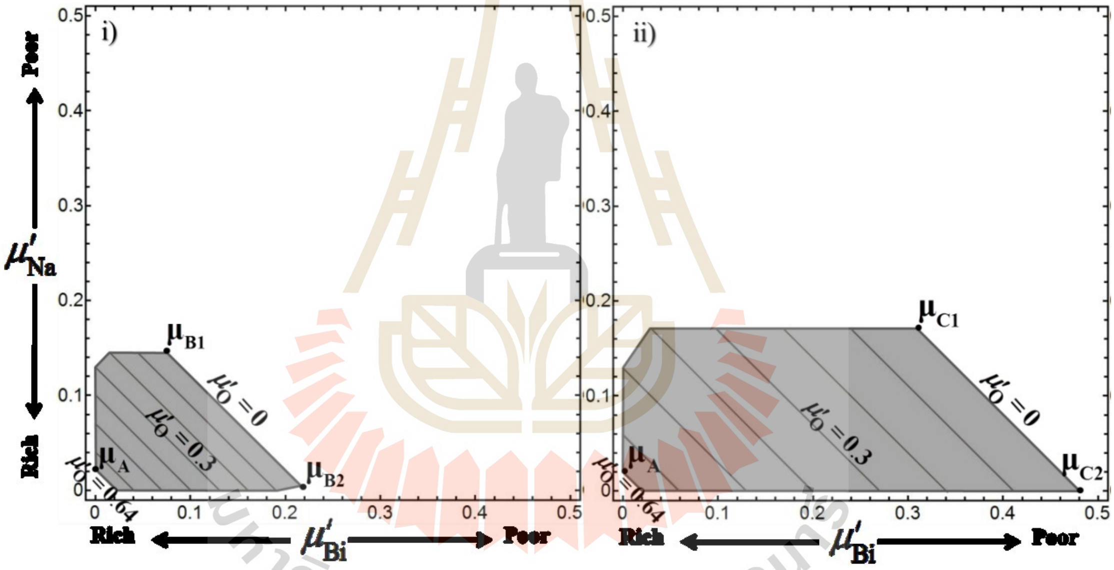

Figure 7.3 The possible chemical potentials of Bi and Na (shade area) that depend on chemical potential of O in each condition along the lines connecting (i) points (a) to (b) and (ii) points (a) to (c) in Figure 7.2.

Table 7.3 Chemical potentials of Bi, Na, Ti, O, and Ca for different growth conditions of BNT.

Point	**μ**	μ_{Bi} **(eV)**	μ_{Na} **(eV)**	μ_{Ti} **(eV)**	μ_{O} **(eV)**	μ_{Ca} **(eV)**
a	μ_A	0	-0.52	-4.37	-2.75	-3.16
b	μ_{B1}	-0.65	-2.19	-11.46	0	-5.91
	μ_{B2}	-2.77	-0.06	-11.46	0	-5.91
c	μ_{C1}	-3.94	-2.20	-9.77	0	-5.91
	μ_{C2}	-6.20	0	-9.77	0	-5.91

For calcium defects, the formation energies depend on the chemical potential of Ca. The Ca-rich conditions give the lowest formation energies, i.e., the richer Ca the easier the formation of Ca defects. To properly investigate the plausible phase precipitate limits for Ca, common natural phases of Ca, i.e., CaO, were considered and used to define the phase precipitate limits for Ca. The chemical potential of Ca, μ_{Ca} can be written as:

$$\mu_{\mathrm{Ca}} = E_{tot}(\mathrm{CaO}) - \mu_{\mathrm{O}} \tag{7.7}$$

7.4 Formation of Ca in BT and BNT

In Figure 7.4, the formation energies of Ca substituting for Ba (denoted $\mathrm{Ca_{Ba}}$) and Ca substituting for Ti (denoted $\mathrm{Ca_{Ti}}$) defects in BT are plotted as functions of the Fermi energy, E_F. Only the lowest energy charge state of each defect at a given Fermi energy is shown in the plot. The charge state of each defect at each point can be identified from the slope of the plot. $\mathrm{Ca_{Ba}}$ is always neutral for the entire possible Fermi energy range. This is consistent with the fact that Ca and Ba are isovalent. $\mathrm{Ca_{Ti}}$

is a deep double acceptor with the calculated ionization energy of ~200 meV. This is also consistent with the fact that group-II Ca is substituted for Ti, which is 4+ in BT.

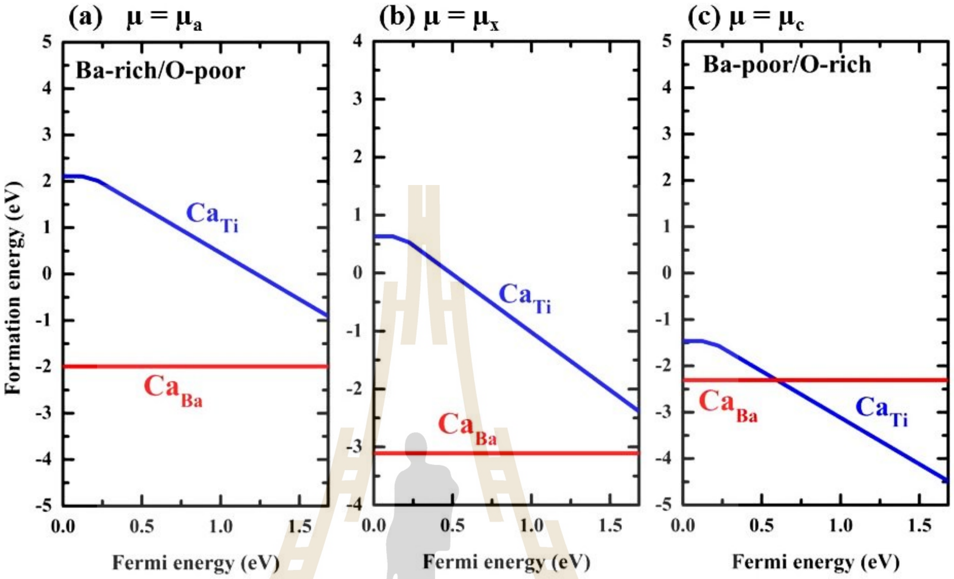

Figure 7.4 The formation energies for Ca defects, i.e., Ca substituting for Ba (denoted Ca_{Ba}) and Ca substituting for Ti (denoted Ca_{Ti}), in $BaTiO_3$ as functions of the Fermi level calculated under different growth conditions. Only the formation energies for the lowest energy charge states are shown. The charge state of each defect at each point can be identified from the slope of the plot.

The plots in Figure 7.4 are for the three choices of growth conditions previously explained and shown in the chemical potential space in Figure 7.1. First, we can clearly see that the formation energy of Ca_{Ba} is always significantly lower than that of Ca_{Ti}. Note that the formation energies of calcium interstitials and calcium anti-site (not shown) are even higher than that of Ca_{Ti}, making them unlikely to form. Under Ba-rich/O-poor growth condition (**μ_a**), the formation energy of Ca_{Ba} is in the negative region, indicating that Ca_{Ba} can rapidly form spontaneously. In reality, under condition $\boldsymbol{\mu_a}$, the chemical potential of Ca has to be lowered below the (precipitation limit) value used here in order to maintain a stable growth of BT and keep the level of Ca incorporation controllable. (Lowering the chemical potential of Ca directly increases the formation energy of Ca related defects.) For Ba-poor/O-rich growth condition $\boldsymbol{\mu_c}$, the formation energy of Ca_{Ba} is slightly lower than that in the condition $\boldsymbol{\mu_a}$. However, the formation energy of Ca_{Ti} is much reduced and turned negative. Ca_{Ti} is a deep double acceptor and the 2- charge state becomes lower in energy than Ca_{Ba} for $E_F > 0.54$ eV (Figure 7.4, right panel). Even under this condition, the neutral charge state of Ca_{Ti} is still almost 1 eV higher in energy than Ca_{Ba}. For the intermediate growth condition, at point "x" the formation energy of Ca_{Ba} is significantly lower than that of Ca_{Ti}. Our results indicate that, for all possible growth conditions (shaded area in the chemical potential space in Figure 7.1), Ca prefer to substitute for Ba (or A-site of the perovskite lattice) in BT.

For Ca in BNT, there are three types of cations. For the A-site of a perovskite lattice, there are two cations, Bi and Na. For B-site, there is only one type of cation (Ti). Therefore, we studied three substitutional defects, i.e., Ca substituting for Ba (denoted Ca_{Ba}), Ca substituting for Na (denoted Ca_{Na}) and Ca substituting for Ti (denoted Ca_{Ti}). In Figure 7.5, the formation energies of the three substitutional defects as functions of the Fermi energy are plotted. The plots are for the different choices of growth conditions previously discussed and shown in the chemical potential space in Figure 7.2 and Figure 7.3. We found that Ca_{Ti} is a deep double acceptor with the calculated ionization energy 0/-1 of about 150 meV and -1/-2 of about 400 meV.

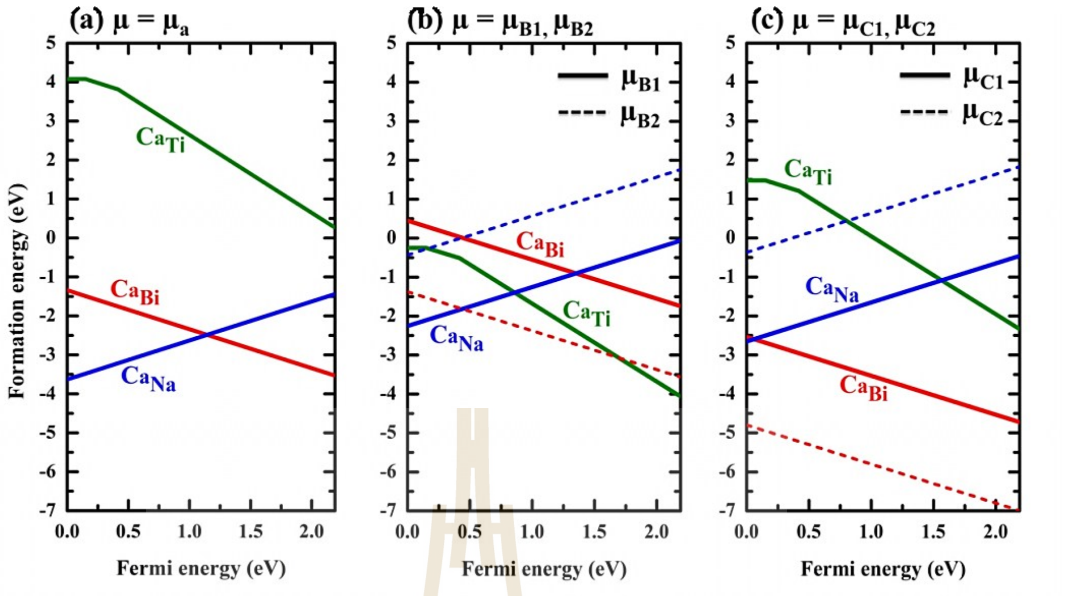

Figure 7.5 The formation energies of Ca defects, i.e., Ca substituting for Ba (denoted Ca_{Ba}), Ca substituting for Na (denoted Ca_{Na}), and Ca substituting for Ti (denoted Ca_{Ti}) in $Bi_{0.5}Na_{0.5}TiO_3$ as functions of Fermi level calculated under $\mathbf{\mu_A}$, $\mathbf{\mu_{B1}}$, $\mathbf{\mu_{B2}}$ (dash lines), $\mathbf{\mu_{C1}}$ and $\mathbf{\mu_{C2}}$ (dash lines) conditions. Only the formation energies for the lowest energy charge states are shown. The charge state of each defect at each point can be identified from the slope of the plot.

Ca_{Bi} is a shallow single acceptor while Ca_{Na} is a shallow single donor. These are consistent with what can be expected due to the electron counting. Calcium has two valence electrons therefore when it substitutes for Ti^{4+}, Bi^{3+}, and Na^{1+} , it is expected to behave as a double acceptor, single acceptor and single donor, respectively. For the O-poor condition ($\mathbf{\mu_A}$), the formation energies are shown in the left panel of Figure 7.5. Under this condition, the formation energy of Ca_{Ti} is much higher than for Ca on A-site (Ca_{Bi} and Ca_{Na}). If the charge neutrality condition is required, the Fermi level is pinned at the crossing point between the Ca_{Bi} and Ca_{Na} line. At this crossing point, the formation energy of Ca_{Bi} and Ca_{Na} are equal and the two have the same concentration and fully charge compensate each other. Note, however, that the values of the formation energy shown are negative. In reality, the chemical potential of Ca has to be lowered to the point where the crossing point is in the positive region; leading to a low concentration of Ca and steady growth of BNT. For the O-rich conditions, one can vary the chemical potentials of Ti to its richest possible value and at the same time the average value of the chemical potentials of Bi and Na, i.e., $(\mu_{Bi}+\mu_{Na})/2$, moves to its poor value. This is the condition $\boldsymbol{\mu_B}$. For this condition, the formation energies of Ca substitutional defects are shown in the middle panel of Figure 7.5. For a given average value of the chemical potentials of Bi and Na, the chemical potentials of Bi and Na can vary from Bi-rich Na-poor (B1) to Bi-poor Na-rich (B2). To present the formation energy in the same plot, the formation energies of substitutional Ca corresponding to B1 are shown using solid lines and B2 using dashed lines. We can see that for B1 condition, Ca_{Na} is the most stable donor and it would compensate by Ca_{Ti} acceptor to maintain charge neutrality, the condition needed at a high Ca concentration. However for B2 condition, Ca_{Bi} becomes the lowest formation energy acceptor; making Ca_{Ti} never stable. In an extreme n-type condition (when the Fermi level is near the conduction band minimum) the crossing of Ca_{Ti} below Ca_{Bi} is irrelevant because there is no compensating donor to pin down the Fermi energy in this region. Even if the Fermi level started in this region, as soon as the first few Ca_{Ti} acceptors started to form, the Fermi energy would immediately move lower toward the valence band – the region where Ca_{Bi} becomes more stable. Next, the O-rich conditions with the chemical potentials of Ti at its poorest possible value and at the same time the average value of the chemical potentials of Bi and Na, i.e., $(\mu_{Bi}+\mu_{Na})/2$, moves to its highest possible value labelled by condition $\mathbf{\mu_C}$ will be discussed. For this condition, the formation energies of Ca substitutional defects are shown in the right panel of Figure 7.5. While maintaining the average value, i.e. $(\mu_{Bi}+\mu_{Na})/2$, the chemical potential of Bi and Na can vary from Bi-rich Na-poor (C1) to Bi-poor Na-rich (C2). For the C1 condition, the relevant compensating donor and acceptor are Ca_{Na} and Ca_{Bi} which cross near the valence band maximum Fermi energy. For the C2 condition, Ca_{Bi} is the only stable acceptor without a compensating donor. Similar to the case of B2, the Ca_{Bi} acceptor would be the only species that forms and the Fermi energy would move to the valence band maximum value (in the plot, the formation energy of Ca_{Na} is much higher and never crosses Ca_{Bi} at any point under B2 and C2 conditions). Our results indicate that, in BNT, Ca prefers to occupy the A-site, i.e., substituting for Bi or Na for almost all growth conditions with the exception of condition B1 where Ca should substitute for both A-site and B-site with the concentration of Ca on B-site roughly half of Ca on A-site (Ca_{Ti} is a double acceptor while Ca_{Na} is a single donor).

The fact that Ca favors the A-site over B-site in perovskite BT and BNT is also consistent with the ionic radii. The ionic radii of 12-fold Ba^{2+}, Na^{1+}, and 6-fold Ti^{4+} are 1.61, 1.39, and 0.605 Å, respectively. For Ca^{2+}, the 12-fold and 6-fold ionic radii are 1.34 and 1.0 Å, respectively (Shannon, 1976). We can see that the ionic radius of Ca^{2+} is a better fit with A-site ions (Ba^{2+} and Na^{1+}) than with the B-site ion (Ti^{4+}). The calculated relaxed bond distances of pure BT, BNT and Ca substitutional defects are summarized in Table 7.4. The local structure of Ca_{Ti} for both BT and BNT are similar. The same is also true for the Ca substitutional for the A-site (Ba in BT and Bi/Na in BNT). It is worth mentioning that, in the case of Ca_{Ba} in BT, Ca shifts off-center along the c-axis by about 0.05 Å. This is consistent with the experimental observation that the T_c of the phase transformation of BT (from the low temperature tetragonal phase to the cubic phase) shifts from the bulk value of T_c = 403 K to a higher value when the sample is doped with Ca (Yamada *et al.*, 1969). Regarding the TCC of Ca-doped BNT-BT system, Ca substitutional on the A-site would have the local structure similar to that of $CaTiO_3$, which is known to be a very temperature stable (good TCC) material. Therefore, the improved TCC of BNT-BT system when doped by Ca observed by Yuan *et al.* (Yuan *et al.*, 2010) is consistent with our calculations that Ca prefers to substitute on the A-site.

Table 7.4 Calculated local structure around cations for pure and Ca doped $BaTiO_3$ and $Bi_{0.5}Na_{0.5}TiO_3$.

Structure	**Charge**	**Bond**	**Calculated distance (Å)**	**Coordination numbers**
$BaTiO_3$	0	Ba-O	2.814	4
			2.850	4
			2.850	4
		Ti-O	1.990	4
			2.041	2
Ca_{Ba} in $BaTiO_3$	0	Ca-O	2.859	4
			2.902	4
			2.902	4
Ca_{Ti} in $BaTiO_3$	2-	Ca-O	2.049	4
			2.189	2

Table 7.4 Calculated local structure around cations for pure and Ca doped $BaTiO_3$ and $Bi_{0.5}Na_{0.5}TiO_3$ (Continued).

$Bi_{0.5}Na_{0.5}TiO_3$	0	Na-O	2.834	4
			2.505	4
			3.388	4
		Bi-O	2.838	4
			2.292	4
			3.263	4
		Ti-O	1.998	4
			2.258, 1.794	2
Ca_{Na} in $Bi_{0.5}Na_{0.5}TiO_3$	1+	Ca-O	2.833	4
			2.505	4
			3.382	4
Ca_{Bi} in $Bi_{0.5}Na_{0.5}TiO_3$	1-	Ca-O	2.831	4
			2.312	4
			3.257	4
Ca_{Ti} in $Bi_{0.5}Na_{0.5}TiO_3$	2-	Ca-O	2.054	4
			2.233, 2.021	2

7.5 Local Structure of Ca Dopant in $BaTiO_3$-$(Bi_{0.5}Na_{0.5})TiO_3$ System

From section 7.4, we found that Ca atoms prefer to substitute for cations. Substitutional Ca in the A-site of the perovskite lattice, i.e., Ca_{Ba} for $BaTiO_3$ and Ca_{Bi} and Ca_{Na} for $Bi_{0.5}Na_{0.5}TiO_3$, is the most favorable form of Ca incorporation in this class of materials and will predominantly form in all growth conditions. Only for the case of O-rich/Na-poor in $Bi_{0.5}Na_{0.5}TiO_3$, does Ca_{Ti} have a chance to form in a reasonable amount, i.e., about half of the concentration of Ca_{Na}. However, in practice, BT and BNT are composite compounds in form of (1-x)BNT-xBT such as Yuan *et al.*

(Yuan, 2012) reported. Therefore, the role of Ca doping in BT-BNT system is still unclear, if we doped Ca in BT-BNT samples, because Ca donor-type impurity can occupy on *A*-site (Ba and Na atoms) and B-site (Ti) in some case for BNT by our formation energy suggestion. Consequently, in order to gain more fundamental understanding, in this section, we will show identification the site of Ca in Ca-doped $BaTiO_3$-$(Bi_{0.5}Na_{0.5})TiO_3$ (BT-BNT) ceramics samples by using a combination of first-principles calculations and x-ray absorption technique.

In our study, The BT-BNT samples are used in this study were prepared by our collaboration and doped via a conventional method of mixing oxides by sintering in different temperature which is corresponded with our O-poor condition. The ratio of BT/BNT in all samples are 90/10 with different CaO concentrations varying from 0.2, 0.3 0.35, and 0.4 mol%. The local environment around Ca atom in each sample was characterized by using x-ray absorption measurements performed in the fluorescent mode with a 13-component Ge detector (Canbera) at beam line 8 of the Siam Photon Source (electron energy of 1.2 GeV, beam current 80–120 mA), Synchrotron Light Research Institute, Thailand. A double crystal monochromator $KTiOPO_4$ was used to scan the synchrotron x ray with the photon energy step of 0.25 eV in the range of 4000–4120 eV, covering the XANES region of Ca *K*-edge. The measured spectra are illustrated in Figure 7.6.

In order to identify the location of Ca atom in BT-BNT samples, the measured Ca *K*-edge XANES spectra were performed as illustrated in Figure 7.6(a). By both performing XANES experiment and independently calculating first-principles XANES with Ca at different locations were compared. The experimental Ca *K*-edge XANES spectrum is shown in Figure 7.6(a), no different in the spectral features are measured except for a difference in the signal to noise ratio due to the different concentrations of Ca atoms in $0.9BaTiO_3$-$0.1(Bi_{1/2}Na_{1/2})TiO_3$ system . The XANES spectra have the pre-edge peaks at 4041 eV (P1) and 4044 eV (the second pre-edge peak merged into the edge and appear only as and onset in the slope of the edges; labelled as P2). The main feature in spectra is composed of the main peak at 4049 eV (P4) with two lower energy shoulder at 4047 eV (P3) and 4051 eV (P5), and followed by other peak at 4063 eV (P6), 4069 eV (P7), and 4080 eV (P8) which are smaller.

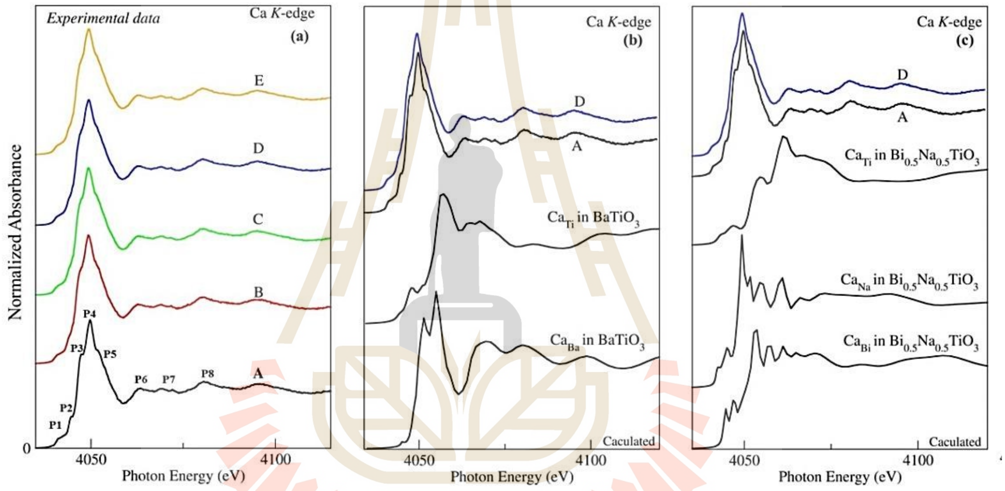

Figure 7.6 (a) The measured Ca *K*-edge spectra of (1) $0.9BaTiO_3$-$0.1(Bi_{1/2}Na_{1/2})TiO_3$-$0.035CaO$ ceramics sintered at 1160 °C, (2) $0.9BaTiO_3$-$0.1(Bi_{1/2}Na_{1/2})TiO_3$-$0.020CaO$ ceramics sintered at 1220 °C: pulverized powder, (3)$0.9BaTiO_3$-$0.1(Bi_{1/2}Na_{1/2})TiO_3$-$0.030CaO$ ceramics sintered at 1220 °C: pulverized powder (4) $0.9BaTiO_3$-$0.1(Bi_{1/2}Na_{1/2})TiO_3$-$0.035CaO$ ceramics sintered at 1220 °C: pulverized powder, and (5) $0.9BaTiO_3$-$0.1(Bi_{1/2}Na_{1/2})TiO_3$-$0.040CaO$ ceramics sintered at 1220 °C: pulverized powder. (b) and (c) show the simulated spectra from different local structure of Ca in BT and BNT, respectively, compared with the measured spectra (A and D samples).

The calculated formation energy for BT and BNT perovskite structure, suggest that there are two potential Ca sites for O-poor conditon, i.e., Ca substituting on the Ba and Na site (Ca_{Ba} and Ca_{Na} , also known as *A*-site). The calculated XANES spectra for Ca_{Ba} and Ca_{Ti} in BT compare with measured spectra are shown in Figure 7.6(b), and the calculated XANES spectra for Ca_{Na}, Ca_{Bi} and Ca_{Ti} in BNT are shown in Figure 7.6(c), respectively. The result shown that the measured XANES is clearly consistent with the calculation of Ca on *A*-site perovskite (Ba, Bi and Na site), especially Ba site and in consistent with Ca at *B*-site or Ti location. The measured of the A and D samples compare with other experimental: 5 at.% Ca doped $BaTiO_3$ (Ca substituting on Ba) sample, $CaTiO_3$ reference sample (Okajima, 2010), and calculated XANES spectra of Ca_{Ba} in $BaTiO_3$ and $CaTiO_3$ are shown in Figure 7.7. It is clear from inspection of the Figure 7.7 that the measured XANES matches very well the Ca doped $BaTiO_3$ (Ca substituting on Ba) reference sample and slightly different from Ca in $CaTiO_3$, on the other hand, the case of Ca_{Bi} and Ca_{Na} can be clearly ruled out . This result indicates that Ca in the $0.9BaTiO_3$-$0.1(Bi_{1/2}Na_{1/2})TiO_3$ sample are substituted at Ba sites in $BaTiO_3$. However, only six peaks that corresponding with measured XANES are observed in the calculated spectra of Ca_{Ba} in $BaTiO_3$, as shown in Figure 7.7, P2 and P6 peaks in XANES spectra of Ca in the $0.9BaTiO_3$-$0.1(Bi_{1/2}Na_{1/2})TiO_3$ are not observed in this calculated spectrum, The two peaks might be indication that a small fraction of $CaTiO_3$ phase, which has it main peaks (M2 and M5) in this region. A small amount of $CaTiO_3$ will lead to an increase in the absorption this region, which would tend to peak at P2 and P6 as observed in the measured XANES (as show in Figure 7.7). Based on our calculation, not only are the spectra qualitatively similar but energy differences between prominent features are in quantitative agreement: the separation between in each peaks in the measured XANES are E(P3)-E(P1)=6 eV, whereas the calculated XANES gives 6 eV. Reasonable agreement also observed for the separation of measured XANES, i.e., E(P4)-E(P3)=2 eV, E(P5)-E(P4)=3eV, E(P7)-E(P5)= 8 eV, and E(P8)-E(P7)= 10 eV and calculated are 3 eV, 4 eV, 9 eV, and 11 eV, respectively.

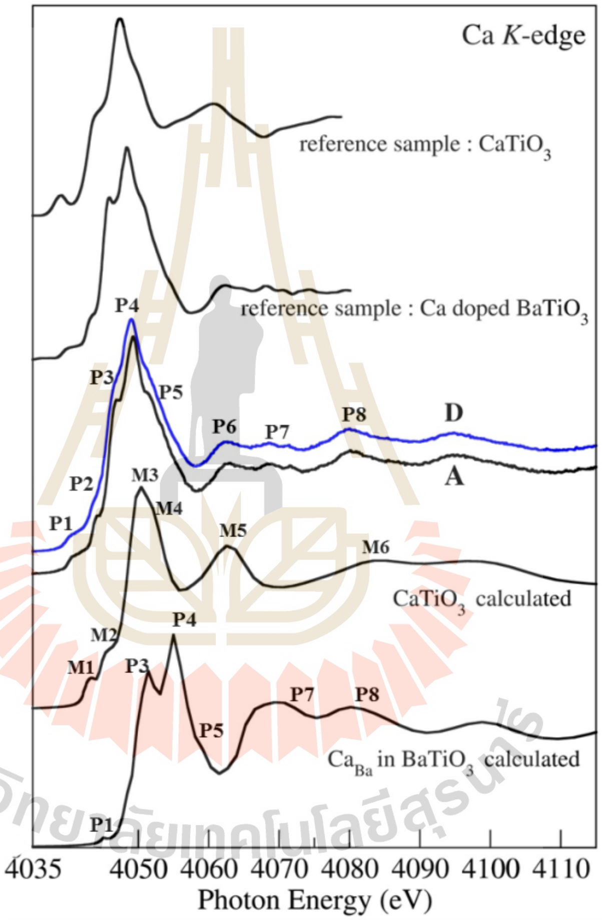

Figure 7.7 Comparison of experimental (sample A and D, reference sample CaTiO$_3$ and Ca$_{Ba}$ in BaTiO$_3$ (T.Okajima, 2010)) and calculated XANES spectra of Ca$_{Ba}$ in BaTiO$_3$ and CaTiO$_3$ (calculated spectra peaks that corresponding with measured spectra are labelled P1-P8 and M1-M6, respectively).

7.6 Conclusion

Calcium defects in $BaTiO_3$ and $Bi_{0.5}Na_{0.5}TiO_3$ were studied by first principles calculations. Different growth conditions were investigated by introducing phase diagrams to show the possible range of chemical potentials of starting elements. It is found that Ca atoms prefer to substitute for cations. Calcium in the interstitial forms and anti-site (substitute for oxygen) have high formation energies and are unlikely to form. Substitutional Ca in the A-site of the perovskite lattice, i.e., Ca_{Ba} for $BaTiO_3$ and Ca_{Bi} and Ca_{Na} for $Bi_{0.5}Na_{0.5}TiO_3$, is the most favorable form of Ca incorporation in this class of materials and will predominantly form in all growth conditions. Only for the case of O-rich/Na-poor (condition B1) in $Bi_{0.5}Na_{0.5}TiO_3$, does Ca_{Ti} have a chance to form in a reasonable amount, i.e., about half of the concentration of Ca_{Na}. In most cases, Ca does not lead to electrical doping in $BaTiO_3$ and $Bi_{0.5}Na_{0.5}TiO_3$. Ca is incorporated either as an electrical neutral defect (for the case of Ca_{Ba} in $BaTiO_3$) or self-compensating donor-acceptor pairs (for the cases of Ca_{Bi}/Ca_{Na} and Ca_{Ti}/Ca_{Na} pairs in $Bi_{0.5}Na_{0.5}TiO_3$). Only for the case of O-rich/Bi-poor in $Bi_{0.5}Na_{0.5}TiO_3$ (condition C2), do Ca_{Bi} acceptors have a chance to predominantly form without self-compensation by Ca donors. We have identified the lattice location of Ca in BT-BNT system by XANES experiment. Our observed Ca *K*-edge XANES spectrum clearly matches our independent first-principles XANES simulation of a Ca atom substituting for Ba, indicating that almost all of Ca atom are occupying the Ba site. A few differences between the measure and calculated XANESs are compatible with the presence of a small amount of $CaTiO_3$ phase. This work illustrates that combination of XANES measurements and first-principles calculations is very powerful way to unambiguously identify structures of an impurity in composite compound such as BT-BNT crystal, which is a topic of immense interest over a broad range of materials science.

CHAPTER VIII

EFFECTS OF STRUCTURAL RELAXATION, INTERDIFFUSION, AND SURFACE TERMINATION ON TWO DIMENSIONAL ELECTRON GAS FORMATION AT THE $LaAlO_3/SrTiO_3$ (001) INTERFACE

8.1 Introduction

The two-dimensional electron gas (2DEG) formation at the $LaAlO_3/SrTiO_3$ (or LAO/STO) interfaces has received a great deal of attention since its discovery by Ohtomo and Hwang (Ohtomo and Hwang, 2004). Several mechanisms have been proposed for this phenomenon: (1) electronic reconstruction to avoid the polar discontinuity, (2) oxygen vacancies in the STO or LAO layers, (3) interdiffusion of Ti or Sr into the LAO layer and vice versa, or combinations of the above mechanisms. It is now well established that the role of oxygen vacancies in the STO depends strongly on the growth conditions, in particular the oxygen partial pressure during pulsed laser deposition. However it can be controlled by annealing and is assumed to make a negligible contribution for sheet carrier densities of order 10^{13} e/cm^2. There has also been ample evidence for some degree of interdiffusion, most recently through a medium-energy ion scattering (MEIS) study by Zaid *et al.* (Zaid *et al.*, 2016). The gradual change in *c*/*a* ratio observed in these measurements could be well explained by models including a gradually changing interdiffusion model (we will discuss in section 8.6 and 8.7).

The original polar discontinuity model (Ohtomo and Hwang, 2004) is based on the idea that in STO each layer SrO or TiO_2 is neutral but in LAO the nominal charge per unit cell alternates between −1 for the LaO and +1 for the AlO_2 layers. This discontinuity would set up a field with an ever increasing potential in the LAO layer, until the potential difference exceeds the band gap and charge is transferred from the surface to the interface. Within this model, a net charge of 1/2 electron per unit cell corresponding to about 3×10^{14} e/cm^2 is required at the interface to cancel the field. On the other hand, experimentally one usually finds a significantly lower charge density. This model also predicts a corresponding hole gas at the surface, which has not been observed. Evidence for a sloped potential in the LAO region has not been established conclusively experimentally either. While in principle explaining the presence of a critical layer thickness for observing a 2DEG, the quantitative determination of the critical layer thickness is complicated by the possibility of relaxation of each layer (Pentcheva and Pickett, 2008; Pentcheva and Pickett, 2009) the fact that the gap is underestimated by the usual semi-local density functional calculations, and so on. Janotti and Van de Walle (Janotti *et al.*, 2012) took a somewhat different viewpoint assuming that the discontinuity is immediately met at the interface by the interface bond configuration but proposed that the interface charge may subsequently be partially transferred to the surface depending on the configuration considered and the surface passivation. They used this model to address the question of why less than 1/2 electron per unit cell area is often found at the interface. Other possible explanations are that part of the charge at the interface is not detected in transport because it resides in less mobile interface states (Popović *et al.*, 2008). A related question is why a 2D hole gas is not observed at the surface. Several possibilities have been offered for this asymmetry between the n- and p-type interface (Janotti *et al.*, 2012; Chen *et al.*, 2010; Zhong *et al.*, 2010). Another possibility is that the holes form self-trapped polarons in these oxides (Pentcheva and Pickett, 2006).

It is by now more or less accepted that the above mentioned mechanisms are not mutually exclusive but may each contribute to the 2DEG formation to a varying degree depending on growth conditions and so on. The role of defects has been addressed recently by Yu and Zunger (Yu and Zunger, 2014). They explained the occurrence of a critical layer thickness in terms of the energy of formation of oxygen vacancies on the LAO surface which becomes negative when the layer exceeds a critical thickness. However, this dependence of the energy of formation of the V_O on the position of the V_O relative to the interface results itself from the sloped potential, as was pointed out in several earlier papers (Zhong *et al.*, 2010; Li *et al.*, 2011; Zhang *et al.*, 2010). However Yu and Zunger proposed that the discontinuity for thicknesses below the critical thickness is already removed by the antisite defects of Ti on Al sites at the surface transferring its electron to an Al on Ti sites across the interface on the STO side. So, it is then not clear why V_O would still form at the surface if interdiffusion is already removing the sloped potential.

On the other hand, in the classic polar catastrophe explanation, the slope in the LAO region is not removed since the Fermi level becomes pinned slightly below the valence band maximum (VBM) of the AlO_2 surface layer of LAO and slightly above the conduction band minimum (CBM) at the STO (TiO_2) interface layer. Lee and Demkov (Lee and Demkov, 2008) claimed that the polar catastrophe model could quantitatively explain the charge density at the interface. Using the LDA+*U* method, they found that it resides in interface states of the Ti below the STO CBM.

The surface termination is also known to play an important role. This is most clear from the experiments by Cen *et al*. (Cen *et al.*, 2008; Cen *et al.*, 2009; Cheng *et al.*, 2011; Cheng *et al.*, 2013; Bi *et al.*, 2010) in which it was shown that regions of 2DEG at the buried interface can be induced by modifying the surface adsorbates with an appropriately biased atomic force microscopy (AFM) tip.

The literature on the LAO/STO at this point in time has become too extensive to review comprehensively, so the above is only a sampling of the key ideas relative to the origin of the 2DEG. In this paper, we first revisit the original polar catastrophe idea by modeling LAO overlayers on STO of various thickness and studying both the ionic relaxations, the partial densities of states, and the planar-averaged electrostatic potential profile. We determine quantitatively the interface sheet carrier density in the conduction band of the STO and interface region. These results are presented in section 8.3 and 8.4. Subsequently, we study the effects of surface termination with H, OH, and both together in section 8.5. Next, we consider interdiffusion of Ti-Al and Sr-La in section 8.6 and 8.7. Interdiffusion of the Ti and Al sides in the near-interface layers was recently observed by MEIS (Zaid *et al.*, 2016). These various models clarify the behavior of the interface charge density and the way in which the polar catastrophe, or more precisely the slope in electrostatic potential, is mitigated and are a step along the way to build a quantitative model for determining the relative contributions of each type of mechanism. The main conclusions of our study, highlighting our findings, are summarized in section 8.8. Before we present our results, a brief description of our computational models and methods is given in section 8.2.

8.2 Computational Method

In this chapter, The calculations are carried out within the framework of density functional theory and using a plane wave basis set with projector augmented wave potentials (PAW) (Blöchl, 1994; Kresse and Joubert, 1999) using the VASP code (Kresse and Furthmüller, 1996; Kresse and Hafner, 1994) The PBE-GGA approximation is used for the exchange correlation potential (Perdew *et al.*, 1996). The electron wave functions were described using a plane wave basis set with the energy cutoff of 500 eV. This energy cutoff is sufficient to provide a well-converged basis set to describe oxides when using ultrasoft pseudopotentials (Vanderbilt, 1990)

To study the LAO/STO(001) interface, the supercells were set up in a symmetric way with 5.5 (001) oriented STO layers (meaning 6 TiO_2 layers and 5 SrO layers) and either 3, 4, or 5 unit cell LAO layers on either side, followed by 20 Å of vacuum. This allows us to include the surface effects with different terminations. We focus exclusively on the TiO_2/LaO interface, which is the n-type interface in which the 2DEG is experimentally observed. Several previous studies have also considered the SrO/AlO_2 p-type interface, for example Ref. (Zhang *et al.*, 2010) and references therein. The symmetric geometry with two identical interfaces is chosen so as to avoid spurious fields from the periodic boundary conditions. The thickness of the vacuum region is sufficient to avoid spurious slab-slab interactions. For the first part of the study we pick a 1×1 2D surface cell. For the surface adsorption studies or the interdiffusion models we choose a 2×2 2D cell. In that case, the surface AlO_2 layer has 8 O atoms and 4 Al atoms. Thus, we can go down to a H surface concentration of 1/8 and OH concentration on Al of 1/4. Additional calculations with full surface coverage were done on the 1×1 surface cell. Similarly for the interdiffusion we also used a 2×2 2D cell, so that we can model for example a 25% Ti, 75% Al layer. In addition, we can choose to simply add Ti instead of Al or swap Al and Ti from the STO to the LAO side of the cell and we can choose which layer to place the swapped atoms in: closer to the interface or further away. Similar considerations apply to Sr-La interdiffusion. The actual models studied will be presented along with the results. For structure relaxation, the in-plane lattice constant of the slab was constrained at the calculated value of STO bulk (a = 3.8695 Å). All coordinates of atomic positions were fully relaxed until the residual Hellmann-Feynman forces (Feynman, 1939) become less than 0.02 eV/Å. For k-space integrations, we used the Monkhorst-Pack scheme(Monkhorst and Pack, 1976) with 7×7×1 k-point sampling.

8.3 Structural Relaxation in Models without Interdiffusion.

We start by examining the ionic relaxation as function of LAO overlayer thickness. These results are shown in Figure 8.1. We present the results as a buckling of the mixed cation anion layers, in other words, the relative z coordinate [normal to the (001) planes] of the cation minus that of the anion in each layer. One may see that, in agreement with early results of Pentcheva and Pickett (Pentcheva and Pickett, 2008; Pentcheva and Pickett, 2009), the surface AlO_2 layer remains unbuckled. However, as we approach the interface, the AlO_2 layer buckling increases. On the other hand, the buckling of the LaO layers is stronger and is reversed: it increases toward the surface although not entirely linearly with distance from the interface. We note that the displacement of positive cations toward the surface relative to the negative anions means that dipoles in each layer are formed which counteract the slope of the potential. Thus the potential slope, resulting from the valence discontinuity, is in part avoided by relaxing the layers.

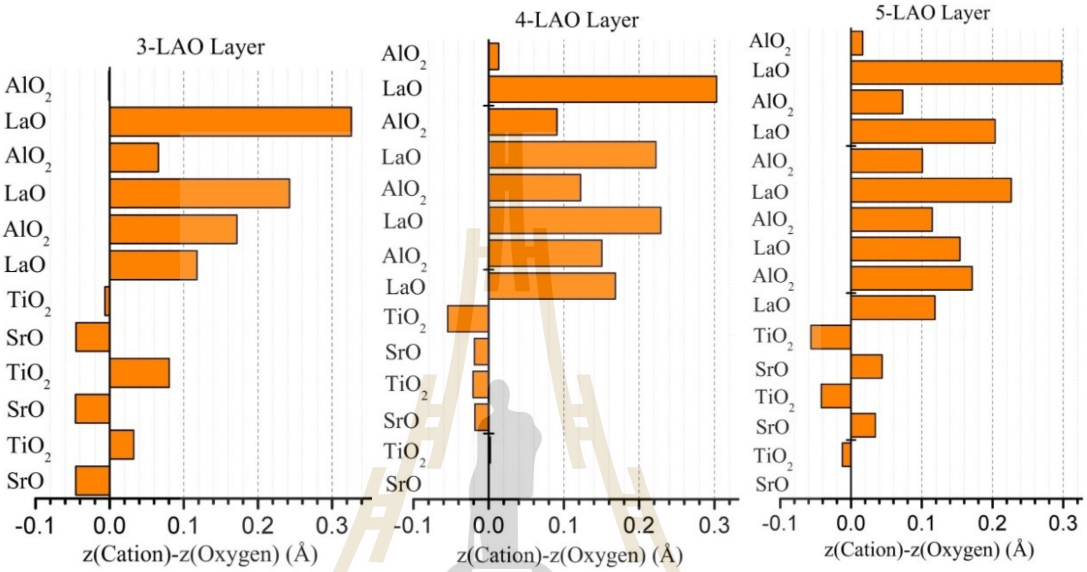

Figure 8.1 Buckling of layers in LAO/STO models. The bar graphs show $\Delta z = z_{\mathrm{oxygen}} - z_{\mathrm{cation}}$ with z the distance normal to the interface and positive toward the surface.

8.4 Electronic Structure in Models without Interdiffusion

Next, we consider the layer-projected densities of states in Figure 8.2. We can see that for the 3-LAO layer case, the layer-projected densities of states (PDOS) in the LAO are shifted from layer to layer displaying the expected electric field from the polar discontinuity. This sloped potential leads to a strong decay of the states near the top of the valence band in the LAO away from the surface. This occurs over about a 1 eV range below the surface VBM. It shows that the LAO VBM becomes almost like a surface state and reflects simply the band bending.

The VBM of the surface LAO in the 3-LAO layer, however, stays below the CBM of the STO and hence no charge transfer occurs between the two. For the 4-layer and 5-layer cases there is a charge transfer. One can also see that the charge density in the STO is spread over all TiO_2 layers in our model. So, it is spread out over several layers near the interface. In Figure 8.2, we show the results only for the 3-LAO and 5-LAO layer cases. Those for the 4-LAO layer case look similar to the 5-LAO layer case but with the Fermi level slightly closer to the STO CBM in the interface layer. We see no evidence for a localized interface state splitting off below the CBM in these figures.

We also examine more closely whether an interface state occurs at the interface by performing spin-polarized calculations. In this case, we find for the 5-LAO layer case a separate small peak in the PDOS for majority spin. This is shown in Figure 8.3. It agrees qualitatively with the conclusions of Lee and Demkov (Lee and Demkov, 2008). These authors used LSDA+U in which the Hubbard U further shifts the occupied interface state down into the gap. We see that this already occurs without Hubbard U. In other words by placing a small amount of charge in the bottom of the conduction band it becomes favorable to induce a magnetic moment by splitting the up and down spin bands. The total magnetic moment of the cell was found to be $0.12\mu_B$ for the 5-LAO layer and $0.08\mu_B$ for the 4-LAO layer case. This corresponds to two interfaces, so per interface the values should be halved. This occurrence of a weak magnetization is somewhat surprising because the density of states near the conduction band minimum is not very high, so one would not expect the Stoner criterion to be fulfilled. In fact, for the 4-LAO layer case, the up and down spin

PDOSs stay essentially the same but for the 5-LAO layer case, a sharper interface state of only majority spin splits off.

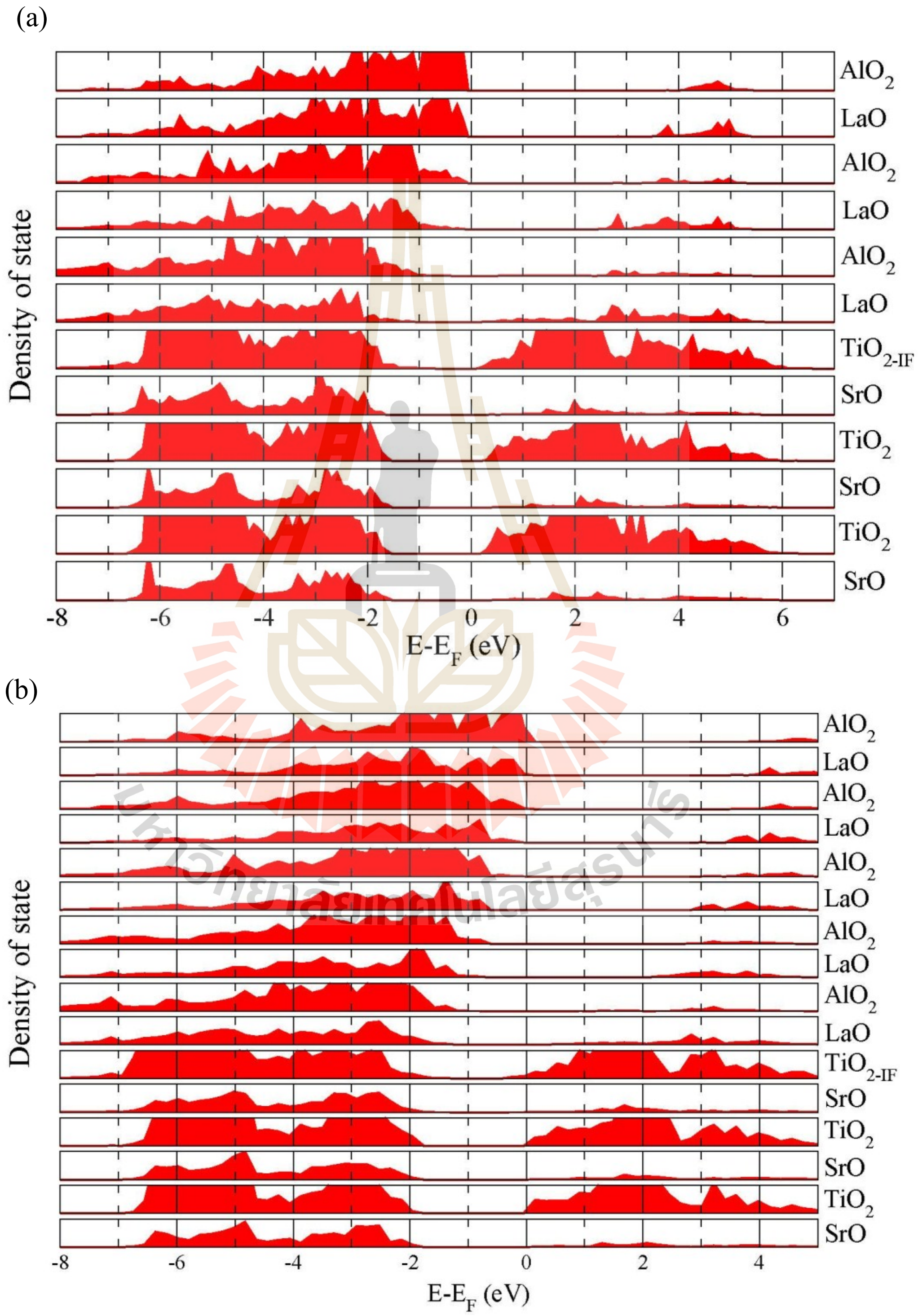

Figure 8.2 Layer-projected density of states of (a) 3-LAO layer and (b) 5-LAO layer.

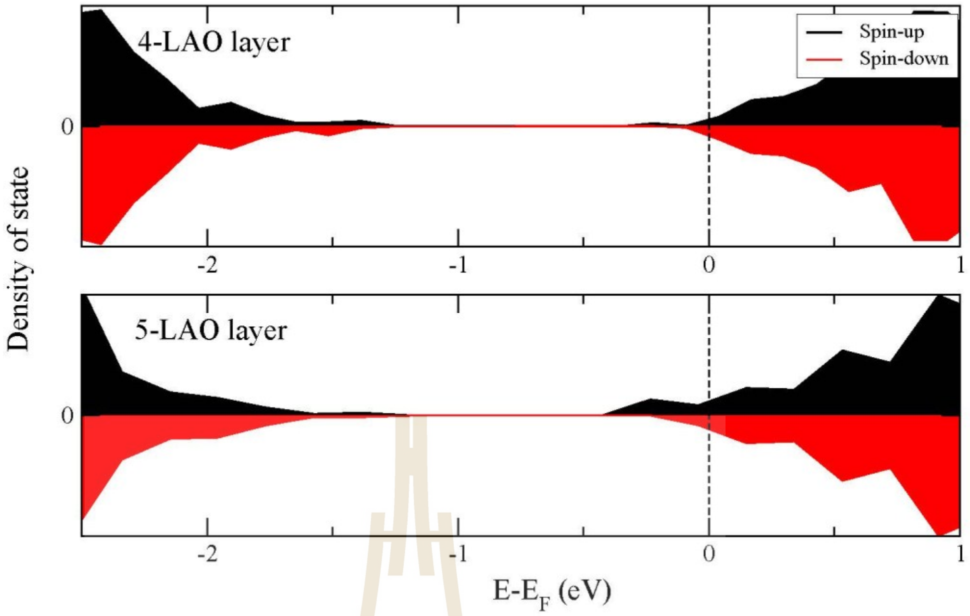

Figure 8.3 Layer-projected density of states, focus on interface layer of 4- and 5-LAO layers, including spin polarization.

Next, we determine the interface sheet electron density of free carriers in the STO conduction band. The conduction band 2D charge densities at the interface were determined by first extracting the charge density accumulated only over states from some level in the gap up to the Fermi energy, then planar-averaging it over the *xy* planes parallel to the interface and then integrating only over the layers near the interface and in the STO region. This is illustrated in Figure 8.4 and Figure 8.5

In Figure 8.4, we show a 3D plot of the structure with the electron density integrated between a lower energy limit E_a chosen in the gap and the Fermi energy E_F. As can be seen this charge density has a large contribution near the free surface. This is because E_a cuts through the LAO valence band PDOS near the surface. Here, we would actually be rather interested in the hole density, i.e., the integral from the Fermi level to an upper level above the local VBM.

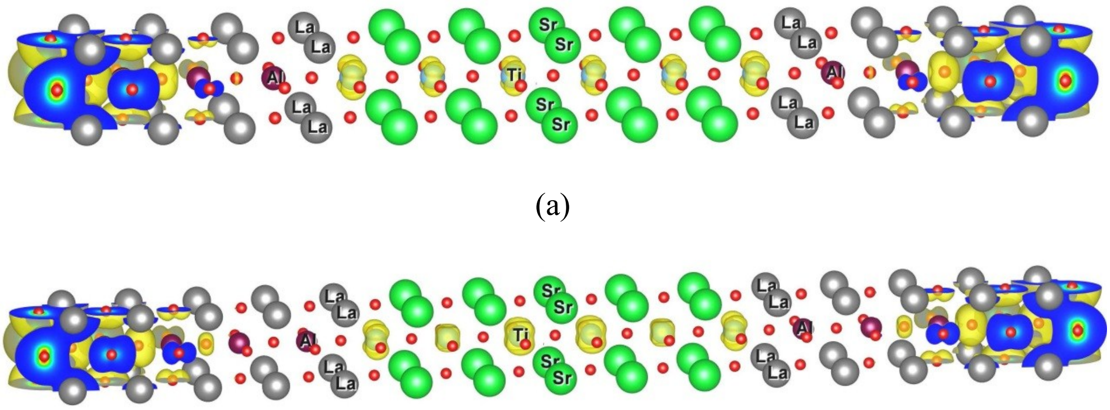

(a)

(b)

Figure 8.4 Structure and charge density in energy range between STO middle of the gap and Fermi energy (3D plot) for (a) 4-LAO layer and (b) 5-LAO layer. The yellow surface is an isosurface of the charge density; the blue shows the inside of this surface where the unit cell cuts through it.

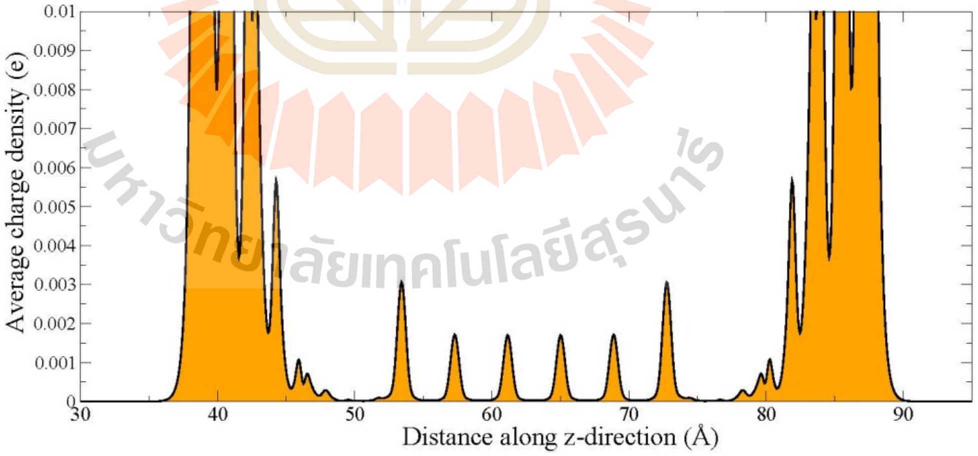

Figure 8.5 Charge density in energy range between STO middle of the gap and Fermi energy averaged over the *xy* plane for the 4-LAO layer model.

For our present purpose of determining the interface electron density, we next planar-average it over xy planes as shown in Figure 8.5, and simply integrate over z only over the middle region from about 50 Å to 75 Å. The zero of the distance perpendicular to the layers is chosen in the middle of the vacuum region. In practice, we include only the layers in LAO where the lower energy limit already lies above the VBM. However, it does include the whole STO region and thus gives truly the sheet density whether it is localized near the STO interface or spreads out over a few STO layers. The resulting net sheet densities are 1.43×10^{13} e/cm^2 and 2.14×10^{13} e/cm^2 for the 4-LAO layer and 5-LAO layer cases, respectively. These are in good agreement with experimental values of Thiel *et al.* (Thiel *et al.*, 2006) and indeed much smaller than the nominal charge of $1/2e$ per interface unit cell area as assumed in the polar discontinuity model. From Figure 8.5, only shown for the 4-layer case, we can also see that the charge density is slightly higher near the interface but decays rather slowly into the STO region.

Returning to Figure 8.4, we may notice that the charge density also provides information on the orbital character of the interface charge. In the 4-LAO layer case, it clearly consists of d_{xy}-like states throughout the STO region. In the 5-LAO layer case, the isosurfaces inside the STO look more cubic, because now the d_{xz} and d_{yz}, i.e., the other t_{2g} orbitals, also contribute. This is related to the fact that we have a significantly higher interface sheet density in the 5-LAO layer case. In fact, the thin STO layer confinement effects are more strongly affecting the d_{xz} and d_{yz} states than the d_{xy} states. Thus, for low carrier concentration, we only fill the d_{xy} bands, while for the higher concentration we start to fill both but near the interface, the states are still predominantly d_{xy}-like. Similar observations on the nature of the interface states were made in Ref. (Popović *et al.*, 2008).

Next, we also examine the layer-averaged electrostatic potentials (in Figure 8.6) and examine the slope in the LAO layer. This gives a field of 0.21 eV/Å for the 3-layer case. Within the framework of the polar discontinuity model, this field should be given by $E=4\pi\sigma/\varepsilon$. Using a static dielectric constant of $\varepsilon=28$ from Ref. (Reinle-Schmitt *et al.*, 2012) this gives a $\sigma=3.2\times10^{14}$ e/cm^2, as expected from the discontinuity model. This charge results from the total nuclear plus electronic charge and reflects the true discontinuity in electric field arising from the juxtaposition of nominally alternatingly positive (LaO) and negative (AlO_2) layers on top of the STO neutral layers. However, we see that once the gap is closed and some charge is transferred from the surface to the interface as in the 4 and 5 layer cases, the slope is reduced. However, it is not reduced to zero as is also clear from the PDOS in Figure 8.2. This is consistent with the significantly lower conduction band interface charge or sheet density we found above. Part of the potential slope is reduced also by the dipoles resulting from the ionic displacements discussed in the previous section. Furthermore we can see that near the interface, the slope in the 5-layer case is similar to the 4-layer case but the potential then flattens out as we approach the surface. In that sense the somewhat larger net interface charge indeed avoided the polar catastrophe. If one would add more layers of LAO, presumably the sloped potential region would only occur near the interface after which the potential would remain flat. In the present case, the next layer is however already close to the surface where another dipole potential obviously is present to the vacuum level outside the layer.

The above detailed analysis clarifies what actually happens in the purely electronic reconstruction model in terms of "avoiding the polar catastrophe."

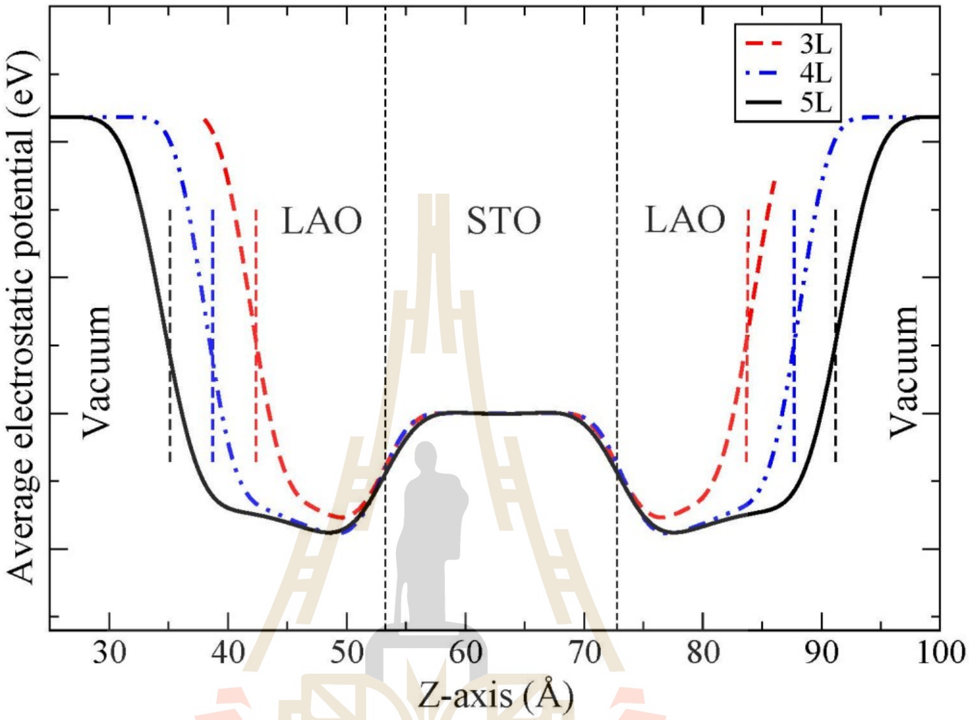

Figure 8.6 Macroscopically averaged electrostatic potentials of the 3-, 4-, and 5-LAO layer cases. The potentials are averaged over the *xy* plane and filtered by a running average in the *z* direction to filter out layer-by-layer variations. The vertical dashed lines show the position of the O in the TiO_2 interface layer and the position of the O in the AlO_2 surface for each case are marked by short vertical dashed lines.

8.5 Surface Terminations

Next we consider the effects of surface terminations. In Figure 8.7(a) we show the layer-by-layer PDOS for a 2×2 cell with one H on the surface O in the AlO_2 surface layer. This means that it corresponds to a 1/8 surface coverage with H. A structural model of the surface configuration is included at the top of the figure. The PDOS shows that the H forms bonding and antibonding states with the surface O-2*s* and O-2*p*. We can see these H bonding below the O-2*p* band at -8 eV. The ones below the O-2*s* occur at -21 eV just below our energy range cutoff and are thus not visible in the figure. The corresponding antibonding state lies high in the conduction band. There are however no extra states below the Fermi energy near the surface. Thus the additional electron from H finds its way to the lowest available empty states which are at the CBM of STO in the TiO_2 layers. These calculations were performed for an LAO thickness of only 3 unit cells. In other words, even below the critical thickness, covering the LAO surface with hydrogen coverage of only 1/8 already provides the necessary charge for eliminating the polar catastrophe. In fact, the slope in the potential on the different LaO or AlO_2 layers is seen to be almost zero. In this case, the charge density at the interface determined as explained in the previous section is 1.20×10^{13} *e*/cm^2. On the other hand, we also studied a full coverage of H using the 1×1 2D cell model. In that case, we find that the interface charge increases only to 3.01×10^{13} *e*/cm^2. However, there is now a significant charge density near the surface. This is shown in Figure 8.7(b). In fact, in this case the polar catastrophe is overcompensated. One may now see that the potential slope is reversed and the potentials shift down from the interface to the surface. This leads to a downward shift of the LAO conduction band, which now also becomes partially filled. This implies that we now would have both the surface and interface layers to become conducting. The electron density in the surface layer was also determined in a similar manner to that in the interface and amounts to 6.2×10^{13} *e*/cm^2. This calculation for full H coverage was also repeated for a 4-LAO layer model. Similar results are obtained but now the 2DEG sheet density increased to 9×10^{13} e/cm^2. This indicates that the H effects are accumulative with the charge already there from surface to interface charge transfer. For the 3-LAO layer model with a half H coverage we obtain 2.88×10^{13} e/cm^2. These results indicate that even a small amount of H adsorption on the surface is sufficient to eliminate the potential slope. The interface 2DEG density can be further increased in proportion to the H concentration. However the interface 2D electron gas sheet density cannot be increased much beyond the 10^{13} e/cm^2 level without overcompensating the fields and creating an opposite polar catastrophe, which now also leads to a surface conducting layer.

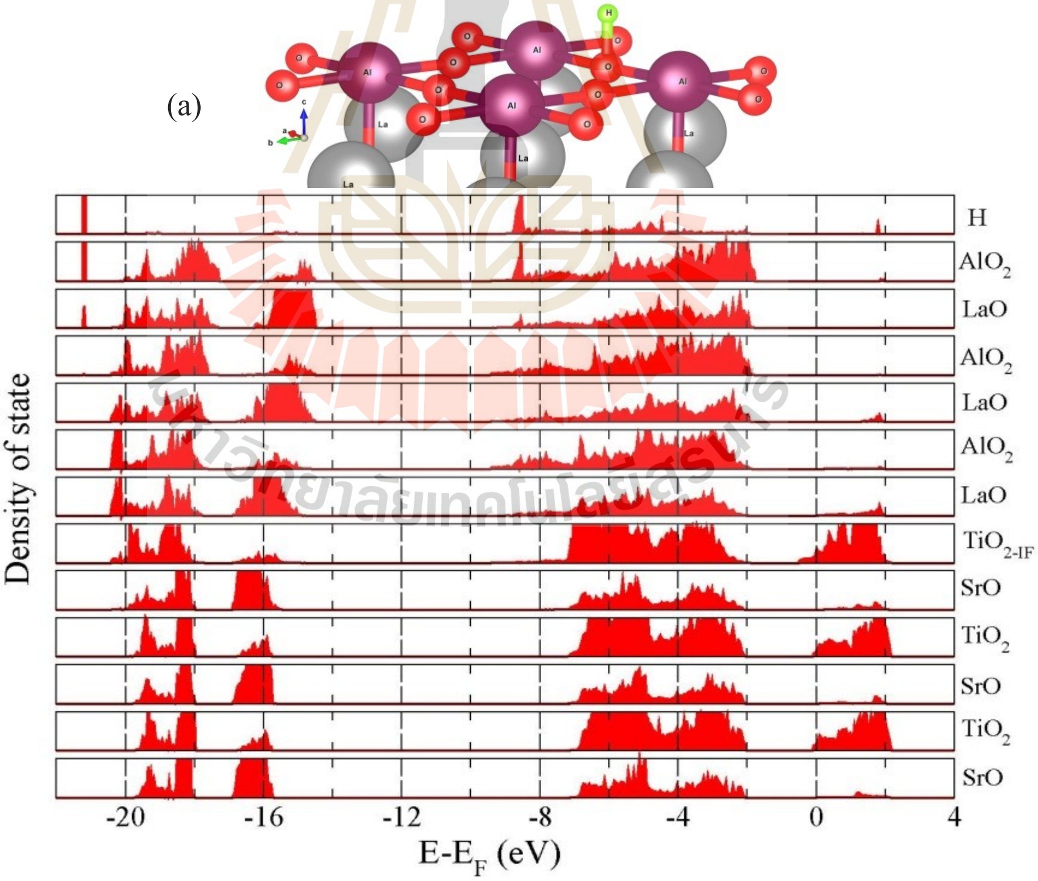

Figure 8.7 Layer-projected density of states and their surface structure in the case of (a) 1/8 H atom coverage and (b) full coverage by H atoms.

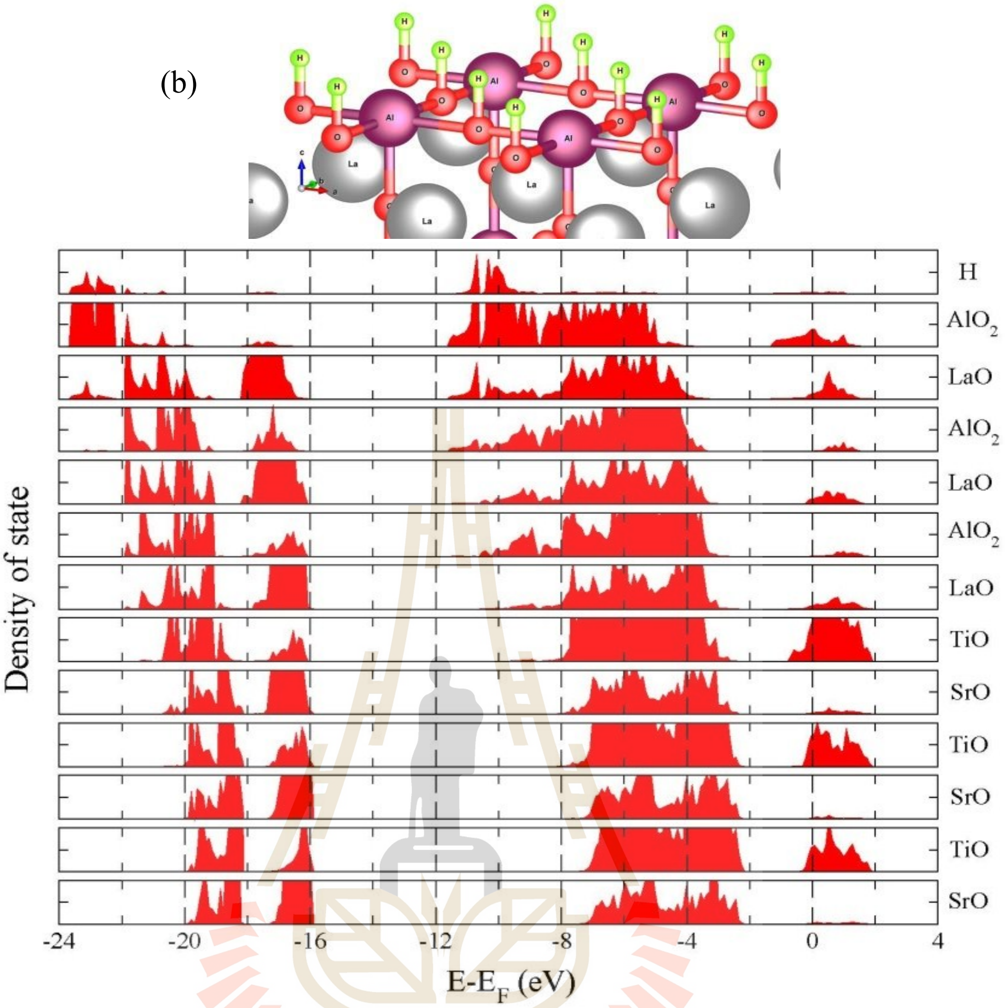

Figure 8.7 (Continued) Layer-projected density of states and their surface structure in the case of (a) 1/8 H atom coverage and (b) full coverage by H atoms.

Next, we consider OH attached to the surface Al. Again, this is done for the 2×2 2D cell and 3 layers of LAO. The result is shown in Figure 8.8(a). It leads to a surface state just above the VBM which stays empty. This can be explained as follows. We add 8 states for the O-2*s* and O-2*p* below the VBM but we add only 7 electrons. So, the Fermi level crosses through the VBM or rather between the VBM and the surface state which then becomes a p-type surface. However, we still have a strongly sloped potential and no electrons in the interface, so no 2DEG formation. As expected, when we have one of each, OH and H [as shown in Figure 8.8(b)], the two effects compensate each other and we obtain essentially the same sloped potential as before for the bare surface for the 3-LAO layer case, i.e., no 2DEG formation at the interface.

These results are relevant for the surface modification effects as studied by Cen *et al.* (Cen *et al.*, 2008; Bi *et al.*, 2010). These authors proposed a model for their AFM tip surface manipulation studies. The assumption is that in the native state, the surface is covered by equal amounts of H and OH resulting from water in the atmosphere which is split and adsorbed separately as OH on Al and H on surface O. Our calculations indeed indicate that the total energy for H_2O adsorbed on an Al is higher than an OH and H separately adsorbed on Al and surface O, respectively, by 1.8 eV per H_2O molecule. This is obtained from separate studies of OH and H and H2O adsorption on a pure LAO slab. For absorption on the LAO/STO/LAO slab we find a somewhat smaller but still positive energy of 0.6 eV. Thus the interface seems to have some effect on this reaction energy. However, in any case the separate adsorption of H and OH and splitting of the water molecule is preferred.

One may now assume that the tip removes OH and thereby activates locally the H to donate its electrons to the interface and create locally a 2DEG. Interestingly, our present calculations indicate that this by no means requires a full coverage of the surface with H_2O. In fact, a full coverage of the surface with H would overcompensate the polarity discontinuity field. Further experimental work to elucidate the actual surface coverages with H and OH in dependence on the partial pressures in the gas would be quite interesting. At present we cannot yet fully quantitatively determine what the maximum 2DEG carrier concentration that is achievable in this way. It is also unclear whether the same effect would add to the 2DEG charge density at the interface if the starting system with compensated H and OH is already above the critical layer thickness. Our one calculation for a 4-LAO layer and full H coverage indicates the effects are accumulative.

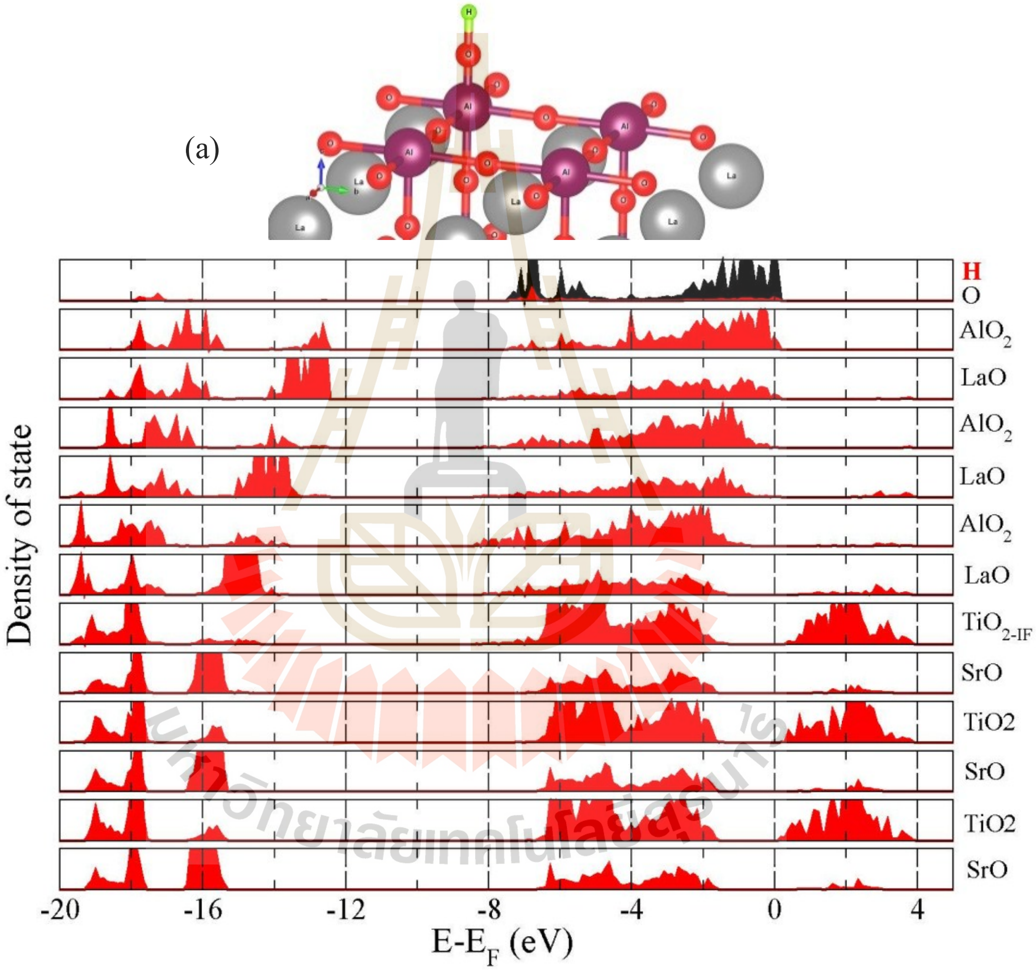

Figure 8.8 Layer-projected density of states and their surface structure in the case of surface partially covered by (a) OH and (b) H2O (dissociated into OH and H).

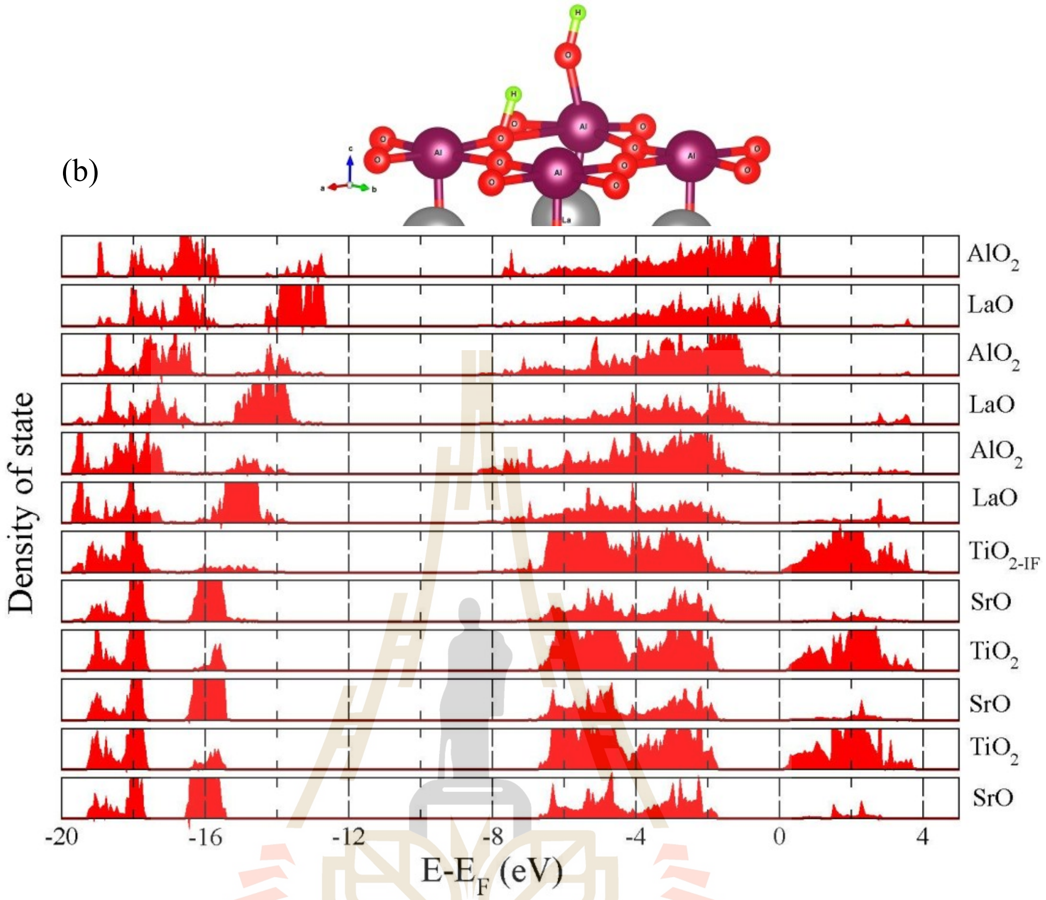

Figure 8.8 (Continue) Layer-projected density of states and their surface structure in the case of surface partially covered by (a) OH and (b) H2O (dissociated into OH and H).

8.6 Ti-Al Interdiffusion Effects

In this section, we consider various effects of interdiffusion. First we start with replacing one Al in the first LaO layer next to the interface by Ti in the 2×2 2D supercell. After relaxing the structure, we found that the Ti was slightly displaced away from the interface. This agrees with observations by Zaid *et al*. (Zaid *et al.*, 2016). This can be seen in the structural panel (left) and buckling panel (middle) in Figure 8.9.

The effect on the PDOS can be seen in the right panel of Figure 8.9. The macroscopically averaged electrostatic potential is shown along with that of other cases, to be discussed in Figure 8.10. The potential for the case of an added Ti_{Al} in the first AlO_2 layer is shown by the red-dotted curve, labeled Ti_{Al}. While potential slopes in this curve remain visible near the interface and near the surface, compared with the no interdiffusion case (solid line), the potential in the central region of the LAO layer now looks flat, whereas it had a monotonic slope toward the surface in the abrupt interface case without interdiffusion. One could conclude that the added Ti_{Al}, i.e., a 4-valent atom on a 3-valent site, had the effect of compensating the valence discontinuity at the interface. The remaining slopes near the surface are also clearly seen in the PDOS in Figure 8.9. The Fermi level lies above the STO CBM. We can see that the Ti in the mixed layer however did not produce a defect level in that layer. The Ti-like PDOS in this layer lies well above the Fermi level with peaks at about 1 eV above the Fermi level and it has donated its electron to the interface. This implies that the interdiffused Ti_{Al} did not convert to Ti^{3+} as is often assumed. Instead because of the higher electrostatic potential of this layer, it turned out to be preferable to let this extra electron move to the interface. So, in some sense it contributes to the electronic reconstruction. Only, instead of the charge coming from a p-type surface it came from the Ti_{Al} site in the mixed LaO interface layer. The sheet density of the 2DEG in the interface in this case is 1.1×10^{13} e/cm^2.

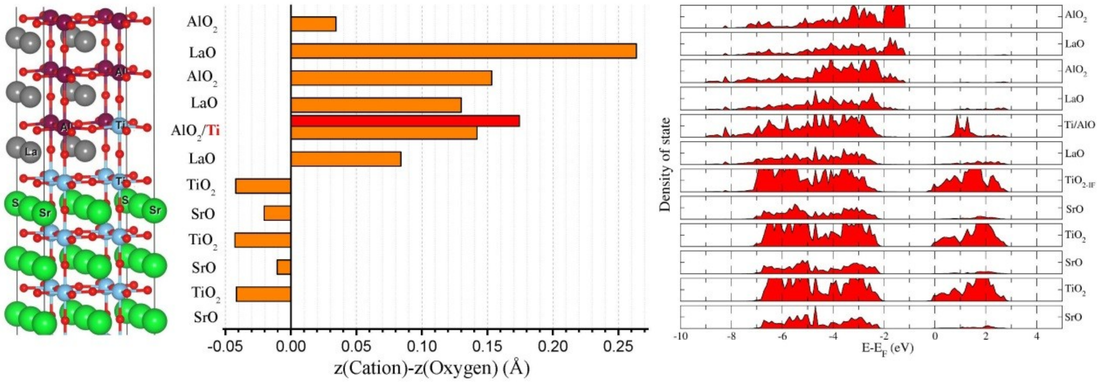

Figure 8.9 Structural model (left), buckling of layers ($z_{\text{cation}}{-}z_{\text{oxygen}}$) (middle), and PDOS (right) for the 25% Ti, 75% Al layer model. For the mixed layer, the Ti displacement is indicated in red, the Al displacement in orange.

We now consider the PDOS in Figure 8.9. in the four topmost layers starting from the surface. We here see a decreasing PDOS in the energy range −1 eV to −2 eV from the surface inward. These states persist all the way down to the first LaO layer above the mixed Ti-AlO$_2$ layer but are not present in the LaO layer near the interface. In that sense there is an abrupt change in the upper valence band state of the second and third LaO layer (counting down from the surface). It looks in other words like a localized surface state. This is similar to the models without interdiffusion discussed in section 8.3. In some sense, what the added Ti did was shift the interface closer to the surface so it is now only two LAO layers below the surface instead of three. This slope in potential over the near-surface layers can also be seen in Figure 8.10.

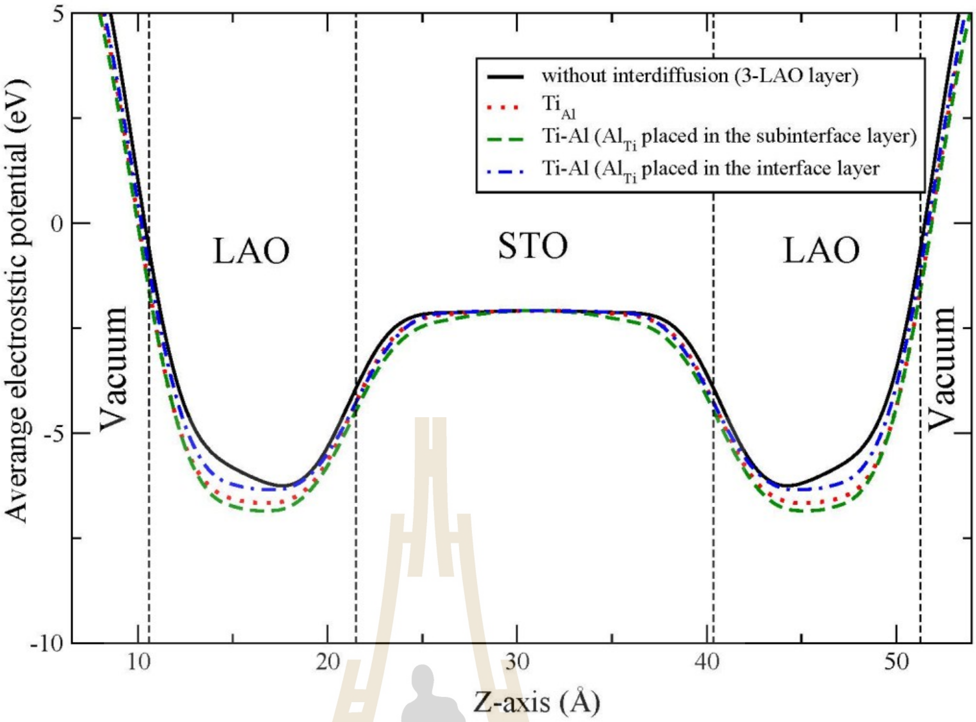

Figure 8.10 Macroscopically averaged electrostatic potentials for three Ti-Al interdiffusion models compared with the case of no interdiffusion. The vertical dashed lines show the position of the surface and interface layers.

Next, instead of adding Ti, we studied swapping a Ti from the STO side with an Al in the LAO. The results are shown in Figure 8.11. On the right of this figure, we show the model indicating in which layer the Ti_{Al} and Al_{Ti} are placed. In the middle we show the layer buckling after relaxation and on the right the PDOS. The corresponding electrostatic potential profiles are shown in Figure 8.10. We considered two cases: in both the Ti_{Al} occurs in the AlO_2 layer closest to the interface. In model (a), the Al_{Ti} is placed deeper into the STO region, one TiO_2 layer removed from the interface layer; in model (b) it is placed in the interface TiO_2 layer. First we note that both the Al and Ti were displaced away from the interface. Their displacements relative to the O in their plane were 0.15 Å for the Ti_{Al} compared to 0.14 Å for the Al in the same layer. For the Al_{Ti} on the STO side, the displacement relative to the oxygen was −0.03 Å compared to −0.02 Å for Ti in that layer.

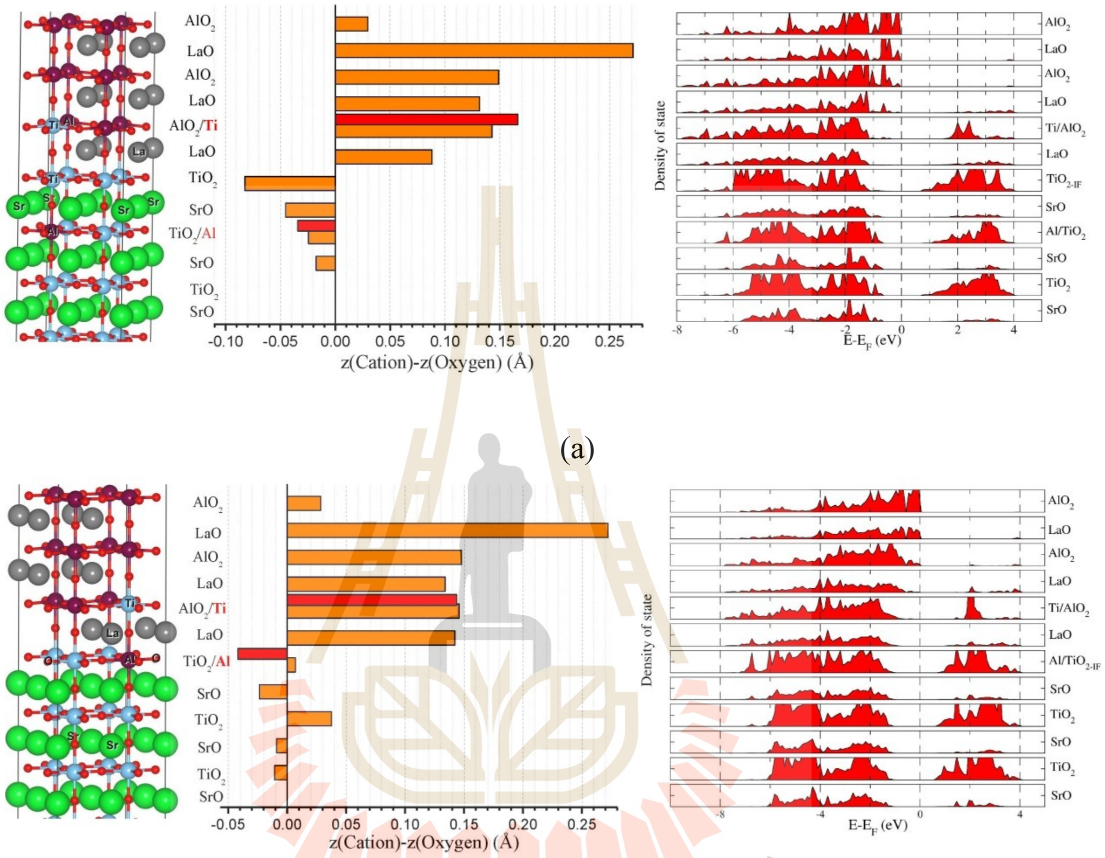

(a)

(b)

Figure 8.11 Structural model (left), buckling of layers (middle), and PDOS (right) for two Ti-Al intermixing models. The bar graphs show $\Delta z = z_{\text{oxygen}} - z_{\text{cation}}$ with z the distance normal to the interface. In (a) the Al_{Ti} is placed in the subinterface TiO_2 layer; in (b) it is in the interface layer.

The results are similar to the previous case where we only added Ti. One can see that the Ti_{Al} PDOS in the Al layer is located at about 2 eV above the Fermi level, well above the CBM of STO. Thus their electron is transferred to the STO. However, the TiO_2 layer on the STO now lacks an electron by having one Ti replaced by Al, and thus no electrons accumulate in the STO. This is true in both models, neither of which show a 2DEG. In the case where the Al is placed deeper into the STO, one can see that the electrostatic potential is higher in that layer by the energy shift of the local PDOS.

The dipoles related to the swap and corresponding atomic displacements are such that the potential slope is reduced or taken care of within the near-interface region, as can be seen in Figure 8.10. The three cases all show a more or less flat potential in the LAO region near the interface and a sloped potential near the surface. We can also see changes in the potential on the STO region of the interface. Depending on how deep the Al is placed, the potential slope in the interface region becomes more spread out. As expected the interdiffusion widens the interface region.

In summary, the Ti_{Al} in the LAO appears in each case to donate its electrons to the interface or STO region rather than forming Ti^{3+} in its own layer. However, if we also place Al on the STO side as would occur in actual interdiffusion without Ti enrichment, then the Al on the STO side compensates the added electrons and no 2DEG results. Nonetheless, the linear potential variation of the models without interdiffusion is no longer seen. The dipoles induced by the atomic displacements modify the potential profile and eliminate the overall slope in the near-interface region. However, a potential slope remains in the surface region and leads to a surface-state-like decay of the AlO_2 PDOS. In other words, there is a surface band bending effect.

8.7 Sr-La Interdiffusion Effects

In this section, we present our results for Sr-La interdiffusion effects as studied in the same 3-LAO layer 2×2 2D supercell case. The results are shown in Figure 8.12. In the first example we place SrLa in the LAO layer right next to the interface and LaSr in the first SrO layer next to the TiO_2 interface layer. In terms of the structure, we find that Sr_{La} moves less toward the surface from its oxygen layer than the La in the same layer. In other words, relative to the La, the Sr moves closer to the interface. This trend is opposite to that of Ti_{Al} in the previous section. The PDOS shows that no 2DEG forms.

As a second Sr-Al swap case we placed the Sr_{La} in the LaO layer farther away from the interface, in fact in the middle LaO layer, but kept the La_{Sr} in the SrO layer next to the TiO_2. The Sr_{La} was still found to move toward the interface relative to the La but slightly less so than in the near-surface layer, studied in the previous case. Remarkably in this case we do find an interface state in the TiO_2 interface layer and formation of a 2DEG. Apparently just shifting the Sr_{La} one layer farther away from the interface results in a somewhat different electrostatic potential profile which allows some of the surface charge to transfer to the TiO_2. It should be noted that in this case the Sr_{La} lies in the middle of the 3-layer LAO layer film and in some sense allows the surface to communicate with the interface, whereas in the previous case, the slope potential and any charge transfer were restricted to the near-interface region. The net sheet density in this case however is found to be only 6.0×10^{12} e/cm^2.

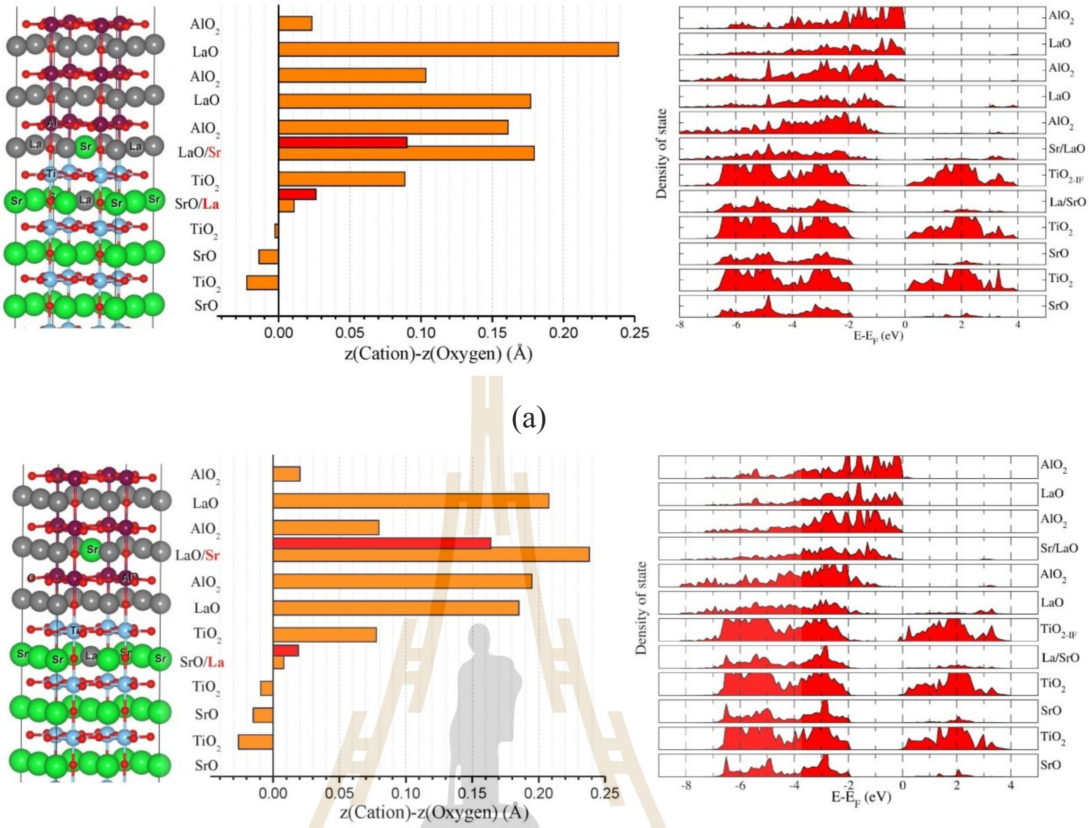

(a)

(b)

Figure 8.12 Structural model (left), buckling of layers (middle), and PDOS (right) for two Sr-La interdiffusion models. The bar graphs show $\Delta z = z_{oxygen} - z_{cation}$ with z the distance normal to the interface. In case (a) Sr_{La} occurs closer to the interface than in case (b).

The potential profile for both Sr_{La} positions is shown in Figure 8.13. For the case of Sr close to the interface, shown by the dashed red line, the profile is smooth and shows a flat region in the center of the LAO layer. For the Sr_{La} farther away from the interface, shown by the dashed-dotted blue line, the profile is more complex with a vanishing slope at about 49 Å and another one at about 44 Å. Overall the slopes in potential in the LAO region are reduced compared to the model without any interdiffusion (shown as solid black line) but the effect of the valence discontinuity is not entirely removed.

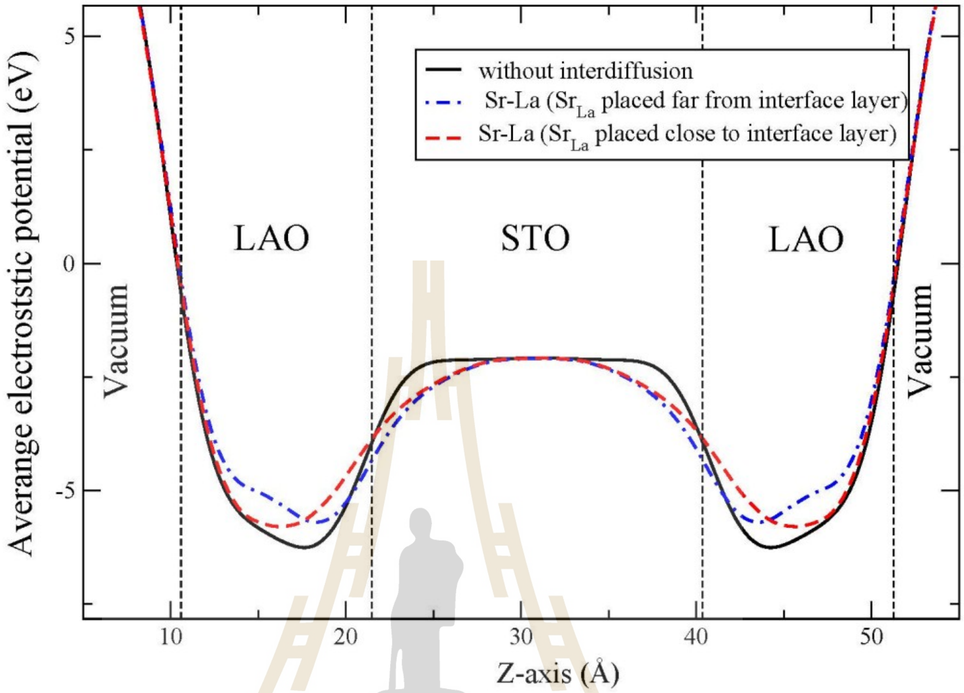

Figure 8.13 Macroscopically averaged electrostatic potentials for two cases of Sr-La interdiffusion compared with the case of no interdiffusion. The vertical dashed lines show the positions of the interface and surface layers.

In summary of this section, the situation for a Sr-La swap is slightly more complex. Essentially the dipoles help adjust the potential slope in the near-interface region. However, the Sr_{La} may also contribute to the 2DEG formation if it lies in the middle of the LAO region. The variations in electrostatic potential layer by layer in that case seem to facilitate some transfer from surface to interface. The potential in the mixed Sr-La layer is raised and thereby the surface state extends deeper into the LAO region from the surface and allows charge to be transferred to the interface.

However, the contribution to the sheet density was found to be smaller than for the other mechanisms discussed in the previous sections.

8.8 Conclusions

In this chapter we studied various models of LAO/STO interfaces with the goal of evaluating different possible mechanisms to avoid the polar discontinuity with or without formation of a 2DEG or electronic reconstruction. Our main conclusions can be summarized as follows.

First, we studied abrupt LAO/STO interface models with bare surfaces and without any interdiffusion. In agreement with previous work we find a critical layer thickness for formation of a 2DEG of 4 layers of LAO. We also determined quantitatively the electron density in the 2DEG and studied its spread over the STO layers. We find a 2DEG concentration on the order of 10^{13} e/cm^2 in qualitative agreement with experiment and also studied how this affects the slopes of the potential that remain near the interface. The 2DEG concentrations for the various cases studied are summarized in Table 8.1.

We also analyzed the contributions of the lattice relaxation to this problem. The displacements are such as to reduce the potential slope. A larger sheet density is found for the 5-LAO layer case than the 4-LAO layer case and this result in a different orbital character of the states contributing to the 2DEG. In the 4-LAO layer case, only d_{xy}-like states are occupied while in the 5-LAO layer case, d_{xy}-like states are occupied near the interface but in addition d_{xz}- and d_{yz}-like states are also partially occupied in the deeper STO layers.

Table 8.1 Summary of occurrence of 2DEG and its interface sheet density σ for various cases.

System	**2DEG**	σ **(10^{13} e/cm^2)**
3-LAO layer	No	-
4-LAO layer	Yes	1.43
5-LAO layer	Yes	2.14
3-LAO + (1/8)H coverage	Yes	1.20
3-LAO + (1/2) H coverage	Yes	2.88
3-LAO+ full H coverage	Yes	3.01[a]
4-LAO+ full H coverage	Yes	9.00
3-LAO + (1/4)Ti_{Al}	Yes	1.10
3-LAO + (1/4)Ti_{Al} +Al_{Ti}	No	-
3-LAO + (1/4)Sr_{La} at interface + La_{Sr}	No	-
3-LAO + (1/4)Sr_{La} in middle LAO + La_{Sr}	Yes	0.6

[a] In this case, a surface 2DEG of 6.2×10^{13} e/cm^2 is also present.

Next, we studied surface termination effects or surface passivation effects by water absorption. We did this for the situation of a below critical thickness LAO layer of only 3 unit cells thick. We find first that H_2O absorbed on Al prefers to split into OH on Al and H on surface O. We found that H on O donates its electrons to the interface rather than forming surface states in the AlO_2 layer. However, this is only true if the H concentration is not too high. Here we studied only two limiting cases, a low coverage of 1/8 H restricted by the size of cell we can deal with and a high coverage of 1 H per surface O. In the latter case, the potential slope problem is reversed and a significant electron density is found in surface states below the LAO CBM.

Adsorption of OH on the Al on the other hand leads to a p-type surface and with acceptor-like surface states above the LAO VBM. This does not help to reduce the polar discontinuity potential and in fact compensates the H 2DEG if both are present simultaneously.

Finally we studied both Ti-Al and Sr-La interdiffusion effects. We found that Ti_{Al} and Al_{Ti} tend to be displaced away from the interface. These dipoles already would help reduce the potential slope resulting from the polar discontinuity. On the other hand, Ti_{Al} is found not to convert to $Ti3^{+}$ but rather to donate its electrons to the STO. If there is excess Ti and the STO remains unmixed, the polar discontinuity is avoided and a sizable 2DEG concentration is achieved. On the other hand, if the T_{iAl} is compensated by an Al_{Ti} in the STO TiO_2 interface layer, then the extra Al on the TiO_2 layer contributes a compensating hole so that no net 2DEG forms. A significant surface potential bending remains in the LAO layer leading to a surface-state-like decay of the LaO and AlO_2 layer PDOSs.

For Sr-La interdiffusion we found that both Sr_{La} and La_{Sr} tend to be displaced toward the interface. Both Sr and La are merely donors in their respective crystals and so do not contribute relevant energy levels near the VBM or CBM. The nuclear charge swaps simply compensate and no 2DEG forms if both are close to the interface. However, we found that they nonetheless affect the electrostatic potentials in the layers in which they reside. Thereby they can influence the potential profile and for example for Sr_{La} placed in the middle of the 3-layer LAO, we found that it helped transferring charge from the surface to the interface so that now a 2DEG formed even for a layer thickness below the normal critical layer thickness.

Although some interesting and unexpected effects of the interdiffusion were found here, we caution that a full study of this would require a statistical averaging and taking into account how much actual interdiffusion takes place and how the interdiffused atoms are distributed over the layers. Such information is recently becoming available from MEIS studies by Zaid *et al.* (Zaid *et al.*, 2016). However, the gradual interdiffusion profile is too complex to treat directly with first-principles simulations. A small concentration in a any given layer would require a much larger 2D cell than we here can afford with present computational power. Second, some of the effects we found here could compensate each other. Therefore the value of the present results lies more in the qualitative findings. A fully quantitative treatment of these various effects on the 2DEG electron density requires probably a simpler modeling approach in which some of these qualitative aspects are incorporated. Still, some of our predictions are worth further testing experimentally, in particular the prediction that Ti_{Al} on the LAO side after interdiffusion would stay Ti^{4+}. In both cases, of course it contributes to the overall 2DEG electron density but our calculation predicts the latter should stay confined to the STO rather than making the whole LAO film n-type doped.

CHAPTER IX

CORE-LEVEL BINDING ENERGY SHIFTS AS A TOOL TO STUDY SURFACE PROCESSES ON $LaAlO_3/SrTiO_3$

9.1 Introduction

From chapter VIII, surface termination effects are known to play a key role in the formation of an interface two-dimensional electron gas (2DEG) at thin film $LaAlO_3/SrTiO_3$ (LAO/STO) heterostructures. This was most clearly demonstrated by the work of Cen *et al.* (Cen *et al.*, 2008; Cen *et al.*, 2009; Cheng *et al.*, 2011; Cheng *et al.*, 2013) and Xie *et al.* (Xie *et al.*, 2010). They showed that the 2DEG could be locally induced by means of an atomic force microscopy tip several layers under the surface of an LAO layer on STO with thickness below the critical thickness for formation of the 2DEG. It can be reversibly erased as well by altering the bias of the tip and leads to the possibility of patterned scribing and erasing of conducting stripes at the LAO/STO interface, in other words, reconfigurable electronics. This was explained (Bi *et al.*, 2010) in terms of surface processes, the so-called “water-cycle”, which is based on the fact that H_2O on the surface is dissociated into separate OH adsorbed on Al and H on O. The tip is then proposed to remove OH in the writing cycle, and remove H in the erasing cycle, thereby modifying the balance of H and OH on the surface. An excess of H^+ on the surface is supposed to add electrons to the 2DEG while an excess of OH^- would reduce the 2DEG electron concentration. In a previous chapter, we indeed showed that even a small concentration of adsorbed H on the LAO surface of the LAO/STO system can induce a 2DEG below it, while OH instead creates a p-type surface state. On the other hand, we also found that too high a concentration of H on the surface would also create an excess electron concentration in H related surface states and could even bend the potential opposite to what occurs in the LAO/STO overlayer system. Several questions about these processes remain open: for example, could re-absorption instead of desorption also play role, how much H and OH is on the surface as function of the partial pressures in the vapor phase in contact with the surface, at what temperature do these species desorb from the surface, what is their binding energy?

X-ray photoemission spectroscopy (XPS) provides a powerful technique to monitor surface composition. The core-level specificity to each element provides immediate chemical information on the composition. Moreover, small changes in binding energy for the same species depending on different environments provide fine-tuned information on the chemical neighborhood of each detected element. For example, atoms at surfaces with different coordination than in the bulk are known to show a surface core-level shift. Similarly, atoms in different valence states typically have different core-level binding energies. For example this allows one to distinguish Ti3^{+} from Ti^{4+}. For the present problem it allows us possibly to distinguish surface oxygen bound to H from bare surface oxygen or oxygen in an OH species bonded to surface Al or O in various carbonaceous species from bulk oxygen.

In this chapter, we performed experimental XPS studies of both the O1*s* and C1*s* core levels as function of growth conditions of the LAO fillm and annealing conditions. We find a satellite peak in the O1*s* spectrum at about 2.2 eV higher binding energy from the main peak is removed at about 500 °C. Changes occur also in the C_{1s} spectrum. Concurrently we perform first-principles calculations of the core-level binding energy (CL-BE) shifts to explore how fine-tuned information we can possibly extract from these measurement. We first show that the absolute core-level binding energies can be obtained when properly including core-hole final state effects.

Both changes in screening and changes in the electrostatic potential may influence the core level binding energy shifts. We map out the core-level binding energies for different O species and their different near neighborhood environments. Combined with these core-level binding energy calculations, we also calculate the energetics or atomic binding energies to explore the energetic probability of different adsorption/desorption processes. By comparing theory with experiment we will show that the conventional explanation, which associates the 2.2 eV O1*s* satellite peak with easier removable OH groups from the Al sites than the H from surface O-sites is incompatible with the calculations. Instead we argue that this is related to carbonaceous species containing O, specifically carboxylic acids and possibly esters, physisorbed on the surface.

9.2 Method

9.2.1 Experiment

All the measurements were done on LAO layers deposited on STO substrates using Pulsed Laser Deposition (PLD). For more specific details see Refs. (Zaid *et al.*, 2016; Wei and Sehirlioglu, 2012). X-ray Photoelectron Spectroscopy (XPS) was conducted at the Air Force Research Laboratory (AFRL) at the Wright Patterson Air Force Base in Dayton, OH. Films grown were exposed to air for at least

24 hours in between deposition and XPS measurements. This is typical for the exposure conditions between deposition and subsequent electrical characterization. Thin films grown via PLD were subjected to XPS with a Kratos Axis Ultra spectrometer outfitted with an in-situ heated stage. Samples were irradiated with a monochromatic Al$K\alpha$ beam with $h\nu$ = 1486 eV in ultra high vacuum (UHV) at close to 10^{-10} Torr. Survey scans for each sample were conducted at pass energy of 160 eV, while high resolution scans for O1*s* and C1*s* were conducted at pass energy of 20 eV. Samples were also subject to charge compensation to neutralize the positive charge buildup on the irradiated surface.

9.2.2 Computational approach

The basic underlying theory of our computational method is density functional theory (DFT) in the generalized gradient approximation (GGA), for which we use the Perdew-Burke-Ernzerhof (PBE) parametrization. (Perdew *et al.*, 1996) The Vienna Ab-initio Simulation Package VASP code (Kresse and Furthmüller, 1996; Kresse and Hafner, 1994), implementing the projector augmented plane wave method (PAW) (Blöchl, 1994; Kresse and Joubert, 1999) is used to solve the DFT Kohn-Sham equations. Some calculations are also performed using the full-potential linearized muffin-tin orbital method (FP-LMTO) as implemented by Methfessel and van Schilfgaarde. (Methfessel *et al.*, 1999; Kotani and van Schilfgaarde, 2010).

Absolute core level binding energies are not well described by one-electron Kohn-Sham levels. This is because of two reasons: first, the GGA does not exactly cancel the self-energy error; secondly, a core-hole is a local excitation, which is accompanied by screening or final-state effects, often called the core-levelrelaxation energy. In a many-body perturbation theoretical framework, these could be described by the self-energy operator, for example in the GW approximation. (Hedin and Lundqvist, 1970) An alternative is to exploit the local nature of the excitation, treating it as an impurity and thus calculating the excitation energy directly as a difference between two total energies. This is called the ΔSCF approach. The core level binding energy in this approach is given by

$$\begin{aligned} E_B(i) &= E(N-1,i) - E(N), \\ &= \int_1^0 \varepsilon_i(n_i)\,dn_i, \\ &\approx \varepsilon_i(1/2), \\ &\approx \frac{\varepsilon_i(1)+\varepsilon_i(0)}{2}. \end{aligned} \tag{9.1}$$

Here $E(N\text{-}1;\, i)$ is the total energy of the N-1 electron system with the electron removed from state i, $E(N)$ is the ground state total energy of the N-electron system. We used Janak's theorem (Janak, 1978), according to which $\varepsilon_i=\partial E/\partial n_i$, with $\varepsilon_i(n_i)$ the one-particle Kohn-Sham energy level viewed as a function of the occupation number n_i of that level. This leads to Slater's transition state $\varepsilon_i(1/2)$ or using the average of the core level energy with and without core hole as an approximation for the binding energy. In an all-electron method, we can explicitly create the core hole. We have done this with the FP-LMTO approach, (Methfessel *et al.*, 1999) as implemented in the lm-suite (from https://www.questaal.org/). In this approach, when a core-hole is created, an electron is added to the lowest available empty state, i.e. the conduction band minimum (CBM), to preserve charge neutrality. The core-level binding energy calculated from this total energy difference clearly corresponds to the excitation of the electron from the core state to the CBM. This means the proper energy reference level to be used is the CBM. The total energies do not depend on the reference level for the potential because both the one-electron levels and effective potential use the same reference and thus it cancels out when calculating the total kinetic energy from

$$T = \sum_{i}^{occ} \varepsilon_i - \int n(r)\upsilon_{eff}(r)d^3r \qquad (9.2)$$

However, the one-electron levels ε_i do depend on the reference level. Commonly this is chosen as the average electrostatic potential, volume averaged over the unit cell. To compare with the total energy difference, both need to be referred to the same reference level. Thus we need to shift the reference energy from the average electrostatic potential to the CBM in order to compare the two expressions. Using this approach we get the O1*s* core level binding energy to be 540.0 eV relative to the CBM reference level, either directly from the total energy difference or from the Janak's theorem approximations.

Alternatively, one can represent the system with core-hole by means of the *Z*+1 approximation in the projector augmented wave (PAW) method. In the PAW method after the valence electrons have been made self-consistent for the atom placed in a specific environment (but keeping core-electrons frozen) one can reconstruct the actual potential inside the atomic sphere and calculate its Kohn-Sham core levels and hence determine ε_i. In the VASP code, the reference level for the core levels is again the average electrostatic potential. Shifting to the CBM as reference level, we obtain 540.4 eV in close agreement with the LMTO all-electron approach.

We note that this absolute core level binding energy is different from the experimental value, which for the LAO system is at about 530 eV. This however reflects just a change in reference level. The absolute zero of energy in the experimental XPS electron kinetic energy does not correspond to the CBM of LAO but to the Fermi level of the sample holder. From here on, we will focus entirely on core level binding energy shifts. Specifically, we will compare all core-level binding energies to that of the center layer O atom in our LAO slab.

Core level binding energy (CL-BE) shifts arise from two effects: first, the electrostatic potential can vary from site to site, depending on the local charge state and chemical environment, second the screening of the core hole in the final state can vary. For example for atoms at the surface or in adsorbed species sticking of the surface, there are fewer nearest neighbors around to contribute to the screening. Therefore, even for CL-BE shifts, not just the absolute energies, it is important to include the final state core-hole effects. When comparing core level shifts from different systems, a more suitable reference level is the vacuum level. Thus for loosely bound or physisorbed species such as carbonaceous species, we will use the CL-BE relative to the vacuum level of the molecules calculated separately. We then align the vacuum level with that of the LAO slab to determine the CL-BE of O atoms in the molecules relative to that of the O in the middle of the slab in bulk-like LAO. To this end we also need to determine the position of the CBM in our LAO slab relative to the vacuum electrostatic potential.

In the case of physisorbed molecules, we found, it is more suitable to use only initial state core-level shifts. In fact, in the weakly bound molecules, the core-level extraction is not compensated by a screening electron being added to the lowest unoccupied molecular orbital (LUMO) as our VASP calculations would assume. Instead, the molecule really becomes ionized as charge transfer from the solid system to the molecule is not facilitated so easily. We will compare binding energies of the C1*s* core levels in various functional groups in molecules relative to those in C bonded only to C or H in two ways: either assuming an electron is transferred to the LUMO and using the final state effect or simply using only initial state shifts We will show that the latter gives better agreement with experiment. The same approximation is thus used for the O1*s* core level shifts in the physisorbed molecules.

Further details of our computational method are as follows. We use a symmetric 4.5 layer LAO slab, meaning 4 layers of AlO_2 and 5 of LaO, with AlO_2 surface terminations, with a 3×3 surface unit cell. The in-plane lattice constant is fixed at the PBE relaxed lattice constant of bulk $LaAlO_3$. The interplanar distances as well as any other atomic coordinates are fully relaxed. A vacuum region of 20 Å thick separates the slabs in the periodic boundary condition model. For various absorption models we adsorb the same species on both surfaces. The pure LAO slab contains 207 atoms. A plane wave cut-off 500 eV, sufficient to deal with the deepest O PAW potentials is adopted and a 3×3×1 Monkhorst-Pack k-point mesh is used to sample the Brillouin zone. We have also used a LAO/STO/LAO slab model with 3-LAO layers on either side of a STO slab, as used previously in chapter VIII.

9.3 Experiment and Initial Discussion

Four films of different thicknesses, 2 unit cells, and 5 unit cells, grown at different oxygen partial pressures, 1×10^{-4} Torr and 1×10^{-6} Torr, each, were analyzed at both room temperature and up to temperatures of 1000 °C. The spectra are of two representative samples are shown in Figure 9.1.

All spectra can be deconvoluted into a main peak and two satellite peaks on the higher binding energy side, a 2.2 eV and 1.2 eV satellite. The reduction of the +2.2 eV shoulder of each O1*s* peak was observed at 500 °C, with a near total reduction of the shoulder after 3 hours. No significant further changes to the reduced O1*s* peak were observed even after heating to 1000 °C. An overview of the relevant peak positions and their corresponding concentrations as determined from the survey scan are given in Table 9.1.

Table 9.1 Binding energies (B.E.) in eV and atomic concentrations in % of the relevant deconvoluted peaks.

Temp	pO_2		O-oxide	+1.2 ev	+2.2 eV	C1*s*
Room	10^{-6}	B.E.	529.44	530.50	531.28	284.8
		Atm. %	34.09	9.06	9.66	18.74
	10^{-4}	B.E.	529.39	530.65	531.38	284.8
		Atm. %	29.92	8.97	6.11	29.38
500 °C	10^{-6}	B.E.	529.47	530.65	-	284.8
		Atm. %	40.20	12.06	0.00	16.02
	10^{-4}	B.E.	529.40	530.65	-	284.8
		Atm. %	38.97	10.36	0.00	21.87

A tentative initial interpretation of these data is that OH groups bonded to Al would be less strongly bonded to the surface than H on the surface O. The 2.2 eV-peak would then be associated with OH groups and the 1.2 eV peak with surface O bonded to H. A similar interpretation has been given in literature. (Holloway, 2009; Sunding *et al.*, 2011; Niu *et al.*, 2000; Biesinger *et al.*, 2009) These arise from the decomposition of H_2O and thus one would assume there to be equal amounts of OH and H on the surface and most likely a fairly high surface coverage. One may note that the 2.2 eV peak is stronger relative to the 1.2 eV peak in the 10^{-6} Torr sample. In the latter, one would expect there to be more oxygen vacancies, including on the surface. This would imply that some of the OH from the decomposition of H_2O could fit into an oxygen vacancy and thus be indistinguishable from a surface O with adsorbed H. This would be expected to reduce the Al-OH related peak. However, this prediction is in contradiction with the interpretation, discussed above.

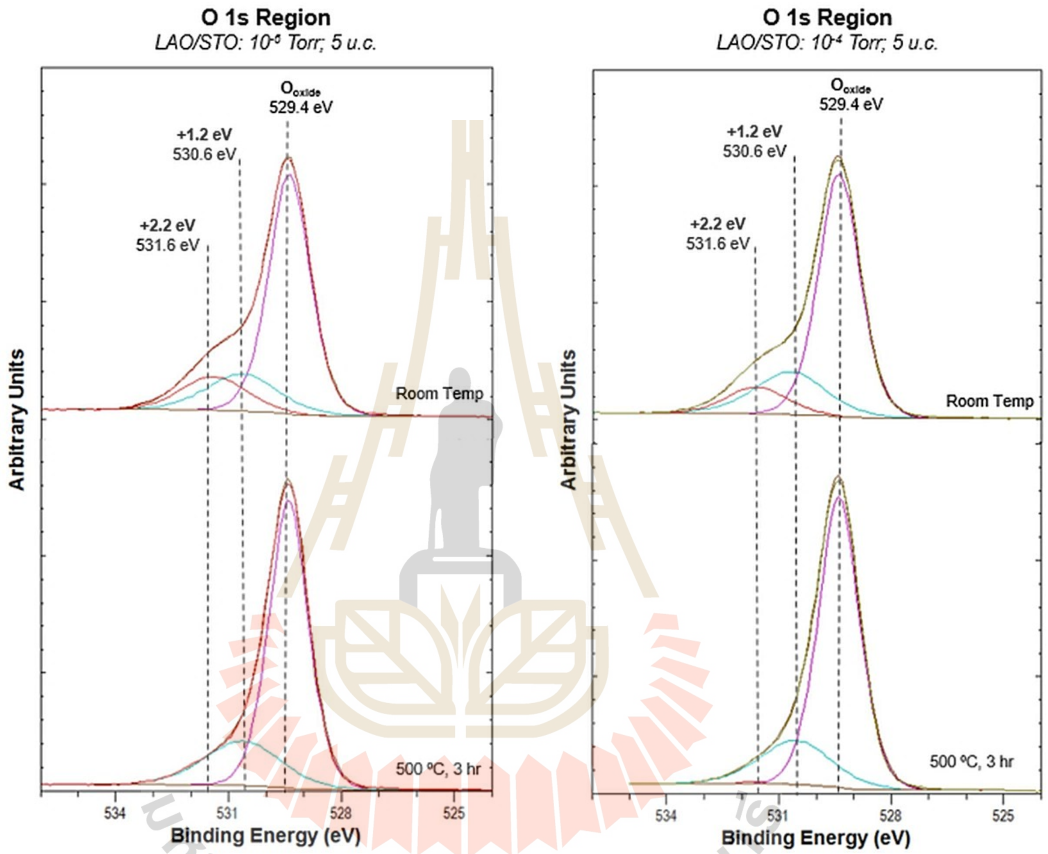

Figure 9.1 XPS spectra of LAO films grown at 10^{-6} Torr (left) and 10^{-4} Torr (right) before (top) and after (bottom) annealing at 500 °C.

In addition, higher core-level binding energies have been related to formation of oxides with cations in their higher oxidation state (e.g., instead of NiO, Ni_2O_3) (Norton *et al.*, 1977) which are sometimes also described as defective oxides. This term here corresponds to oxides with cation vacancies where oxygen atoms are adjacent to Ni vacancies (Biesinger *et al.*, 2009; Payne *et al.*, 2012; Hagelin-Weaver *et al.*, 2004). These peaks were also related to the hydride form of the oxides (e.g. $NiOH_{0.2}$) (Norton *et al.*, 1977). This corresponds to H adsorbed on the surface oxygen as we study here. In LAO, neither A-site cations (La) nor B-site cations (with Al forming the surface layer) change valence and no structural change associated with different oxidation state is observed. Generally, deposition at 10^{-4} Torr results in compositions with no detectable oxygen vacancies per our past EELS (Energy Electron Loss Spectroscopy) study (Zaid *et al.*, 2016) which provides more unambiguous results in comparison with XPS if two different oxides and suboxides exist (Norton *et al.*, 1977). At 10^{-6} Torr, however, the deposited films have greater amount of oxygen vacancies. In these heterointerfaces, the charge associated with the oxygen vacancies are believed to be compensated by a change in the valence of Ti cations near the interface as Ti-3*d* orbitals form the conduction band. Furthermore, below we study the O-corelevel shifts at oxygens close to an oxygen vacancy and will show that this cannot account for the observed shifts.

In the remainder of the paper, we scrutinize this interpretation in various ways. First, we calculate the bonding energies of various species on the surface to compare the bonding strength of H on surface O (O_s-H) with that of OH on Al. We will show that indeed the latter is slightly weaker bound. However, both are bonded rather strongly, compared to k_BT at 500 °C. Secondly, we calculate the core-level binding energies and find that when the surface is highly covered, Al_s-OH and O_s-H have similar CL-BE shifts closer to 1.2 eV than to 2.2 eV. We then hypothesize that the latter may arise from carbonaceous O, i.e. oxygen occurring in organic molecules physisorbed on top of the surface, already covered with H and OH. To test this hypothesis, we measure the C1*s* region of the spectrum and study its changes under the same annealing conditions.

The C1*s* spectra before and after annealing are shown in Figure 9.2. The C1*s* spectra show a main peak at about 284.8 eV, associated with C bonded only to other C or H, and several high binding energy satellites, corresponding to C bonded to O in different types of functional groups, which can be interpreted following Payne *et al.* (Payne *et al.*, 2009) We also test this interpretation by performing calculations of the core-level shifts for C1*s* and O1*s* in various types of organic molecules. More detail on this is discussed later in this chapter.

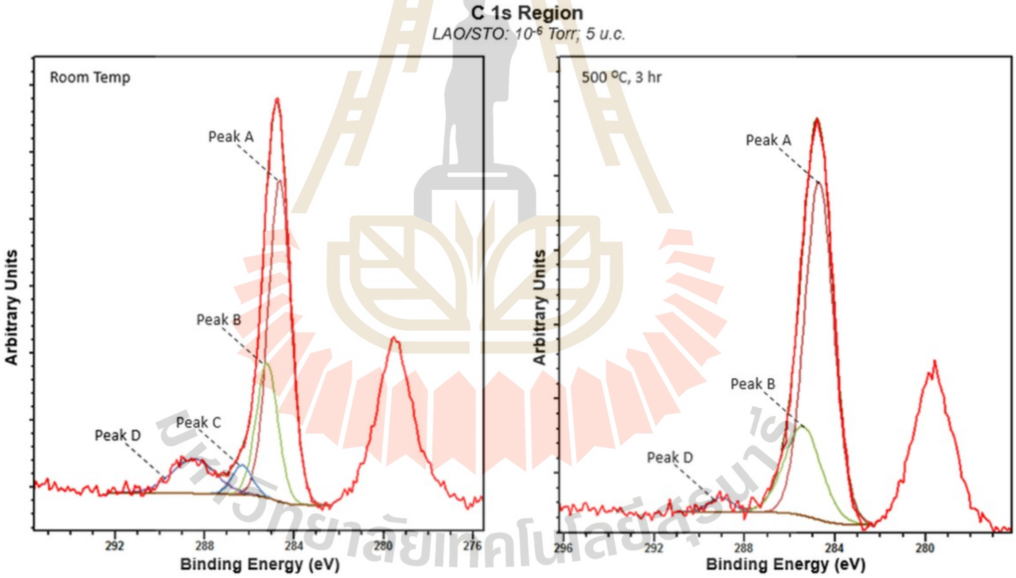

Figure 9.2 Carbon 1*s* core level spectrum at room temperature and after annealing at 500 °C measured on a LAO/STO 5 unit cell layer LAO sample grown at 10^{-6} Torr.

9.4 Energies of Formation and Adsorption

In this section we report our findings on total energies of formation, atomic binding energies and reaction energies. It is important to emphasize the difference between the term binding energy in this section, which refers to the binding energy of molecules or atoms, from the term core-level binding energy (CL-BE) in the next section, which refers to an electron-binding energy. We started by studying various models of water adsorption on the LAO surface. Binding energies need to be referred to appropriate reference chemical potentials. For example, we may define the binding energy of H_2O adsorbed on the Al by

$$E_B(\mathrm{H_2O}) = [E(\mathrm{LAO} + \mathrm{H_2O}) - E(\mathrm{LAO}) - 2\mu_{\mathrm{H_2O}}]/2 \tag{9.3}$$

Here $E(\mathrm{LAO} + \mathrm{H_2O})$ is the total energy of the system with an H_2O molecule adsorbed on one of the Al on both surfaces of the slab, $E(\mathrm{LAO})$ is the total energy of the bare LAO slab and $\mu_{\mathrm{H_2O}}$ is the total energy of a H_2O molecule. Absolute chemical potentials are used in conjunction with total energies for the slabs. Alternatively, we can already subtract the reference energies of all the free atoms from the total energies and also in the definition of the chemical potentials. Similarly, for OH adsorption, we may define the binding energy as:

$$E_B(\mathrm{OH}) = [E(\mathrm{LAO} + \mathrm{OH}) - E(\mathrm{LAO}) - 2\mu_{\mathrm{OH}}]/2 \tag{9.4}$$

and or H adsorption,

$$E_B(\mathrm{H}) = [E(\mathrm{LAO} + \mathrm{H}) - E(\mathrm{LAO}) - 2\mu_{\mathrm{H}}]/2 \tag{9.5}$$

The question is: what to use as chemical potentials for H and OH? Rather than using a H_2 molecule, which would be appropriate for a reducing H_2 atmosphere, we assume that the surfaces are in contact with moist air, which contains O_2 and H_2O. We thus assume that H atoms desorbing from the surface would immediately react with O_2 and form H_2O. That means we assume

$$\mu_{\mathrm{H}} = \frac{1}{2}\left(\mu_{\mathrm{H_2O}} - \frac{1}{2}\mu_{\mathrm{O_2}}\right) \tag{9.6}$$

Similarly, we assume

$$\mu_{\mathrm{OH}} = \mu_{\mathrm{H_2O}} - \mu_{\mathrm{H}} = \frac{1}{2}\mu_{\mathrm{H_2O}} - \frac{1}{4}\mu_{\mathrm{O_2}} \tag{9.7}$$

These equation give μ_{H}=-4.79 eV whereas μ_{H} (H_2)= -3.34 eV. So, H has about 1.45 eV lower chemical potential than in a H_2 molecule and is hence much less reactive. For OH, we find μ_{OH}= -10.03 eV, in other words, a lower energy by 2.28 eV than the OH molecule, unlikely to occur as a separate species. The energy of the OH molecule was indeed calculated to be -7.75 eV. One could go beyond this treatment by considering the chemical potential of oxygen to contain a term $-k_B T \ln pO_2$ and thus take in to account the different chemical environments.

When considering combined adsorption of OH and H on different sites, we have the choice of defining the binding energy with respect to the H_2O molecule or with respect to already separated OH and H species. When comparing with the adsorption of an actual H_2O molecule, it is more convenient to use the same reference species H_2O so that we can directly obtain the reaction energy for the reaction

$$\mathrm{Al}_s - \mathrm{H_2O} \rightarrow \mathrm{Al}_s - \mathrm{OH} + \mathrm{O}_s - \mathrm{H} + \Delta E_r \tag{9.8}$$

The latter will be referred to as the water splitting reaction energy. If $\Delta E_r < 0$ it means the reaction is exothermic and proceeds to the right.

The different models calculated are shown in Figure 9.3. The first one (model A) is a H_2O molecule adsorbed on Al. The second (model B) is an OH adsorbed on Al with an H adsorbed on the nearest neighbor O. In model C, we have only O on Al and two separated H on O_s. Model D has only OH adsorbed on Al. In model E we consider a H adsorbed on O only. In model F we consider Al_s-O and O_s-H separated but either close or far from each other. Finally, in model G, we also consider the energy of formation of an oxygen vacancy on the surface. The latter is defined by

$$E_B(V_O) = [E(\mathrm{LAO} + 2V_O) - E(\mathrm{LAO}) - 2\mu_0]/2 \tag{9.9}$$

The binding energies of these models are listed in Table 9.2 for the choice of chemical potentials discussed above, i.e. under the assumption of equilibrium with O_2 and H_2O.

Table 9.2 Binding energies (in eV) per adsorbed molecule(s) for models shown in Figure 9.3 and oxygen vacancy formation energy, with respect to the chemical potential references defined in the text.

Model	description	E_B
A	H_2O on Al	-2.19
B	Al_s-OH and O_s-H next to each other	-3.08
C	Al_s-O and $2O_s$-H	-1.55
D	Al_s-OH	-0.76
E	O_s-H	-2.25
F1	Al_s-O and O_s-H (close)	-0.78
F2	Al_s-O and O_s-H (far)	0.57
G	surface V_O	-0.21

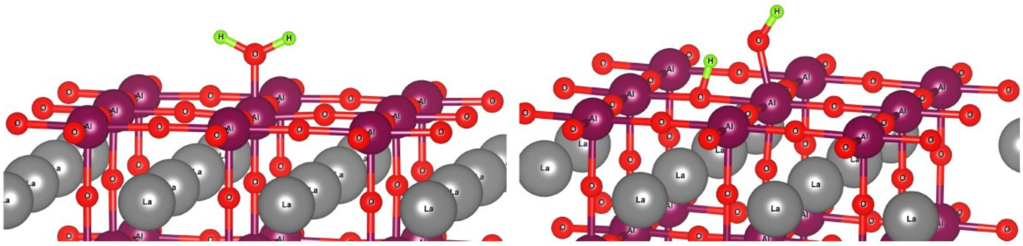

(a) Model A (b) Model B

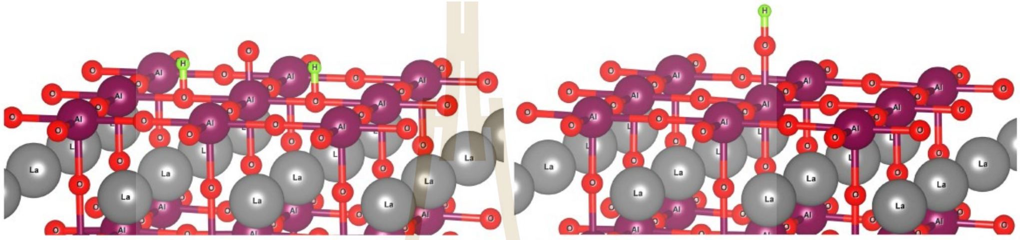

(c) Model C (d) Model D

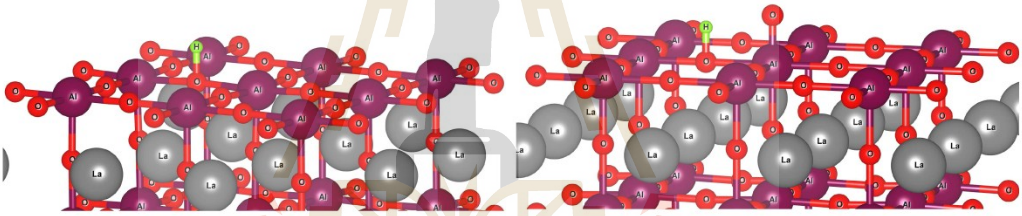

(e) Model E (f) Model F1

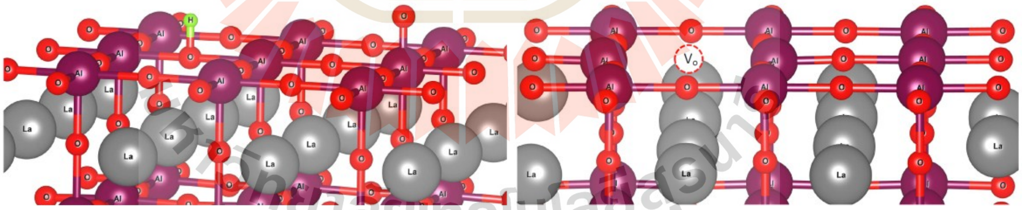

(g) Model F2 (h) Model G

Figure 9.3 Various adsorption models studied.

From these results, we can see that having O bonded to Al_s is not favorable, rather OH stays together on Al_s. We can also see that H_2O wants to split into separate OH on Al_s and H on O_s by 0.89 eV per water molecule. We can also consider the adsorption of OH inside an existing surface oxygen vacancy

$$V_{\mathrm{O}} + \mathrm{OH} \rightarrow \mathrm{O}_s - \mathrm{H} \tag{9.10}$$

The reaction energy for this process is -2.05 eV. Finally, we note that desorption of OH from Al_s is significantly easier than desorption of H from a surface O_s.

9.5 Core-Level Binding Energy Shifts

The calculated CL-BE shifts are given in Table 9.2. The CL-BE shifts are all calculated relative to those of a core-hole placed in the middle of the corresponding LAO slab. We calculated CL-BE for the O1*s* core level for the following models. First we consider an LAO slab with adsorbed OH on Al_s and H on O_s next to each other (case B). Core holes were created in the center of the slab, for O in the adsorbed OH molecule and for an O_s with H attached. This represents the case of high coverage where, as we found before, H_2O is assumed to split but OH and H are expected to be found close to each other on the surface. We find both CL-BE of at deeper for the former. Second, we considered OH-Al_s separately and O_s-H separately on the surface (cases D and E), corresponding to low coverage. When isolated the O_s-H shifts deeper to 2.46 eV, while the OH-Al_s shifts back toward the main CL-BE of bulk O. The only CL-BE close to 2 eV found here, corresponds to O_s-H, and in all cases, the O_s-H has higher CL-BE than the Al_s-OH. This is in clear contradiction with the initial (and commonly made) hypothesis. The role of the H and OH CL-BE seem to be exactly reversed from what we need according to that hypothesis. Also, if OH is preferentially desorbed and the O_s-H becomes thereby more isolated than it would shift to higher BE and increase the 2.2 eV peak rather than decreasing it. The fact that both the OH and H correspond to the 1.2 eV peak which is not affected under annealing suggest that the surface stays fully covered with OH and H and that another interpretation must be sought for the 2.2 eV peak.

We also modeled a core hole placed in an O_s without H for comparison with that with H. These O_s without H have only small CL-BE shifts compared to bulk O.

In addition, we considered the possibility of a negative charge state of the OH adsorbed on Al_s as expected to occur when the Fermi level is high in the gap. This could occur in the presence of a 2DEG at a nearby STO/LAO interface. Note that from chapter VIII, the OH adsorbed on Al_s produces levels just above the VBM and could thus become filled if the Fermi level lies above them. For the isolated Al_s-OH, this leads to a shift to higher BE but it is still near 1.24 eV only, so not explaining the 2.2 eV peak. Furthermore, to model the negative charge state, we add a homogeneous background charge density to maintain the system neutral. In a slab calculation, this background extends somewhat unphysically in the vacuum region rather than being confined to the slab. This would possibly overestimate the CL-BE shift due to the charging. For the O_s-H and OH-Al_s together, the electrons go from the donor O_s-H to the acceptor OH-Al_s and thus the system is overall neutral, so this problem is avoided.

Next, we considered the role of V_O on the surface and place the core hole in a nearby O_s and we also added V_O to the previous models of OH-Al_s and O_s-H and examined the changes in core hole shifts on the latter when the V_O is nearby. Compared to the same cases without V_O the CL-BE shifts seem to increase by the presence of nearby V_O. This seems plausible because V_O should present an attractive electrostatic potential and thus shift levels down to deeper CL-BE. However, these models are still not compatible with the 2.2 eV peak being associated with OH.

Table 9.3 Core-hole binding energy shifts of O1*s* state (in eV) relative to center (bulk O) in the LAO slab or center of the STO slab in the LAO/STO/LAO cases. Positive values mean higher binding energy.

slab	**slab termination**	**core-hole site**	**CL-BE shift**
LAO	Al_s-OH+O_s-H	O_s-H	1.19
		OH-Al_s	0.71
	Al_s-OH	OH-Al_s	0.02
		O_s	-0.68
	Al_s-OH^{-1}	OH-Al_s	1.24
		O_s	0.7
	O_s-H	O_s-H	2.46
		O_s	-0.14
	V_O	O_s	0.1
	V_O+Al_s-OH	OH-Al_s	0.54
		O_s	-0.45
	V_O+O_s-H	O_s-H	3.17
		O_s	-0.04
	COH	O on COH	6.88
		O beneath COH	5.08
	COH with Al_s-OH+O_s-H	O on COH	5.07
		O beneath COH	3.57
LAO/STO	Al_s-OH+O_s-H	O_s-H	1.93
		OH-Al_s	1.16
		O_s	0.14

Finally, the question may arise if the above results which were obtained on a pure LAO slab would change if we take into account the presence of the nearby 2DEG at an LAO/STO interface. We thus considered explicitly an LAO/STO/LAO with various terminations: OH-Al_s+H-O_s, or each separate. In these cases, we calculated the CL-BE shift relative to the O in the middle of the STO layer. This seems to shift the core levels toward slightly lower CL-BE but not enough to explain the 2.2 eV peak.

An alternative origin for the 2.2 eV peak might come from carbonaceous species. In fact, Payne *et al*. (Payne *et al.*, 2009) show that molecules with –COO groups, that is –O–C=O as in carboxylic acids or esters have a relative high binding energy shift. As a first attempt to model O bonded to C bonded to the surface, we considered a COH molecule chemisorbed on the surface. This leads to very high CL-BE either for the O_s underneath them or the O in the molecule itself. They are in excess of 5 eV, and not found in the experiment. From this we conclude that carbonaceous species, if responsible for the 2.2 eV peak should not be directly adsorbed on the surface. Rather, we need to consider physisorbed molecules on the already covered surface. We do that in the next section.

9.6 Core-Level Binding Energies in Physisorbed Molecules

In this section, we consider carbonaceous species or H_2O physisorbed on the already OH and H covered LAO surface. To deal with the physisorbed case, we calculate the molecules in a separate calculation, not attached to the surface and align the O1*s* levels to those in the slab by referring both to the common vacuum level. To test this approach, we first calculate the C1*s* levels in different molecules. Following

Payne *et al*. (Payne *et al.*, 2009) we consider different organic groups involving O and compare the C1*s* CL-BE with those in C only bonded to C or H.

For all carbonaceous isolated molecules, we consider a periodic boundary conditions model with sufficient separation between the molecules and they are treated in the Γ point approximation. Their geometry optimizations are carried out at the PBE level. This is done without any constraints, and the structure are considered relaxed until the Hellmann-Feynmann forces less than 0.01 eV/Å. Periodically repeated images of isolated molecules are separated by 15 Å and the vacuum levels are obtained by plotting the average electrostatic potential in the three directions inside this 15 Å box. We compare the CL-BE shifts calculated either with initial state shift only, or with the procedure used in the previous section. In the latter case, we should note that the core hole is each time compensated by an added electron in the lowest unoccupied molecular orbital (LUMO). In the initial-state-only calculation, the advantage is that no charge is added which closer represents the physical situation, on the other hand, no changes in screening due to the different molecular environment are not taken into account. In any case, by calculating the LUMO we can refer all BE to the vacuum level.

We consider the following molecules: methyl-alcohol (CH_3-OH), ethyl alcohol (CH_3CH_2-OH); dimethyl ether (CH_3-O-CH_3), diethyl ether ((C_2H_5)-O-(C_2H_5)); acetone as an example of a ketone (CH_3-(C=O)-CH_3), ester (CH_3-(C=O)-O-CH_3), carboxylic acid (CH_3-(C=O)-O-H) and carbonate CO_3. We then calculate the core-level binding energy in the C in pure CH_3 groups not bonded to any O, and average over the different molecules. Next, we consider the two alcohols and average the C1*s* CL-BE in the C-OH group. The C-O-C group occurs in both ethers and in the C at the end of the (O=C)-O-C group in the ester. The C in the middle of the (O=C)-O occurs in both the ester R-(O=C)-O-R and the carboxylic acid R-(O=C)-OH and is also averaged. Finally the C=O without an additional O occurs in the ketone.

Table 9.4 C1*s* core-level binding energy shifts in different organic groups. The column labeled screened, means CL-BE is calculated from ε_{C1s} averaged with and without core-hole and electron added to LUMO, initial means only initial state shift. Experimental values from Payne *et al*. (Payne *et al*., 2009). For the CH_3 we give the actual calculated CL-BE with respect to vacuum, for the others the shift relative to this one.

group	**screened**	**initial**	**Expt.**
CH_3	291.3	266.1	284.8
C-OH	1.0	1.3	1.5
C-O-C	1.2	1.3	1.5
C=O	0.6	2.6	2.9
O=C-O	1.7	3.6	3.8
CO_3	5.6	6.4	5.5

The results are shown in Table 9.4. Except for the CO_3 case, the results agree better with experiment for the initial state shift calculation. This is because in the case of the calculation including a final state shift, a charge transfer to the molecule is assumed and this overestimates the screening. We note that the absolute values cannot be directly compared to experiment because they use different reference levels. Clearly the shifts increase with increasing number of O bonded to C or O bonded more strongly (e.g. double bonded) to C. The alcohols and ethers provide different shift because the O is either bonded to another C (O shared between two C) or O is shared between a C and a H. The deviations between different molecules containing the same group are of order a few 0.1 eV, which shows that the idea of associating the shift with different O environments makes sense. In fact the O is expected to pull electrons away from the C and therefore increases the binding energy.

Next, we consider the corresponding O1*s* CL-BE shifts. Based on the previous results for C1*s* shifts, we think the initial state shift calculations are more reliable but nonetheless, we have given both for comparison. We can see that the shifts again have a systematic trend with the number of carbons per oxygen. They are the lowest in the ethers where two C are bonded to the O, then in the alcohol. The shift in the ketone is also small. The largest shifts occur for the carbonate. Shifts of about 2.2 eV occur for the single bonded O in the O=C-O group, either in the ester or the carboxylic acid.

These trends agree with the results of Payne *et al.* (Payne *et al.*, 2009). The results suggest that the O1*s* peak at 2.2 eV shifted from the main peak could be explained by esters or carboxylic acids physisorbed on the LAO surface, already covered by H and OH. The same functional group has a carbon contributing to the D peak in the C1*s* spectrum (Figure 9.2). It also has a carbon corresponding to peak B in the C1*s* spectrum. Both of these peaks indeed lose intensity under annealing at 500 °C.

In Table 9.6, we summarize concentration and full width at half maximum (FWHM) corresponding to the different subpeaks of the C1*s* spectrum before and after annealing. The main change in the C1*s* spectrum actually occurs in the C-peak corresponding to ketones. But as we see in Table 9.5, the corresponding O peak does not match the 2.2 eV O1*s* peak. The reduction in the B-peak may have contributions from ethers and alcohols. However, there should be more or less a one-to one match in the D-peak loss and the O1*s* 2.2 eV peak loss. In order to calibrate quantitatively how much of this 2.2 eV peak can be ascribed to the corresponding loss in D-peak, additional considerations are required. The total C and O loss in the spectrum would have to be normalized in the overview spectrum relative to the La peak, which is assumed to stay unchanged. We have not pursued to carry this out in detail. While the D-peak is reduced upon annealing it does not completely disappear as does the O 2.2 eV peak. Nonetheless, we may conclude that the O1*s* peak could be ascribed reasonably to esters and carboxylic acid physisorbed on the surface. These molecules being weakly bonded only to the surface, it appears reasonable that they desorb much easier than the chemisorbed H and OH.

Now that we have determined the origin of the 2.2 eV peak in the O1*s* spectrum as carbonaceous in origin, it is interesting that the amount of such physisorbed species seems to differ depending on the growth conditions of the film. The amount is larger for the 10^{-6} Torr grown samples, which are more conductive because they have a larger concentration of oxygen vacancies. No change is observed depending on the thickness of the LAO film being below or above the critical thickness for formation of a 2DEG. Thus it is not clear that conductivity of the surface plays a role in the amount of carbonaceous species deposited. It appears that under the lower partial pressure of O_2 a higher amount of Carbonaceous species are available in the growth environment, or, possibly, the negatively charged surface oxygen vacancies could locally attract greater amount of atmospheric carbon.

Table 9.5 Core level binding energy relative to vacuum and core-hole binding energy shifts of O1*s* state (in eV) in the different molecules relative to center of the slab (already covered with OH and H) in the LAO slab after we align them with the vacuum level (539.05 eV). Positive values mean higher binding energy.

molecule	chemical formula	O-site	screened	shift	initial	shift
LAO bare ref.			539.05	0.00	505.34	0.00
water	H_2O		540.39	1.34	506.45	1.11
Methanol	CH_3-OH		539.99	0.94	506.39	1.05
ethanol	CH_3-CH_2-OH		540.13	1.19	506.4	1.06
dimethyl ether	CH_3-O-CH_3		540.72	1.68	506.66	1.32
diethyl ether	CH_3-CH_2-O-CH_2-CH_3		540.71	1.66	506.38	1.04
ketone	CH_3-(C=O)-CH_3		538.53	-0.50	506.08	0.74
ester	CH_3-(C=O)-O-CH_3	C=O	538.67	-0.38	505.96	0.62
		C-O-C	540.99	1.94	507.86	2.2
carboxylic acid	CH_3-(C=O)-O-H	C=O	538.95	-0.10	506.31	0.4
		C-O-H	540.85	1.80	507.70	2.1
carbonate	CO_3	C=O	541.37	2.32	509.97	4.63
		C-O	541.47	2.42	509.80	4.53

Table 9.6 Concentrations *c* in % and FWHM *w* (eV) of subpeaks of the C1*s* spectrum.

Temp	pO_2	A		B		C		D	
°C	(Torr)	*c*	*w*	*c*	*w*	*c*	*w*	*c*	*w*
Room	10^{-6}	59.17	1.18	23.69	1.12	4.88	1.04	12.26	2.26
Temp	10^{-4}	63.66	1.12	20.63	1.16	6.35	1.21	9.36	1.91
500	10^{-6}	72.80	1.49	24.54	1.90	0.00	0.00	2.66	1.24
	10^{-4}	76.36	1.33	21.15	1.75	0.00	0.00	2.49	1.22

9.7 Conclusions

In this chapter, we combined an experimental XPS study of the adsorbed species on LAO surfaces and their desorption under annealing with calculated analysis of the atomic bonding energies and the core-level binding energies. We showed, that OH is indeed less strongly bonded to the surface than H. However, both are too strongly bonded to explain desorption at 500 °C. The core-level calculations show that the peak shifted to 2.2 eV higher binding energy from the main O peak cannot be due to either OH or surface O with H. Instead it is related to carbonaceous species such as esters and carboxylic acids. Consistent losses in both the C1*s* and O1*s* spectra were observed under the same annealing conditions to support this interpretation. In terms of the calculations, we showed core-level binding energy shift calculations require a careful analysis of the reference level questions as well as consideration of the final state screening effects. For the chemisorbed species, we obtained good agreement in a model in which screening changes are included and compensation of the core-hole by electrons added at the lowest empty levels are assumed. For the molecules which are physisorbed, we showed that we can nonetheless align these core level shifts with those on the surface by referring all to a common vacuum level. On the other hand, for the molecules we should not assume a transfer of electrons to the molecule LUMO as this would overestimate the screening effects. Initial state core level shifts in this case provided a better agreement with experimental data.

REFERENCES

REFERENCES

Bagus, P. S., Ilton, E. S. and Nelin, C. J. (2013). The interpretation of XPS spectra: Insights into materials properties. **Surface Science Reports** 68: 273.

Bednorz, J. G. and Müller, K. A. (1984). $Sr_{(1-x)}Ca_xTiO_3$: An Quantum Ferroelectric with Transition to Randomness. **Physical Review Letters** 52: 2289.

Bednorz, J. G. and Müller, K. A. (1986). Possible high T_c superconductivity in the Ba−La−Cu−O system. **Zeitschrift für Physik B Condensed Matter** 64: 189.

Berne, B. J., Ciccotti, G. and Coker, D. F. (1998). **Classical and quantum dynamics in condensed phase simulations**. World Scientific.

Bi, F., Bogorin, D. F., Cen, C., Bark, C. W., Park, J.-W., Eom, C.-B. and Levy, J. (2010). "Water-cycle" mechanism for writing and erasing nanostructures at the $LaAlO_3/SrTiO_3$ interface. **Applied Physics Letters** 97: 173110.

Biesinger, M. C., Payne, B. P., Lau, L. W., Gerson, A. and Smart, R. S. C. (2009). X-ray photoelectron spectroscopic chemical state quantification of mixed nickel metal, oxide and hydroxide systems. **Surface and Interface Analysis** 41: 324.

Blöchl, P. E. (1994). Projector augmented-wave method. **Physical Review B** 50: 17953.

Boonchun, A., Smith, M., Cherdhirunkorn, B. and Limpijumnong, S. (2007). First principles study of Mn impurities in $PbTiO_3$ and $PbZrO_3$. **Journal of Applied Physics** 101: 43521.

Brühwiler, P., Maxwell, A., Puglia, C., Nilsson, A., Andersson, S. and Mårtensson, N. (1995). π* and σ* Excitons in C1*s* Absorption of Graphite. **Physical Review Letters** 74: 614.

Buttner, R. H., Maslen, E. N. (1992). Structural parameters and electron difference density in $BaTiO_3$. **Acta Crystallogr** 48: 764.

Cen, C., Thiel, S., Hammerl, G., Schneider, C., Andersen, K., Hellberg, C., Mannhart, J. and Levy, J. (2008). Nanoscale control of an interfacial metal–insulator transition at room temperature. **Nature materials** 7: 298.

Cen, C., Thiel, S., Mannhart, J. and Levy, J. (2009). Oxide nanoelectronics on demand. **Science** 323: 1026.

Ceperley, D. M. and Alder, B. J. (1980). Ground State of the Electron Gas by a Stochastic Method. **Physical Review Letters** 45: 566.

Chassé, T., Hallmeier, K. H., Hecht, J. D. and Frost, F. (2002). X-ray absorption near edge structure investigations of group III nitrides and nitrided aiii-bv semiconductor surfaces FeFF calculations and electron yield measurements. **Surface Review and Letters** 09: 381.

Chen, H., Kolpak, A. and Ismail-Beigi, S. (2010). First-principles study of electronic reconstructions of $LaAlO_3/SrTiO_3$ heterointerfaces and their variants. **Physical Review B** 82: 085430.

Cheng, G., Siles, P. F., Bi, F., Cen, C., Bogorin, D. F., Bark, C. W., Folkman, C. M., Park, J.-W., Eom, C.-B. and Medeiros-Ribeiro, G. (2011). Sketched oxide single-electron transistor. **Nature Nanotechnology** 6: 343.

Cheng, G., Veazey, J. P., Irvin, P., Cen, C., Bogorin, D. F., Bi, F., Huang, M., Lu, S., Bark, C.-W. and Ryu, S. (2013). Anomalous transport in sketched nanostructures at the $LaAlO_3/SrTiO_3$ interface. **Physical Review X** 3: 011021.

Choudhury, D., Mukherjee, S., Mandal, P., Sundaresan, A., Waghmare, U., Bhattacharjee, S., Mathieu, R., Lazor, P., Eriksson, O. and Sanyal, B. (2011). Tuning of dielectric properties and magnetism of $SrTiO_3$ by site-specific doping of Mn. **Physical Review B** 84: 125124.

Choudhury, D., Pal, B., Sharma, A., Bhat, S. and Sarma, D. D. (2013). Magnetization in electron-and Mn-doped $SrTiO_3$. **Scientific reports** 3.

Daniel, S., Rye, T. and Graeme, H. (2008). Optimization methods for finding minimum energy paths. **The Journal of Chemical Physics** 128: 134106.

Dawson, J. A., Chen, H. and Tanaka, I. (2014). Combined Ab Initio and Interatomic Potentials Based Assessment of the Defect Structure of Mn-Doped $SrTiO_3$. **The Journal of Physical Chemistry C** 118: 14485.

Du, M. H. and Biswas, K. (2011) Anionic and Hidden Hydrogen in ZnO. **Physical Review Letters** 106: 115502.

Du, M. H., Limpijumnong, S. and Zhang, S. B. (2005). Hydrogen pairs and local vibrational frequencies in H-irradiated $GaAs_{1-y}N_y$. **Physical Review B** 72: 073202.

Eckstein, J. N. (2007). Oxide interfaces: Watch out for the lack of oxygen. **Nature Material** 6: 473.

Eror, N. G. and Balachandran, U. (1982). Electrical conductivity in strontium titanate with nonideal cationic ratio. **Journal of Solid State Chemistry** 42: 227.

Feynman, R. P. (1939). Forces in Molecules. **Physical Review** 56: 340.

Freeman, A. and Wimmer, E. (1995). Density Functional Theory as a Major Tool in Computational Materials Science. **Annual Review of Materials Science** 25: 7.

Frederikse, H. P. R., Thurber, W. R. and Hosler, W. R. (1964). Electronic Transport in Strontium Titanate. **Physical Review** 134: A442.

Galasso, F. S. (2013). **Structure, Properties and Preparation of Perovskite-Type Compounds: International Series of Monographs in Solid State Physics**. Elsevier.

Gao, L., Huang, Y., Hu, Y. and Du, H. (2007). Dielectric and ferroelectric properties of (1-x)$BaTiO_3$–x$Bi_{0.5}Na_{0.5}TiO_3$ ceramics. **Ceramics International** 33: 1041.

Ge, W., Li, J., Viehland, D. and Luo, H. (2010). Influence of Mn Doping on the Structure and Properties of $Na_{0.5}Bi_{0.5}TiO_3$ Single Crystals. **Journal of the American Ceramic Society** 93: 1372.

Giannozzi, P. and Baroni, S. (1994). Vibrational and dielectric properties of C60 from density-functional perturbation theory. **The Journal of Chemical Physics** 100: 8537.

Gonze, X. (2005). A brief introduction to the ABINIT software package. In Zeitschrift für Kristallographie. **Crystalline Materials** 220: 558.

Gou, Q., Wu, J., Li, A., Wu, B., Xiao, D. and Zhu, J. (2012). Enhanced d_{33} value of $Bi_{0.5}Na_{0.5}TiO_3$–$(Ba_{0.85}Ca_{0.15})(Ti_{0.90}Zr_{0.10})O_3$ lead-free ceramics. **Journal of Alloys and Compounds** 521: 4.

Graeme, H., Blas, P. U. and Hannes, J. (2000). A climbing image nudged elastic band method for finding saddle points and minimum energy paths. **The Journal of Chemical Physics** 113: 9901.

Graeme, H. and Hannes, J. (2000). Improved tangent estimate in the nudged elastic band method for finding minimum energy paths and saddle points. **The Journal of Chemical Physics** 113: 9978.

Gupta, F., Brillant, G. and Pasturel, A. (2007). Correlation effects and energetics of point defects in uranium dioxide: a first principle investigation. **Philosophical Magazine** 87: 2561.

Hagelin-Weaver, H. A., Weaver, J. F., Hoflund, G. B. and Salaita, G. N. (2004). Electron energy loss spectroscopic investigation of Ni metal and NiO before and after surface reduction by Ar^+ bombardment. **Journal of Electron Spectroscopy and Related Phenomena** 134: 139.

Harrison, N. (2003). An introduction to density functional theory. **nato science series sub series III computer and systems sciences** 187: 45.

Hedin, L. and Lundqvist, S. (1970). Effects of electron-electron and electron-phonon interactions on the one-electron states of solids. **Solid state physics** 23: 1.

Henkelman, G. and Jónsson, H. (2000). Improved tangent estimate in the nudged elastic band method for finding minimum energy paths and saddle points. **The Journal of Chemical Physics** 113: 9978.

Henkelman, G., Uberuaga, B. P. and Jónsson, H. (2000). A climbing image nudged elastic band method for finding saddle points and minimum energy paths. **The Journal of Chemical Physics** 113: 9901.

Hlaing Oo, W. M., Tabatabaei, S., McCluskey, M. D., Varley, J. B., Janotti, A. and Van de Walle, C. G. (2010). Hydrogen donors in SnO_2 studied by infrared spectroscopy and first-principles calculations. **Physical Review B** 82: 193201.

Holloway, P. H. (2009). **Characterization of metals and alloys**. Momentum Press.

Houde, D., Lépine, Y., Pépin, C., Jandl, S. and Brebner, J. L. (1987). High-resolution infrared spectroscopy of hydrogen impurities in strontium titanate. **Physical Review B** 35: 4948.

Huber, K. P. (2013). **Molecular spectra and molecular structure: IV. Constants of diatomic molecules**. Springer Science & Business Media.

Iwazaki, Y., Suzuki, T. and Tsuneyuki, S. (2010). Negatively charged hydrogen at oxygen-vacancy sites in $BaTiO_3$: Density-functional calculation. **Journal of Applied Physics** 108: 083705.

Jain, T. A., Chen, C. C. and Fung, K. Z. (2009). Effects of $Bi_4Ti_3O_{12}$ addition on the microstructure and dielectric properties of modified $BaTiO_3$ under a reducing atmosphere. **Journal of the European Ceramic Society** 29: 2595.

Janak, J. (1978). Proof that $\partial E/\partial n_i = \varepsilon$ in density-functional theory. **Physical Review B** 18: 7165.

Janotti, A., Bjaalie, L., Gordon, L. and Van de Walle, C. G. (2012). Controlling the density of the two-dimensional electron gas at the $SrTiO_3/LaAlO_3$ interface. **Physical Review B** 86: 241108.

Janotti, A. and Van de Walle, C. G. (2007). Native point defects in ZnO. **Physical Review B** 76: 165202.

Jia, Q. X., Chang, L. H. and Anderson, W. A. (1994). Surface and interface properties of ferroelectric $BaTiO_3$ thin films on Si using RuO_2 as an electrode. **Journal of Materials Research** 9: 2561.

Johansson, B. and Mårtensson, N. (1980). Core-level binding-energy shifts for the metallic elements. **Physical Review B** 21: 4427.

Johnsson, M. and Lemmens, P. (2007). Crystallography and chemistry of perovskites. **Handbook of magnetism and advanced magnetic materials**.

Johnsson, M. and Lemmens, P. (2008). Perovskites and thin films—crystallography and chemistry. **Journal of physics: condensed matter** 20: 264001.

Jones, G. O. and Thomas, P. A. (2000). The tetragonal phase of $Na_{0.5}Bi_{0.5}TiO_3$ – a new variant of the perovskite structure. **Acta Crystallographica Section B** 56: 426.

Jones, R. O. and Gunnarsson, O. (1989). The density functional formalism, its applications and prospects. **Reviews of Modern Physics** 61: 689.

Jung, Y.-S., Na, E.-S., Paik, U., Lee, J. and Kim, J. (2002). A study on the phase transition and characteristics of rare earth elements doped $BaTiO_3$. **Materials Research Bulletin** 37: 1633.

Kapphan, S., Koppitz, J. and Weber, G. (1980). O-D and O-H stretching vibrations in monodomain $SrTiO_3$. **Ferroelectrics** 25: 585

King, P. D. C., Lichti, R. L., Celebi, Y. G., Gil, J. M., Vil, atilde, o, R. C., Alberto, H. V., Piroto Duarte, J., Payne, D. J., Egdell, R. G., McKenzie, I., McConville, C. F., Cox, S. F. J. and Veal, T. D. (2009). Shallow donor state of hydrogen in In_2O_3 and SnO_2: Implications for conductivity in transparent conducting oxides. **Physical Review B** 80: 081201.

Klauer, S. and Wohlecke, M. (1992). Local symmetry of hydrogen in cubic and tetragonal $SrTiO_3$ and $KTaO_3$:Li determined by polarized Raman scattering. **Physical Review Letters** 68: 3212.

Kleemann, W., Shvartsman, V. V., Bedanta, S., Borisov, P., Tkach, A. and Vilarinho, P. M. (2008). (Sr,Mn)TiO_3 a magnetoelectrically coupled multiglass. **Journal of Physics: Condensed Matter** 20: 434216.

Kohan, A. F., Ceder, G., Morgan, D. and Van de Walle, C. G. (2000). First-principles study of native point defects in ZnO. **Physical Review B** 61: 15019.

Kohn, W. and Sham, L. J. (1965). Self-Consistent Equations Including Exchange and Correlation Effects. **Physical Review** 140: A1133.

Koningsberger, D. and Prins, R. (1988). X-ray absorption: principles, applications, techniques of EXAFS, SEXAFS, and XANES.

Kotani, T. and van Schilfgaarde, M. (2010). Fusion of the LAPW and LMTO methods: The augmented plane wave plus muffin-tin orbital method. **Physical Review B** 81: 125117.

Kresse, G. and Furthmüller, J. (1996). Efficiency of ab-initio total energy calculations for metals and semiconductors using a plane-wave basis set. **Computational Materials Science** 6: 15.

Kresse, G. and Furthmüller, J. (1996). Efficient iterative schemes for ab initio total-energy calculations using a plane-wave basis set. **Physical Review B** 54: 11169.

Kresse, G. and Hafner, J. (1993). Ab initio molecular dynamics for liquid metals. **Physical Review B** 47: 558.

Kresse, G. and Hafner, J. (1994). Norm-conserving and ultrasoft pseudopotentials for first-row and transition-elements. **Journal of Physics Condensed Matter** 6: 8245.

Kresse, G. and Hafner, J. (1994). Norm-conserving and ultrasoft pseudopotentials for first-row and transition elements. **Journal of physics: condensed matter** 6: 8245.

Kresse, G. and Hafner, J. (1994). Ab initio molecular-dynamics simulation of the liquid-metal amorphous-semiconductor transition in germanium. **Physical Review B** 49: 14251.

Kresse, G. and Joubert, D. (1999). From ultrasoft pseudopotentials to the projector augmented-wave method. **Physical Review B** 59: 1758.

Kun, Z., Kui-juan, J., Yanhong, H., Songqing, Z., Huibin, L., Meng, H., Zhenghao, C., Yueliang, Z. and Guozhen, Y. (2006). Ultraviolet fast-response photoelectric effect in tilted orientation $SrTiO_3$ single crystals. **Applied Physics Letters** 89: 173507.

Lavrov, E. V., Weber, J., ouml, rrnert, F., Van de Walle, C. G. and Helbig, R. (2002). Hydrogen-related defects in ZnO studied by infrared absorption spectroscopy. **Physical Review B** 66: 165205.

Lee, J. and Demkov, A. A. (2008). Charge origin and localization at the n-type $SrTiO_3/LaAlO_3$ interface. **Physical Review B** 78: 193104.

Lemanov, V. V., Smirnova, E. P., Sotnikov, A. V. and Weihnacht, M. (2003) Dielectric relaxation in $SrTiO_3$: Mn. **Physics of the Solid State** 46: 1442.

Lemanov, V. V., Smirnova, E. P., Syrnikov, P. P. and Tarakanov, E. A. (1996). Phase transitions and glasslike behavior in $Sr_{1-x}Ba_xTiO_3$. **Physical Review B** 54: 3151.

Levin, I., Krayzman, V., Woicik, J. C., Tkach, A. and Vilarinho, P. M. (2010). X-ray absorption fine structure studies of Mn coordination in doped perovskite SrTiO3. **Applied Physics Letters** 96: 052904.

Li, Q., Wang, B., Woo, C. H., Wang, H. and Wang, R. (2007). First-principles study on the formation energies of intrinsic defects in $LiNbO_3$. **Journal of Physics and Chemistry of Solids** 68: 1336.

Li, X.-B., Limpijumnong, S., Tian, W. Q., Sun, H.-B. and Zhang, S. B. (2008). Hydrogen in ZnO revisited: Bond center versus antibonding site. **Physical Review B** 78: 113203.

Li, Y., Chen, W., Zhou, J., Xu, Q., Sun, H. and Xu, R. (2004). Dielectric and piezoelecrtic properties of lead-free $(Na_{0.5}Bi_{0.5})TiO_3$–$NaNbO_3$ ceramics. **Materials Science and Engineering: B** 112: 5.

Li, Y., Phattalung, S. N., Limpijumnong, S., Kim, J. and Yu, J. (2011). Formation of oxygen vacancies and charge carriers induced in the n-type interface of a $LaAlO_3$ overlayer on $SrTiO_3$ 001. **Physical Review B** 84: 245307.

Limpijumnong, S., Li, X., Wei, S.-H. and Zhang, S. B. (2005). Substitutional diatomic molecules NO, NC, CO, N_2, and O_2: Their vibrational frequencies and effects on p doping of ZnO. **Applied Physics Letters** 86: 211910.

Limpijumnong, S., Reunchan, P., Janotti, A. and Van de Walle, C. G. (2009). Hydrogen doping in indium oxide: An ab initio study. **Physical Review B** 80: 193202.

Limpijumnong, S., Rujirawat, S., Boonchun, A., Smith, M. and Cherdhirunkorn, B. (2007). Identification of Mn site in Pb(Zr, Ti)O_3 by synchrotron x-ray absorption near-edge structure: Theory and experiment. **Applied Physics Letters** 90: 103113.

Limpijumnong, S., Smith, M. F. and Zhang, S. B. (2006). Characterization of As-doped, p-type ZnO by x-ray absorption near-edge structure spectroscopy: Theory. **Applied Physics Letters** 89: 222113.

Limpijumnong, S. and Van de Walle, C. G. (2004). Diffusivity of native defects in GaN. **Physical Review B** 69: 035207.

Limpijumnong, S. and Zhang, S. B. (2005). Resolving hydrogen binding sites by pressure A first-principles prediction for ZnO. **Applied Physics Letters** 86: 151910.

Lin, D., Xiao, D., Zhu, J. and Yu, P. (2006). Piezoelectric and ferroelectric properties of lead-free $Bi_{(1-y)}Na_{(1-x-y)}Li_{x-0.5}Ba_yTiO_3$ ceramics. **Journal of the European Ceramic Society** 26: 3247.

Lytle, F. W. (1964). X-Ray Diffractometry of Low-Temperature Phase Transformations in Strontium Titanate. **Journal of Applied Physics** 35: 2212.

Maiti, T., Guo, R. and Bhalla, A. S. (2008). Structure-Property Phase Diagram of $BaZr_xTi_{1-x}O_3$ System. **Journal of the American Ceramic Society** 91: 1769.

Martin, R. M. (2004). **Electronic structure: basic theory and practical methods**. Cambridge university press.

Måtensson, N. and Nilsson, A. (1995). On the origin of core-level binding energy shifts. **Journal of Electron Spectroscopy and Related Phenomena** 75: 209.

Mattila, T. and Nieminen, R. M. (1996). Ab initio study of oxygen point defects in GaAs, GaN, and AlN. **Physical Review B** 54: 16676.

Merz, W. J. (1949). The Electric and Optical Behavior of $BaTiO_3$ Single-Domain Crystals. **Physical Review** 76: 1221.

Mete, E., Shaltaf, R. and Ellialtıoğlu, Ş. (2003). Electronic and structural properties of a 4*d* perovskite: Cubic phase of $SrZrO_3$. **Physical Review B** 68: 035119.

Methfessel, M., van Schilfgaarde, M. and Casali, R. (1999) A full-potential LMTO method based on smooth Hankel functions. In Electronic Structure and Physical Properies of SolidsSpringer, pp. 114.

Mills, G., Jonsson, H. and Schenter, G. K. (1995). Reversible work transition state theory: application to dissociative adsorption of hydrogen. **Surface Science** 324: 305.

Miyake, S. and Ueda, R. (1948). On Transitional Region in Phase Change of Barium Titanate. **Journal of the Physical Society of Japan** 3: 177.

Monkhorst, H. J. and Pack, J. D. (1976). Special points for Brillouin-zone integrations. **Physical Review B** 13: 5188.

Moriwake, H. (2004). First-principles calculation of formation energy of neutral point defects in perovskite-type $BaTiO_3$. **International Journal of Quantum Chemistry** 99: 824.

Moura, F., Simões, A. Z., Stojanovic, B. D., Zaghete, M. A., Longo, E. and Varela, J. A. (2008). Dielectric and ferroelectric characteristics of barium zirconate titanate ceramics prepared from mixed oxide method. **Journal of Alloys and Compounds** 462: 129.

Müller, K. A. and Burkard, H. (1979). $SrTiO_3$: An intrinsic quantum paraelectric below 4 K. **Physical Review B** 19: 3593.

Nilsson, A. and Pettersson, L. G. M. (2004). Chemical bonding on surfaces probed by X-ray emission spectroscopy and density functional theory. **Surface Science Reports** 55: 49.

Niu, C., Shepherd, K., Martini, D., Tong, J., Kelber, J., Jennison, D. and Bogicevic, A. (2000). Cu interactions with α-Al_2O_3 (0001): effects of surface hydroxyl groups versus dehydroxylation by Ar-ion sputtering. **Surface Science** 465: 163.

Northrup, J. E. and Zhang, S. B. (1993). Dopant and defect energetics: Si in GaAs. **Physical Review B** 47: 6791.

Norton, P., Tapping, R. and Goodale, J. (1977). A photoemission study of the interaction of Ni (100),(110) and (111) surfaces with oxygen. **Surface Science** 65: 13.

Nyberg, M., Luo, Y., Triguero, L., Pettersson, L. G. and Ågren, H. (1999). Core-hole effects in X-ray-absorption spectra of fullerenes. **Physical Review B** 60: 7956.

Ohno, K., Esfarjani, K. and Kawazoe, Y. (2012). **Computational materials science: from ab initio to Monte Carlo methods**. Springer Science & Business Media.

Ohtomo, A. and Hwang, H. Y. (2004). A high-mobility electron gas at the $LaAlO_3/SrTiO_3$ heterointerface. **Nature** 427: 423.

Orlando Auciello, J. F. S., Ramamoorthy Ramesh (1998) The Physics of Ferroelectric Memories. Vol. 51 Physic Toda, pp. 22.

Parija, B., Badapanda, T., Senthil, V., Rout, S. K. and Panigrahi, S. (2012). Diffuse phase transition, piezoelectric and optical study of $Bi_{0.5}Na_{0.5}TiO_3$ ceramic. **Bull Mater Sci** 35: 197.

Payne, B., Biesinger, M. and McIntyre, N. (2009). The study of polycrystalline nickel metal oxidation by water vapour. **Journal of Electron Spectroscopy and Related Phenomena** 175: 55.

Payne, B., Biesinger, M. and McIntyre, N. (2012). Use of oxygen/nickel ratios in the XPS characterisation of oxide phases on nickel metal and nickel alloy surfaces. **Journal of Electron Spectroscopy and Related Phenomena** 185: 159.

Pentcheva, R. and Pickett, W. E. (2006). Charge localization or itineracy at $LaAlO_3$/ $SrTiO_3$ interfaces: Hole polarons, oxygen vacancies, and mobile electrons. **Physical Review B** 74: 035112.

Pentcheva, R. and Pickett, W. E. (2008). Ionic relaxation contribution to the electronic reconstruction at the n-type $LaAlO_3/SrTiO_3$ interface. **Physical Review B** 78: 205106.

Pentcheva, R. and Pickett, W. E. (2009). Avoiding the polarization catastrophe in $LaAlO_3$ overlayers on $SrTiO_3$ (001) through polar distortion. **Physical Review Letters** 102: 107602.

Perdew, J. P., Burke, K. and Ernzerhof, M. (1996). Generalized Gradient Approximation Made Simple. **Physical Review Letters** 77: 3865.

Perdew, J. P., Burke, K. and Ernzerhof, M. (1997). Generalized Gradient Approximation Made Simple [Phys. Rev. Lett. 77, 3865 (1996)]. **Physical Review Letters** 78: 1396.

Perry, C. and McNelly, T. (1967). Ferroelectric" Soft" Mode in $KTaO_3$. **Physical Review** 154: 456.

Popović, Z. S., Satpathy, S. and Martin, R. M. (2008). Origin of the two-dimensional electron gas carrier density at the $LaAlO_3$ on $SrTiO_3$ interface. **Physical Review Letters** 101: 256801.

Preston, A. R. H., Ruck, B. J., Piper, L. F. J., DeMasi, A., Smith, K. E., Schleife, A., Fuchs, F., Bechstedt, F., Chai, J. and Durbin, S. M. (2008). Band structure of ZnO from resonant x-ray emission spectroscopy. **Physical Review B** 78: 155114.

Rao, G. M. and Krupanidhi, S. B. (1994). Study of electrical properties of pulsed excimer laser deposited strontium titanate films. **Journal of Applied Physics** 75: 2604.

Rehr, J. J., Kas, J. J., Prange, M. P., Sorini, A. P., Takimoto, Y. and Vila, F. (2009). Ab initio theory and calculations of X-ray spectra. **Comptes Rendus Physique** 10: 548.

Reinle-Schmitt, M., Cancellieri, C., Li, D., Fontaine, D., Medarde, M., Pomjakushina, E., Schneider, C., Gariglio, S., Ghosez, P. and Triscone, J.-M. (2012). Tunable conductivity threshold at polar oxide interfaces. **Nature communications** 3: 932.

Sata, N., Hiramoto, K., Ishigame, M., Hosoya, S., Niimura, N. and Shin, S. (1996). Site identification of protons in $SrTiO_3$: Mechanism for large protonic conduction. **Physical Review B** 54: 15795.

Scharfschwerdt, R., Mazur, A., Schirmer, O. F., Hesse, H. and Mendricks, S. (1996). Oxygen vacancies in $BaTiO_3$. **Physical Review B** 54: 15284.

Seung-Hee, N. and Ho-Gi, K. (1992). The effect of heat treatment on the $SrTiO_3$ thin films prepared by radio frequency magnetron sputtering. **Journal of Applied Physics** 72: 2895.

Shannon, R. (1976). Revised effective ionic radii and systematic studies of interatomic distances in halides and chalcogenides. **Acta Crystallographica Section A** 32: 751.

Shannon, R. t. (1976). Revised effective ionic radii and systematic studies of interatomic distances in halides and chalcogenides. **Acta Crystallographica Section A: Crystal Physics, Diffraction, Theoretical and General Crystallography** 32: 751.

Shimanouchi, T. (1972). Tables of Molecular Vibrational Frequencies Part 5. **Journal of Physical and Chemical Reference Data** 1: 189.

Springborg, M. (2000). **Methods of electronic-structure calculations**. Wiley Chichester.

Stampfl, C. and Van de Walle, C. G. (1999). Density-functional calculations for III-V nitrides using the local-density approximation and the generalized gradient approximation. **Physical Review B** 59: 5521.

Suchuan, Z., Guorong, L., Aili, D., Tianbao, W. and Qingrui, Y. (2006). Ferroelectric and piezoelectric properties of $(Na, K)_{0.5}Bi_{0.5}TiO_3$ lead free ceramics. **Journal of Physics D: Applied Physics** 39: 2277.

Sundell, P. G., Björketun, M. E. and Wahnström, G. (2007). Density-functional calculations of prefactors and activation energies for H diffusion in $BaZrO_3$. **Physical Review B** 76: 094301.

Sunding, M., Hadidi, K., Diplas, S., Løvvik, O., Norby, T. and Gunnæs, A. (2011). XPS characterisation of in situ treated lanthanum oxide and hydroxide using tailored charge referencing and peak fitting procedures. **Journal of Electron Spectroscopy and Related Phenomena** 184: 399.

T-Thienprasert, J., Klaithong, S., Niltharach, A., Worayingyong, A., Na-Phattalung, S. and Limpijumnong, S. (2011). Local structures of cobalt in Co-doped TiO_2 by synchrotron x-ray absorption near edge structures. **Current Applied Physics** 11: S279.

T-Thienprasert, J., Limpijumnong, S., Du, M. H. and Singh, D. J. (2012). First principles study of O defects in CdSe. **Physica B: Condensed Matter** 407: 2841.

T-Thienprasert, J., Limpijumnong, S., Janotti, A., Van de Walle, C., Zhang, L., Du, M.-H. and Singh, D. J. (2010). Vibrational signatures of O Te and O_{Te}–V_{Cd} in CdTe: A first-principles study. **Computational Materials Science** 49: S242.

T-Thienprasert, J., Rujirawat, S., Klysubun, W., Duenow, J. N., Coutts, T. J., Zhang, S. B., Look, D. C. and Limpijumnong, S. (2013). Compensation in Al-Doped ZnO by Al-Related Acceptor Complexes: Synchrotron X-Ray Absorption Spectroscopy and Theory. **Physical Review Letters** 110: 055502.

T.Okajima, K. Y. a. N. U. (2010). **. Electron Spectroscopy and Related Phenomena** 180.

Takenaka, T., Maruyama, K. and Sakata, K. (1991). $(Bi_{1/2}Na_{1/2})TiO_3$-$BaTiO_3$ System for Lead-Free Piezoelectric Ceramics. **Japanese Journal of Applied Physics** 30: 2236.

Tarun, M. C. and McCluskey, M. D. (2011). Infrared absorption of hydrogen-related defects in strontium titanate. **Journal of Applied Physics** 109: 063706.

Teweldeberhan, A. M. and Fahy, S. (2005). Calculated pressure dependence of the localized vibrational mode of nitrogen in GaN_xAs_{1-x}. **Physical Review B** 72: 195203.

Thiel, S., Hammerl, G., Schmehl, A., Schneider, C. and Mannhart, J. (2006). Tunable quasi-two-dimensional electron gases in oxide heterostructures. **Science** 313: 1942.

Tkach, A., Vilarinho, P. M. and Kholkin, A. (2004). Structural and Dielectric Properties of Mn-Doped Strontium Titanate Ceramics. **Ferroelectrics** 304: 87.

Tkach, A., Vilarinho, P. M. and Kholkin, A. L. (2006). Dependence of dielectric properties of manganese-doped strontium titanate ceramics on sintering atmosphere. **Acta Materialia** 54: 5385.

Tkach, A., Vilarinho, P. M., Nuzhnyy, D. and Petzelt, J. (2010). Sr-and Ti-site substitution, lattice dynamics, and octahedral tilt transition relationship in $SrTiO_3$: Mn ceramics. **Acta Materialia** 58: 577.

Trellakis, A., Zibold, T., Andlauer, T., Birner, S., Smith, R. K., Morschl, R. and Vogl, P. (2006). The 3D nanometer device project nextnano: Concepts, methods, results. **Journal of Computational Electronics** 5: 285.

Valant, M., Kolodiazhnyi, T., Arčon, I., Aguesse, F., Axelsson, A.-K. and Alford, N. M. (2012). The Origin of Magnetism in Mn-Doped $SrTiO_3$. **Advanced Functional Materials** 22: 2114.

Van Benthem, K., Elsässer, C. and French, R. (2001). Bulk electronic structure of $SrTiO_3$: Experiment and theory. **Journal of Applied Physics** 90: 6156.

Van de Walle, C. G. (2000). Hydrogen as a Cause of Doping in Zinc Oxide. **Physical Review Letters** 85: 1012.

Van de Walle, C. G., Limpijumnong, S. and Neugebauer, J. (2001). First-principles studies of beryllium doping of GaN. **Physical Review B** 63: 245205.

Van de Walle, C. G. and Neugebauer, J. (2004). First-principles calculations for defects and impurities: Applications to III-nitrides. **Journal of Applied Physics** 95: 3851.

Vanderbilt, D. (1990). Soft self-consistent pseudopotentials in a generalized eigenvalue formalism. **Physical Review B** 41: 7892.

Wang, H., Wang, B., Li, Q., Zhu, Z., Wang, R. and Woo, C. H. (2007). First-principles study of the cubic perovskites $BiMO_3$ (M= Al, Ga, In, and Sc). **Physical Review B** 75: 245209.

Weber, G., Kapphan, S. and Wohlecke, M. (1986). Spectroscopy of the O-H and O-D stretching vibrations in $SrTiO_3$ under applied electric field and uniaxial stress. **Physical Review B** 34: 8406.

Wei, W. and Sehirlioglu, A. (2012). Strain relaxation analysis of $LaAlO_3/SrTiO_3$ heterostructure using reciprocal lattice mapping. **Applied Physics Letters** 100: 071901.

Wei, X. and Yao, X. (2007). Preparation, structure and dielectric property of barium stannate titanate ceramics. **Materials Science and Engineering: B** 137: 184.

Wemple, S. H. (1970). Polarization Fluctuations and the Optical-Absorption Edge in $BaTiO_3$. **Physical Review B** 2: 2679.

Witek, S., Smyth, D. M. and Piclup, H. (1984). Variability of the Sr/Ti Ratio in $SrTiO_3$. **Journal of the American Ceramic Society** 67: 372.

Wu, X. D., Dijkkamp, D., Ogale, S. B., Inam, A., Chase, E. W., Miceli, P. F., Chang, C. C., Tarascon, J. M. and Venkatesan, T. (1987). Epitaxial ordering of oxide superconductor thin films on (100) $SrTiO_3$ prepared by pulsed laser evaporation. **Applied Physics Letters** 51: 861.

Xie, Y., Bell, C., Yajima, T., Hikita, Y. and Hwang, H. Y. (2010). Charge Writing at the $LaAlO_3/SrTiO_3$ Surface. **Nano Letters** 10: 2588.

Yuan, C. J. Z., Li, S. R. Zhang, X. H. Zhou (2012). High-Temperature Capacitor Based on Ca-Doped $Bi_{0.5}Na_{0.5}TiO_3$-$BaTiO_3$ Ceramics. **J. Electron. Mater** 39: 2471.

Yamada, Y., Shirane, G. and Linz, A. (1969). Study of Critical Fluctuations in $BaTiO_3$ by Neutron Scattering. **Physical Review** 177: 848.

Yang, C., Liu, T., Cheng, Z., Gan, H. and Chen, J. (2012). Study on Mn-doped $SrTiO_3$ with first principle calculation. **Physica B: Condensed Matter** 407: 844.

Yoshii, K., Hiruma, Y., Nagata, H. and Takenaka, T. (2006). **Jpn. J. Appl. Phys.** 45: 4493.

Yu, L. and Zunger, A. (2014). A polarity-induced defect mechanism for conductivity and magnetism at polar-nonpolar oxide interfaces. **arXiv preprint arXiv:1402.0895**.

Yuan, Y., Zhang, S. R., Zhou, X. H., Tang, B. and Li, B. (2009). High-Temperature Capacitor Materials Based on Modified $BaTiO_3$. **Journal of Electronic Materials** 38: 706.

Yuan, Y., Zhou, X. H., Zhao, C. J., Li, B. and Zhang, S. R. (2010). High-Temperature Capacitor Based on Ca-Doped $Bi_{0.5}Na_{0.5}TiO_3$-$BaTiO_3$ Ceramics. **Journal of Electronic Materials** 39: 2471.

Zaid, H., Berger, M. H., Jalabert, D., Walls, M., Akrobetu, R., Fongkaew, I., Lambrecht, W. R. L., Goble, N. J., Gao, X. P. A., Berger, P. and Sehirlioglu, A. (2016). Atomic-resolved depth profile of strain and cation intermixing around $LaAlO_3/SrTiO_3$ interfaces. **Scientific reports** 6: 28118.

Železný, V., Cockayne, E., Petzelt, J., Limonov, M., Usvyat, D., Lemanov, V. and Volkov, A. (2002). Temperature dependence of infrared-active phonons in $CaTiO_3$: a combined spectroscopic and first-principles study. **Physical Review B** 66: 224303.

Zhang, C., Wang, C.-L., Li, J.-C. and Yang, K. (2007). Structural and electronic properties of Fe-doped $BaTiO_3$ and $SrTiO_3$. **Chinese Physics** 16: 1422.

Zhang, L., Zhou, X.-F., Wang, H.-T., Xu, J.-J., Li, J., Wang, E. and Wei, S.-H. (2010). Origin of insulating behavior of the p-type $LaAlO_3/SrTiO_3$ interface: Polarization-induced asymmetric distribution of oxygen vacancies. **Physical Review B** 82: 125412.

Zhong, Z., Xu, P. and Kelly, P. J. (2010). Polarity-induced oxygen vacancies at $LaAlO_3/SrTiO_3$ interfaces. **Physical Review B** 82: 165127.

APPENDIX

APPENDIX

PUBLICATIONS AND PRESENTATION

1. List of publication

Fongkaew, I., Akrobetu, R., Sehirlioglu, A., Vovoedin, A., Limpijumnong, S. and Lambrecht, W. R. L. (2017). Core-level binding energy shifts as a tool to study surface processes on $LaAlO_3/SrTiO_3$, **J. Electron Spectrosc. Relat. Phenom** 218: 21.

Fongkaew, I., T-Thienprasert, J. and Limpijumnong, S. (2017). Identification of Mn site in Mn-doped $SrTiO_3$: First principles study, **Ceramic International**, In press, DOI: doi.org/10.1016/j.ceramint.2017.05.258

Eknapakul, T., Fongkaew, I., Siriroj, S., Vidyasagar, R., Denlinger, J. D., Bawden, L., Mo, S.-K., King, P. D. C., Takagi, H., Limpijumnong, S. and Meevasana, W. (2016). Nearly-free-electron system of monolayer Na on the surface of single-crystal $HfSe_2$, **Physical Review B** 94: 201121(**R**).

Zaid, H., Berger, M. H., Jalabert, D., Walls, M., Akrobetu, R., Fongkaew, I., Lambrecht, W. R. L., Goble, N. J., Gao, X. P. A., Berger, P. and Sehirlioglu, A. (2016). Atomic-resolved depth profile of strain and cation intermixing around $LaAlO_3/SrTiO_3$ interfaces. **Scientific reports** 6: 28118.

Fongkaew, I., Limpijumnong, S. and Lambrecht, W. R. (2015). Effects of structural relaxation, interdiffusion, and surface termination on two-dimensional electron gas formation at the $LaAlO_3/SrTiO_3$ (001) interface. **Physical Review B** 92: 155416.

Fongkaew, I., T-Thienprasert, J. and Limpijumnong, S. (2015). First principles study of Ca in $BaTiO_3$ and $Bi_{0.5}Na_{0.5}TiO_3$. **Philosophical Magazine** 95: 3785.

T-Thienprasert, J., Watcharatharapong, T., Fongkaew, I., Du, M., Singh, D. and Limpijumnong, S. (2014). Identification of oxygen defects in CdTe revisited: First-principles study. **Journal of Applied Physics** 115: 203511.

Fongkaew, I., Jiraroj, T., Singh, D., Du, M.-H. and Limpijumnong, S. (2013). First principles calculations of Hydrogen-Titanium vacancy complexes in $SrTiO_3$. **Ceramics International** 39: S273.

Jiraroj, T., Fongkaew, I., Singh, D., Du, M.-H. and Limpijumnong, S. (2012). Identification of hydrogen defects in $SrTiO_3$ by first-principles local vibration mode calculations. **Physical Review B** 85: 125205.

2. List of presentation (oral)

Fongkaew, I., T-Thienprasert, J. and Limpijumnong, S. (December 2016). Local structure of Mn impurities in $SrTiO_3$: First principles study. In **The 10th Asian Meeting on Electroceramics (AMEC-2016).** Taipei, Taiwan.

Fongkaew, I., Limpijumnong, S. and Lambrecht, W. R. (March 2015). Electric field and spin-orbit coupling effects on the band structure of monolayer WSe_2. In **The American Physical Society (APS) March meeting 2015**. San Antonio, Texas, USA.

Fongkaew, I., T-Thienprasert, J. and Limpijumnong, S. (May 2016). First Principles study of native defects in $SrTiO_3$. In **Siam Physics Congress SPC 2012.** Ayuttaya, Thailand.

3. List of presentation (poster)

Fongkaew, I., T-Thienprasert, J. and Limpijumnong, S. (November 2013). Local structure of Ca impurity in $BaTiO_3$ by first-principles calculations. **In The 3rd academic conference on natural science for master and Ph.D. students from asean countries (CASEAN 2013)**. Phnom Penh, Cambodia.

Fongkaew, I., T-Thienprasert, J. and Limpijumnong, S. (March 2013). First principles study of Fe impurity in $BaTiO_3$. In **Siam Physics Congress SPC 2013.** Chiang mai, Thailand.

Fongkaew, I., and Limpijumnong, S. (December 2012). First principles study of Ca in $BaTiO_3$ and $(Bi_{0.5}Na_{0.5})TiO_3$. In **The 8th Asian Meeting on Ferroelectrics (AMF-8).** Ameri Hotel Pattaya, Thailand.

Manuscript submitted in Journal of Electron Spectroscopy and Related Phenomena

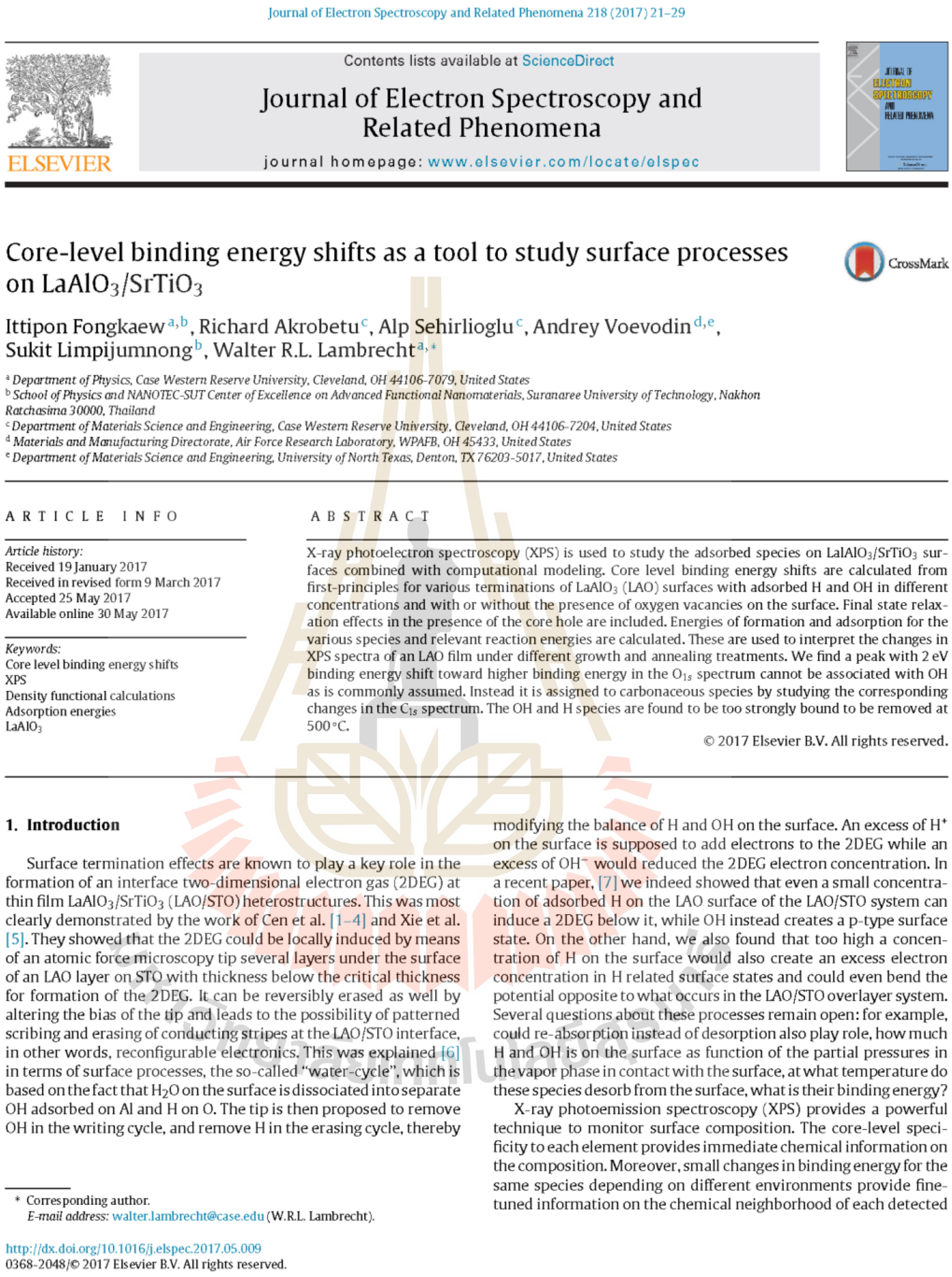

Journal of Electron Spectroscopy and Related Phenomena 218 (2017) 21–29

Contents lists available at ScienceDirect

Journal of Electron Spectroscopy and Related Phenomena

journal homepage: www.elsevier.com/locate/elspec

Core-level binding energy shifts as a tool to study surface processes on $LaAlO_3/SrTiO_3$

Ittipon Fongkaew[a,b], Richard Akrobetu[c], Alp Sehirlioglu[c], Andrey Voevodin[d,e], Sukit Limpijumnong[b], Walter R.L. Lambrecht[a,*]

[a] Department of Physics, Case Western Reserve University, Cleveland, OH 44106-7079, United States
[b] School of Physics and NANOTEC-SUT Center of Excellence on Advanced Functional Nanomaterials, Suranaree University of Technology, Nakhon Ratchasima 30000, Thailand
[c] Department of Materials Science and Engineering, Case Western Reserve University, Cleveland, OH 44106-7204, United States
[d] Materials and Manufacturing Directorate, Air Force Research Laboratory, WPAFB, OH 45433, United States
[e] Department of Materials Science and Engineering, University of North Texas, Denton, TX 76203-5017, United States

ARTICLE INFO

Article history:
Received 19 January 2017
Received in revised form 9 March 2017
Accepted 25 May 2017
Available online 30 May 2017

Keywords:
Core level binding energy shifts
XPS
Density functional calculations
Adsorption energies
$LaAlO_3$

ABSTRACT

X-ray photoelectron spectroscopy (XPS) is used to study the adsorbed species on $LalAlO_3/SrTiO_3$ surfaces combined with computational modeling. Core level binding energy shifts are calculated from first-principles for various terminations of $LaAlO_3$ (LAO) surfaces with adsorbed H and OH in different concentrations and with or without the presence of oxygen vacancies on the surface. Final state relaxation effects in the presence of the core hole are included. Energies of formation and adsorption for the various species and relevant reaction energies are calculated. These are used to interpret the changes in XPS spectra of an LAO film under different growth and annealing treatments. We find a peak with 2 eV binding energy shift toward higher binding energy in the O_{1s} spectrum cannot be associated with OH as is commonly assumed. Instead it is assigned to carbonaceous species by studying the corresponding changes in the C_{1s} spectrum. The OH and H species are found to be too strongly bound to be removed at 500 °C.

1. Introduction

Surface termination effects are known to play a key role in the formation of an interface two-dimensional electron gas (2DEG) at thin film $LaAlO_3/SrTiO_3$ (LAO/STO) heterostructures. This was most clearly demonstrated by the work of Cen et al. [1–4] and Xie et al. [5]. They showed that the 2DEG could be locally induced by means of an atomic force microscopy tip several layers under the surface of an LAO layer on STO with thickness below the critical thickness for formation of the 2DEG. It can be reversibly erased as well by altering the bias of the tip and leads to the possibility of patterned scribing and erasing of conducting stripes at the LAO/STO interface, in other words, reconfigurable electronics. This was explained [6] in terms of surface processes, the so-called "water-cycle", which is based on the fact that H_2O on the surface is dissociated into separate OH adsorbed on Al and H on O. The tip is then proposed to remove OH in the writing cycle, and remove H in the erasing cycle, thereby modifying the balance of H and OH on the surface. An excess of H^+ on the surface is supposed to add electrons to the 2DEG while an excess of OH^- would reduced the 2DEG electron concentration. In a recent paper, [7] we indeed showed that even a small concentration of adsorbed H on the LAO surface of the LAO/STO system can induce a 2DEG below it, while OH instead creates a p-type surface state. On the other hand, we also found that too high a concentration of H on the surface would also create an excess electron concentration in H related surface states and could even bend the potential opposite to what occurs in the LAO/STO overlayer system. Several questions about these processes remain open: for example, could re-absorption instead of desorption also play role, how much H and OH is on the surface as function of the partial pressures in the vapor phase in contact with the surface, at what temperature do these species desorb from the surface, what is their binding energy?

X-ray photoemission spectroscopy (XPS) provides a powerful technique to monitor surface composition. The core-level specificity to each element provides immediate chemical information on the composition. Moreover, small changes in binding energy for the same species depending on different environments provide fine-tuned information on the chemical neighborhood of each detected

---

[*] Corresponding author.
E-mail address: walter.lambrecht@case.edu (W.R.L. Lambrecht).

http://dx.doi.org/10.1016/j.elspec.2017.05.009
0368-2048/© 2017 Elsevier B.V. All rights reserved.

element. For example, atoms at surfaces with different coordination than in the bulk are known to show a surface core-level shift. Similarly, atoms in different valence states typically have different core-level binding energies. For example this allows one to distinguish Ti^{3+} from Ti^{4+}. For the present problem it allows us possibly to distinguish surface oxygen bound to H from bare surface oxygen or oxygen in an OH species bonded to surface Al or O in various carbonaceous species from bulk oxygen.

In the present study we performed experimental XPS studies of both the O_{1s} and C_{1s} core levels as function of growth conditions of the LAO film and annealing conditions. We find a satellite peak in the O_{1s} spectrum at about 2.2 eV higher binding energy from the main peak is removed at about 500 °C. Changes occur also in the C_{1s} spectrum. Concurrently we perform first-principles calculations of the core-level binding energy (CL-BE) shifts to explore how fine-tuned information we can possibly extract from these measurement. We first show that the absolute core-level binding energies can be obtained when properly including core-hole final state effects. Both changes in screening and changes in the electrostatic potential may influence the core level binding energy shifts. We map out the core-level binding energies for different O species and their different near neighborhood environments. Combined with these core-level binding energy calculations, we also calculate the energetics or atomic binding energies to explore the energetic probability of different adsorption/desorption processes. By comparing theory with experiment we will show that the conventional explanation, which associates the 2.2 eV O_{1s} satellite peak with easier removable OH groups from the Al sites than the H from surface O-sites is incompatible with the calculations. Instead we argue that this is related to carbonaceous species containing O, specifically carboxylic acids and possibly esters, physisorbed on the surface.

2. Methods

2.1. Experiment

All the measurements were done on LAO layers deposited on STO substrates using Pulsed Laser Deposition (PLD). For more specific details see Refs. [8,9]. X-ray Photoelectron Spectroscopy (XPS) was conducted at the Air Force Research Laboratory (AFRL) at the Wright Patterson Air Force Base in Dayton, OH. Films grown were exposed to air for at least 24 h in between deposition and XPS measurements. This is typical for the exposure conditions between deposition and subsequent electrical characterization. Thin films grown via PLD were subjected to XPS with a Kratos Axis Ultra spectrometer outfitted with an in situ heated stage. Samples were irradiated with a monochromatic Al*Kα* beam with $h\nu = 1486$ eV in ultra high vacuum (UHV) at close to 10^{-10} Torr. Survey scans for each sample were conducted at a pass energy of 160 eV, while high resolution scans for O1s and C1s were conducted at a pass energy of 20 eV. Samples were also subject to charge compensation to neutralize the positive charge buildup on the irradiated surface.

2.2. Computational approach

The basic underlying theory of our computational method is density functional theory (DFT) in the generalized gradient approximation (GGA), for which we use the Perdew–Burke–Ernzerhof (PBE) parameterization [10,11]. The Vienna Ab-initio Simulation Package (VASP) code [12–14], implementing the projector augmented plane wave method (PAW) [15,16] is used to solve the DFT Kohn–Sham equations. Some calculations are also performed using the full-potential linearized muffin-tin orbital method (FP-LMTO) as implemented by Methfessel and van Schilfgaarde [17,18].

Absolute core level binding energies are not well described by one-electron Kohn–Sham levels. This is because of two reasons: first, the GGA does not exactly cancel the self-energy error, secondly, a core-hole is a local excitation, which is accompanied by screening or final-state effects, often called the core-level relaxation energy. In a many-body perturbation theoretical framework, these could be described by the self-energy operator, for example in the *GW* approximation [19]. An alternative is to exploit the local nature of the excitation, treating it as an impurity and thus calculating the excitation energy directly as a difference between two total energies. This is called the ΔSCF approach. The core level binding energy in this approach is given by

$$\begin{aligned} E_B(i) &= E(N-1,i) - E(N), \\ &= \int_1^0 \epsilon_i(n_i)dn_i, \\ &\approx \epsilon_i(1/2), \\ &\approx \frac{\epsilon_i(1)+\epsilon_i(0)}{2}. \end{aligned} \tag{1}$$

Here $E(N-1, i)$ is the total energy of the $N-1$ electron system with the electron removed from state i, $E(N)$ is the ground state total energy of the N-electron system. We used Janak's theorem [20], according to which $\epsilon_i = \partial E/\partial n_i$, with $\epsilon_i(n_i)$ the one-particle Kohn–Sham energy level viewed as a function of the occupation number n_i of that level. This leads to Slater's transition state $\epsilon_i(1/2)$ or using the average of the core level energy with and without core hole as an approximation for the binding energy. In an all-electron method, we can explicitly create the core hole. We have done this with the FP-LMTO approach [17], as implemented in the lm-suite [21]. In this approach, when a core-hole is created, an electron is added to the lowest available empty state, i.e. the conduction band minimum (CBM), to preserve charge neutrality. The core-level binding energy calculated from this total energy difference clearly corresponds to the excitation of the electron from the core state to the CBM. This means the proper energy reference level to be used is the CBM. The total energies do not depend on the reference level for the potential because both the one-electron levels and effective potential use the same reference and thus it cancels out when calculating the total kinetic energy from $T = \sum_i^{occ} \epsilon_i - \int d^3r\ n(\mathbf{r})v_{eff}(\mathbf{r})$. However, the one-electron levels ϵ_i do depend on the reference level. Commonly this is chosen as the average electrostatic potential, volume averaged over the unit cell. To compare with the total energy difference, both need to be referred to the same reference level. Thus we need to shift the reference energy from the average electrostatic potential to the CBM in order to compare the two expressions. Using this approach we get the O_{1s} core level binding energy to be 540.0 eV relative to the CBM reference level, either directly from the total energy difference or from the Janak theorem approximations.

Alternatively, one can represent the system with core-hole by means of the $Z+1$ approximation in the projector augmented wave (PAW) method. In the PAW method after the valence electrons have been made self-consistent for the atom placed in a specific environment (but keeping core-electrons frozen) one can reconstruct the actual potential inside the atomic sphere and calculate its Kohn–Sham core levels and hence determine ϵ_i. In the VASP code, the reference level for the core levels is again the average electrostatic potential. Shifting to the CBM as reference level, we obtain 540.4 eV in close agreement with the LMTO all-electron approach.

We note that this absolute core level binding energy is different from the experimental value, which for the LAO system is at about 530 eV. This however reflects just a change in reference level. The absolute zero of energy in the experimental XPS electron kinetic energy does not correspond to the CBM of LAO but to the Fermi

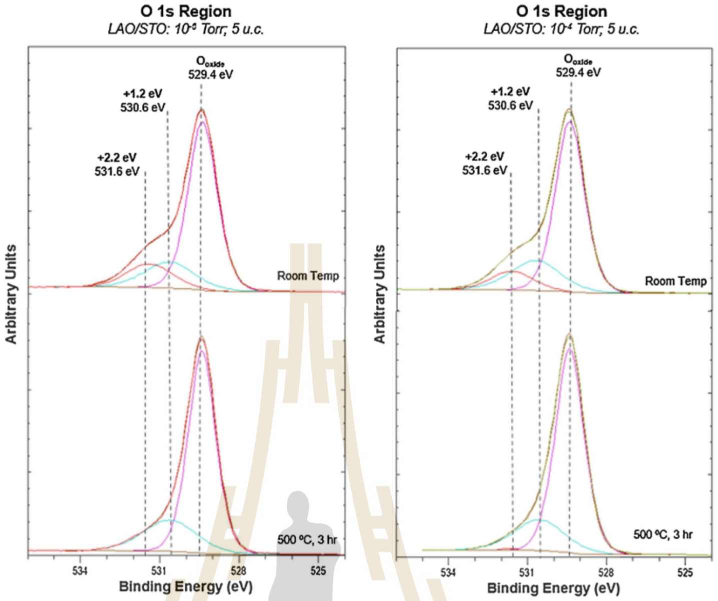

Fig. 1. XPS spectra of LAO films grown at 10^{-6} Torr (left) and 10^{-4} Torr (right) before (top) and after (bottom) annealing at 500 °C.

level of the sample holder. From here on, we will focus entirely on core level binding energy shifts. Specifically, we will compare all core-level binding energies to that of the center layer O atom in our LAO slab.

Core level binding energy (CL-BE) shifts arise from two effects: first, the electrostatic potential can vary from site to site, depending on the local charge state and chemical environment, second the screening of the core hole in the final state can vary. For example for atoms at the surface or in adsorbed species sticking of the surface, there are fewer nearest neighbors around to contribute to the screening. Therefore, even for CL-BE shifts, not just the absolute energies, it is important to include the final state core-hole effects. When comparing core level shifts from different systems, a more suitable reference level is the vacuum level. Thus for loosely bound or physisorbed species such as carbonaceous species, we will use the CL-BE relative to the vacuum level of the molecules calculated separately. We then align the vacuum level with that of the LAO slab to determine the CL-BE of O atoms in the molecules relative to that of the O in the middle of the slab in bulk-like LAO. To this end we also need to determine the position of the CBM in our LAO slab relative to the vacuum electrostatic potential.

In the case of physisorbed molecules, we found, it is more suitable to use only initial state core-level shifts. In fact, in the weakly bound molecules, the core-level extraction is not compensated by a screening electron being added to the lowest unoccupied molecular orbital (LUMO) as our VASP calculations would assume. Instead, the molecule really becomes ionized as charge transfer from the solid system to the molecule is not facilitated so easily. We will compare binding energies of the C_{1s} core levels in various functional groups in molecules relative to those in C bonded only to C or H in two ways: either assuming an electron is transferred to the LUMO and using the final state effect or simply using only initial state shifts We will show that the latter gives better agreement with experiment. The same approximation is thus used for the O_{1s} core level shifts in the physisorbed molecules.

Further details of our computational method are as follows. We use a symmetric 4.5 layer LAO slab, meaning 4 layers of AlO_2 and 5 of LaO, with AlO_2 surface terminations, with a 3 × 3 surface unit cell. The in-plane lattice constant is fixed at the PBE relaxed lattice constant of bulk $LaAlO_3$. The interplanar distances as well as any other atomic coordinates are fully relaxed. A vacuum region of 20 Å thick separates the slabs in the periodic boundary condition model. For various absorption models we adsorb the same species on both surfaces. The pure LAO slab contains 207 atoms. A plane wave cut-off 500 eV, sufficient to deal with the deepest O PAW potentials is adopted and a 3 × 3 × 1 Monkhorst–Pack **k**-point mesh is used to sample the Brillouin zone. We have also used a LAO/STO/LAO slab model with 3 LAO layers on either side of a STO slab, as used previously in Ref. [7].

3. Results

3.1. Experiment and initial discussion

Four films of different thicknesses, 2 unit cells and 5 unit cells, grown at different oxygen partial pressures, 1×10^{-4} Torr and 1×10^{-6} Torr, each, were analyzed at both room temperature and up to temperatures of 1000 °C. The spectra are of two representative samples are shown in Fig. 1.

All spectra can be deconvoluted into a main peak and two satellite peaks on the higher binding energy side, a 2.2 eV and 1.2 eV satellite. The reduction of the +2.2 eV shoulder of each O1s peak was observed at 500 °C, with a near-total reduction of the shoulder after 3 h. No significant further changes to the reduced O1s peak

Table 1
Binding energies (B.E.) in eV and atomic concentrations in % of the relevant deconcoluted peaks.

Temp.	p_{O_2}		O-oxide	+1.2 eV	+2.2 eV	C_{1s}
Room	10^{-6}	B.E.	529.44	530.50	531.28	284.8
		Atm. %	34.09	9.06	9.66	18.74
	10^{-4}	B.E.	529.39	530.65	531.38	284.8
		Atm %	29.92	8.97	6.11	29.38
500 °C	10^{-6}	B.E.	529.47	530.65		284.8
		Atm %	40.20	12.06	0.00	16.02
	10^{-4}	B.E.	529.40	530.65		284.8
		Atm %	38.97	10.36	0.00	21.87

were observed even after heating to 1000 °C. An overview of the relevant peak positions and their corresponding concentrations as determined from the survey scan are given in Table 1.

A tentative initial interpretation of these data is that OH groups bonded to Al would be less strongly bonded to the surface than H on the surface O. The 2.2 eV-peak would then be associated with OH groups and the 1.2 eV peak with surface O bonded to H. A similar interpretation has been given in literature [22–25]. These arise from the decomposition of H_2O and thus one would assume there to be equal amounts of OH and H on the surface and most likely a fairly high surface coverage. One may note that the 2.2 eV peak is stronger relative to the 1.2 eV peak in the 10^{-6} Torr sample. In the latter, one would expect there to be more oxygen vacancies, including on the surface. This would imply that some of the OH from the decomposition of H_2O could fit into an oxygen vacancy and thus be indistinguishable from a surface O with adsorbed H. This would be expected to reduce the Al–OH related peak. However, this prediction is in contradiction with the interpretation, discussed above.

In addition, higher core-level binding energies have been related to formation of oxides with cations in their higher oxidation state (e.g., instead of NiO, Ni_2O_3) [26] which are sometimes also described as defective oxides. This term here corresponds to oxides with cation vacancies where oxygen atoms are adjacent to Ni vacancies [27,25,28]. These peaks were also related to the hydride form of the oxides (e.g. $NiOH_{0.2}$) [26]. This corresponds to H adsorbed on the surface oxygen as we study here. In LAO, neither A-site cations (La) nor B-site cations (with Al forming the surface layer) change valence and no structural change associated with different oxidation state is observed. Generally, deposition at 10^{-4} Torr results in compositions with no detectable oxygen vacancies per our past EELS (Energy Electron Loss Spectroscopy) study [8] which provides more unambiguous results in comparison with XPS if two different oxides and suboxides exist [26]. At 10^{-6} Torr, however, the deposited films have greater amount of oxygen vacancies. In these heterointerfaces, the charge associated with the oxygen vacancies are believed to be compensated by a change in the valence of Ti cations near the interface as Ti-3*d* orbitals form the conduction band. Furthermore, below we study the O-corelevel shifts at oxygens close to an oxygen vacancy and will show that this cannot account for the observed shifts.

In the remainder of the paper, we scrutinize this interpretation in various ways. First, we calculate the bonding energies of various species on the surface to compare the bonding strength of H on surface O (O_s—H) with that of OH on Al. We will show that indeed the latter is slightly weaker bound. However, both are bonded rather strongly, compared to k_BT at 500 °C. Secondly, we calculate the core-level binding energies and find that when the surface is highly covered, Al_s-OH and O_s—H have similar CL-BE shifts closer to 1.2 eV than to 2.2 eV. We then hypothesize that the latter may arise from carbonaceous O, i.e. oxygen occurring in organic molecules physisorbed on top of the surface, already covered with H and OH. To test this hypothesis, we measure the C_{1s} region of the spectrum and study its changes under the same annealing conditions.

The C_{1s} spectra before and after annealing are shown in Fig. 2. The C_{1s} spectra show a main peak at about 284.8 eV, associated with C bonded only to other C or H, and several high binding energy satellites, corresponding to C bonded to O in different types of functional groups, which can be interpreted following Payne et al. [29]. We also test this interpretation by performing calculations of the core-level shifts for C_{1s} and O_{1s} in various types of organic molecules. More detail on this are discussed later in the paper.

3.2. Energies of formation and adsorption

In this section we report our findings on total energies of formation, atomic binding energies and reaction energies. It is important to emphasize the difference between the term binding energy in this section, which refers to the binding energy of molecules or atoms, from the term core-level binding energy (CL-BE) in the next section, which refers to an electron-binding energy. We started by studying various models of water adsorption on the LAO surface. Binding energies need to be referred to appropriate reference chemical potentials. For example, we may define the binding energy of H_2O adsorbed on the Al by

$$E_B(\mathrm{H_2O}) = \frac{[E(\mathrm{LAO+H_2O}) - E(\mathrm{LAO}) - 2\mu_{\mathrm{H_2O}}]}{2} \tag{2}$$

Here $E(\mathrm{LAO+H_2O})$ is the total energy of the system with an H_2O molecule adsorbed on one of the Al on both surfaces of the slab, $E(\mathrm{LAO})$ is the total energy of the bare LAO slab and $\mu_{\mathrm{H_2O}}$ is the total energy of a H_2O molecule. Absolute chemical potentials are used in conjunction with total energies for the slabs. Alternatively, we can already subtract the reference energies of all the free atoms from the total energies and also in the definition of the chemical potentials. Similarly, for OH adsorption, we may define the binding energy as:

$$E_B(\mathrm{OH}) = \frac{[E(\mathrm{LAO+OH}) - E(\mathrm{LAO}) - 2\mu_{\mathrm{OH}}]}{2} \tag{3}$$

and for H adsorption,

$$E_B(\mathrm{H}) = \frac{[E(\mathrm{LAO+H}) - E(\mathrm{LAO}) - 2\mu_{\mathrm{H}}]}{2}. \tag{4}$$

The question is: what to use as chemical potentials for H and OH? Rather than using a H_2 molecule, which would be appropriate for a reducing H_2 atmosphere, we assume that the surfaces are in contact with moist air, which contains O_2 and H_2O. We thus assume that H atoms desorbing from the surface would immediately react with O_2 and form H_2O. That means we assume

$$\mu_H = \frac{1}{2}\left(\mu_{\mathrm{H_2O}} - \frac{1}{2}\mu_{\mathrm{O_2}}\right) \tag{5}$$

Similarly, we assume

$$\mu_{\mathrm{OH}} = \mu_{\mathrm{H_2O}} - \mu_H = \frac{1}{2}\mu_{\mathrm{H_2O}} + \frac{1}{4}\mu_{\mathrm{O_2}} \tag{6}$$

These equations give $\mu_H = -4.79$ eV whereas $\mu_H(\mathrm{H_2}) = -3.34$ eV. So, H has about 1.45 eV lower chemical potential than in a H_2 molecule and is hence much less reactive. For OH, we find $\mu_{\mathrm{OH}} = -10.03$ eV, in other words, a lower energy by 2.28 eV than the OH molecule, unlikely to occur as a separate species. The energy of the OH molecule was indeed calculated to be −7.75 eV. One could go beyond this treatment by considering the chemical potential of oxygen to contain a term $-k_BT \ln p_{O_2}$ and thus take in to account the different chemical environments.

When considering combined adsorption of OH and H on different sites, we have the choice of defining the binding energy with respect to the H_2O molecule or with respect to already separated

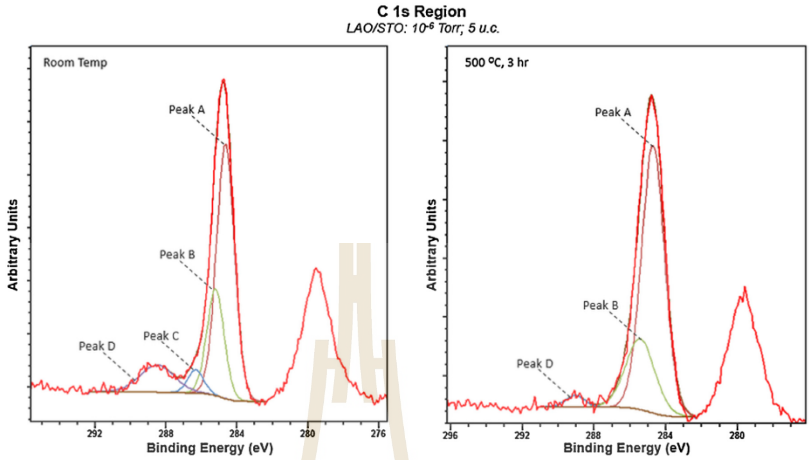

Fig. 2. Carbon 1s core level spectrum at room temperature and after annealing at 500 °C measured on a LAO/STO 5 unit cell layer LAO sample grown at 10^{-6} Torr.

Table 2
Binding energies (in eV) per adsorbed molecule(s) for models shown in Fig. 3 and oxygen vacancy formation energy, with respect to the chemical potential references defined in the text.

Model	Description	E_B
A	H_2O on Al	−2.19
B	Al_s—OH and O_s—H next to each other	−3.08
C	Al_s—O and 2 O_s—H	−1.55
D	Al_s—OH	−0.76
E	O_s—H	−2.25
F1	Al_s—O and O_s—H (close)	−0.78
F2	Al_s—O and O_s—H (far)	0.57
G	surface V_O	−0.21

Table 3
Core-hole binding energy shifts of O-1s state (in eV) relative to center (bulk O) in the LAO slab or center of the STO slab in the LAO/STO/LAO cases. Positive values mean higher binding energy.

Slab	Slab termination	Core-hole site	CL-BE-shift
LAO	Al_s—OH+O_s—H	O_s—H	1.19
		OH—Al_s	0.71
	Al_s—OH	OH—Al_s	0.02
		O_s	−0.68
	Al_s—OH^{-1}	OH—Al_s	1.24
		O_s	0.7
	O_s—H	O_s—H	2.46
		O_s	−0.14
	V_O	O_s	0.10
	V_O+Al_s—OH	OH—Al_s	0.54
		O_s	−0.45
	V_O+O_s—H	O_s—H	3.17
		O_s	−0.04
	COH	O on COH	6.88
		O beneath COH	5.08
	COH with Al_s—OH+O_s—H	O on COH	5.07
		O beneath COH	3.57
LAO/STO	Al_s—OH+O_s—H	O_s—H	1.93
		OH—Al_s	1.16
		O_s	0.14

OH and H species. When comparing with the adsorption of an actual H_2O molecule, it is more convenient to use the same reference species H_2O so that we can directly obtain the reaction energy for the reaction

$$Al_s - H_2O \rightarrow Al_s - OH + O_sH + \Delta E_r \tag{7}$$

The latter will be referred to as the water splitting reaction energy. If $\Delta E_r < 0$ it means the reaction is exothermic and proceeds to the right.

The different models calculated are shown in Fig. 3. The first one (model A) is a H_2O molecule adsorbed on Al. The second (model B) is an OH adsorbed on Al with an H adsorbed on the nearest neighbor O. In model C, we have only O on Al and two separated H on O_s. Model D has only OH adsorbed on Al. In model E we consider a H adsorbed on O only. In model F we consider Al_s-O and O_s—H separated but either close or far from each other. Finally, in model G, we also consider the energy of formation of an oxygen vacancy on the surface. The latter is defined by

$$E_{for}(V_O) = \frac{[E(LAO + 2V_O) - E(LAO) + 2\mu_O]}{2} \tag{8}$$

The binding energies of these models are listed in Table 2 for the choice of chemical potentials discussed above, i.e. under the assumption of equilibrium with O_2 and H_2O.

From these results, we can see that having O bonded to Al_s is not favorable, rather OH stays together on Al_s. We can also see that H_2O wants to split into separate OH on Al_s and H on O_s by 0.89 eV/water molecule. We can also consider the adsorption of OH inside an existing surface oxygen vacancy

$$V_O + OH \rightarrow O_s - H \tag{9}$$

The reaction energy for this process is −2.05 eV. Finally, we note that desorption of OH from Al_s is significantly easier than desorption of H from a surface O_s.

3.3. Core-level binding energy shifts

The calculated CL-BE shifts are given in Table 3. The CL-BE shifts are all calculated relative to those of a core-hole placed in the middle of the corresponding LAO slab. We calculated CL-BE for the O_{1s} core level for the following models. First we consider an LAO slab

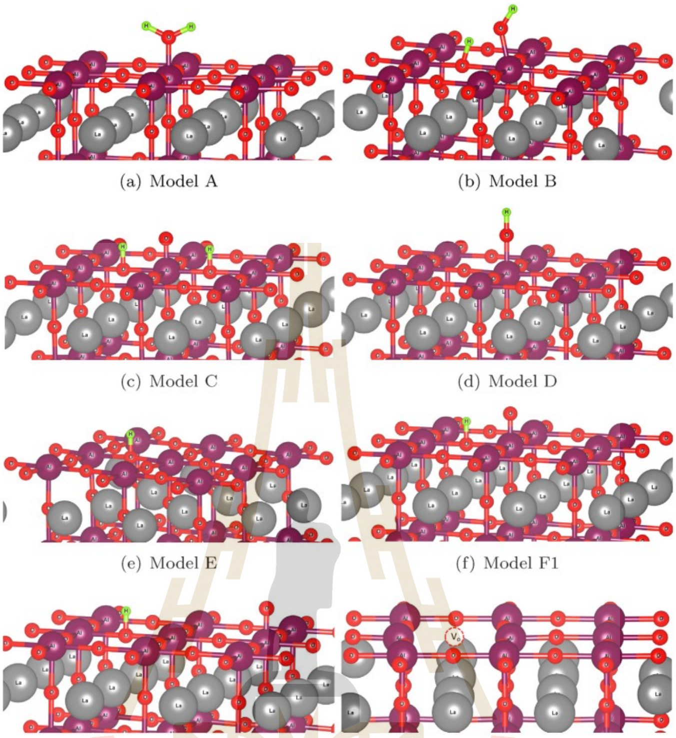
(a) Model A (b) Model B

(c) Model C (d) Model D

(e) Model E (f) Model F1

(g) Model F2 (h) Model G

Fig. 3. Various adsorption models studied.

with adsorbed OH on Al$_s$ and H on O$_s$ next to each other (case B). Core holes were created in the center of the slab, for O in the adsorbed OH molecule and for an O$_s$ with H attached. This represents the case of high coverage where, as we found before, H_2O is assumed to split but OH and H are expected to be found close to each other on the surface. We find both CL-BE of O$_s$—H and OH—Al$_s$ to be near 1 eV but somewhat deeper for the former. Second, we considered OH—Al$_s$ separately and O$_s$—H separately on the surface (cases D and E), corresponding to low coverage. When isolated the O$_s$—H shifts deeper to 2.46 eV, while the OH—Al$_s$ shifts back toward the main CL-BE of bulk O. The only CL-BE close to 2 eV found here, corresponds to O$_s$—H, and in all cases, the O$_s$—H has higher CL-BE than the Al$_s$-OH. This is in clear contradiction with the initial (and commonly made) hypothesis. The role of the H and OH CL-BE seem to be exactly reversed from what we need according to that hypothesis. Also, if OH is preferentially desorbed and the O$_s$—H becomes thereby more isolated than it would shift to higher BE and increase the 2.2 eV peak rather than decreasing it. The fact that both the OH and H correspond to the 1.2 eV peak which is not affected under annealing suggest that the surface stays fully covered with OH and H and that another interpretation must be sought for the 2.2 eV peak.

We also modeled a core hole placed in an O$_s$ without H for comparison with that with H. These O$_s$ without H have only small Cl-BE shifts compared to bulk O.

In addition, we considered the possibility of a negative charge state of the OH adsorbed on Al$_s$ as expected to occur when the Fermi level is high in the gap. This could occur in the presence of a 2DEG at a nearby STO/LAO interface. Note that from our previous work [7], the OH adsorbed on Al$_s$ produces levels just above the VBM and could thus become filled if the Fermi level lies above them. For the isolated Al$_s$-OH, this leads to a shift to higher BE but it is still near 1.24 eV only, so not explaining the 2.2 eV peak. Furthermore, to model the negative charge state, we add a homogeneous background charge density to maintain the system neutral. In a slab calculation, this background extends somewhat unphysically in the vacuum region rather than being confined to the slab. This would possibly overestimate the CL-BE shift due to the charging. For the O$_s$—H and OH—Al$_s$ together, the electrons go from the donor O$_s$—H to the acceptor OH—Al$_s$ and thus the system is overall neutral, so this problem is avoided.

Next, we considered the role of V_O on the surface and place the core hole in a nearby O$_s$ and we also added V_O to the previous models of OH—Al$_s$ and O$_s$—H and examined the changes in core hole

shifts on the latter when the V_O is nearby. Compared to the same cases without V_O the CL-BE shifts seem to increase by the presence of nearby V_O. This seems plausible because V_O should present an attractive electrostatic potential and thus shift levels down to deeper CL-BE. However, these models are still not compatible with the 2.2 eV peak being associated with OH.

Finally, the question may arise if the above results which were obtained on a pure LAO slab would change if we take into account the presence of the nearby 2DEG at an LAO/STO interface. We thus considered explicitly an LAO/STO/LAO with various terminations: OH—Al$_s$ + H—O$_s$, or each separate. In these cases, we calculated the CL-BE shift relative to the O in the middle of the STO layer. This seems to shift the core levels toward slightly lower CL-BE but not enough to explain the 2.2 eV peak.

An alternative origin for the 2.2 eV peak might come from carbonaceous species. In fact, Payne et al. [29] show that molecules with *—COO* groups, that is *—O—C═O* as in carboxylic acids or esters have a relative high binding energy shift. As a first attempt to model O bonded to C bonded to the surface, we considered a COH molecule chemisorbed on the surface. This leads to very high CL-BE either for the O$_s$ underneath them or the O in the molecule itself. They are in excess of 5 eV, and not found in the experiment. From this we conclude that carbonaceous species, if responsible for the 2.2 eV peak should not be directly adsorbed on the surface. Rather, we need to consider physisorbed molecules on the already covered surface. We do that in the next subsection.

3.4. Core-level binding energies in physisorbed molecules

In this subsection, we consider carbonaceous species or H_2O physisorbed on the already OH and H covered LAO surface. To deal with the physisorbed case, we calculate the molecules in a separate calculation, not attached to the surface and align the O_{1s} levels to those in the slab by referring both to the common vacuum level. To test this approach, we first calculate the C_{1s} levels in different molecules. Following Payne et al. [29], we consider different organic groups involving O and compare the C_{1s} CL-BE with those in C only bonded to C or H.

For all carbonaceous isolated molecules, we consider a periodic boundary conditions model with sufficient separation between the molecules and they are treated in the Γ point approximation. Their geometry optimizations are carried out at the PBE level. This is done without any constraints, and the structure are considered relaxed until the Hellmann–Feynmann forces less than 0.01 eV/Å. Periodically repeated images of isolated molecules are separated by 15 Å and the vacuum levels are obtained by plotting the average electrostatic potential in the three directions inside this 15 Å box. We compare the CL-BE shifts calculated either with initial state shift only, or with the procedure used in the previous section. In the latter case, we should note that the core hole is each time compensated by an added electron in the lowest unoccupied molecular orbital (LUMO). In the initial-state-only calculation, the advantage is that no charge is added which closer represents the physical situation, but on the other hand, no changes in screening due to the different molecular environment are not taken into account. In any case, by calculating the LUMO we can refer all BE to the vacuum level.

Table 4
C_{1s} core-level binding energy shifts in different organic groups. The column labeled screened, means CL-BE is calculated from ϵ_{C1s} averaged with and without core-hole and electron added to LUMO, initial means only initial state shift. Experimental values from Payne et al. [29]. For the CH_3 we give the actual calculated CL-BE with respect to vacuum, for the others the shift relative to this one.

Group	Screened	Initial	Expt.
CH_3	291.3	266.1	284.8
C—OH	1.0	1.3	1.5
C—O—C	1.2	1.3	1.5
C═O	0.6	2.6	2.9
O═C—O	1.7	3.6	3.8
CO_3	5.6	6.4	5.5

We consider the following molecules: methyl-alcohol (CH_3-OH), ethyl alcohol (CH_3CH_2-OH); dimethyl ether (CH_3-O-CH_3), diethyl ether (C_2H_5)-O-(C_2H_5); acetone as an example of a ketone (CH_3—(C═O)—CH_3), ester (CH_3—(C═O)—O—CH_3), carboxylic acid (CH_3—(C═O)—O—H) and carbonate CO_3. We then calculate the core-level binding energy in the C in pure CH_3 groups not bonded to any O, and average over the different molecules. Next, we consider the two alcohols and average the C_{1s} CL-BE in the C—OH group. The C—O—C group occurs in both ethers and in the C at the end of the (O═C)—O—C group in the ester. The C in the middle of the (O═C)—O occurs in both the ester R—(O═C)—O—R and the carboxylic acid R—(O═C)—OH and is also averaged. Finally the C═O without an additional O occurs in the ketone.

The results are shown in Table 4. Except for the CO_3 case, the results agree better with experiment for the initial state shift calculation. This is because in the case of the calculation including a final state shift, a charge transfer to the molecule is assumed and this overestimates the screening. We note that the absolute values cannot be directly compared to experiment because they use different reference levels. Clearly the shifts increase with increasing number of O bonded to C or O bonded more strongly (e.g. double bonded) to C. The alcohols and ethers provide different shift because the O is either bonded to another C (O shared between two C) or O is shared between a C and a H. The deviations between different molecules containing the same group are of order a few 0.1 eV, which shows that the idea of associating the shift with different O environments makes sense. In fact the O is expected to pull electrons away from the C and therefore increases the binding energy.

Table 5
Core level binding energy relative to vacuum and core-hole binding energy shifts of O_{1s} state (in eV) in the different molecules relative to center of the slab (already covered with OH and H) in the LAO slab after we align them with the vacuum level (539.05 eV). Positive values mean higher binding energy.

Molecule	Chemical formula	O-site	Screened	shift	Initial	shift
LAO bare ref.			539.05	0.00	505.34	0.00
Water	H_2O		540.39	1.34	506.45	1.11
Methanol	CH_3—OH		539.99	0.94	506.39	1.05
Ethanol	CH_3—CH_2—OH		540.13	1.19	506.4	1.06
Dimethyl ether	CH_3—O—CH_3		540.72	1.68	506.66	1.32
Diethyl ether	CH_3—CH_2—O—CH_2—CH_3		540.71	1.66	506.38	1.04
Ketone	CH_3—(C═O)—CH_3		538.53	−0.50	506.08	0.74
Ester	CH_3—(C═O)—O—CH_3	C═O	538.67	−0.38	505.96	0.62
		C—O—C	540.99	1.94	507.86	2.2
Carboxylic acid	CH_3—(C═O)—O—H	C═O	538.95	−0.10	506.31	0.4
		C—O—H	540.85	1.80	507.70	2.1
Carbonate	CO_3	C═O	541.37	2.32	509.97	4.63
		C—O	541.47	2.42	509.80	4.53

Table 6
Concentrations *c* in % and FWHM *w* (eV) of subpeaks of the C_{1s} spectrum.

Temp (°C)	p_{O_2} (Torr)	A		B		C		D	
		c	*w*	*c*	*w*	*c*	*w*	*c*	*w*
Room Temp	10^{-6}	59.17	1.18	23.69	1.12	4.88	1.04	12.26	2.26
	10^{-4}	63.66	1.12	20.63	1.16	6.35	1.21	9.36	1.91
500	10^{-6}	72.80	1.49	24.54	1.90	0.00	0.00	2.66	1.24
	10^{-4}	76.36	1.33	21.15	1.75	0.00	0.00	2.49	1.22

Next, we consider the corresponding O_{1s} CL-BE shifts. Based on the previous results for C_{1s} shifts, we think the initial state shift calculations are more reliable but nonetheless, we have given both for comparison. We can see that the shifts again have a systematic trend with the number of carbons per oxygen. They are the lowest in the ethers where two C are bonded to the O, then in the alcohol. The shift in the ketone is also small. The largest shifts occur for the carbonate. Shifts of about 2.2 eV occur for the single bonded O in the O═C—O group, either in the ester or the carboxylic acid. These trends agree with the results of Payne et al. [29].

The results suggest that the O_{1s} peak at 2.2 eV shifted from the main peak could be explained by esters or carboxylic acids physisorbed on the LAO surface, already covered by H and OH. The same functional group has a carbon contributing to the D peak in the C_{1s} spectrum (Fig. 2). It also has a carbon corresponding to peak B in the C_{1s} spectrum. Both of these peaks indeed lose intensity under annealing at 500 °C. In Table 6 we summarize concentration and full width at half maximum (FWHM) corresponding to the different subpeaks of the C_{1s} spectrum before and after annealing. The main change in the C_{1s} spectrum actually occurs in the C-peak corresponding to ketones. But as we see in Table 5 the corresponding O peak does not match the 2.2 eV O_{1s} peak. The reduction in the B-peak may have contributions from ethers and alcohols. However, there should be more or less a one-to one match in the D-peak loss and the O_{1s} 2.2 eV peak loss. In order to calibrate quantitatively how much of this 2.2 eV peak can be ascribed to the corresponding loss in D-peak, additional considerations are required. The total C and O loss in the spectrum would have to be normalized in the overview spectrum relative to the La peak, which is assumed to stay unchanged. We have not pursued to carry this out in detail. While the D-peak is reduced upon annealing it does not completely disappear as does the O 2.2 eV peak. Nonetheless, we may conclude that the O_{1s} peak could be ascribed reasonably to esters and carboxylic acid physisorbed on the surface. These molecules being weakly bonded only to the surface, it appears reasonable that they desorb much easier than the chemisorbed H and OH.

Now that we have determined the origin of the 2.2 eV peak in the O_{1s} spectrum as carbonaceous in origin, it is interesting that the amount of such physisorbed species seems to differ depending on the growth conditions of the film. The amount is larger for the 10^{-6} Torr grown samples, which are more conductive because they have a larger concentration of oxygen vacancies. No change is observed depending on the thickness of the LAO film being below or above the critical thickness for formation of a 2DEG. Thus it is not clear that conductivity of the surface plays a role in the amount of carbonaceous species deposited. It appears that under the lower partial pressure of O_2 a higher amount of Carbonaceous species are available in the growth environment, or, possibly, the negatively charged surface oxygen vacancies could locally attract greater amount of atmospheric carbon.

4. Conclusions

In this paper, we combined an experimental XPS study of the adsorbed species on LAO surfaces and their desorption under annealing with calculated analysis of the atomic bonding energies and the core-level binding energies. We showed, that OH is indeed less strongly bonded to the surface than H. However, both are too strongly bonded to explain desorption at 500 °C. The core-level calculations show that the peak shifted to 2.2 eV higher binding energy from the main O peak cannot be due to either OH or surface O with H. Instead it is related to carbonaceous species such as esters and carboxylic acids. Consistent losses in both the C_{1s} and O_{1s} spectra were observed under the same annealing conditions to support this interpretation. In terms of the calculations, we showed core-level binding energy shift calculations require a careful analysis of the reference level questions as well as consideration of the final state screening effects. For the chemisorbed species, we obtained good agreement in a model in which screening changes are included and compensation of the core-hole by electrons added at the lowest empty levels are assumed. For the molecules which are physisorbed, we showed that we can nonetheless align these core level shifts with those on the surface by referring all to a common vacuum level. On the other hand, for the molecules we should not assume a transfer of electrons to the molecule LUMO as this would overestimate the screening effects. Initial state core level shifts in this case provided a better agreement with experimental data.

Acknowledgements

This work was supported by the U.S. Air Force Office of Scientific Research under Grant No. FA9550-12-1-0441. One of the authors (I.F.) was supported by the Development and Promotion of Science and Technology Talents Project (DPST). S.L. and I.F. acknowledge the support from the NANOTEC-SUT Center for Excellence on Advanced Functional Nanomaterials. The calculations used the High Performance Computing Resource in the Core Facility for Advanced Research Computing at Case Western Reserve University. We thank Dr. Michael Jesperson for assistance with the XPS measurements.

References

[1] C. Cen, S. Thiel, G. Hammerl, C.W. Schneider, K.E. Andersen, C.S. Hellberg, J. Mannhart, J. Levy, Nanoscale control of an interfacial metal–insulator transition at room temperature, Nat. Mater. 7 (2008) 298–302, http://dx.doi.org/10.1038/nmat2136.

[2] C. Cen, S. Thiel, J. Mannhart, J. Levy, Oxide nanoelectronics on demand, Science 323 (5917) (2009) 1026–1030, http://dx.doi.org/10.1126/science.1168294, http://www.sciencemag.org/content/323/5917/1026.full.pdf, http://www.sciencemag.org/content/323/5917/1026.abstract.

[3] G. Cheng, P.F. Siles, F. Bi, C. Cen, D.F. Bogorin, C.W. Bark, C.M. Folkman, J.-W. Park, C.-B. Eom, G. Medeiros-Ribeiro, J. Levy, Sketched oxide single-electron transistor, Nat. Nanotechnol. 6 (2011) 343–347, http://dx.doi.org/10.1038/NNANO.2011.56.

[4] G. Cheng, J.P. Veazey, P. Irvin, C. Cen, D.F. Bogorin, F. Bi, M. Huang, S. Lu, C.-W. Bark, S. Ryu, K.-H. Cho, C.-B. Eom, J. Levy, Anomalous transport in sketched nanostructures at the $LaAlO_3/SrTiO_3$ interface, Phys. Rev. X 3 (2013) 011021, http://dx.doi.org/10.1103/PhysRevX.3.011021.

[5] Y. Xie, C. Bell, T. Yajima, Y. Hikita, H.Y. Hwang, Charge writing at the $LaAlO_3/SrTiO_3$ surface, Nano Lett. 10 (7) (2010) 2588–2591, http://dx.doi.org/10.1021/nl1012695, pMID:20518539.

[6] F. Bi, D.F. Bogorin, C. Cen, C.W. Bark, J.-W. Park, C.-B. Eom, J. Levy, Water-cycle mechanism for writing and erasing nanostructures at the $LaAlO_3/SrTiO_3$ interface, Appl. Phys. Lett. 97 (17) (2010), http://dx.doi.org/10.1063/1.3506509 http://scitation.aip.org/content/aip/journal/apl/97/17/10.1063/1.

[7] I. Fongkaew, S. Limpijumnong, W.R.L. Lambrecht, Effects of structural relaxation, interdiffusion, and surface termination on two-dimensional

Manuscript submitted in Journal of Electron Spectroscopy and Related Phenomena

electron gas formation at the laalo$_3$/srtio$_3$ (001) interface, Phys. Rev. B 92 (2015) 155416, http://dx.doi.org/10.1103/PhysRevB.92.155416.

[8] H. Zaid, M. Berger, D. Jalabert, M. Walls, N.G.R. Akrobetu, X. Gao, P. Berger, I. Fongkaew, W.R.L. Lambrecht, A. Sehirlioglu, Atomic-resolved depth profile of strain and cation intermixing around LaAlO$_3$/SrTiO$_3$ interfaces, Sci. Rep. 6 (2016), http://dx.doi.org/10.1038/srep28118.

[9] W. Wei, A. Sehirlioglu, Strain relaxation analysis of LaAlO$_3$/SrTiO$_3$ heterostructure using reciprocal lattice mapping, Appl. Phys. Lett. 100 (7) (2012) 071901, http://dx.doi.org/10.1063/1.3685463.

[10] J.P. Perdew, K. Burke, M. Ernzerhof, Generalized gradient approximation made simple, Phys. Rev. Lett. 78 (1997) 1396, http://dx.doi.org/10.1103/PhysRevLett.78.1396.

[11] J.P. Perdew, K. Burke, M. Ernzerhof, Generalized gradient approximation made simple, Phys. Rev. Lett. 77 (1996) 3865–3868, http://dx.doi.org/10.1103/PhysRevLett.77.3865.

[12] G. Kresse, J. Furthmiiller, Efficiency of ab-initio total energy calculations for metals and semiconductors using a plane-wave basis set, Comput. Mater. Sci. 6 (1996) 15–50, http://dx.doi.org/10.1016/0927-0256(96)00008-0.

[13] G. Kresse, J. Hafner, Norm-conserving and ultrasoft pseudopotentials for first-row and transition elements, J. Phys.: Condens. Matter 6 (40) (1994) 8245 http://stacks.iop.org/0953-8984/6/i=40/a=015.

[14] G. Kresse, D. Joubert, From ultrasoft pseudopotentials to the projector augmented-wave method, Phys. Rev. B 59 (1999) 1758–1775, http://dx.doi.org/10.1103/PhysRevB.59.1758.

[15] P.E. Blöchl, Projector augmented-wave method, Phys. Rev. B 50 (1994) 17953–17979, http://dx.doi.org/10.1103/PhysRevB.50.17953.

[16] G. Kresse, D. Joubert, From ultrasoft pseudopotentials to the projector augmented-wave method, Phys. Rev. B 59 (1999) 1758–1775, http://dx.doi.org/10.1103/PhysRevB.59.1758.

[17] M. Methfessel, M. van Schilfgaarde, R.A. Casali, A full-potential LMTO method based on smooth Hankel functions, in: H. Dreyssé (Ed.), Electronic Structure and Physical Properties of Solids. The Use of the LMTO Method, Vol. 535 of Lecture Notes in Physics, Springer-Verlag, Berlin, 2000, p. 114.

[18] T. Kotani, M. van Schilfgaarde, Fusion of the LAPW and LMTO methods: the augmented plane wave plus muffin-tin orbital method, Phys. Rev. B 81 (12) (2010) 125117, http://dx.doi.org/10.1103/PhysRevB.81.125117.

[19] L. Hedin, S. Lundqvist, Effects of electron-electron and electron–phonon interactions on the one-electron states of solids, in: F. Seitz, D. Turnbull, H. Ehrenreich (Eds.), Solid State Physics, Advanced in Research and Applications, vol. 23, Academic Press, New York, 1969, p. 1-181.

[20] J.F. Janak, Proof that $\frac{\partial e}{\partial n_i} = \epsilon$ in density-functional theory, Phys. Rev. B 18 (1978) 7165–7168, http://dx.doi.org/10.1103/PhysRevB.18.7165.

[21] https://www.questaal.org/.

[22] P. Holloway, P. Vaidyanathan, Characterization of metals and alloys, in: Materials Characterization Series, Momentum Press, 2010.

[23] M. Sunding, K. Hadidi, S. Diplas, O. Løvvik, T. Norby, A. Gunnæs, XPS characterisation of in situ treated lanthanum oxide and hydroxide using tailored charge referencing and peak fitting procedures, J. Electron Spec. Rel. Phenom. 184 (7) (2011) 399–409, http://dx.doi.org/10.1016/j.elspec.2011.04.002 http://www.sciencedirect.com/science/article/pii/S0368204811000727.

[24] C. Niu, K. Shepherd, D. Martini, J. Tong, J. Kelber, D. Jennison, A. Bogicevic, Cu interactions with α-Al$_2$O$_3$(0001): effects of surface hydroxyl groups versus dehydroxylation by Ar-ion sputtering, Surf. Sci. 465 (1–2) (2000) 163–176, http://dx.doi.org/10.1016/S0039-6028(00)00728-7 http://www.sciencedirect.com/science/article/pii/S0039602800007287.

[25] M.C. Biesinger, B.P. Payne, L.W.M. Lau, A. Gerson, R.S.C. Smart, X-ray photoelectron spectroscopic chemical state quantification of mixed nickel metal, oxide and hydroxide systems, Surf. Interface Anal. 41 (4) (2009) 324–332, http://dx.doi.org/10.1002/sia.3026.

[26] P. Norton, R. Tapping, J. Goodale, A photoemission study of the interaction of Ni(100), (110) and (111) surfaces with oxygen, Surf. Sci. 65 (1) (1977) 13–36, http://dx.doi.org/10.1016/0039-6028(77)90289-8 http://www.sciencedirect.com/science/article/pii/0039602877902898.

[27] B.P. Payne, M.C. Biesinger, N.S. McIntyre, Use of oxygen/nickel ratios in the {XPS} characterisation of oxide phases on nickel metal and nickel alloy surfaces, J. Electron Spec. Rel. Phenom. 185 (2012) 159–166, http://dx.doi.org/10.1016/j.elspec.2012.06.008 http://www.sciencedirect.com/science/article/pii/S0368204812000631.

[28] H.A.E. Hagelin-Weaver, J.F. Weaver, G.B. Hoflund, G.N. Salaita, Electron energy loss spectroscopic investigation of Ni metal and NiO before and after surface reduction by Ar+ bombardment, J. Electron Spec. Rel. Phenom. 134 (2004) 139, http://dx.doi.org/10.1016/j.elspec.2003.10.002 http://www.sciencedirect.com/science/article/pii/S0368204803001786.

[29] B. Payne, M. Biesinger, N. McIntyre, The study of polycrystalline nickel metal oxidation by water vapour, J. Electron Spec. Rel. Phenom. 175 (1–3) (2009) 55–65, http://dx.doi.org/10.1016/j.elspec.2009.07.006 http://www.sciencedirect.com/science/article/pii/S0368204809001923.

Manuscript submitted in Ceramics International

ARTICLE IN PRESS

Ceramics International xxx (xxxx) xxx–xxx

Contents lists available at ScienceDirect

Ceramics International

journal homepage: www.elsevier.com/locate/ceramint

Identification of Mn site in Mn-doped $SrTiO_3$: First principles study

Ittipon Fongkaew[a,b,c], Jiraroj T-Thienprasert[d], Sukit Limpijumnong[a,b,c,*]

[a] School of Physics and NANOTEC-SUT Center of Excellence on Advanced Functional Nanomaterials, Suranaree University of Technology, Nakhon Ratchasima 30000, Thailand
[b] Synchrotron Light Research Institute, Nakhon Ratchasima 30000, Thailand
[c] Thailand Center of Excellence in Physics (ThEP Center), Commission on Higher Education, Bangkok 10400, Thailand
[d] Department of Physics, Faculty of Science, Kasetsart University, Bangkok 10900, Thailand

ARTICLE INFO

Keywords:
$SrTiO_3$
First-principles calculations
Mn defects
XANES

ABSTRACT

Manganese can incorporate into perovskite $SrTiO_3$ at either on the Sr-site (*A*-site) or Ti-site (*B*-site) depending on the growth conditions. However, there is no clear explanation on what conditions lead to *A*-site or *B*-site occupations and what are the local structures around Mn. In this work, first-principles calculations were carried out to study Mn in $SrTiO_3$ under different growth conditions. The calculations showed that Mn prefers to substitute for Ti site under a wide range of growth conditions; indicating that the substitution it is difficult to avoid even when one intentionally tries to dope Mn into the *A*-site. Due to a large size difference, Mn cannot fit in the Sr site. Instead, a charged interstitial Mn has rather low formation energy, especially under O-poor conditions. In addition, Mn_i can bind with Sr vacancy which has the compensating charge with a very high binding energy to form Mn_i-V_{Sr} complex. Mn_i-V_{Sr} has an equivalent chemical composition to Mn_{Sr}. Therefore, one might view Mn_i-V_{Sr} as an off-center Mn_{Sr}. In this view point, Mn *A*-site has a large cation off-centering consistent with experimental observations. We further relate our local structure models with the experiments by calculating the Mn *K*-edge x-ray absorption near-edge spectroscopy (XANES) spectra associated with Mn_{Ti}, Mn_{Sr} (on regular Sr lattice), and Mn_i-V_{Sr} or off-center Mn_{Sr} defects to compare with the measured Mn *K*-edge XANES spectra. Our results show good agreement with the measured spectra.

1. Introduction

Manganese-doped $SrTiO_3$ (STO) has been widely studied experimentally and theoretically due to its excellent physical properties, including dielectric, electronic and magnetic properties [1–4]. Mn atom is known to exist in two oxidation states, *i.e.*, Mn^{2+} and Mn^{4+}. The oxidation state suggests that Mn might incorporate at either Sr^{2+} or Ti^{4+} site. Nevertheless, other factors, such as the mismatch in size with the host atom and coordination number of the local structure, also play roles. Recently, different dielectric and structural properties of Mn-doped STO have been observed in the samples grown under different conditions [4,5]. This suggests that Mn might substitute into different sites in STO. It is expected that when Sr^{2+} (*A*-site) is substituted by a smaller Mn^{2+} ion, Mn should shift off-center from the *A*-site by a significant amount. This could lead to several favorable properties, such as large polarization response, low temperature dielectric relaxation, polar behavior, dilute magnetic, and magnetoelectric multiglass [6–9]. On the other hand, Ti^{4+} (*B*-site) should be nicely fit with Mn^{4+} with a small distortion around Mn^{4+} because their ionic radii are comparable. This is expected to suppress the dielectric permittivity as observed by Tkach et al. [5] However, it remains unclear if the site substitution of Mn can be effectively controlled by limiting the cation composition during growth, *i.e.*, using the compositions $Sr_{1-x}Mn_xTiO_3$ or $SrTi_{1-x}Mn_xO_3$, for on *A*-site and *B*-site, respectively. By using the extended x-ray absorption fine structure (EXAFS) spectroscopy, Levin *et al.* revealed that the samples, which are prepared by solid state reaction with the composition intended for Mn to substitute on *A*-site ($Sr_{1-x}Mn_xTiO_3$) with sintering temperature at 1500 °C under nitrogen or oxygen gas for 5 h, show some Mn occupying *B*-site [7]. In addition, some controversies on the key factors responsible for the observed anomalous magnetic and dielectric properties in Mn-doped STO samples have been reported [9–12]. This could be attributed to the substitution of Mn at different sites in different samples. Regarding theoretical study, by using first-principles calculations with hybrid functional, Yang *et al.* suggested that Mn substituted for Ti (Mn_{Ti}) can effectively narrow the band gap of STO, but the band gap does not change when Mn substitutes for Sr (Mn_{Sr}) [13]. This difference in band gap narrowing might be the effect of different band filling between Mn_{Ti} and Mn_{Sr}. They also reported that Ti-site (or *B*-site) is the most energetic preferred site under O-rich conditions. In contrary, another

---

[*] Correspondence to: School of Physics, Suranaree University of Technology, Nakhon Ratchasima 30000, Thailand.
E-mail addresses: ittipon_aof@yahoo.com (I. Fongkaew), sukit@sut.ac.th (S. Limpijumnong).

http://dx.doi.org/10.1016/j.ceramint.2017.05.258

Please cite this article as: Fongkaew, I., Ceramics International (2017), http://dx.doi.org/10.1016/j.ceramint.2017.05.258

theoretical work based on molecular dynamic simulation combined with *ab-initio* calculations suggested that Mn preferred to substitute for Sr [1]. Therefore, the substitution of Mn on Sr or Ti site under different growth conditions needs to be clarified. In addition, other Mn-related defects, such as Mn interstitial and Mn complex defects, have not been studied in previous works. Here, we employed first-principles calculations, like what previously used to study Mn in $PbTiO_3$ [14], to investigate Mn-related defects in STO. The most favorable sites of Mn in STO under different growth conditions are examined and the fully relaxed structures were used to simulate the Mn *K*-edge XANES spectra [15–17] to compare with the available measured Mn *K*-edge XANES spectra from literature [11]. Valant et al. dope Mn into STO by ball milling under different conditions: (1) $(Sr_{1-x}Mn^{2+}{}_{x})TiO_3$ sample fired at 1500 °C in N_2 atmosphere for 10 h (named A1500N$_2$) and (2) $Sr(Ti_{1-y}Mn^{4+}{}_{y})O_3$ sample fired at 1150 °C in air for 10 h (named B1150air) and measured their XANES spectra. This result can help us to directly compare the simulation with the experiment to identify the Mn site in each sample.

2. Method

We utilized first-principles calculations based on spin-polarized density functional theory (DFT) within the generalized gradient approximation (GGA) parameterized by Perdew, Burke, and Ernzerhof (PBE) [18]. To describe the electron-ion interactions, the projector-augmented wave (PAW) method as implemented in VASP codes was used [19–21]. The energy cutoff for expanding the plane wave basis set was set at 500 eV. The calculated lattice parameter of STO is 3.952 Å in good agreement with the experimental value [22]. To study the Mn-related defects in STO, a supercell approach with a 135-atom cell, which is a repetition of the conventional cubic-perovskite unit cell by 3 × 3 × 3, was carried out. For *k*-space integrations, we used the Monkhorst-Pack scheme [23] with a shifted sampling *k*-point mesh of 2 × 2 × 2. All atoms in the supercell were allowed to relax until the residual Hellmann-Feynman forces [24] became less than 10^{-2} eV/Å.

To determine the likelihood of defect formations, we calculated a defect formation energy (ΔH_f) defined by [25–27],

$$\Delta H_f = E_{tot}(D^q) - E_{tot}(bulk) + \sum \Delta n_X \mu_X + q(E_F + E_{VBM} + \Delta V) \tag{1}$$

where $E_{tot}(D^q)$ is the calculated total energy of a supercell containing a defect D in charge state q, $E_{tot}(bulk)$ is the calculated total energy of a defect-free supercell, Δn_X is the number of atom species X being added to (removed from, if negative) a supercell to create the defect D, μ_X is the corresponding atomic chemical potentials described below, E_F is the Fermi level referenced to the valence band maximum (E_{VBM}), which is corrected by the ΔV as described in Ref. [4].

Under thermodynamic equilibrium, the following conditions must be satisfied to obtained a homogeneous single crystal STO during growth,

$$\mu_{Sr} + \mu_{Ti} + 3\mu_O = E_{tot}(SrTiO_3). \tag{2}$$

Other undesired phases, such as metallic-Sr, metallic-Ti, O_2 gas as well as other oxide phases, including SrO, SrO_2, TiO, TiO_2, and Ti_2O_3, might also form. To prevent undesired phases, following constraints must be taken into consideration:

$$\begin{gathered}\mu_{Sr} < E_{tot}(\mathrm{Sr-metallic}), \quad \mu_{Sr} + \mu_O < E_{tot}(\mathrm{SrO}), \quad \mu_{Sr} + 2\mu_O < E_{tot}(\mathrm{SrO_2}),\\ \mu_{Ti} < E_{tot}(\mathrm{Ti-metallic}), \quad \mu_{Ti} + \mu_O < E_{tot}(\mathrm{TiO}), \quad \mu_{Ti} + 2\mu_O < E_{tot}(\mathrm{TiO_2}),\\ 2\mu_{Ti} + 3\mu_O < E_{tot}(\mathrm{Ti_2O_3}), \quad \mu_O < E_{tot}(\mathrm{O_2})/2.\end{gathered} \tag{3}$$

Eqs. (2) and (3) leave us with a set of possible μ_{Sr}, μ_{Ti}, and μ_O for STO equilibrium growth; illustrated with the shade area in Fig. 1. In Fig. 1, μ_O is projected onto the μ_{Sr} and μ_{Ti} plane and all chemical potentials were referenced to their natural phases, *i.e.*, metallic-Sr, metallic-Ti, and O_2 gas are all set to 0. The labels A – D in Fig. 1 represent the points at the boundary associated with four extreme conditions, *i.e.*, (Sr-rich/O-poor), (Ti-rich/O-poor), (Sr-poor/O-rich), and (Ti-poor/O-rich), respectively. Because the formation energies are functions of chemical potentials, these points representing four extreme conditions and the formation energy at other chemical potentials can then be estimated. When a defect containing Mn, the formation of undesired metallic-Mn as well as Mn-oxide phases should be avoided. Therefore, μ_{Mn} was limited by MnO_2 and metallic-Mn phases for O-rich and O-poor growth conditions, respectively.

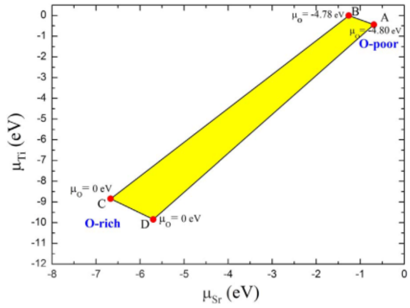

Fig. 1. Chemical potential domain for thermal equilibrium growth of $SrTiO_3$ crystal. The chemical potentials of Sr and Ti are plotted on the *x* and *y* axes, respectively, while the chemical potential of O is related by the constrain explained in the text. The shaded area represents the allowed chemical potentials satisfied the constraints in Eqs. (2) and (3).

To simulate XANES spectrum, the fully relaxed local structures of Mn-related defects in STO obtained from VASP codes were used as an input coordinates for FEFF8.2 codes [28,29]. FEFF8.2 is employed to calculate Mn *K*-edge XANES spectrum based on the multiple-scattering expansion within the muffin-tin potentials. The Hedin-Lundqvist was used as the exchange-correlation potential with an imaginary part of 0.5 eV to simulate the experimental broadening. The radii for self-consistent potential and full-multiple scattering calculations were set at 0.55 and 0.80 nm, respectively.

3. Result and discussion

In Fig. 2, the formation energies of simple Mn defects, namely, Mn substitution for Sr (Mn_{Sr}), Mn substitution for Ti (Mn_{Ti}) and Mn interstitial (Mn_i), are plotted as a function of Fermi energy under four extreme conditions as described before. In the plot, only the charge state with the lowest energy for each defect at a given Fermi energy is shown. (The charge state of the defect can be determined from the slope of the line.) The Fermi-energy range is extended to the calculated band gap of ~1.98 eV. Note that the calculated band gap is lower than the experimental band gap of 3.25 eV [30] due to the well-known DFT problems. Our calculations found that Mn_{Sr} is a donor with defect transition level at ε(+ 2/ + 1) = 0.25 eV, while Mn_{Ti} is a charge neutral for the entire possible Fermi energy range. Mn_i is a donor with two transition levels at ε(+ 4/ + 3) = 0.20 eV and ε(+ 3/ + 2) = 1.57 eV. The local structures of Mn_{Ti}, Mn_{Sr}, and Mn_i defects are illustrated in Fig. 3(a)–(c). It appears that Mn substitutes for Sr (or Ti) atom does not lead to a large local structure distortion or large off-center shift. However, for Mn_{Sr}, this is not the lowest energy configuration which will be explained later. The lowest-energy site for interstitial Mn (Mn_i) is at the center of Sr–Sr bond. After inserting the Mn in between two Sr host atoms, the two atoms slightly relax outward. Mn_{Ti} and Mn_i are energetically most favorable (hence, the dominant) defects under both O-rich and O-poor growth conditions, respectively. Note that, the breaking symmetry of Mn on Sr site (shift Mn away from the Sr site) can lower the energy, however, its formation energy remains higher

Manuscript submitted in Ceramics International

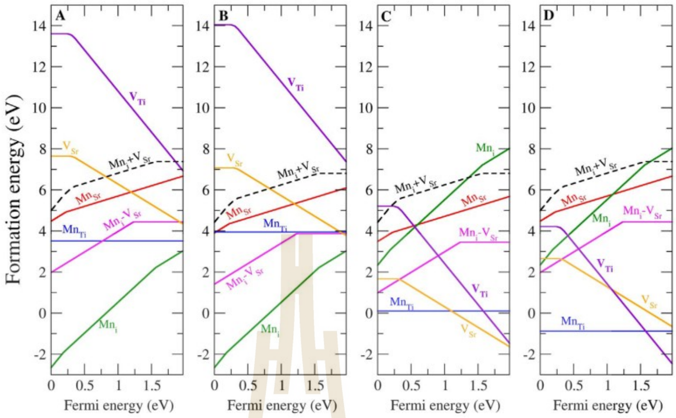

Fig. 2. Defect formation energies as functions of Fermi energy under different growth conditions, *i.e.*, A, B, C, and D from left to right panels, respectively. The slope of each line indicates the charge state of the defect. The dashed black line represents the sum of the formation energies of Mn$_i$ and V_{Sr} defects.

than that of Mn$_i$ and Mn$_{Ti}$ defects. Therefore, Mn$_{Sr}$ cannot be the lowest energy defect at any growth conditions considered. However, experimental results showed that under certain growth conditions, (Sr$_{1-x}$Mn$_x$)TiO$_3$ samples (A-site substitution) can be achieved with distinct properties from the usually observed Mn$_{Ti}$ [5,11]. In addition, they found that the (Sr$_{1-x}$Mn$_x$)TiO$_3$ samples show the co-existence of Mn on *A*-site and *B*-site. Our calculations showed that Mn$_{Ti}$ is likely to exist in most growth conditions and difficult to be avoided, which agree well with the experimental finding. However, Mn$_{Sr}$ has high formation energy and its existence need further explanation as will be explained

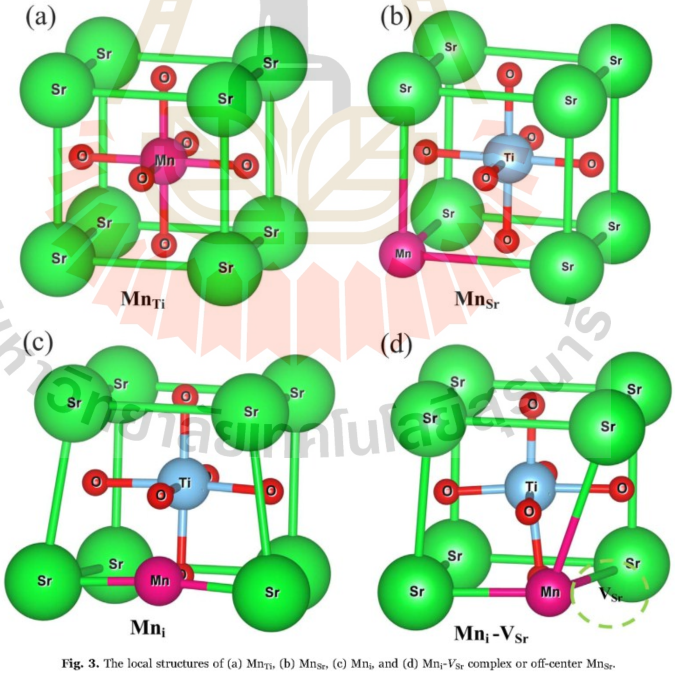

Fig. 3. The local structures of (a) Mn$_{Ti}$, (b) Mn$_{Sr}$, (c) Mn$_i$, and (d) Mn$_i$-V_{Sr} complex or off-center Mn$_{Sr}$.

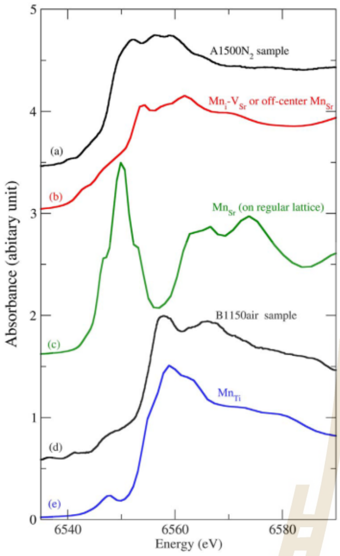

Fig. 4. Comparison between the calculated and measured Mn *K*-edge XANES spectra. The measured Mn *K*-edge XANES spectra [11] of $(Sr_{1-x}Mn_x)TiO_3$ sample (A1500N$_2$) and $Sr(Ti_{1-x}Mn_x)O_3$ sample (B1150air) are marked by (a) and (d). The calculated Mn *K*-edge XANES spectra associated with Mn_i-V_{Sr} (or off-center Mn_{Sr}), Mn_{Sr}, and Mn_{Ti} are labeled by (b), (c), and (e), respectively.

next.

Interstitial Mn (Mn_i) is a charged defect because Mn is a donor, which can be stable in +4, +3 and +2 charge states. As a charged defect, it can be compensated by an opposite charge native defect; forming a neutral complex. For intrinsic point defects, the potential compensating native point defects are Sr vacancy Sr (V_{Sr}) and Ti vacancy (V_{Ti}), both of which are acceptor. The calculated the formation energies of V_{Sr} and V_{Ti} are shown in Fig. 2. The formation energy of V_{Sr} is lower than that of V_{Ti} under several growth conditions. Therefore, V_{Sr} can be the compensating defect in $(Sr_{1-x}Mn_x)TiO_3$ samples. We investigated the complex defect formation between Mn_i and V_{Sr}, *i.e.*, Mn_i-V_{Sr} complex and found that the complex is a deep donor with two defect transition levels at $\varepsilon(+2/0) = 1.25$ eV. To determine the stability of the complex, we calculated the binding energy defined by

$$E_{bind}(A-B) = E_f(A) + E_f(B) - E_f(A-B) \tag{4}$$

where E_f and $E_f(B)$ are the formation energies of the defects *A* and *B*, and $E_f(A-B)$ is the formation energy of the *A*–*B* complex. If the complex has a large binding energy, it is more likely to form. As shown in Fig. 2, the dashed line represents the sum of the formation energies of Mn_i and V_{Sr}. The binding energy of Mn_i-V_{Sr} complex is the difference between the dashed black line and the magenta (Mn_i-V_{Sr}) line. We found that the binding energy of the complex is more than 2.6 eV which is high; indicating that such complex is likely to exist in a high concentration and very stable.

The local structures of Mn_i-V_{Sr} complex is shown in Fig. 3(d). The interstitial Mn atom move toward V_{Sr}, but not into the center of it. This structure can also be viewed as a largely distorted Mn_{Sr}, where Mn atom is largely shifted away from the regular Sr site; resulting in a large off-centering Mn_{Sr}. This structure is in good agreement with the experimental observation [7,11]. (In principle, slightly shift Mn off-center during the Mn_{Sr} calculation should lead to this structure shown in Fig. 3(d) after relaxation. However, our actual calculation did not give this result, instead we obtained a slightly distorted Mn_{Sr}).

To directly compare our calculated results with the experiment, we calculated the Mn *K*-edge XANES spectra associated with Mn_{Sr} (on regular lattice), Mn_{Ti}, and Mn_i-V_{Sr} or off-center Mn_{Sr} defects. Our calculated results are illustrated in Fig. 4 along with the experimental Mn *K*-edge XANES spectra obtained from $(Sr_{1-x}Mn_x)O_3$ and $Sr(Ti_{1-x}Mn_x)O_3$ samples that are experimentally assigned to be associated with Mn substitutions for *A*-site and *B*-site, respectively [11]. It is clear that the features of the calculated XANES spectrum of Mn_{Sr} defect (on regular Sr lattice) is significantly distinct from that of the measured XANES spectrum of $(Sr_{1-x}Mn_x)O_3$ sample. On the other hand, the features of the calculated XANES spectrum of Mn_i-V_{Sr} complex (or off-center Mn_{Sr}) are similar to that of the measured XANES spectrum of $(Sr_{1-x}Mn_x)O_3$ sample. The calculated XANES spectrum of Mn_{Ti} is in good agreement with the measured XANES spectrum of $Sr(Ti_{1-x}Mn_x)O_3$ sample. Our XANES calculations confirm the assignment of Mn in $Sr(Ti_{1-x}Mn_x)O_3$ sample to be Mn_{Ti} and the assignment of Mn in $(Sr_{1-x}Mn_x)O_3$ sample to be Mn_i-V_{Sr} complex (or off-center Mn_{Sr}).

4. Conclusion

We use first-principles DFT calculations to investigate Mn-related defects in STO under different growth conditions. We found that Mn_{Ti} is the lowest energy defect under most growth conditions. Therefore, Mn_{Ti} defect can be observed in most of the Mn-doped STO regardless of how the elemental composition is forced, *i.e.*, both $(Sr_{1-x}Mn_x)TiO_3$ and $Sr(Ti_{1-x}Mn_x)O_3$ samples. In addition, our calculations show that a substitutional-vacancy complex Mn_i-V_{Sr}, which has the same chemical composition as Mn_{Sr} but with Mn atom largely shifted off-center, can form in certain growth conditions with reasonably low formation energy. This off-center Mn_{Sr} explains the observed *A*-site substitution in $(Sr_{1-x}Mn_x)TiO_3$ samples. Our calculated XANES spectra associated with Mn_{Ti}, and off-center Mn_{Sr} agree nicely with the measured XANES spectra of $Sr(Ti_{1-x}Mn_x)O_3$ and $(Sr_{1-x}Mn_x)TiO_3$ samples, respectively. This confirms the experimental assignment of Mn substitution for *B*-site and *A*-site with detailed energetic description to support the assignment.

Conflict of interest

We declare that we do not have any commercial or associative interest that represents a conflict of interest in connection with the work submitted.

Acknowledgements

This work was supported by NANOTEC-SUT Center of Excellence on Advanced Functional Nanomaterials and Thailand Center of Excellence in Physics. One of the authors (IF) was partially supported by the Development and Promotion of Science and Technology Talents Project (DPST, Thailand). JT is supported by the Faculty of Science, Kasetsart University and Kasetsart University Research and Development Institute (KURDI). Computing resources provided by Theoretical Computation Section, Synchrotron Light Research Institute (Public Organization).

References

[1] J.A. Dawson, H. Chen, I. Tanaka, Combined ab initio and interatomic potentials based assessment of the defect structure of Mn-doped $SrTiO_3$, J. Phys. Chem. C 118 (2014) 14485–14494.
[2] D. Choudhury, B. Pal, A. Sharma, S. Bhat, D.D. Sarma, Magnetization in electron- and Mn-doped $SrTiO_3$, Sci. Rep. 3 (2013).
[3] D. Choudhury, S. Mukherjee, P. Mandal, A. Sundaresan, U. Waghmare, S. Bhattacharjee, R. Mathieu, P. Lazor, O. Eriksson, B. Sanyal, Tuning of dielectric

Manuscript submitted in Ceramics International

properties and magnetism of $SrTiO_3$ by site-specific doping of Mn, Phys. Rev. B 84 (2011) 125124.

[4] A. Tkach, P.M. Vilarinho, A.L. Kholkin, Dependence of dielectric properties of manganese-doped strontium titanate ceramics on sintering atmosphere, Acta Mater. 54 (2006) 5385–5391.

[5] A. Tkach, P.M. Vilarinho, A. Kholkin, Structural and dielectric properties of Mn-doped strontium titanate ceramics, Ferroelectrics 304 (2004) 87–90.

[6] V.V. Lemanov, E.P. Smirnova, A.V. Sotnikov, M. Weihnacht, Dielectric Relaxation in $SrTiO_3$: Mn, Phys. Solid State, 46 pp. 1442–1448.

[7] I. Levin, V. Krayzman, J.C. Woicik, A. Tkach, P.M. Vilarinho, X-ray absorption fine structure studies of Mn coordination in doped perovskite $SrTiO_3$, Appl. Phys. Lett. 96 (2010) 052904.

[8] C.G. Van de Walle, J. Neugebauer, First-principles calculations for defects and impurities: applications to III-nitrides, J. Appl. Phys. 95 (2004) 3851–3879.

[9] B. Radisavljevic, A. Radenovic, J. Brivio, V. Giacometti, A. Kis, Single-layer MoS2 transistors, Nat. Nano 6 (2011) 147–150.

[10] W. Kleemann, V.V. Shvartsman, S. Bedanta, P. Borisov, A. Tkach, P.M. Vilarinho, (Sr,Mn)TiO_3 – a magnetoelectrically coupled multiglass, J. Phys.: Condens. Matter 20 (2008) 434216.

[11] M. Valant, T. Kolodiazhnyi, I. Arčon, F. Aguesse, A.-K. Axelsson, N.M. Alford, The origin of magnetism in Mn-doped $SrTiO_3$, Adv. Funct. Mater. 22 (2012) 2114–2122.

[12] A. Tkach, P.M. Vilarinho, D. Nuzhnyy, J. Petzelt, Sr-and Ti-site substitution, lattice dynamics, and octahedral tilt transition relationship in $SrTiO_3$: Mn ceramics, Acta Mater. 58 (2010) 577–582.

[13] C. Yang, T. Liu, Z. Cheng, H. Gan, J. Chen, Study on Mn-doped $SrTiO_3$ with first principle calculation, Phys. B: Condens. Matter 407 (2012) 844–848.

[14] A. Boonchun, M. Smith, B. Cherdhirunkorn, S. Limpijumnong, First principles study of Mn impurities in $PbTiO_3$ and $PbZrO_3$, J. Appl. Phys. 101 (2007) (43521-43521).

[15] J. T-Thienprasert, S. Klaithong, A. Niltharach, A. Worayingyong, S. Na-Phattalung, S. Limpijumnong, Local structures of cobalt in Co-doped TiO_2 by synchrotron x-ray absorption near edge structures, Curr. Appl. Phys. 11 (2011) S279–S284.

[16] S. Limpijumnong, M.F. Smith, S.B. Zhang, Characterization of As-doped, p-type ZnO by x-ray absorption near-edge structure spectroscopy: theory, Appl. Phys. Lett. 89 (2006) 222113.

[17] J. T-Thienprasert, S. Rujirawat, W. Klysubun, J.N. Duenow, T.J. Coutts, S.B. Zhang, D.C. Look, S. Limpijumnong, Compensation in Al-doped ZnO by Al-related acceptor complexes: synchrotron X-ray absorption spectroscopy and theory, Phys. Rev. Lett. 110 (2013) 055502.

[18] J.P. Perdew, K. Burke, M. Ernzerhof, Generalized gradient approximation made simple, Phys. Rev. Lett. 77 (1996) 3865.

[19] G. Kresse, J. Furthmüller, Efficiency of ab-initio total energy calculations for metals and semiconductors using a plane-wave basis set, Comput. Mat. Sci. 6 (1996) 15–50.

[20] G. Kresse, J. Hafner, Norm-conserving and ultrasoft pseudopotentials for first-row and transition-elements, J. Phys. Condens. Matter 6 (1994) 8245.

[21] G. Kresse, D. Joubert, From ultrasoft pseudopotentials to the projector augmented-wave method, Phys. Rev. B 59 (1999) 1758.

[22] F.W. Lytle, X-ray diffractometry of low-temperature phase transformations in strontium titanate, J. Appl. Phys. 35 (1964) 2212–2215.

[23] H.J. Monkhorst, J.D. Pack, Special points for Brillouin-zone integrations, Phys. Rev. B 13 (1976) 5188.

[24] R.P. Feynman, Forces in molecules, Phys. Rev. 56 (1939) 340.

[25] S.B. Zhang, J.E. Northrup, Chemical potential dependence of defect formation energies in GaAs: application to Ga self-diffusion, Phys. Rev. Lett. 67 (1991) 2339–2342.

[26] J.E. Northrup, S.B. Zhang, Energetics of the As vacancy in GaAs: the stability of the 3+ charge state, Phys. Rev. B 50 (1994) 4962–4964.

[27] F. Gupta, G. Brillant, A. Pasturel, Correlation effects and energetics of point defects in uranium dioxide: a first principle investigation, Philos. Mag. 87 (2007) 2561–2569.

[28] A.L. Ankudinov, C.E. Bouldin, J.J. Rehr, J. Sims, H. Hung, Phys. Rev. B 65 (2002) 1–11.

[29] A.L. Ankudinov, B. Ravel, J.J. Rehr, S.D. Conradson, Phys. Rev. B 58 (12) (1998) 7565.

[30] K. Van Benthem, C. Elsässer, R. French, Bulk electronic structure of $SrTiO_3$: experiment and theory, J. Appl. Phys. 90 (2001) 6156–6164.

Manuscript submitted in Physical Review B

RAPID COMMUNICATIONS

PHYSICAL REVIEW B **94**, 201121(R) (2016)

Nearly-free-electron system of monolayer Na on the surface of single-crystal $HfSe_2$

T. Eknapakul,[1] I. Fongkaew,[1,2] S. Siriroj,[1] R. Vidyasagar,[1] J. D. Denlinger,[3] L. Bawden,[4] S.-K. Mo,[3] P. D. C. King,[4]
H. Takagi,[5,6] S. Limpijumnong,[1,7] and W. Meevasana[1,7,*]
[1]*School of Physics, Suranaree University of Technology, Nakhon Ratchasima 30000, Thailand*
[2]*Synchrotron Light Research Institute, Nakhon Ratchasima 30000, Thailand*
[3]*Advanced Light Source, Lawrence Berkeley National Laboratory, Berkeley, California 94720, USA*
[4]*SUPA, School of Physics and Astronomy, University of St. Andrews, St. Andrews, Fife KY16 9SS, United Kingdom*
[5]*Department of Physics, University of Tokyo, Hongo, Tokyo 113-0033, Japan*
[6]*Magnetic Materials Laboratory, RIKEN Advanced Science Institute, Wako, Saitama 351-0198, Japan*
[7]*NANOTEC-SUT Center of Excellence on Advanced Functional Nanomaterials, Suranaree University of Technology, Nakhon Ratchasima 30000, Thailand*

(Received 30 September 2016; revised manuscript received 4 November 2016; published 28 November 2016)

The electronic structure of a single Na monolayer on the surface of single-crystal $HfSe_2$ is investigated using angle-resolved photoemission spectroscopy. We find that this system exhibits an almost perfect "nearly-free-electron" behavior with an extracted effective mass of $\sim 1m_e$, in contrast to heavier masses found previously for alkali-metal monolayers on other substrates. Our density-functional-theory calculations indicate that this is due to the large lattice constant, causing both exchange and correlation interactions to be suppressed, and to the weak hybridization between the overlayer and the substrate. This is therefore an ideal model system for understanding the properties of two-dimensional materials.

DOI: 10.1103/PhysRevB.94.201121

Understanding and controlling electrons in reduced dimensions, for example, at the interfaces between disparate semiconductors, underpins modern electronic devices [1–4]. In recent years, this has found renewed prominence through the study of electrons naturally confined in atomically thin layers, such as in graphene or monolayer transition-metal dichalcogenides, opening prospects to achieve novel functionality such as ultrafast electronic [5], spintronic, or valleytronic devices [6–11]. To progress towards these goals, it is critical to understand the behavior of electrons in two-dimensional (2D) solids, and the influence of many-body interactions between them.

Angle-resolved photoemission spectroscopy (ARPES) is a powerful tool to achieve this. It directly measures the electronic structure of materials, and can provide valuable information on carrier masses and the interactions between electrons in the system. This has been applied to numerous two-dimensional (or quasi-two-dimensional systems), including surface states of noble metals (e.g., Cu [12,13], Ag and Au [14,15]), semiconductors [16–20], and metal oxides [21,22], and alkali metals grown as two-dimensional layers on metallic substrates [23–28]. Despite many of these systems being generally considered weakly interacting, there is hardly any example of a system which displays true nearly-free-electron behavior manifested by a parabolic band dispersion with an effective carrier mass ($m^* = 1m_e$). For example, even for an alkali metal, in the cases of Na monolayers on Cu(111) [24] and Ni(100) [25] surfaces, the effective mass was reported to be at least 30% heavier than the bare electron mass. This was attributed to a hybridization between the Na-derived electronic states and those of the underlying substrate. Moreover, exchange interactions can even lead to a lowering of the effective mass below unity [29,30], making achieving true free-electron-like behavior very rare. In this Rapid Communication, we show how just such behavior is manifested in a single Na layer stabilized on a semiconducting $HfSe_2$ substrate. We attribute this to particularly weak hybridization with the substrate due to a large out-of-plane lattice constant, and to a particularly weak exchange and correlation interaction.

$1T$-$HfSe_2$ single crystals, which we use as a substrate, were grown using the flux method. This compound crystallizes in the CdI_2 structure with a hexagonal unit cell with in-plane and out-of-plane lattice constant of $a = 3.74$ Å and $c = 6.14$ Å [31,32], respectively [see Fig. 1(a)]. To obtain a clean surface, the crystal was cleaved in ultrahigh vacuum at a pressure better than 4×10^{-11} Torr. ARPES measurements were performed immediately after cleaving, and following the deposition of sodium (Na) on the sample surface from a SAES alkali-metal source. The measurements were performed at beamlines 4.0.3 and 10.0.1 of the Advanced Light Source (USA) using Scienta R4000 hemispherical electron analyzers. Photon energies were set to be in the range between 50 and 80 eV. The sample temperature was maintained at between 40 and 80 K throughout the experiment.

Figures 1(b) and 1(c) show ARPES data measured after Na atoms were deposited on the cleaved surface of single-crystal $HfSe_2$ for 5 min. A dispersive band with a parabolic shape is clearly observed. By fitting momentum distribution curves (MDCs) of this parabolic band, we extracted the effective mass to be $m^* = (1.00 \pm 0.04)m_e$, which is within error identical to the free-electron mass. The corresponding Fermi surface has a circular shape, again consistent with a free-electron gas. From this measured Fermi surface, we extract a surface carrier density from the Luttinger area, $n_{2D} = k_F^2/2\pi = 8.72 \times 10^{14}$ cm^{-2}. We also note the possible presence of a second smaller band near E_F marked by an arrow in Fig. 1(b) (see Fig. S1 in the Supplemental Material [33]

---

[*] Corresponding author: worawat@g.sut.ac.th

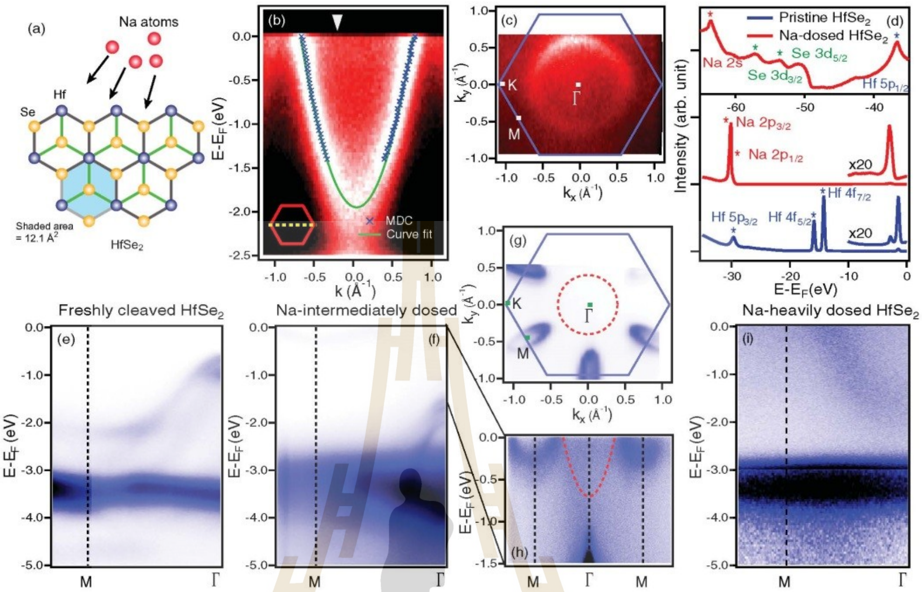

FIG. 1. (a) The atomic structure of HfSe$_2$ surface (top view). (b) Parabolic band dispersion of heavily evaporated Na atoms on the surface of HfSe$_2$. (c) Corresponding Fermi surface map of the band in (b). (d) Angle-integrated photoemission spectra of freshly cleaved and Na heavily evaporated HfSe$_2$, showing the core levels of Hf and Na (photon energy = 50 and 80 eV, respectively). (e), (f), and (i) show the valence bands of freshly cleaved, intermediately dosed (2 min of dosing), and heavily dosed HfSe$_2$ (5 min of dosing), respectively. (h) shows the zoom-in data of the HfSe$_2$ band dispersion in (f), as indicated; the dashed line shows a faint Na band dispersion. (g) shows the Fermi surface map of intermediately dosed HfSe$_2$; note that this map is a different sample with similar dosing.

for higher contrast); this may be due to a possible intercalation of a small fraction of Na atoms into the first van der Waals gap in HfSe$_2$, similar to the case of MoS$_2$ [18].

Our observations of a dispersive band and a clearly defined Fermi surface are indicative of a uniform and well-ordered metallic layer atop our semiconducting HfSe$_2$ substrate. To estimate the Na coverage, we perform additional measurements for shorter Na deposition times. As shown in Figs. 1(e)–1(h), after depositing Na on the surface for 2 min, the HfSe$_2$ valence bands present in the freshly cleaved material [Fig. 1(e)] are still clearly visible, but shifted to a higher binding energy concomitant with filling of the HfSe$_2$-derived conduction band states (charge transfer from the Na to the HfSe$_2$ populates the conduction band with carriers). The total electron density extracted from the Luttinger area of these conduction band pockets is estimated to be around 3.8×10^{14} cm^{-2}. Assuming a constant deposition rate, and assuming that each Na donates one electron, this would give a Na coverage of 9.4×10^{14} atoms cm^{-2} for the 5 min deposition. This is very close to the experimentally extracted Luttinger count identified from the heavier dose above, implying that the results shown in Figs. 1(b) and 1(i) are from approximately 1.1 monolayers (ML) of Na on HfSe$_2$.

This is further confirmed by comparing the angle-integrated core-level spectra before and after Na evaporation, as shown in Fig. 1(d). Before evaporation, Hf ($4f_{5/2}$ and $4f_{7/2}$) peaks can be clearly observed at a binding energy of around 14–17 eV [32,34]. After the heavy Na evaporation, Na ($2p_{3/2}$ and $2p_{1/2}$) peaks at ~30 eV binding energy become pronounced [35] while the spectral weight of the Hf $4f$ peaks is almost completely suppressed. This confirms a uniform coverage of the Na overlayer. Additional Hf- and Se-derived core levels are still observed at higher binding energies [e.g., between 35 and 60 eV, Fig. 1(d)]. Due to the extreme surface sensitivity of photoemission performed at these photon energies, these results (i.e., suppression of intensity for HfSe$_2$ bands at both the Fermi level and at higher binding energy) are entirely consistent with a single monolayer coverage of Na.

We now turn to our key observation that this Na monolayer hosts carriers with an effective mass so close to that of a free electron. In particular, this can be contrasted with similar systems such as a single monolayer of Na on Cu(111) where the measured effective mass has been determined to be as heavy as $1.3m_e$ [24]. This was suggested as a possible result of hybridization with the Cu substrate. We note that, in that case, the much smaller in-plane lattice constant of Cu(111)

Manuscript submitted in Physical Review B

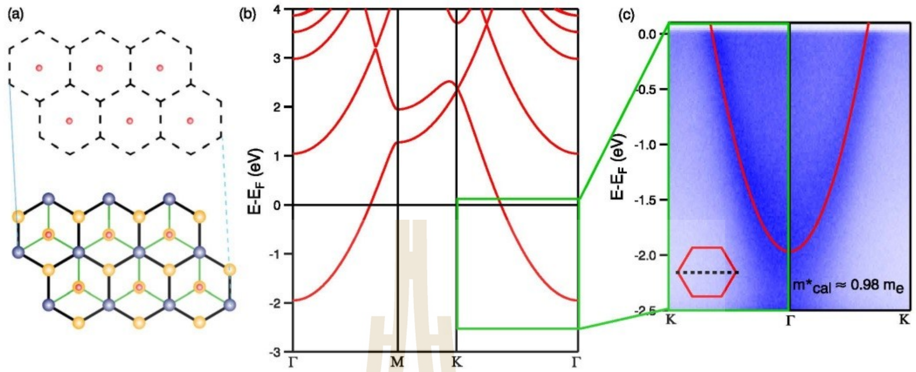

FIG. 2. (a) Atomic structures of monolayer Na on HfSe$_2$ (below) and bare monolayer Na (above) which is used for calculating the band structure in (b). (c) shows the zoom-in bands in the indicated box on top of the experimental data from Fig. 1(a).

(2.21 Å [36]) as compared to bulk sodium ($a = 3.77$ Å) may cause a greater overlap of the wave functions of Na and Cu, implying such a hybridization can easily occur. Here, however, the in-plane lattice constant of the substrate (HfSe$_2$; $a = 3.74$ Å) is very similar to that of the Na lattice. Moreover, HfSe$_2$ is a layered material, dominated by weak van der Waals bonding between layers as in other transition-metal dichalcogenides [18,37,38]. As such, hybridization between the Na- and HfSe$_2$-derived states can be expected to be substantially weaker.

Based on this assumption of such a weak interaction, we perform first-principles calculations of the band structure of an isolated Na monolayer (see Fig. 2). The calculations were carried out within the framework of density functional theory with projector augmented wave potentials (PAW) [39] as implemented in the VASP code. The Perdew-Burke-Ernzerhof (PBE) approximation is used for the exchange correlation terms [40,41]. The electron wave functions were described using a plane wave basis set with an energy cutoff of 520 eV. To calculate the 2D electronic band structures of the Na monolayer, a periodic slab of monolayer Na[001] ($P6_3/mmc$ hexagonal structure) with 20 Å vacuum spacing between layers to prevent interlayer interactions was used. The positions of Na atoms were relaxed until the Hellmann-Feynman forces become less than 0.001 eV/Å [42] while the in-plane cell vectors are kept at the theoretical relaxed bulk value $a =$ 3.76 Å (experiment 3.77 Å) which is approximately the same as the HfSe$_2$; this should therefore be a reasonable representation of our situation realized experimentally, as previous low-energy electron diffraction (LEED) studies show that Na overlayers form commensurate with the underlying substrate [e.g., Cu(111) and Ru(0001) [43–45]]. For k-space integrations, we used the Monkhorst-Pack scheme [46] with $11 \times 11 \times 1$ k-point sampling.

The calculated bands are shown in Fig. 2(b). These show a clearly dispersive band, which has an effective mass, $m^*_{\mathrm{cal}} \approx 0.98 m_e$. This is in excellent agreement with our ARPES data, as shown in Fig. 2(c), where the calculations are overlaid on the data. This suggests that the larger lattice constant of this substrate as compared to previously investigated examples could be key in stabilizing the free-electron-like behavior in a

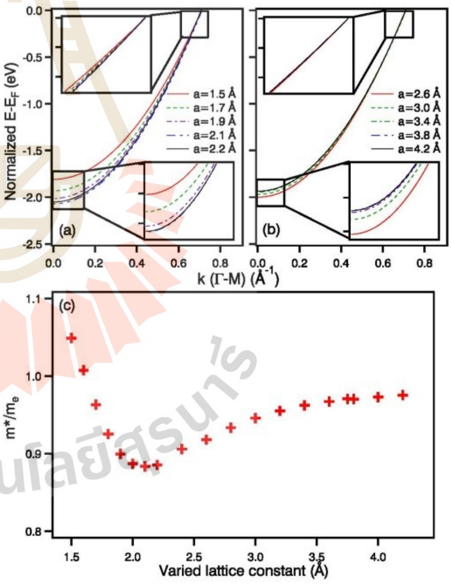

FIG. 3. (a) and (b) show calculated band dispersions of bare monolayer Na with various lattice constants between 1.5 and 4.2 Å. The insets show the zoom-in bands at the Fermi level and the band bottoms. (c) shows the effective masses extracted from the calculations in (a) and (b).

Manuscript submitted in Physical Review B

monolayer of Na. We note, also, that the high carrier densities can be expected to lead to very strong electronic screening, and, as such, the exchange interaction (which can make the effective mass lighter) will remain small in comparison to the kinetic energy. This is in contrast to other two-dimensional electron gases (2DEGs) stabilized in much more poorly screening materials, such as at the interfaces/surfaces of oxides and low-doped dichalcogenides [19,29,30]. We note that, as the lattice constant is reduced in our calculations (Fig. 3), and where screening can be expected to become less efficient, the effective mass of an isolated layer of Na can indeed become smaller than 1. At the smallest values, below 2.1 Å, however, an increase in correlation energies cause the correlation term to dominate over exchange, leading to a steep increase in the effective mass.

Our findings show that, even for a simple model system of an alkali-metal single layer, there is a possibility to engineer band structures via a judicious choice of material substrates. In other words, a two-dimensional material cannot be considered in isolation. Its electronic structure can be influenced directly, via hybridization with the supporting medium, but also via many-body effects, e.g., by balancing and controlling the ratio of the exchange and correlation energies both to each other and to the kinetic energy. Understanding the fundamentals of this process will be key to designing desired properties in two-dimensional materials, e.g., negative electronic compressibility [19] and fast band-gap renormalization [47,48]. Here, we show that by using a transition-metal dichalcogenide semiconductor as a support for a metallic Na single layer, we demonstrate that it is possible to minimize both of these effects, realizing the unusual situation of an almost ideal nearly-free-electron system with $m^* \sim 1m_e$.

We acknowledge S. Chaiyachad, W. Jindata, C. Jaisuk, Y. Kaekhamchan, and P. Chanprakhon for useful information. This work was supported by Suranaree University of Technology and by the Higher Education Research Promotion and NRU Project of Thailand, Office of the Higher Education Commission. The Advanced Light Source is supported by the Office of Basic Energy Science of the U.S. DOE under Contract No. DE-AC02-05CH11231. L.B. acknowledges studentship funding from the Engineering and Physical Sciences Research Council, U.K., through Grant No. EP/G03673X/1. P.D.C.K. acknowledges support from the Royal Society through a University Research Fellowship and the EPSRC (Grant No. EP/I031014/1).

Data underpinning this publication can be accessed at http://personal.sut.ac.th/worawat/PRB2016a/.

[1] J. Bardeen and H. Brattain, Phys. Rev. **75**, 1208 (1949).
[2] C. Weiner, IEEE Spectrum **10**, 24 (1973).
[3] G. Abstreiter, Surf. Sci. **98**, 117 (1980).
[4] H. L. Störmer, Surf. Sci. **142**, 130 (1984).
[5] L. Britnell, R. V. Gorbachev, R. Jalil, B. D. Belle, F. Schedin, A. Mishchenko, T. Georgiou, M. I. Katsnelson, L. Eaves, S. V. Morozov, N. M. R. Peres, J. Leist, A. K. Geim, K. S. Novoselov, and L. A. Ponomarenko, Science **335**, 947 (2012).
[6] J. Schliemann, J. C. Egues, and D. Loss, Phys. Rev. Lett. **90**, 146801 (2003).
[7] S. Bandyopadhyay and M. Cahay, Appl. Phys. Lett. **85**, 1814 (2004).
[8] A. F. Morpurgo, Nat. Phys. **9**, 532 (2013).
[9] K. Sugawara, T. Sato, Y. Tanaka, S. Souma, and T. Takahashi, Appl. Phys. Lett. **107**, 071601 (2015).
[10] T. Cao, G. Wang, W. Han, H. Ye, C. Zhu, J. Shi, Q. Niu, P. Tan, E. Wang, B. Liu, and J. Feng, Nat. Commun. **3**, 887 (2012).
[11] K. F. Mak, K. He, J. Shan, and T. F. Heinz, Nat. Nanotechnol. **7**, 494 (2012).
[12] F. Baumberger, T. Greber, and J. Osterwalder, Phys. Rev. B **64**, 195411 (2001).
[13] A. Tamai, W. Meevasana, P. D. C. King, C. W. Nicholson, A. de la Torre, E. Rozbicki, and F. Baumberger, Phys. Rev. B **87**, 075113 (2013).
[14] G. Nicolay, F. Reinert, S. Hüfner, and P. Blaha, Phys. Rev. B **65**, 033407 (2001).
[15] M. Hoesch, M. Muntwiler, V. N. Petrov, M. Hengsberger, L. Patthey, M. Shi, M. Falub, T. Greber, and J. Osterwalder, Phys. Rev. B **69**, 241401(R) (2004).
[16] P. D. C. King, R. C. Hatch, M. Bianchi, R. Ovsyannikov, C. Lupulescu, G. Landolt, B. Slomski, J. H. Dil, D. Guan, J. L. Mi, E. D. L. Rienks, J. Fink, A. Lindblad, S. Svensson, S. Bao, G. Balakrishnan, B. B. Iversen, J. Osterwalder, W. Eberhardt, F. Baumberger, and Ph. Hofmann, Phys. Rev. Lett. **107**, 096802 (2011).
[17] Y. Zhang, T. R. Chang, B. Zhou, Y. T. Cui, H. Yan, Z. Liu, F. Schmitt, J. Lee, R. Moore, Y. Chen, H. Lin, H. T. Jeng, S.-K. Mo, Z. Hussain, A. Bansil, and Z.-X. Shen, Nat. Nanotechnol. **9**, 111 (2014).
[18] T. Eknapakul, P. D. C. King, M. Asakawa, P. Buaphet, R. H. He, S.-K. Mo, H. Takagi, K. M. Shen, F. Baumberger, T. Sasagawa, S. Jungthawan, and W. Meevasana, Nano Lett. **14**, 1312 (2014).
[19] J. M. Riley, W. Meevasana, L. Bawden, M. Asakawa, T. Takayama, T. Eknapakul, T. K. Kim, M. Hoesch, S.-K. Mo, H. Takagi, T. Sasagawa, M. S. Bahramy, and P. D. C. King, Nat. Nanotechnol. **10**, 1043 (2015).
[20] H. Cao, R. Venkatasubramanian, C. Liu, J. Pierce, H. Yang, M. Z. Hasan, Y. Wu, and Y. P. Chen, Appl. Phys. Lett. **101**, 162104 (2012)
[21] P. Kushwaha, V. Sunko, P. J. W. Moll, L. Bawden, J. M. Riley, N. Nandi, H. Rosner, M. P. Schmidt, F. Arnold, E. Hassinger, T. K. Kim, M. Hoesch, A. P. Mackenzie, and P. D. C. King, Sci. Adv. **1**, e1500692 (2015)
[22] P. Richard, T. Sato, S. Souma, K. Nakayama, H. W. Liu, K. Iwaya, T. Hitosugi, H. Aida, H. Ding, and T. Takahashi, Appl. Phys. Lett. **101**, 232105 (2012).
[23] W. Schröder and J. Hölzl, Solid State Commun. **24**, 777 (1977)
[24] N. Fischer, S. Schuppler, R. Fischer, Th. Fauster, and W. Steinmann, Phys. Rev. B **43**, 14722 (1991).
[25] E. Jensen and E. W. Plummer, Phys. Rev. Lett. **55**, 1912 (1985).
[26] N. Fischer, S. Schuppler, R. Fischer, Th. Fauster, and W. Steinmann, Phys. Rev. B **47**, 4705 (1993).
[27] M. Caragiu and S. Finberg, J. Phys.: Condens. Matter. **17**, R995 (2005).

[28] J. Algdal, T. Balasubramanian, M. Breitholtz, V. Chis, B. Hellsing, S.-Å. Lindgren, and L. Walldén, Phys. Rev. B **78**, 085102 (2008).

[29] W. Meevasana, P. D. C. King, R. H. He, S.-K. Mo, M. Hashimoto, A. Tamai, P. Songsiririthigul, F. Baumberger, and Z.-X. Shen, Nat. Mater. **10**, 114 (2011).

[30] L. Li, C. Richter, S. Paetel, T. Kopp, J. Mannhart, and R. C. Ashoori, Science **332**, 825 (2011).

[31] X.-G. Zheng, H. Kuriyaki, and K. Hirakawa, J. Phys. Soc. Jpn. **58**, 622 (1989).

[32] R. Yue, A. T. Barton, H. Zhu, A. Azcatl, L. F. Pena, J. Wang, X. Peng, N. Lu, L. Cheng, R. Addou, S. McDonnell, L. Colombo, J. W. P. Hsu, J. Kim, M. J. Kim, R. M. Wallace, and C. L. Hinkle, ACS Nano **9**, 474 (2015).

[33] See Supplemental Material at http://link.aps.org/supplemental/10.1103/PhysRevB.94.201121 for possible evidence for second band at the Fermi level.

[34] C. Morant, L. Galan, and J. M. Sanz, Surf. Interface Anal. **16**, 304 (1990).

[35] S. P. Kowalczyk, L. Ley, F. R. McFeely, R. A. Pollak, and D. A. Shirley, Phys. Rev. B **8**, 3583 (1973).

[36] S. Nakanishi and T. Horiguchi, Jpn. J. Appl. Phys. **20**, L214 (1981).

[37] L. F. Mattheiss, Phys. Rev. B **8**, 3719 (1973).

[38] R. Coehoorn, C. Haas, J. Dijkstra, C. J. F. Flipse, R. A. deGroot, and A. Wold, Phys. Rev. B **35**, 6195 (1987).

[39] P. E. Blöchl, Phys. Rev. B **50**, 17953 (1994).

[40] J. P. Perdew, K. Burke, and M. Ernzerhof, Phys. Rev. Lett. **77**, 3865 (1996).

[41] J. P. Perdew, K. Burke, and M. Ernzerhof, Phys. Rev. Lett. **78**, 1396 (1997).

[42] R. P. Feynman, Phys. Rev. **56**, 340 (1939).

[43] T. Hertel, H. Over, H. Bludau, M. Gierer, and G. Ertl, Surf. Sci. **301**, 1 (1994).

[44] J. Kliewer and R. Berndt, Surf. Sci. **477**, 250 (2001).

[45] R. Duszak and R. H. Prince, Surf. Sci. **216**, 14 (1989).

[46] H. J. Monkhorst and J. D. Pack, Phys. Rev. B **13**, 5188 (1976).

[47] S. Ulstrup, A. G. Cabo, J. A. Miwa, J. M. Riley, S. S. Grønborg, J. C. Johannsen, C. Cacho, O. Alexander, R. T. Chapman, E. Springate, M. Bianchi, M. Dendzik, J. V. Lauritsen, P. D. C. King, and P. Hofmann, ACS Nano **10**, 6315 (2016).

[48] M. M. Ugeda, A. J. Bradley, S.-F. Shi, F. H. da Jornada, Y. Zhang, D. Y. Qiu, W. Ruan, S.-K. Mo, Z. Hussain, Z.-X. Shen, F. Wang, S. G. Louie, and F. Crommie, Nat. Mater. **13**, 1091 (2014).

Manuscript submitted in Scientific reports

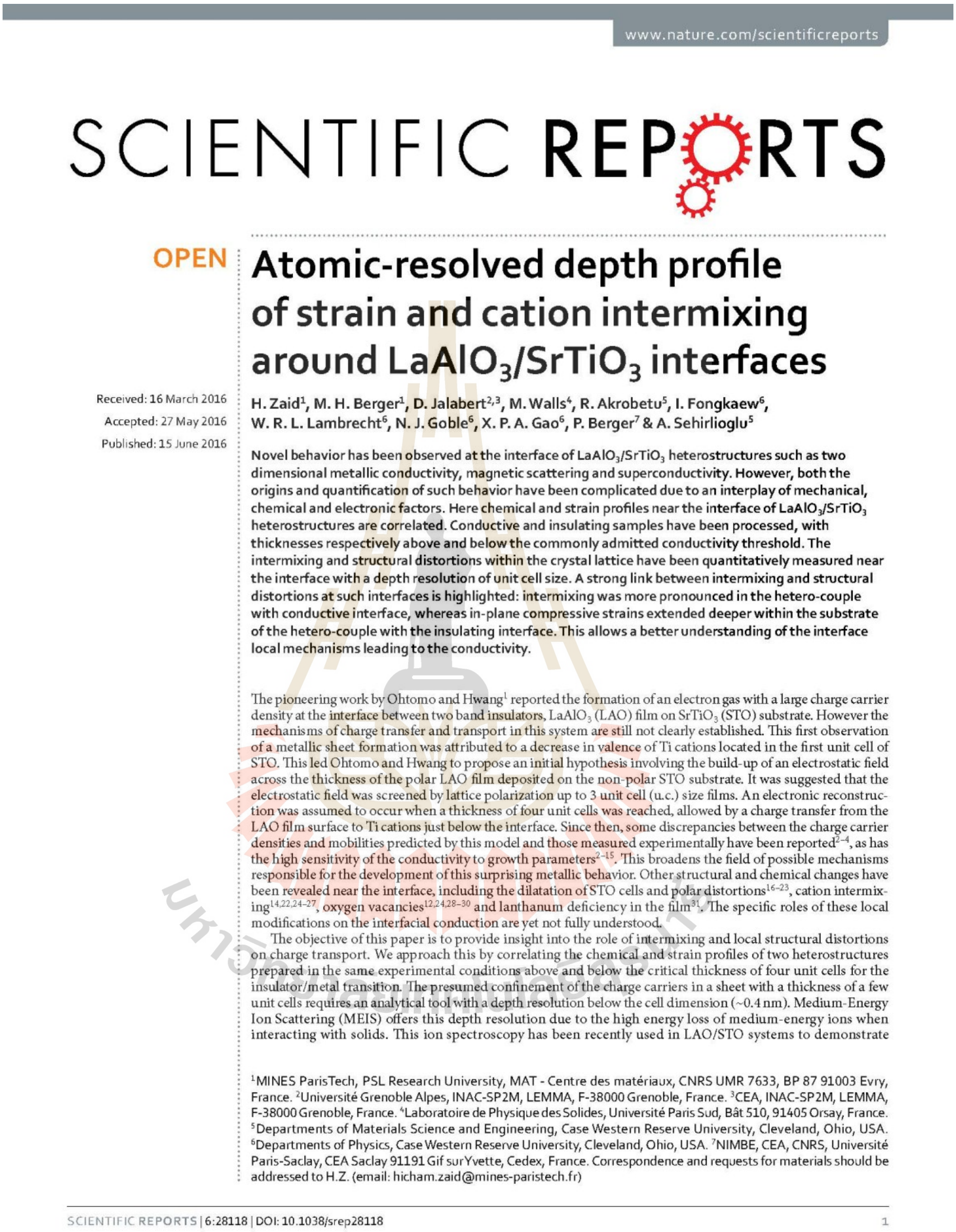

www.nature.com/scientificreports

SCIENTIFIC REPORTS

OPEN

Atomic-resolved depth profile of strain and cation intermixing around $LaAlO_3/SrTiO_3$ interfaces

Received: 16 March 2016
Accepted: 27 May 2016
Published: 15 June 2016

H. Zaid[1], M. H. Berger[1], D. Jalabert[2,3], M. Walls[4], R. Akrobetu[5], I. Fongkaew[6], W. R. L. Lambrecht[6], N. J. Goble[6], X. P. A. Gao[6], P. Berger[7] & A. Sehirlioglu[5]

Novel behavior has been observed at the interface of $LaAlO_3/SrTiO_3$ heterostructures such as two dimensional metallic conductivity, magnetic scattering and superconductivity. However, both the origins and quantification of such behavior have been complicated due to an interplay of mechanical, chemical and electronic factors. Here chemical and strain profiles near the interface of $LaAlO_3/SrTiO_3$ heterostructures are correlated. Conductive and insulating samples have been processed, with thicknesses respectively above and below the commonly admitted conductivity threshold. The intermixing and structural distortions within the crystal lattice have been quantitatively measured near the interface with a depth resolution of unit cell size. A strong link between intermixing and structural distortions at such interfaces is highlighted: intermixing was more pronounced in the hetero-couple with conductive interface, whereas in-plane compressive strains extended deeper within the substrate of the hetero-couple with the insulating interface. This allows a better understanding of the interface local mechanisms leading to the conductivity.

The pioneering work by Ohtomo and Hwang[1] reported the formation of an electron gas with a large charge carrier density at the interface between two band insulators, $LaAlO_3$ (LAO) film on $SrTiO_3$ (STO) substrate. However the mechanisms of charge transfer and transport in this system are still not clearly established. This first observation of a metallic sheet formation was attributed to a decrease in valence of Ti cations located in the first unit cell of STO. This led Ohtomo and Hwang to propose an initial hypothesis involving the build-up of an electrostatic field across the thickness of the polar LAO film deposited on the non-polar STO substrate. It was suggested that the electrostatic field was screened by lattice polarization up to 3 unit cell (u.c.) size films. An electronic reconstruction was assumed to occur when a thickness of four unit cells was reached, allowed by a charge transfer from the LAO film surface to Ti cations just below the interface. Since then, some discrepancies between the charge carrier densities and mobilities predicted by this model and those measured experimentally have been reported[2–4], as has the high sensitivity of the conductivity to growth parameters[2–15]. This broadens the field of possible mechanisms responsible for the development of this surprising metallic behavior. Other structural and chemical changes have been revealed near the interface, including the dilatation of STO cells and polar distortions[16–23], cation intermixing[14,22,24–27], oxygen vacancies[12,24,28–30] and lanthanum deficiency in the film[31]. The specific roles of these local modifications on the interfacial conduction are yet not fully understood.

The objective of this paper is to provide insight into the role of intermixing and local structural distortions on charge transport. We approach this by correlating the chemical and strain profiles of two heterostructures prepared in the same experimental conditions above and below the critical thickness of four unit cells for the insulator/metal transition. The presumed confinement of the charge carriers in a sheet with a thickness of a few unit cells requires an analytical tool with a depth resolution below the cell dimension (~0.4 nm). Medium-Energy Ion Scattering (MEIS) offers this depth resolution due to the high energy loss of medium-energy ions when interacting with solids. This ion spectroscopy has been recently used in LAO/STO systems to demonstrate

[1]MINES ParisTech, PSL Research University, MAT - Centre des matériaux, CNRS UMR 7633, BP 87 91003 Evry, France. [2]Université Grenoble Alpes, INAC-SP2M, LEMMA, F-38000 Grenoble, France. [3]CEA, INAC-SP2M, LEMMA, F-38000 Grenoble, France. [4]Laboratoire de Physique des Solides, Université Paris Sud, Bât 510, 91405 Orsay, France. [5]Departments of Materials Science and Engineering, Case Western Reserve University, Cleveland, Ohio, USA. [6]Departments of Physics, Case Western Reserve University, Cleveland, Ohio, USA. [7]NIMBE, CEA, CNRS, Université Paris-Saclay, CEA Saclay 91191 Gif sur Yvette, Cedex, France. Correspondence and requests for materials should be addressed to H.Z. (email: hicham.zaid@mines-paristech.fr)

Manuscript submitted in Scientific reports

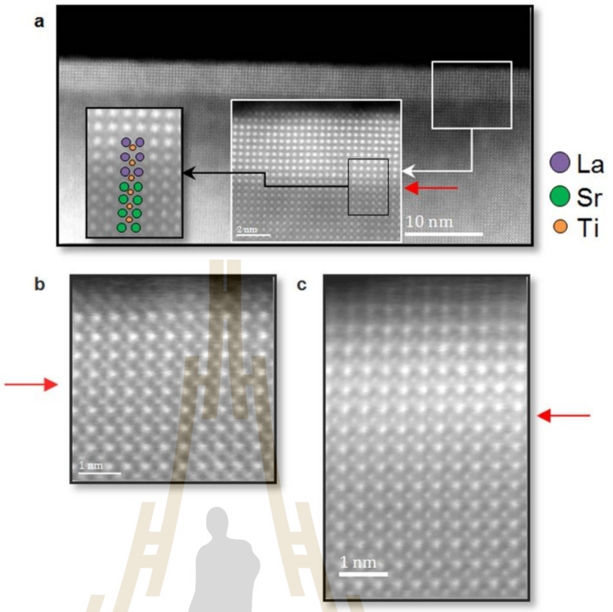

Figure 1. Representative HAADF images of $LaAlO_3$ films grown pseudomorphically on $SrTiO_3$. HAADF of (**a**) 10 u.c. (**b**) 3 u.c. (**c**) 5 u.c.-thick films deposited on a $SrTiO_3$ substrate. The same process conditions were used to deposit the films. The interfaces are shown by a red arrow. No misfit dislocations could be detected at LAO/STO interfaces along the entire distance observed via Nion UltraSTEM. The left inset in (**a**) highlights the off-center displacement of Ti near the interface.

qualitatively cation intermixing[14,26]. MEIS was also used to establish strain profiles in non-oxide semiconductor nano-objects[32,33]. Here we present, for the first time, quantitative profiles of the strontium and lanthanum concentrations correlated with profiles of the cell parameter variations around these atoms for both insulating and conductive hetero-structures. Epitaxial strains taking into account the chemical gradients cannot explain the magnitude of cell distortions measured. Charge defects have to be considered, with distinct spatial distributions between the insulating and conducting heterostructures.

Results and Discussion

Interface characterizations.

Interface morphology, Ti valence and oxygen vacancies. Epitaxial films with 3 and 5 u.c. thickness were grown by Pulsed Laser Deposition. The oxygen partial pressure during deposition was fixed at 10^{-4} Torr, and the temperature reached 750 °C. The parameter misfit between the substrate ($a_{STO} = 3.905$ Å) and the film ($a_{LAO} = 3.791$ Å using a pseudo cubic description) did not induce strain relaxations via interfacial misfit dislocations as no dislocations could be detected along the foil observed for both samples, as seen on Fig. 1.

The 5 u.c. sample exhibited a conductive interface while for the 3 u.c. film the resistance exceeded our instrumental limits (>100 MΩ) (Electrical measurements are reported in the Supplementary Fig. S1). Thus, consistently with previous studies[4,14,34–36], the critical thickness lies between 3 and 5 u.c. These samples are good candidates to investigate structural and/or chemical differences between conductive and insulating samples.

In the original hypothesis from Nakagawa *et al.*[24] the diverging electrostatic potential in the growing polar film is removed by the transfer of half an electron per unit cell into the first STO layer below the interface. A theoretical average valence of $Ti^{3.5+}$ would be thus expected resulting in a 2D carrier density of $3.3 \times 10^{14}\,cm^{-2}$. Electron Energy Loss Spectroscopy (EELS) profiles across the interface of the selected samples were used to deduce the contribution of Ti^{3+} to the Ti-L_2L_3 absorption edges. A minimum valence of $Ti^{3.9+(+/-0.05)}$ was found located in the first unit cell below the interface of both samples (Fig. 2). This would lead to a maximum theoretical density of free charge carriers of 6.6×10^{13} $(+/-3.28 \times 10^{13})$ cm^{-2} if we assume that all the carriers originate from Ti^{4+} reduction. Experimental measurements of Hall coefficient on the 5 u.c. sample below 10 K (reported in the Supplementary Information) revealed a 2D charge carrier density ($\approx 3 \times 10^{14}\,cm^{-2}$) that

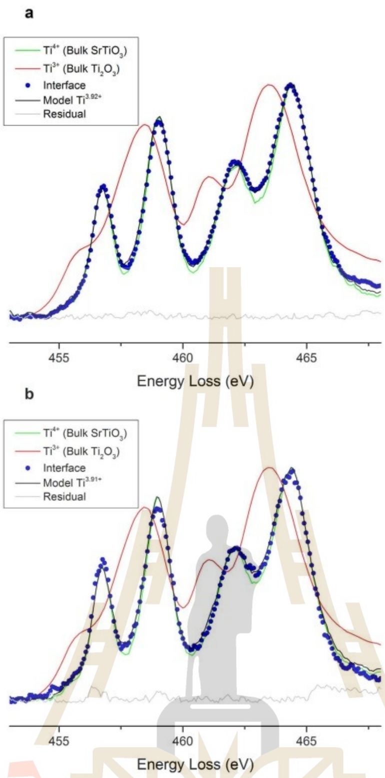

Figure 2. Ti-$L_{2,3}$ edge EELS taken at the $LaAlO_3$/$SrTiO_3$ interface. EELS spectrum at the interface of the (**a**) 3 u.c. (**b**) 5 u.c. sample. The contributions of Ti^{4+} and T^{3+} to the Ti edge were deduced from a linear combination of two reference spectra, a green one for Ti^{4+} ($SrTiO_3$ away from the interface of the (**a**) 3 u.c. (**b**) 5 u.c. sample) and a red one Ti^{3+} (Bulk Ti_2O_3) recorded on the same spectrometer. The method of least squares has been used to fit the experimental and the simulation spectra. The blue dots spectra correspond to the experimental EELS measurement at the very first unit cell below the interface. The black curves represent the best simulation that fitted the experimental spectrum. One observes that the Ti oxidation state is quite similar between the conductive and insulating samples grown in the same conditions.

was comparable to theoretical density (3.3×10^{14} cm^{-2}). However, 2D charge carrier density at room temperature ($n > 1.2 \times 10^{15}$ cm^{-2}), was much higher than the density calculated based on EELS valence measurements. This suggests that the conduction was not purely bidimensional. The hypothesis of a quasi 2D conduction zone restricted to the first layers above and below the interface, still underestimates the charge carrier density with respect to the Hall measurements (EELS measurements of Ti oxidation state measured 1 u.c. above and under the interface are presented in the Supplementary Fig. S2). This would confirm the three dimensionality of the conduction. This delocalization of the carriers normal to the interface was suggested to explain the weak contribution of Ti^{3+} on the EELS measurements at the interface[29,37,38]. The similar Ti valences measured below the interfaces in the conducting and insulating samples does not play in favor of charge injection by a polar catastrophe[29,38,39], at least for such film thicknesses. This highlights the role of the carrier mobility to explain the observed discrepancies in terms of electrical conduction.

At the partial pressure of 10^{-4} Torr used during the PLD growth, no signature of oxygen vacancies could be detected in the O-K edge recorded in the substrate and around the interface by EELS, as observed on Fig. 3. The interfacial O-K EELS spectra reflect intermixing rather than oxygen vacancies[40,41]. Although a low level of oxygen non-stoichiometry is not excluded, it would be insufficient to explain the sheet resistance measured and the differences between the 3 and 5 u.c. samples.

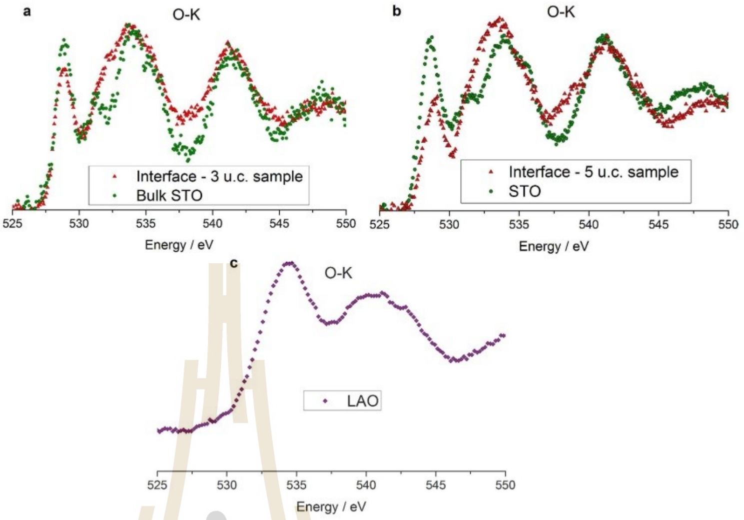

Figure 3. **EELS fine structure of the O-K absorption edge across two $LaAlO_3/SrTiO_3$ heterostructures.** (**a**,**b**) Experimental spectra recorded at the (**a**) 3 u.c. (**b**) 5 u.c. sample hetero-interface (red triangles) and deeper into the $SrTiO_3$ substrate of same sample (green dots). (**c**) Experimental spectrum for $LaAlO_3$ away from the interface. Experimental spectra are clearly influenced by cation intermixing rather than extrinsic donors[40].

Therefore we have focused our work on two mechanisms suspected to play a significant role in the insulator/conductor transition of the hetero-structure: intermixing and structural distortions.

A-site intermixing. The investigation of La ↔ Sr intermixing around the interface has been carried out by Medium Energy Ion Spectroscopy (MEIS) with a 100 keV He^+ beam in the random mode configuration for the 3 and 5 u.c. samples. In this "random" mode, the orientation of the sample was chosen to avoid a channeling of the beam by dense atomic planes and to minimize the probability of a second scattering for the scattered He^+ on their way out. The energy E of the backscattered He^+ particles varies with the target element weight, its depth and the scattered angle, θ_{sc}. This "random" mode was selected to extract the chemical profiles of Sr and La. Further explanations can be found in the Supplementary Information.

Figure 4a,b show the random maps (E, θ_{sc}, N) recorded for the 3 and 5 u.c. samples respectively, where N expresses the count number. The N = f(E) curves extracted from these maps at a fixed θ_{sc} are shown in Fig. 4c,d where the red dots correspond to the experimental data. For both samples of 3 u.c. and 5 u.c. thickness, La was distributed over a larger depth than the film thickness and the Sr signal started above the substrate surface clearly exhibiting La ↔ Sr intermixing.

The La ↔ Sr intermixing was quantified by simulations of composition gradients with unit cell resolution. For each layer the ratio x = La/(La + Sr) was optimized to permit the best fit to the experimental curves (see Supplementary Fig. S3). The resulting variations of x across the interface are shown in Fig. 4e. Strontium was found in each layer up to the surface for both films, and the La counter-diffusion depths (≈4–5 u.c) were similar for the two samples. The substitution of La by Sr was slightly larger in the 5 u.c. film than in the 3 u.c. film at any depth, whereas within the substrate, only the first layer contained more La in the 5 u.c. sample than in the 3 u.c. one. The cumulative Sr content in the film was greater than the cumulative La content in the substrate for 5 u.c. film, while the opposite was true for the 3 u.c. film.

The atomically-resolved MEIS depth profiles clearly demonstrated La and Sr intermixing. These exchanges of cations with different oxidation states can stabilize the interface and thus can lead to compensation of the dipole energy which otherwise would form at an ideal, abrupt-interface[22,24–26]. A $La^{3+} \leftrightarrow Sr^{2+}$ cation exchange around the interface would generate donor-type point defects $La_{Sr}^{\cdot}$ and compensating electrons e' in the conduction band (CB) of STO. When all cations are considered, intermixing creates a $La_xSr_{1-x}Al_yTi_{1-y}O_3$ layer, where Al would act as an acceptor dopant. Asymmetry in the intermixing depths on A and B sites occurred as shown experimentally by EELS measurements on Fig. 5, which is consistent with observations in the literature[22]: Al intermixes with Ti at shallower depths and lower ratio than La does with Sr. Therefore x > y implies a net donor doping effect below the interface; however with compensating carrier content (x-y) smaller than the value (x) that would be expected for hypothetical $La_xSr_{1-x}TiO_3$ layer. It has to be mentioned that the deeper diffusion of La measured by EELS

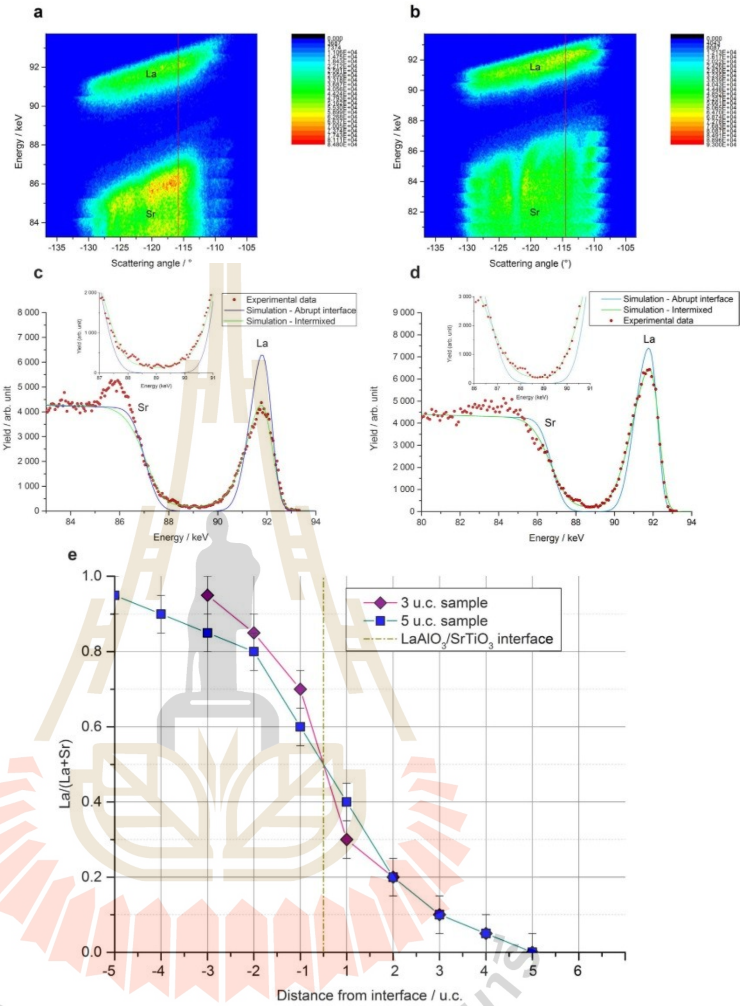

Figure 4. MEIS data in random mode. Incident particles : 100 keV He^+ ions. (**a**,**b**) MEIS random maps (E_1, θ_{sc}, N) of the samples with a film thicknesses of (**a**) 3 u.c. (**b**) 5 u.c. Top (-bottom) layers of highest (-lowest) energies correspond to He^+ particles backscattered on La (-Sr) respectively. Red lines locate the position (at a fixed scattering angle) of the profiles extracted. (**c**,**d**) Random MEIS experimental and simulated spectra of the (**c**) 3 u.c. sample with a backscattering angle of 115,4° (**d**) 5 u.c. sample with a backscattering angle of 114,5°. The blue curves simulate MEIS theoretical spectra for non-intermixed and fully stoichiometric LAO/STO heterostructures. Experimental spectra are plotted with red dots, whereas the best simulated hetero-structures are represented by a green curve. (**e**) La/(La+Sr) profile throughout the first atomic layers. The x coordinates locate the cations by the number of unit cells to the interface (+1 = first u.c. in STO, −1 = first u.c. in LAO …). The film contains a cumulative amount of 0.9 +/− 0.05 Sr in the 5 u.c. sample (thus 4.1 +/− 0.05 La) and 0.5 +/− 0.05 Sr in the 3 u.c. one (thus 2.5 +/− 0.05 La). The La counter-diffusion depths were similar for the two samples, with 0.8 La for 5 u.c., and 0.7 La for 3 u.c. films.

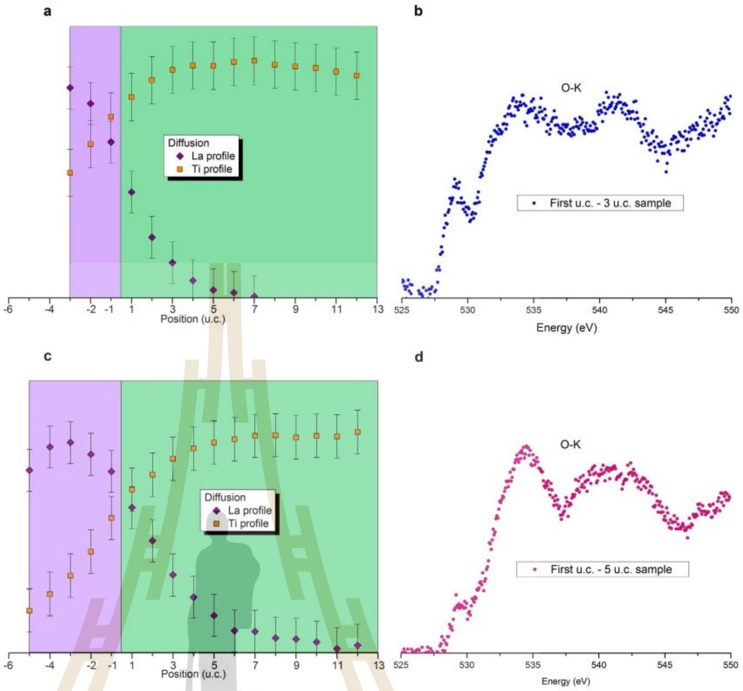

Figure 5. Cationic intermixing A-sites vs B-sites. (**a–c**) Diffusion profiles of Ti and La from EELS analyses for the (**a**) 3 u.c. (**c**) 5 u.c. sample. The x coordinates locate the cations by the number of unit cells to the interface (+1 = first u.c. in STO, −1 = first u.c. in LAO …). Ti diffused up to the film surface for both samples. Assuming a full occupancy of B-sites, Al would diffuse down to 3/4 u.c. into the substrate of the LAO(3 u.c.)/STO sample, and slightly deeper (4/5 u.c.) into the substrate of the LAO(5 u.c.)/STO sample. La atoms diffused down to about 5 u.c within the substrate of the 3 u.c. sample whereas it was found deeper (6/7 u.c.) into the thicker sample STO. The shallower diffusion depth of B cations compared to A cations results in $La_{Sr^\cdot}$ donor dopants that are not fully compensated by Al_{Ti}' acceptor dopants and can provide charge carriers. It can be noticed that La cations are detected at deeper depth by EELS than by MEIS. This is explained by the straggling of He^+ particles that decreases the sensibility of this ion beam analysis with the depth of the analyzed region. (**b–d**) EELS fine structure of the O-K edge recorded in the first u.c. under the film surface of the (**b**) 3 u.c. (**d**) 5 u.c. sample. The observed O-K pre-peak, between 529 and 531 eV, is characteristic of the Ti-O π^* hybridization[41] which confirmed the presence of Ti atoms within the very first unit cell of each samples.

(Fig. 5) compared to MEIS (Fig. 4) is explained by a weaker accuracy of MEIS quantification in the deeper layers due to stronger He^+ straggling.

However one main finding undermines the scenario of a donor-doped under-layer. The difference in the values of $x = La/(La + Sr)$ ratio just below the interface for 5 u.c ($x = 0.4 +/- 0.05$) and 3 u.c ($x = 0.3 +/- 0.05$) is not sufficient to explain the discrepancy in terms of electrical properties between these two samples. Therefore correlations of intermixing with the strain levels have been investigated.

Local Strain. Experimental stain profiles. The strain profiles have been obtained in a blocking mode configuration. In this mode the sample was oriented to maximize a second scattering of the He^+ particles for a given scattering angle, preventing them to escape the sample. Figure 6a,b present (E, θ_{sc}, N) maps for the 3 u.c. and 5 u.c. samples taken in a scattering geometry that promoted blocking in the [101] direction. The He^+ energy range was selected to analyze both Sr and La scattering centers. A shadowing effect in the distribution of the scattered ions distribution is observed, characteristic of these "blocking dip" patterns. The series of profiles $N = f(\theta_{sc})$ at given energies have been extracted to quantify the shift of the maximum dips as a function of energy. Then energies were converted into depth values with unit cell resolution (Further details are in the Supplementary Information).

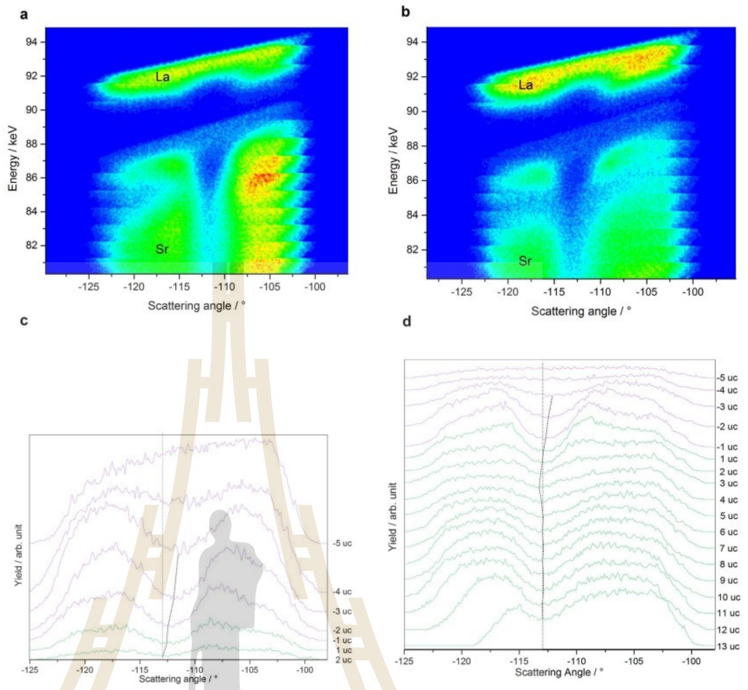

Figure 6. MEIS data in blocking mode. (**a**,**b**) MEIS blocking map (E_1, θ_{sc}, N) of the sample with a film thickness of (**a**) 3 u.c. (**b**) 5 u.c. (**c**,**d**) MEIS [101] blocking dips of the 5 u.c. sample, as a function of depth corresponding to (**c**) La atoms (**d**) Sr atoms located in the film (purple curves) and in the substrate (green curves). Dash-dotted lines are the position of the blocking dips for an unstrained cubic STO ($c/a = 1$). Dashed lines indicate the position of the blocking dips maxima for each unit cell. In the substrate, deviations of these positions from the dash-dotted line reveal structural distortions.

The series of extracted profiles are displayed in Fig. 6c,d for La and Sr. The scattering angle, θ_{bk}, inducing the blocking maximum (minimum of intensity) in the [101] direction, was located for each profile by fitting the dip regions with parabola. The variations of θ_{bk}, were then translated into variations of c/a ratio. The [101] blocking dips in the substrate at 13 u.c., for the 5 u.c. film, and at 14 u.c., for the 3 u.c. film, from the interface were assumed to belong to an unstrained cubic STO. The corresponding blocking angles were taken as the reference, θ_{bk}(ref).

Figure 7a,c present the variation in c/a for the 3 and 5 u.c. films calculated from θ_{bk} as a function of depth for He^+ backscattered on La (purple dots) and Sr (green dots). For both samples, the curves could be divided into three regions. The deeper probed parts of the substrate were unstrained ($c/a = 1$). Then an intermediate region was observed with $c/a > 1$ in the substrate starting from 9 u.c. for the thinner sample and from 5 u.c. for the thicker one and extending up to 2 u.c. below the interface. The maximum c/a was observed at depths of 5 u.c. and 4 u.c into the substrate for the 3 u.c. and 5 u.c. films, respectively. Finally the region extending from 2 u.c. below the interface up to the film surface exhibited $c/a < 1$. The differences between the two samples laid mainly in the thicknesses of these regions as will be discussed later.

We note that for a given depth, the c/a ratios calculated from scattering on La and Sr do not match. For blocking in [101] direction, this indicates that the distance between two A-site cations located on the diagonal of the (010) face is affected by intermixing. In the film, the Sr_{La}-La_{La} distance is longer than the La_{La}-La_{La} one, whereas in the substrate the La_{Sr}-Sr_{Sr} distance is shorter than the Sr_{Sr}-Sr_{Sr} one. Differences in cation radii as well as electrical charges of the hosted atoms could have induced distortions in the cell as well as a buckling of the layer. Such distortions around the hosted cations have been predicted by modelling (see the following sections).

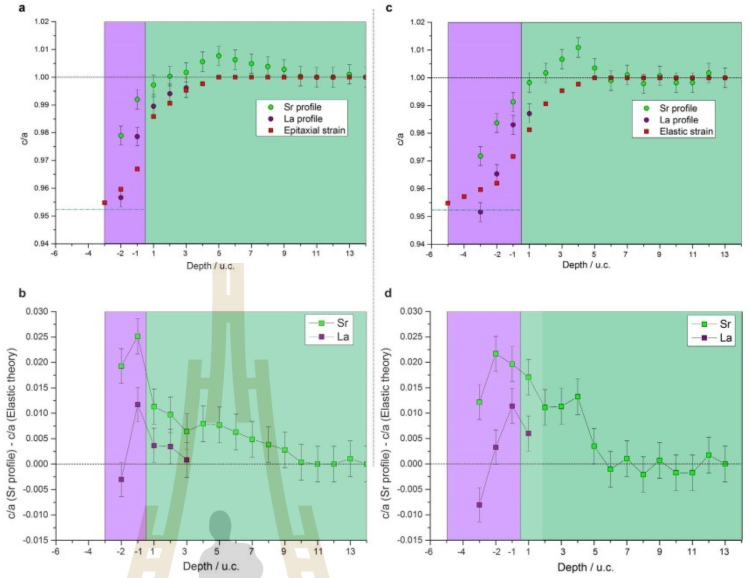

Figure 7. Profiles obtained from MEIS data in blocking mode. The x coordinates locate the cations by the number of unit cells to the interface (+1 = first u.c. in STO, −1 = first u.c. in LAO …). Each data point indicates the distance separating this cation to the A cation located in the above cell. (**a–c**) Profiles of c/a for samples with film thicknesses of (**a**) 3 u.c. (**c**) 5 u.c. Purple circles represent the c/a values around La atoms. Green circles represent the c/a values around Sr atoms. Red squares represent the theoretical c/a values for intermixed heterostructure assuming a sole elastic epitaxial strain. Relaxed cell parameters in this intermixed region were determined from their respective chemical profile obtained experimentally by MEIS random mode. The turquoise dash-dotted line indicates the theoretical c/a value for a fully epitaxial growth of LAO, ($a_{STO} = a_{LAO}$) and without intermixing. (**b–d**) Difference between the c/a values measured experimentally - from He^+ scattered from Sr and La atoms - and those calculated from epitaxial strain are plotted for the (**b**) 3 u.c. sample (**d**) 5 u.c. sample.

Origins of the strain. In order to investigate further the nature of the strain, we have evaluated the contribution of epitaxial strain to the total strain in these hetero-structures. These epitaxial strains were calculated from a purely elastic model based on unstrained cell parameters deduced, in the intermixed region, from Vegard's law between STO and LAO (Calculations are described in the Supplementary Information). The strength of this approach is that the intermixing profiles, obtained from MEIS random mode on the same samples, were used for these elastic calculations. The depth variations of c/a, as predicted from epitaxial elastic strain and based on the chemical profile depicted in Fig. 4e are plotted in red squares in Fig. 7a,c. The c/a ratio measured experimentally with MEIS blocking dips around the interface are clearly larger than the values predicted by purely elastic strains. Thus, epitaxial elastic strain cannot be the only factor that explains the strain level measured.

Figure 7b,d plot the differences between the experimental MEIS strain profiles and the theoretical epitaxial strains. The difference reached a maximum around the interface. Several mechanisms can lead to additional strain in such systems such as Jahn-Teller distortions due to the change in valence of Ti cations, ferroelectric-like distortions due to off-centering of cations and other distortions due to ionic defects such as strontium vacancies. The Ti^{3+} concentration was seen to be the highest near the interface. Since the d orbitals, empty for Ti^{4+}, are occupied by one electron for Ti^{3+}, removal of the degeneracy of the t_{2g} energy levels (d_{xy}, d_{xz}, d_{yz} orbitals) is expected. A first scenario would favor a stabilization of the d_{xz} and d_{yz} orbitals due to an elongation of the octahedron of the first STO cell subjected to in-plane compressive stresses from the film. The additional c-lattice expansion measured compared to the strain provided by epitaxial elastic strain could be explained by this Jahn-Teller-like effect[20–23]. However a second scenario would imply a pure Jahn-Teller effect that stabilizes the d_{xy} orbitals and induces a contraction of the TiO_6 octahedron[11]. The observed elongation of the cell does not exclude such a contraction of the octahedron, through a buckling of Sr-O-Sr chains[11], where the oxygen anion planes depart from the cation ones, as was emphasized using first-principles calculations[42].

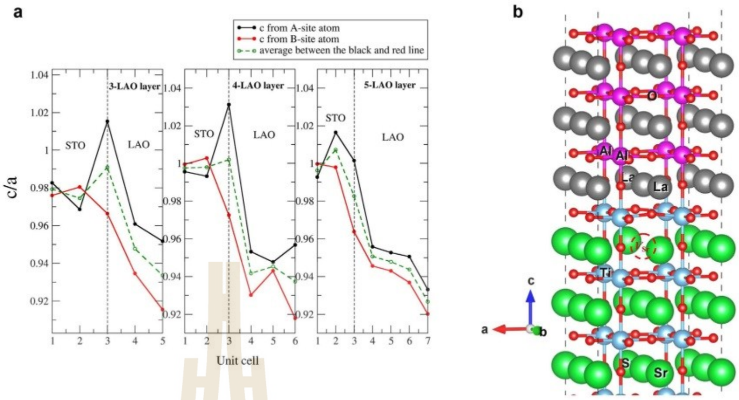

Figure 8. Modeling results. (**a**) Calculated c/a in non-intermixed layers of LAO on a 5 layer STO calculated in a symmetric slab geometry. (The x coordinate "3" for the black curve indicates the La-Sr distance across the interface and corresponds to the x coordinate "1" in Fig. 7). (**b**) Relaxation around a strontium vacancy located in the first u.c. under the interface. The V_{Sr}'' is indicated by a dashed circle. One can see the buckling of the layer above it and the O moving away from it. One can also see the La and Sr directly above the V_{Sr}'' to move toward it. The Ti-Ti distances in the c-direction surrounding the vacancy containing layer is 0.1 Å smaller than in the layer below it without vacancy.

Nevertheless the low concentration of Ti^{3+} indicates that other additional origins for this cell distortion must be searched. Ferroelectric-like distortions were also hypothesized to be directly driving the interface electrical characteristics[21]. While they might contribute around the interface, as Ti cations on HAADF images were seen off centered in the 10 u.c. film (Fig. 1a), they cannot explain the distortions seen deeper in the substrate.

A third factor that can influence the lattice strain is the presence of cation vacancies. Owing to their high formation energies, titanium vacancies $V_{Ti}^{4'}$ will not be considered[43,44]. Strontium vacancy formation is coupled to the creation of oxygen vacancies via Schottky reactions, Frenkel pairs being energetically less favorable[45]. $V_{Sr}'' - V_O''$ defect complexes could be formed during the processing of the STO substrate, after the melt-growth, upon cooling the ingot. V_{Sr}'' concentration in the substrate could either exceed their equilibrium concentration at room temperature due to their low diffusion rates, $V_O^{\cdot\cdot}$ being more mobile, or can be annealed to near equilibrium concentrations. Strontium vacancies could also be formed on the substrate surface sublayer due to Sr-La intermixing. At the oxygen partial pressure used, the La donors are partially compensated by V_{Sr}'' (ionic compensation)[46], the film being a sink for the expelled Sr ions. The lower level of electron compensation at such oxygen partial pressure could explain the high valence measured for Ti cations. Freedman *et al.*[44] found that a strontium vacancy induces an overall expansive strain although the nearby relaxation may differ. As in-plane parameters are more constrained, this may result in an expansion of the cell dimension in the growth direction[39,47]. The reduction of the 2D charge confinement along the c-axis at LAO/STO interface when the substrate is subjected to in-plane compression has been reported[48–50], and explained by a dilution of the interfacial charge carrier density, with the mobile charges transferred deeper in the STO substrate.

Modeling of the structural relaxation around hetero-interface by first-principles calculations.

Structural relaxation around abrupt interfaces. For comparison with the measured strain profiles, we first calculated the structural relaxation for perfect non intermixed structures as reference. Figure 8a reports the c/a ratio in each layer. Here "a" is the common in-plane lattice constant throughout the cell which is set by the unstrained STO lattice constant. The "c" for each unit cell layer is determined either from the A-cation (La or Sr) distance perpendicular to the interface (black curve, to be compared with La or Sr profiles of Fig. 7) or the B-cation (Al or Ti) distance perpendicular to the interface (red curve) or from the average of these A-A and B-B distances (dashed green line). Within linear elastic theory, as explained in the Supplementary Information, the c/a ratio can be calculated for a pure non-intermixed LAO pseudomorphically (biaxially) strained on STO. This predicts a c/a = 0.95, (see blue dashed line in the film region of Fig. 7a,c) which one can see in Fig. 8a is close to the value obtained from the first-principles calculation in the middle of the LAO layer. In agreement with Pentcheva *et al.*[51], we find a buckling of the layers, with the oxygens moving toward the surface relative to the cations in each layer. However, we see that at the free surface layer the local c/a is significantly smaller (0.93 on the average curve) because of surface relaxation that induced a significant decrease of the buckling for top surface AlO_2 layer. Details can be found in Fongkaew *et al.*[42]. The c/a calculated from elastic theory, shown as red squares in Fig. 7, assumes that the local lattice constant is purely determined by Vegard's law based on the degree of intermixing experimentally measured in each layer but does not include this relaxation effect. Adding this effect would make the slope slightly stronger downward toward the surface and would improve the agreement with experiment slightly.

We now address the discussion of the c/a overshoot in the STO region near the interface compared to the elastic model. The calculations suggest that the c/a measured as distance between A cations (black curve in Fig. 8a) decreases from the interface toward the STO. This occurs for both 3 u.c. and 5 u.c. heterostructures, although the highest c/a occurs right at the interface for the 3 u.c. (or 4 u.c.) case and one layer deeper in the STO in the 5 u.c. case. This difference is related to distinct buckling modes. In the 3 u.c. case, the Sr move away from the interface relative to the O in the same layer, whereas in the 5 u.c. case, they move toward the interface. Our modelling shows that, in addition to the variation of the c/a due to intermixing which is modeled by the elasticity theory in Fig. 7 (red squares), there is a trend due to the relaxation of the layers which helps to explain the increased c/a near the interface. Our calculations unfortunately do not allow us to gauge in much detail how this varies as function of distance into the STO for different cases because the thickness of the STO in our model calculation is too small to allow for such an analysis.

Structural relaxation around intermixed interfaces. In order to approach the intermixed case, we have studied the behavior near a Ti and a Sr on the LAO side[42]. On one hand, if we swap a Ti and Al across the interface, both move farther away from the interface, as shown in Figures 10 and 11 of Fongkaew *et al.*[42]. This means the Ti-Ti distance and hence c/a measured locally from B cations across the interface would increase while the Ti-Al with the next AlO_2 layer toward the surface would decrease. This could explain the trend of the Fig. 7b,d curves departing from linear elasticity theory.

On the other hand, if we replace Sr by La in a layer near the interface in STO and vice versa, we find that the buckling of the layer is reduced for the swapped atoms. In the film, Sr moves out less toward the surface than La. In other words, relative to La, Sr is closer to the interface. This means that the c/a measured from the Sr atoms in the film would be larger than from the La atoms. This is in agreement with the measured MEIS profiles (Fig. 7) showing a larger interlayer distance measured from Sr_{La} blocking curves than from La_{La} ones. The effects of these various intermixings on the charge density accumulated at the interface in the 2DEG, the potential profiles and electronic structure are discussed by Fongkaew *et al.*[42].

Structural relaxation near a strontium vacancy. The relaxed structure near a Sr vacancy at the interface has also been modeled. The main result of this modeling is that near the Sr vacancy there is an outward relaxation of the oxygens mainly in interface TiO_2 layer above it. The Ti-Ti distance in the c-direction for the layer without V_{Sr}'' is 3.77 Å, while in the layer with V_{Sr}'' it reaches 3.967 Å. Both these tendencies agree with Freedman *et al.*[44] who have studied the long-range and short-range strain distortions caused by Sr-vacancies using a shell force-constant model including electrostatic effects. Our calculations however show a local decreasing of c/a (as measured from either the A or B atoms) rather than a crystal expansion as indicated by Freedman's calculations. However our model does not allow us to reliably determine the long-range strain effect because of the high concentration of V_{Sr}'' in the model. In Fig. 8b we can clearly see the O above the V_{Sr}'' moving away from the vacancy, and one can also see the La and Sr directly above and below it to move toward the vacancy. This local distortion may be compensated by a long-range overall expansive strain (as indicated by Freedman's calculations).

Conducting versus insulating interfaces. It has been shown that the levels of intermixing and titanium reduction did not differ sufficiently between the 3 and 5 u.c. samples to explain the large discrepancies measured in their electrical conductivities. The main difference lies in the strain field developed into the two STO substrates. Figure 7b,d show that, if regions with c/a > 1 extends deeper in the substrate of the 3 u.c. sample, the area enclosed between c/a > 1 and c/a = 1 in the substrates are similar for the two samples. This indicates a difference in the distributions of the Sr vacancies more than in their concentrations. The lower dipolar field built in the thinner film induces a weaker V_{Sr}'' attraction toward the interface than in the 5 u.c. sample, explaining the deeper region with c/a > 1 in the 3 u.c. assembly. This in turn would increase the dilution of the charge carrier and reduce the conductivity with respect to the 5 u.c. sample.

In the conductive samples the density of electrons transferred to the interface is not sufficient to cancel the electrical field, and structural distortions or point defects are still present to screen the remaining field. The in-plane compression strains observed are reported to reduce the concentration and mobility of the charge carriers. The point defects are known to act as trapping or scattering centers.

This study suggests a competition between electronic compensation and donor doping on the one hand, and polar distortions and point defects on the other hand, to balance the electrostatic field formed due to polarization discontinuity in the polar film, the structural relaxation playing a crucial role on the electronic conduction of such heterostructures.

Conclusion

MEIS was used to correlate the intermixing and the structural distortions with an atomic depth resolution within LAO/STO heterostructures above and below the critical thickness for insulator/conductor transition. In addition, the oxidation state of Ti atoms and the O vacancies were characterized by EELS. Neither electronic reconstruction nor anionic vacancies alone can explain the carrier density observed. Intermixing is demonstrated in the two samples, excluding a donor doping scenario as single mechanism. The measured c/a ratio are larger than those predicted by epitaxial strains obtained from an elastic calculation taking intermixing into account. This indicates that compressive electrostatic forces developed around the interface, and extended deeper into the substrate in the 3 u.c. sample, reducing the confinement and diluting the interfacial charge carrier. A complex competition between donor doping, structural distortions and reconstruction, and ionic compensation is revealed. This paper highlights the complexity of the scenario occurring at the interface responsible for the conductivity in LAO/STO heterostructures.

Manuscript submitted in Scientific reports

Methods

Film Growth. $LaAlO_3$ (LAO) films on $SrTiO_3$ (STO) (001) substrates were grown by Pulsed-Laser Deposition (PLD). Prior to the film growth, the $SrTiO_3$ (STO) substrates were etched with a chemical solution of ammonium fluoride and hydrofluoric acid at pH = 6 to obtain a TiO_2-terminated surface and then annealed at 950 °C for one hour in an oxygen-rich atmosphere. The surface morphology was checked with AFM (Agilent Technologies). In the PLD chamber the base pressure of the chamber was 10^{-6} Torr and was increased to an O_2 partial pressure of 10^{-4} Torr via an MKS Mass Flow Controller and Cold Cathode. The growth was performed at a temperature of about 750 °C with an initial ramping rate of about 10 °C/min up to 500 °C and then about 30 °C/min up to the deposition temperature. The LAO target was ablated using a 248 nm KrF excimer (Coherent Inc.) laser with a fluence of about 1.2 J/cm^2 and a repetition rate of 2 Hz. LAO films were grown at a rate of 15 pulses per layer and the growth rate was followed *in situ* by oscillations in Reflection High-Energy Electron Diffraction (RHEED) patterns (STAIB Instruments). After deposition, films were brought to room temperature at cooling rates of about 10 °C/min then about 5 °C/min.

Following this protocol, films 3 and 5 unit cells (u.c.) thick were grown on TiO_2-terminated STO substrates to optimize the resolution in MEIS, compared to thicker films.

Scanning Transmission Electron Microscopy and Electron Energy-Loss spectroscopy. The growth epitaxy and interface coherency in the experimental conditions used for PLD were analyzed on both samples by Scanning Transmission Electron Microscopy (STEM) using a Nion UltraSTEM 200 operating at 100 kV and a High-Angle Annular Dark-Field (HAADF) detector with an inner collection angle of 70 mrad. The microscope was equipped with a spherical aberration corrector, which enabled a probe-size of under 0.1 nm to be obtained. EELS spectra were acquired with a Gatan Enfina spectrometer and a custom-made EELS camera. The energy resolution attained for this set of experiments was 0.5 eV.

The O-K, Ti-$L_{2,3}$, and La-$M_{4,5}$ absorption edges were recorded to probe the oxygen vacancy concentration throughout the sample, titanium oxidation state around the $LaAlO_3/SrTiO_3$ hetero-interface, and the diffusion of A-site cations vs B-site cations.

Electrical characterization. Electrical transport measurements were made in a physical property measurement system (PPMS, Quantum Design Inc.) with temperature varying from 2 K to room temperature. Sheet resistance, carrier density and Hall mobility were obtained by Hall effect measurements in a four-probe Van der Pauw configuration. The electrical contacts to LAO/STO interface were achieved by direct wirebonding of aluminum wire to the sample. After confirming the Ohmic behavior of contacts, four-probe sheet resistance and Hall resistance of 5 u.c. sample were measured using standard lock-in technique with less than 1 mV excitation at 13 Hz. For the insulating 3 u.c. sample, lock-in measurement of resistance was not possible. D.C. current-voltage measurements indicated a resistance higher than $>100\,M\Omega$.

MEIS. Medium Energy Ion Spectroscopy (MEIS) was performed to investigate the chemical and strain profiles of the LAO/STO heterostructures near the samples surface, using a He^+ collimated beam of 100 keV hitting the film surface at a given incident angle relative to the crystal cell directions. The energy E and angle θ_{sc} of the scattered He^+ that escape the solid are analyzed simultaneously using a toroidal electrostatic analyzer with an energy resolution $\Delta E/E = 3 \times 10^{-3}$ and an angular resolution of 0.1°. The incident angle was carefully chosen to induce two specific scattering geometries, the random and blocking modes. Further details can be found in the Supplementary Information.

Modeling. First-principles calculations were performed within the density functional theory using PBE exchange correlation generalized gradient approximation[52,53] and projector augmented wave potentials[54,55] in the VASP code[56,57]. The supercells were set up in a symmetric way with 5.5 (001) oriented STO layers and either 3, 4, or 5 unit cell LAO layers on either side, followed by a sufficiently thick vacuum region. The systems were fully relaxed until all forces are smaller than 0.02 meV/Å and the plane wave cut-off used was 500 eV. For k-space integration, the Monkhorst-Pack scheme with $7 \times 7 \times 1$ k-point sampling was employed.

References

1. Ohtomo, A. & Hwang, H. Y. A high-mobility electron gas at the $LaAlO_3/SrTiO_3$ heterointerface. *Nature* **427,** 423–426 (2004).
2. Pauli, S. A. & Willmott, P. R. Conducting interfaces between polar and non-polar insulating perovskites. *J. Phys. Condens. Matter* **20,** 264012 (2008).
3. Thiel, S., Hammerl, G., Schmehl, A., Schneider, C. W. & Mannhart, J. Tunable quasi-two-dimensional electron gases in oxide heterostructures. *Science* **313,** 1942–1946 (2006).
4. Huijben, M. *et al.* Structure-Property Relation of $SrTiO_3/LaAlO_3$ Interfaces. *Adv. Mater.* **21,** 1665–1677 (2009).
5. Zubko, P., Gariglio, S., Gabay, M., Ghosez, P. & Triscone, J.-M. Interface Physics in Complex Oxide Heterostructures. *Annu. Rev. Condens. Matter Phys.* **2,** 141–165 (2011).
6. Sato, H. K., Bell, C., Hikita, Y. & Hwang, H. Y. Stoichiometry control of the electronic properties of the $LaAlO_3/SrTiO_3$ heterointerface. *Appl. Phys. Lett.* **102,** 251602 (2013).
7. Schoofs, F. *et al.* Optimized transport properties of $LaAlO_3/SrTiO_3$ heterointerfaces by variation of pulsed laser fluence. *J. Phys. Condens. Matter* **23,** 305002 (2011).
8. Chen, Y. Z. *et al.* On the origin of metallic conductivity at the interface of $LaAlO_3/SrTiO_3$. *Appl. Surf. Sci.* **258,** 9242–9245 (2012).
9. Maurice, J.-L. *et al.* Electron energy loss spectroscopy determination of Ti oxidation state at the (001) $LaAlO_3/SrTiO_3$ interface as a function of $LaAlO_3$ growth conditions. *Eur. Lett* **82,** 17003 (2008).
10. Stornaiuolo, D. *et al.* In-plane electronic confinement in superconducting $LaAlO_3/SrTiO_3$ nanostructures. *Appl. Phys. Lett.* **101,** 222601 (2012).
11. Vonk, V. *et al.* Interface structure of $SrTiO_3/LaAlO_3$ at elevated temperatures studied *in situ* by synchrotron X rays. *Phys Rev B* 75, 235417 (2007).

12. Mannhart, J., Blank, D. H. A., Hwang, H. Y., Millis, A. J. & Triscone, J.-M. Two-dimensional electron gases at oxide interfaces. *MRS Bull.* **33,** 1027–1034 (2008).
13. Connell, J. G., Isaac, B. J., Ekanayake, G. B., Strachan, D. R. & Seo, S. S. A. Preparation of atomically flat $SrTiO_3$ surfaces using a deionized-water leaching and thermal annealing procedure. *Appl. Phys. Lett.* **101,** 251607 (2012).
14. Kalabukhov, A. S. *et al.* Cationic disorder and phase segregation in $LaAlO_3$/$SrTiO_3$ heterointerfaces evidenced by medium-energy ion spectroscopy. *Phys. Rev. Lett.* **103** (2009).
15. Fête, A. *et al.* Growth-induced electron mobility enhancement at the $LaAlO_3$/$SrTiO_3$ interface. *Appl. Phys. Lett.* **106,** 51604 (2015).
16. Verbeeck, J. *et al.* Electronic reconstruction at n -type $SrTiO_3$/$LaAlO_3$ interfaces. *Phys. Rev. B* **81** (2010).
17. Wei, W. & Sehirlioglu, A. Strain relaxation analysis of $LaAlO_3$/$SrTiO_3$ heterostructure using reciprocal lattice mapping. *Appl. Phys. Lett.* **100,** 71901 (2012).
18. Annadi, A. *et al.* Electronic correlation and strain effects at the interfaces between polar and nonpolar complex oxides. *Phys Rev B* **86,** 85450 (2012).
19. Pauli, S. A. *et al.* Evolution of the Interfacial Structure of $LaAlO_3$ on $SrTiO_3$. *Phys. Rev. Lett.* **106,** 36101 (2011).
20. Maurice, J.-L. *et al.* Electronic conductivity and structural distortion at the interface between insulators $SrTiO_3$ and $LaAlO_3$. *Phys. Status Solidi A* **203,** 2145–2145 (2006).
21. Schwingenschlögl, U. & Schuster, C. Interface relaxation and electrostatic charge depletion in the oxide heterostructure $LaAlO_3$/$SrTiO_3$. *EPL Europhys. Lett.* **86,** 27005 (2009).
22. Willmott, P. R. *et al.* Structural basis for the conducting interface between $LaAlO_3$ and $SrTiO_3$. *Phys Rev Lett* **99,** 155502 (2007).
23. Schoofs, F. *et al.* Carrier density modulation by structural distortions at modified $LaAlO_3$/$SrTiO_3$ interfaces. *J. Phys. Condens. Matter Inst. Phys. J.* **25,** 175005 (2013).
24. Nakagawa, N., Hwang, H. Y. & Muller, D. A. Why some interfaces cannot be sharp. *Nat. Mater* **5,** 204–209 (2006).
25. Jia, C. L. *et al.* Oxygen octahedron reconstruction in the $SrTiO_3$/$LaAlO_3$ heterointerfaces investigated using aberration-corrected ultrahigh-resolution transmission electron microscopy. *Phys. Rev. B* **79** (2009).
26. Chambers, S. A. *et al.* Instability, Intermixing and Electronic Structure at the Epitaxial $LaAlO_3$/$SrTiO_3$(001) Heterojunction. *Surf. Sci. Rep.* **65,** 317–352 (2010).
27. Salvinelli, G., Drera, G., Giampietri, A. & Sangaletti, L. Layer-resolved cation diffusion and stoichiometry at the $LaAlO_3$/$SrTiO_3$ heterointerface probed by X-ray photoemission experiments and site occupancy modeling. *ACS Appl. Mater. Interfaces* **7,** 25648–25657 (2015).
28. Kalabukhov, A. S. *et al.* Effect of oxygen vacancies in the $SrTiO_3$ substrate on the electrical properties of the $LaAlO_3$/$SrTiO_3$ interface. *Phys Rev B* **75,** 121404(R) (2007).
29. Chambers, S. A. Understanding the mechanism of conductivity at the $LaAlO_3$/$SrTiO_3$(001) interface. *Surf. Sci.* **605,** 1133–1140 (2011).
30. Liu, Z. Q. *et al.* Dominant role of oxygen vacancies in electrical properties of unannealed $LaAlO_3$/$SrTiO_3$ interfaces. *J. Appl. Phys.* **115,** 54303 (2014).
31. Warusawithana, M. P. *et al.* $LaAlO_3$ stoichiometry is key to electron liquid formation at $LaAlO_3$/$SrTiO_3$ interfaces. *Nat. Commun.* **4,** (2013).
32. Jalabert, D., Curé, Y., Hestroffer, K., Niquet, Y. M. & Daudin, B. Strain state of GaN nanodisks in AlN nanowires studied by medium energy ion spectroscopy. *Nanotechnology* **23,** 425703 (2012).
33. Min, B.-G. *et al.* Behavior of strain at a thin Ge pile-up layer formed by dry oxidation of a Si0.7Ge0.3 film. *Thin Solid Films* **518,** 2065–2069 (2010).
34. Mannhart, J. & Schlom, D. G. Oxide Interfaces–An Opportunity for Electronics. *Science* **327,** 1607–1611 (2010).
35. Breitschaft, M. *et al.* Two-dimensional electron liquid state at $LaAlO_3$-$SrTiO_3$ interfaces. *Phys. Rev. B* **81,** 153414 (2010).
36. Cancellieri, C. *et al.* Influence of the growth conditions on the $LaAlO_3$/$SrTiO_3$ interface electronic properties. *EPL Europhys. Lett.* **91,** 17004 (2010).
37. Basletic, M. *et al.* Mapping the spatial distribution of charge carriers in $LaAlO_3$/$SrTiO_3$ heterostructures. *Nat. Mater.* **7,** 621–625 (2008).
38. Gariglio, S., Fête, A. & Triscone, J.-M. Electron confinement at the $LaAlO_3$/$SrTiO_3$ interface. *J. Phys. Condens. Matter* **27,** 283201 (2015).
39. Vonk, V. *et al.* Polar-discontinuity-retaining A -site intermixing and vacancies at $SrTiO_3$/$LaAlO_3$ interfaces. *Phys. Rev. B* **85** (2012).
40. Muller, D. A., Nakagawa, N., Ohtomo, A., Grazul, J. L. & Hwang, H. Y. Atomic-scale imaging of nanoengineered oxygen vacancy profiles in $SrTiO_3$. *Nature* **430,** 657–661 (2004).
41. Kourkoutis, L. F. *et al.* Atomic-resolution spectroscopic imaging of oxide interfaces. *Philos. Mag.* **90,** 4731–4749 (2010).
42. Fongkaew, I., Limpijumnnong, S. & Lambrecht, W. R. L. Effects of structural relaxation, interdiffusion, and surface termination on two-dimensional electron gas formation at the $LaAlO_3$/$SrTiO_3$ interface. *Phys. Rev. B* **92,** 155416 (2015).
43. Gunkel, F. *et al.* Transport limits in defect-engineered $LaAlO_3$/$SrTiO_3$ bilayers. *Nanoscale* **7,** 1013–1022 (2015).
44. Freedman, D. A., Roundy, D. & Arias, T. A. Elastic effects of vacancies in strontium titanate: Short- and long-range strain fields, elastic dipole tensors, and chemical strain. *Phys Rev B* **80,** 64108 (2009).
45. Liu, B. *et al.* Composition dependent intrinsic defect structures in $SrTiO_3$. *Phys. Chem. Chem. Phys.* **16,** 15590 (2014).
46. Kozuka, Y., Hikita, Y., Bell, C. & Hwang, H. Y. Dramatic mobility enhancements in doped $SrTiO_3$ thin films by defect management. *Appl. Phys. Lett.* **97,** 12107 (2010).
47. Ohnishi, T., Shibuya, K., Yamamoto, T. & Lippmaa, M. Defects and transport in complex oxide thin films. *J. Appl. Phys.* **103,** 103703 (2008).
48. Janotti, A., Steiauf, D. & Van de Walle, C. G. Strain effects on the electronic structure of $SrTiO_3$: Toward high electron mobilities. *Phys. Rev. B* **84,** 201304(R) (2011).
49. Nazir, S. & Yang, K. First-principles characterization of the critical thickness for forming metallic states in strained $LaAlO_3$/$SrTiO_3$ (001) heterostructure. *ACS Appl. Mater. Interfaces* **6,** 22351–22358 (2014).
50. Bark, C. W. *et al.* Tailoring a two-dimensional electron gas at the $LaAlO_3$/$SrTiO_3$ (001) interface by epitaxial strain. *Proc. Natl. Acad. Sci.* **108,** 4720–4724 (2011).
51. Pentcheva, R. & Pickett, W. E. Avoiding the polarization catastrophe in $LaAlO_3$ overlayers on $SrTiO_3$ through polar distortion. *Phys. Rev. Lett.* **102,** 107602 (2009).
52. Perdew, J. P., Burke, K. & Ernzerhof, M. Generalized Gradient Approximation Made Simple. *Phys. Rev. Lett.* **77,** 3865–3868 (1996).
53. Perdew, J. P., Burke, K. & Ernzerhof, M. Generalized Gradient Approximation Made Simple [*Phys. Rev. Lett.* **77,** 3865 (1996)]. *Phys. Rev. Lett.* **78,** 1396–1396 (1997).
54. Blöchl, P. E. Projector augmented-wave method. *Phys. Rev. B* **50,** 17953–17979 (1994).
55. Kresse, G. & Joubert, D. From ultrasoft pseudopotentials to the projector augmented-wave method. *Phys. Rev. B* **59,** 1758–1775 (1999).
56. Kresse, G. & Furthmüller, J. Efficiency of ab-initio total energy calculations for metals and semiconductors using a plane-wave basis set. *Comput. Mater. Sci.* **6,** 15–50 (1996).
57. Kresse, null. & Furthmüller, null. Efficient iterative schemes for ab initio total-energy calculations using a plane-wave basis set. *Phys. Rev. B Condens. Matter* **54,** 11169–11186 (1996).

Manuscript submitted in Scientific reports

Acknowledgements

The MEIS measurements were performed at the laboratory CEA tech/Leti/DTSI/SCMC in Grenoble and François Pierre and Philippe Charrault are gratefully acknowledged. The authors acknowledge financial support from the CNRS-CEA "METSA" French network (FR CNRS 3507) for the USTEM experiments conducted on the LPS (Université Paris-Sud) platform. This work is supported by Air Force Office of Scientific Research (AFOSR) Grant FA 9550-12-1-0441.

Author Contributions

H.Z. and M.H.B. collected the data and performed UltraSTEM, EELS, MEIS analysis. D.J. conceived, carried out the MEIS experiments, and deeply helped in the analysis of MEIS data. M.W. realized the UltraSTEM characterizations. R.A and A.S carried out the film growth by PLD. I.F and W.R.L.L. performed the first-principle calculations. N.J.G and X.P.A.G. collected the electrical measurements. P.B. contributed to the interpretation of the MEIS results. H.Z., M.H.B., A.S. and W.R.L.L. participated to the writing of the manuscript. All authors discussed the results, reviewed, and revised the manuscript.

Additional Information

Supplementary information accompanies this paper at http://www.nature.com/srep

Competing financial interests: The authors declare no competing financial interests.

How to cite this article: Zaid, H. *et al.* Atomic-resolved depth profile of strain and cation intermixing around $LaAlO_3/SrTiO_3$ interfaces. *Sci. Rep.* **6**, 28118; doi: 10.1038/srep28118 (2016).

Manuscript submitted in Physical Review B

PHYSICAL REVIEW B **92**, 155416 (2015)

Effects of structural relaxation, interdiffusion, and surface termination on two-dimensional electron gas formation at the $LaAlO_3/SrTiO_3$ (001) interface

Ittipon Fongkaew,[1,2,3] Sukit Limpijumnong,[2,3] and Walter R. L. Lambrecht[1]
[1]*Department of Physics, Case Western Reserve University, Cleveland, Ohio 44106-7079, USA*
[2]*School of Physics and NANOTEC-SUT Center of Excellence on Advanced Functional Nanomaterials, Suranaree University of Technology, Nakhon Rachasima 30000, Thailand*
[3]*Thailand Center of Excellence in Physics (ThEP Center), Commission on Higher Education, Bangkok 10400, Thailand*

(Received 29 July 2015; published 12 October 2015; corrected 9 March 2016)

First-principles (generalized gradient approximation) calculations are presented for symmetric $LaAlO_3/SrTiO_3/LaAlO_3$ (001) orientation slab models with varying thickness (3, 4, 5 unit cells) of the $LaAlO_3$ (LAO) layers. The buckling of the layers and their effect on the slope of the layer-averaged electrostatic potential and layer-projected densities of states are studied. We find the buckling of the LAO layers to increase from the interface toward the surface, while the buckling of the AlO_2 layers decreases toward the surface. The critical layer thickness for obtaining electrons in the Ti-d band of the $SrTiO_3$ (STO) is determined to be 4 layers within this model. Beyond this point, the sloped potential is confined to the 4 layers of LAO nearest to the interface. The electrons in the Ti-d states extend throughout the 5.5-layer-thick STO region of our calculation. The sheet charge density of electrons in the STO conduction band is determined and found to be of order $(1\text{–}3) \times 10^{13}\ e/\mathrm{cm}^2$, in fair agreement with experimental values and an order of magnitude smaller than required by the polar discontinuity model. We also find still a significant change in the sheet density between the 4-LAO layer and 5-LAO layer model. It results in only d_{xy}-like states being occupied for the 4-LAO layer case but other t_{2g} bands becoming occupied for the 5-LAO layer case. The effects of H adsorption on surface O and OH adsorption on the surface Al are investigated for a model with 1/8 coverage of H and 1/4 coverage of OH. The former leads to electron doping of the STO layer while the latter leads to a p-type surface. When both together are present, they cancel each other. For high H coverage, we find that only a certain fraction of the electrons donated by H can be accommodated at the interface while the remaining go to the surface and lead to a reversal of the slope of the potential in the LAO region. The addition of 25% Ti on Al sites into the first layer of LAO already leads to a cancellation of the field in the LAO layer. It does not lead to Ti^{3+} embedded in the LAO site but rather the Ti donates its additional electron to the interface two-dimensional electron gas (2DEG) confined to the STO TiO_2 layers. A swap of Al with Ti in the layers closest to the interface does not produce a 2DEG because the Al in the TiO_2 interface layer provides holes compensating the electron doping from the Ti. Interdiffusion of Sr and La between the layers nearest to the interface does not lead to a 2DEG. These species are just electron donors in their own respective materials. In a swap compensating dipoles result from the different nuclear charges but the electronic states near the gap are not affected. Thus no 2DEG formation occurs. On the other hand a Sr_{La} placed in the middle of the LAO layer is found to facilitate electron transfer from the surface to the interface and could lead to a 2DEG. However, the latter had only a small sheet density.

DOI: 10.1103/PhysRevB.92.155416 PACS number(s): 73.20.At

I. INTRODUCTION

The two-dimensional electron gas (2DEG) formation at the $LaAlO_3/SrTiO_3$ (or LAO/STO) interfaces has received a great deal of attention since its discovery by Ohtomo and Hwang [1]. Several mechanisms have been proposed for this phenomenon: (1) electronic reconstruction to avoid the polar discontinuity, (2) oxygen vacancies in the STO or LAO layers, (3) interdiffusion of Ti or Sr into the LAO layer and vice versa, or combinations of the above mechanisms. It is now well established that the role of oxygen vacancies in the STO depends strongly on the growth conditions, in particular the oxygen partial pressure during pulsed laser deposition. However it can be controlled by annealing and is assumed to make a negligible contribution for sheet carrier densities of order $10^{13}\ e/\mathrm{cm}^2$. There has also been ample evidence for some degree of interdiffusion, most recently through a medium-energy ion scattering (MEIS) study by Zaid *et al.* [2]. The gradual change in c/a ratio observed in these measurements could be well explained by models including a gradually changing interdiffusion model.

The original polar discontinuity model [1] is based on the idea that in STO each layer SrO or TiO_2 is neutral but in LAO the nominal charge per unit cell alternates between -1 for the LaO and $+1$ for the AlO_2 layers. This discontinuity would set up a field with an ever increasing potential in the LAO layer, until the potential difference exceeds the band gap and charge is transferred from the surface to the interface. Within this model, a net charge of 1/2 electron per unit cell corresponding to about $3 \times 10^{14}\ e/\mathrm{cm}^2$ is required at the interface to cancel the field. On the other hand, experimentally one usually finds a significantly lower charge density. This model also predicts a corresponding hole gas at the surface, which has not been observed. Evidence for a sloped potential in the LAO region has not been established conclusively experimentally either. While in principle explaining the presence of a critical layer thickness for observing a 2DEG, the quantitative determination of the critical layer thickness is complicated by the possibility of relaxation of each layer [3,4], the fact that the gap is underestimated by the usual semilocal density functional calculations, and so on. Janotti and Van de Walle [5] took a somewhat different viewpoint assuming that the discontinuity is immediately met at the interface by the interface bond configuration but proposed that the interface charge may subsequently be partially transferred to the surface depending on the configuration considered and the surface passivation. They used this model to address the question of why less than $1/2$ electron per unit cell area is often found at the interface. Other possible explanations are that part of the charge at the interface is not detected in transport because it resides in less mobile interface states [6]. A related question is why a 2D hole gas is not observed at the surface. Several possibilities have been offered for this asymmetry between the n- and p-type interface [5,7,8]. Another possibility is that the holes form self-trapped polarons in these oxides [9].

It is by now more or less accepted that the above mentioned mechanisms are not mutually exclusive but may each contribute to the 2DEG formation to a varying degree depending on growth conditions and so on. The role of defects has been addressed recently by Yu and Zunger [10]. They explained the occurrence of a critical layer thickness in terms of the energy of formation of oxygen vacancies on the LAO surface which becomes negative when the layer exceeds a critical thickness. However, this dependence of the energy of formation of the $V_{\rm O}$ on the position of the $V_{\rm O}$ relative to the interface results itself from the sloped potential, as was pointed out in several earlier papers [8,11,12]. However Yu and Zunger proposed that the discontinuity for thicknesses below the critical thickness is already removed by the antisite defects of Ti on Al sites at the surface transferring its electron to an Al on Ti sites across the interface on the STO side. So, it is then not clear why $V_{\rm O}$ would still form at the surface if interdiffusion is already removing the sloped potential.

On the other hand, in the classic polar catastrophe explanation, the slope in the LAO region is not removed since the Fermi level becomes pinned slightly below the valence band maximum (VBM) of the $\rm AlO_2$ surface layer of LAO and slightly above the conduction band minimum (CBM) at the STO ($\rm TiO_2$) interface layer. Lee and Demkov [13] claimed that the polar catastrophe model could quantitatively explain the charge density at the interface. Using the LDA + U method, they found that it resides in interface states of the Ti below the STO CBM.

The surface termination is also known to play an important role. This is most clear from the experiments by Cen *et al.* [14–18] in which it was shown that regions of 2DEG at the buried interface can be induced by modifying the surface adsorbates with an appropriately biased atomic force microscopy (AFM) tip.

The literature on the LAO/STO at this point in time has become too extensive to review comprehensively, so the above is only a sampling of the key ideas relative to the origin of the 2DEG. In this paper, we first revisit the original polar catastrophe idea by modeling LAO overlayers on STO of various thickness and studying both the ionic relaxations, the partial densities of states, and the planar-averaged electrostatic potential profile. We determine quantitatively the interface sheet carrier density in the conduction band of the STO and interface region. These results are presented in Secs. III A and III B. Subsequently, we study the effects of surface termination with H, OH, and both together in Sec. III C. Next, we consider interdiffusion of Ti-Al and Sr-La in Secs. III D and III E. Interdiffusion of the Ti and Al sides in the near-interface layers was recently observed by MEIS [2]. These various models clarify the behavior of the interface charge density and the way in which the polar catastrophe, or more precisely the slope in electrostatic potential, is mitigated and are a step along the way to build a quantitative model for determining the relative contributions of each type of mechanism. The main conclusions of our study, highlighting our findings, are summarized in Sec. IV. Before we present our results, a brief description of our computational models and methods is given in Sec. II.

II. COMPUTATIONAL METHOD

The calculations are carried out within the framework of density functional theory and using a plane wave basis set with projector augmented wave potentials (PAW) [19,20] using the VASP code [21,22]. The PBE-GGA approximation is used for the exchange correlation potential [23,24]. The electron wave functions were described using a plane wave basis set with the energy cutoff of 500 eV. This energy cutoff is sufficient to provide a well-converged basis set to describe oxides when using ultrasoft pseudopotentials [25].

To study the LAO/STO(001) interface, the supercells were set up in a symmetric way with 5.5 (001) oriented STO layers (meaning 6 $\rm TiO_2$ layers and 5 SrO layers) and either 3, 4, or 5 unit cell LAO layers on either side, followed by 20 Å of vacuum. This allows us to include the surface effects with different terminations. We focus exclusively on the $\rm TiO_2$/LaO interface, which is the n-type interface in which the 2DEG is experimentally observed. Several previous studies have also considered the SrO/$\rm AlO_2$ p-type interface, for example Ref. [8] and references therein. The symmetric geometry with two identical interfaces is chosen so as to avoid spurious fields from the periodic boundary conditions. The thickness of the vacuum region is sufficient to avoid spurious slab-slab interactions. For the first part of the study we pick a 1×1 2D surface cell. For the surface adsorption studies or the interdiffusion models we choose a 2×2 2D cell. In that case, the surface $\rm AlO_2$ layer has 8 O atoms and 4 Al atoms. Thus, we can go down to a H surface concentration of $1/8$ and OH concentration on Al of $1/4$. Additional calculations with full surface coverage were done on the 1×1 surface cell. Similarly for the interdiffusion we also used a 2×2 2D cell, so that we can model for example a 25% Ti, 75% Al layer. In addition, we can choose to simply add Ti instead of Al or swap Al and Ti from the STO to the LAO side of the cell and we can choose which layer to place the swapped atoms in: closer to the interface or further away. Similar considerations apply to Sr-La interdiffusion. The actual models studied will be presented along with the results.

For structure relaxation, the in-plane lattice constant of the slab was constrained at the calculated value of STO bulk ($a = 3.8695$ Å). All coordinates of atomic positions were fully relaxed until the residual Hellmann-Feynman forces [26] become less than 0.02 eV/Å. For k-space integrations, we used the Monkhorst-Pack scheme [27] with $7 \times 7 \times 1$ k-point sampling.

Manuscript submitted in Physical Review B

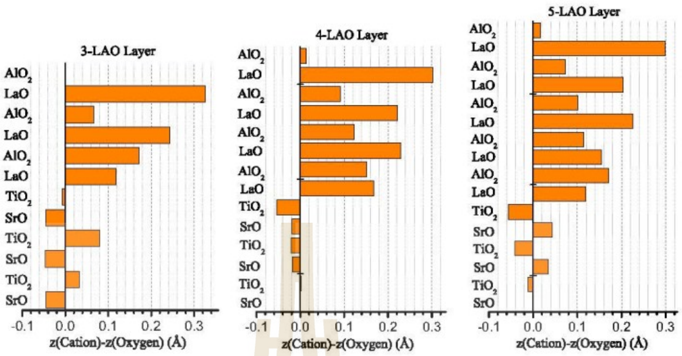

FIG. 1. (Color online) Buckling of layers in LAO/STO models. The bar graphs show $\Delta z = z_{\mathrm{oxygen}} - z_{\mathrm{cation}}$ with z the distance normal to the interface and positive toward the surface.

III. RESULTS

A. Structural relaxation in models without interdiffusion

We start by examining the ionic relaxation as function of LAO overlayer thickness. These results are shown in Fig. 1. We present the results as a buckling of the mixed cation anion layers, in other words, the relative z coordinate [normal to the (001) planes] of the cation minus that of the anion in each layer. One may see that, in agreement with early results of Pentcheva and Pickett [3,4], the surface AlO$_2$ layer remains unbuckled. However, as we approach the interface, the AlO$_2$ layer buckling increases. On the other hand, the buckling of the LaO layers is stronger and is reversed: it increases toward the surface although not entirely linearly with distance from the interface. We note that the displacement of positive cations toward the surface relative to the negative anions means that dipoles in each layer are formed which counteract the slope of the potential. Thus the potential slope, resulting from the valence discontinuity, is in part avoided by relaxing the layers.

B. Electronic structure in models without interdiffusion

Next, we consider the layer-projected densities of states in Fig. 2. We can see that for the 3-LAO layer case, the layer-projected densities of states (PDOS) in the LAO are shifted from layer to layer displaying the expected electric field from the polar discontinuity. This sloped potential leads to a strong decay of the states near the top of the valence band in the LAO away from the surface. This occurs over about a 1 eV range below the surface VBM. It shows that the LAO VBM becomes almost like a surface state and reflects simply the band bending.

The VBM of the surface LAO in the 3-LAO layer, however, stays below the CBM of the STO and hence no charge transfer occurs between the two. For the 4-layer and 5-layer cases there is a charge transfer. One can also see that the charge density in the STO is spread over all TiO$_2$ layers in our model. So, it is spread out over several layers near the interface. In Fig. 2 we show the results only for the 3-LAO and 5-LAO layer cases. Those for the 4-LAO layer case look similar to the 5-LAO layer case but with the Fermi level slightly closer to the STO CBM in the interface layer. We see no evidence for a localized interface state splitting off below the CBM in these figures.

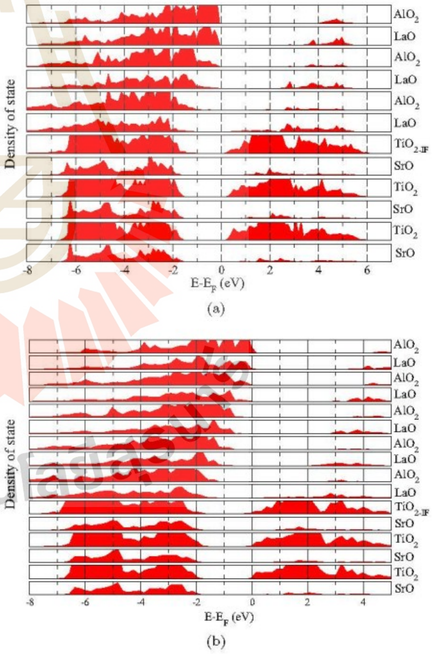

FIG. 2. (Color online) Layer-projected density of states of (a) 3-LAO layer and (b) 5-LAO layer.

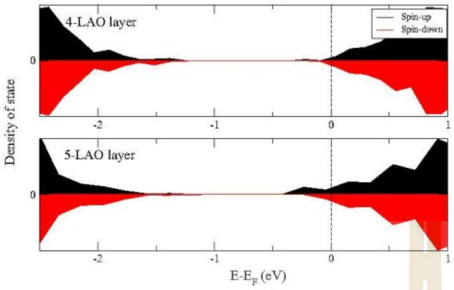

FIG. 3. (Color online) Layer-projected density of states, focus on interface layer of 4- and 5-LAO layers, including spin polarization.

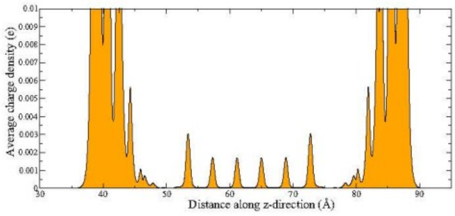

FIG. 5. (Color online) Charge density in energy range between STO middle of the gap and Fermi energy averaged over the xy plane for the 4-LAO layer model.

We also examine more closely whether an interface state occurs at the interface by performing spin-polarized calculations. In this case, we find for the 5-LAO layer case a separate small peak in the PDOS for majority spin. This is shown in Fig. 3. It agrees qualitatively with the conclusions of Lee and Demkov [13]. These authors used LSDA + U in which the Hubbard U further shifts the occupied interface state down into the gap. We see that this already occurs without Hubbard U. In other words by placing a small amount of charge in the bottom of the conduction band it becomes favorable to induce a magnetic moment by splitting the up and down spin bands. The total magnetic moment of the cell was found to be $0.12\,\mu_B$ for the 5-LAO layer and $0.08\,\mu_B$ for the 4-LAO layer case. This corresponds to two interfaces, so per interface the values should be halved. This occurrence of a weak magnetization is somewhat surprising because the density of states near the conduction band minimum is not very high, so one would not expect the Stoner criterion to be fulfilled. In fact, for the 4-LAO layer case, the up and down spin PDOSs stay essentially the same but for the 5-LAO layer case, a sharper interface state of only majority spin splits off.

Next, we determine the interface sheet electron density of free carriers in the STO conduction band. The conduction band 2D charge densities at the interface were determined by first extracting the charge density accumulated only over states from some level in the gap up to the Fermi energy, then planar-averaging it over the xy planes parallel to the interface and then integrating only over the layers near the interface and in the STO region. This is illustrated in Figs. 4 and 5.

In Fig. 4 we show a 3D plot of the structure with the electron density integrated between a lower energy limit E_a chosen in the gap and the Fermi energy E_F. As can be seen this charge density has a large contribution near the free surface. This is because E_a cuts through the LAO valence band PDOS near the surface. Here, we would actually be rather interested in the hole density, i.e., the integral from the Fermi level to an upper level above the local VBM.

For our present purpose of determining the interface electron density, we next planar-average it over xy planes as shown in Fig. 5 and simply integrate over z only over the middle region from about 50 Å to 75 Å. The zero of the distance perpendicular to the layers is chosen in the middle of the vacuum region. In practice, we include only the layers in LAO where the lower energy limit already lies above the VBM. However, it does include the whole STO region and thus gives truly the sheet density whether it is localized near the STO interface or spreads out over a few STO layers. The resulting net sheet densities are 1.43×10^{13} and 2.14×10^{13} e/cm^2 for the 4-LAO layer and 5-LAO layer cases, respectively. These are in good agreement with experimental values of Thiel *et al.*

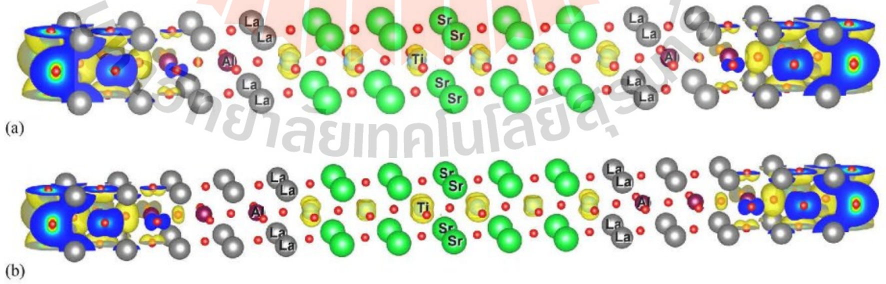

FIG. 4. (Color online) Structure and charge density in energy range between STO middle of the gap and Fermi energy (3D plot) for (a) 4-LAO layer and (b) 5-LAO layer. The yellow surface is an isosurface of the charge density; the blue shows the inside of this surface where the unit cell cuts through it.

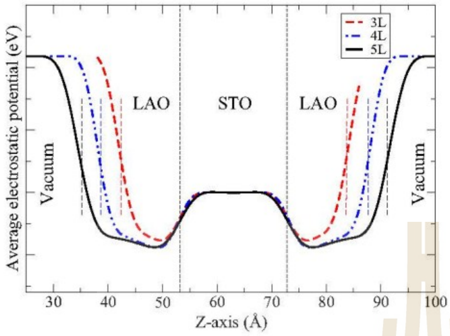

FIG. 6. (Color online) Macroscopically averaged electrostatic potentials of the 3-, 4-, and 5-LAO layer cases. The potentials are averaged over the xy plane and filtered by a running average in the z direction to filter out layer-by-layer variations. The vertical dashed lines show the position of the O in the TiO_2 interface layer and the position of the O in the AlO_2 surface for each case are marked by short vertical dashed lines.

[28] and indeed much smaller than the nominal charge of $1/2\,e$ per interface unit cell area as assumed in the polar discontinuity model. From Fig. 5, only shown for the 4-layer case, we can also see that the charge density is slightly higher near the interface but decays rather slowly into the STO region.

Returning to Fig. 4 we may notice that the charge density also provides information on the orbital character of the interface charge. In the 4-LAO layer case, it clearly consists of d_{xy}-like states throughout the STO region. In the 5-LAO layer case, the isosurfaces inside the STO look more cubic, because now the d_{xz} and d_{yz}, i.e., the other t_{2g} orbitals, also contribute. This is related to the fact that we have a significantly higher interface sheet density in the 5-LAO layer case. In fact, the thin STO layer confinement effects are more strongly affecting the d_{xz} and d_{yz} states than the d_{xy} states. Thus, for low carrier concentration, we only fill the d_{xy} bands, while for the higher concentration we start to fill both but near the interface, the states are still predominantly d_{xy}-like. Similar observations on the nature of the interface states were made in Ref. [6].

Next, we also examine the layer-averaged electrostatic potentials (in Fig. 6) and examine the slope in the LAO layer. This gives a field of 0.21 eV/Å for the 3-layer case. Within the framework of the polar discontinuity model, this field should be given by $E = 4\pi\sigma/\varepsilon$. Using a static dielectric constant of $\varepsilon = 28$ from Ref. [29] this gives a $\sigma = 3.2 \times 10^{14}\ e/\mathrm{cm}^2$, as expected from the discontinuity model. This charge results from the total nuclear plus electronic charge and reflects the true discontinuity in electric field arising from the juxtaposition of nominally alternatingly positive (LaO) and negative (AlO_2) layers on top of the STO neutral layers. However, we see that once the gap is closed and some charge is transferred from the surface to the interface as in the 4 and 5 layer cases, the slope is reduced. However, it is not reduced to zero as is also clear from the PDOS in Fig. 2. This is consistent with the significantly lower conduction band interface charge or sheet density we found above. Part of the potential slope is reduced also by the dipoles resulting from the ionic displacements discussed in the previous section.

Furthermore we can see that near the interface, the slope in the 5-layer case is similar to the 4-layer case but the potential then flattens out as we approach the surface. In that sense the somewhat larger net interface charge indeed avoided the polar catastrophe. If one would add more layers of LAO, presumably the sloped potential region would only occur near the interface after which the potential would remain flat. In the present case, the next layer is however already close to the surface where another dipole potential obviously is present to the vacuum level outside the layer.

The above detailed analysis clarifies what actually happens in the purely electronic reconstruction model in terms of "avoiding the polar catastrophe."

C. Surface terminations

Next we consider the effects of surface terminations. In Fig. 7(a) we show the layer-by-layer PDOS for a 2×2 cell with one H on the surface O in the AlO_2 surface layer. This means that it corresponds to a $1/8$ surface coverage with H. A structural model of the surface configuration is included at the top of the figure. The PDOS shows that the H forms bonding and antibonding states with the surface O-$2s$ and O-$2p$. We can see these H bonding below the O-$2p$ band at -8 eV. The ones below the O-$2s$ occur at -21 eV just below our energy range cutoff and are thus not visible in the figure. The corresponding antibonding state lies high in the conduction band. There are however no extra states below the Fermi energy near the surface. Thus the additional electron from H finds its way to the lowest available empty states which are at the CBM of STO in the TiO_2 layers. These calculations were performed for an LAO thickness of only 3 unit cells. In other words, even below the critical thickness, covering the LAO surface with a hydrogen coverage of only $1/8$ already provides the necessary charge for eliminating the polar catastrophe. In fact, the slope in the potential on the different LaO or AlO_2 layers is seen to be almost zero. In this case, the charge density at the interface determined as explained in the previous section is $1.20 \times 10^{13}\ e/\mathrm{cm}^2$. On the other hand, we also studied a full coverage of H using the 1×1 2D cell model. In that case, we find that the interface charge increases only to $3.01 \times 10^{13}\ e/\mathrm{cm}^2$. However, there is now a significant charge density near the surface. This is shown in Fig. 7(b). In fact, in this case the polar catastrophe is overcompensated. One may now see that the potential slope is reversed and the potentials shift down from the interface to the surface. This leads to a downward shift of the LAO conduction band, which now also becomes partially filled. This implies that we now would have both the surface and interface layers to become conducting. The electron density in the surface layer was also determined in a similar manner to that in the interface and amounts to $6.2 \times 10^{13}\ e/\mathrm{cm}^2$. This calculation for full H coverage was also repeated for a 4-LAO layer model. Similar results are obtained but now the 2DEG sheet density increased to $9 \times 10^{13}\ e/\mathrm{cm}^2$. This indicates that the H effects are accumulative with the charge already there from surface to interface charge transfer.

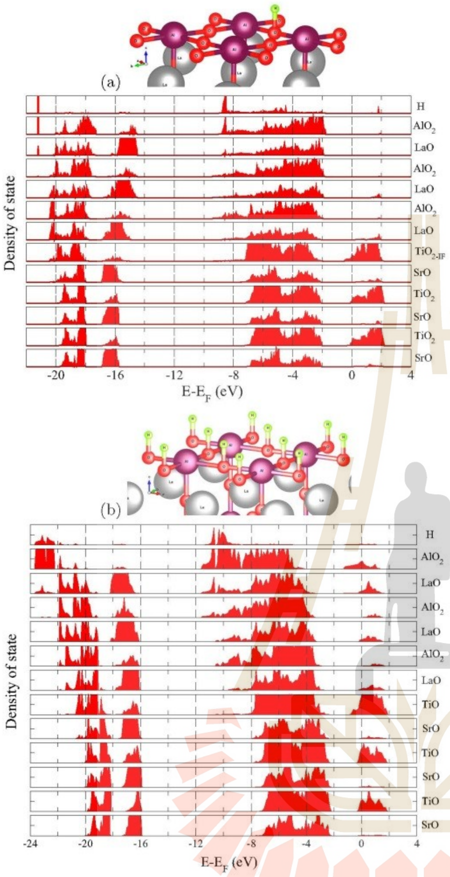

FIG. 7. (Color online) Layer-projected density of states and their surface structure in the case of (a) 1/8 H atom coverage and (b) full coverage by H atoms.

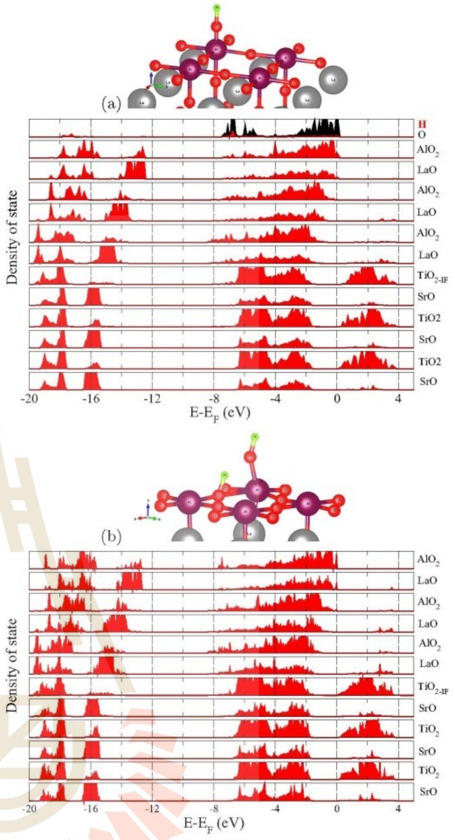

FIG. 8. (Color online) Layer-projected density of states and their surface structure in the case of surface partially covered by (a) OH and (b) H_2O (dissociated into OH and H).

For the 3-LAO layer model with a half H coverage we obtain $2.88 \times 10^{13}\ e/\text{cm}^2$.

These results indicate that even a small amount of H adsorption on the surface is sufficient to eliminate the potential slope. The interface 2DEG density can be further increased in proportion to the H concentration. However the interface 2D electron gas sheet density cannot be increased much beyond the $10^{13}\ e/\text{cm}^2$ level without overcompensating the fields and creating an opposite polar catastrophe, which now also leads to a surface conducting layer.

Next, we consider OH attached to the surface Al. Again, this is done for the 2×2 2D cell and 3 layers of LAO. The result is shown in Fig. 8(a). It leads to a surface state just above the VBM which stays empty. This can be explained as follows. We add 8 states for the O-2s and O-2p below the VBM but we add only 7 electrons. So, the Fermi level crosses through the VBM or rather between the VBM and the surface state which then becomes a p-type surface. However, we still have a strongly sloped potential and no electrons in the interface, so no 2DEG formation. As expected, when we have one of each, OH and H [as shown in Fig. 8(b)], the two effects compensate each other and we obtain essentially the same sloped potential as before for the bare surface for the 3-LAO layer case, i.e., no 2DEG formation at the interface.

These results are relevant for the surface modification effects as studied by Cen *et al.* [14,18]. These authors proposed

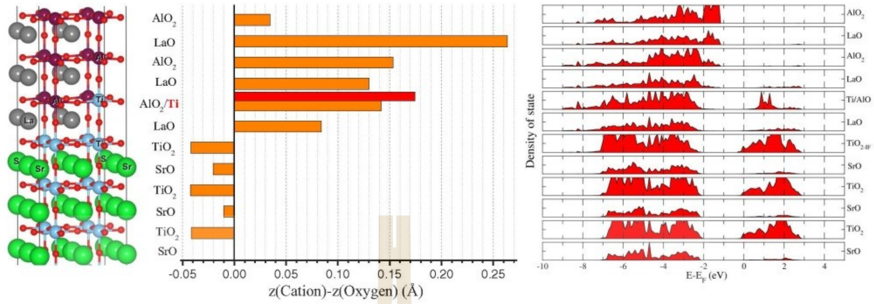

FIG. 9. (Color online) Structural model (left), buckling of layers ($z_{\text{cation}} - z_{\text{oxygen}}$) (middle), and PDOS (right) for the 25% Ti, 75% Al layer model. For the mixed layer, the Ti displacement is indicated in red, the Al displacement in orange.

a model for their AFM tip surface manipulation studies. The assumption is that in the native state, the surface is covered by equal amounts of H and OH resulting from water in the atmosphere which is split and adsorbed separately as OH on Al and H on surface O. Our calculations indeed indicate that the total energy for H_2O adsorbed on an Al is higher than an OH and H separately adsorbed on Al and surface O, respectively, by 1.8 eV per H_2O molecule. This is obtained from separate studies of OH and H and H_2O adsorption on a pure LAO slab. For absorption on the LAO/STO/LAO slab we find a somewhat smaller but still positive energy of 0.6 eV. Thus the interface seems to have some effect on this reaction energy. However, in any case the separate adsorption of H and OH and splitting of the water molecule is preferred.

One may now assume that the tip removes OH and thereby activates locally the H to donate its electrons to the interface and create locally a 2DEG. Interestingly, our present calculations indicate that this by no means requires a full coverage of the surface with H_2O. In fact, a full coverage of the surface with H would overcompensate the polarity discontinuity field. Further experimental work to elucidate the actual surface coverages with H and OH in dependence on the partial pressures in the gas would be quite interesting. At present we cannot yet fully quantitatively determine what the maximum 2DEG carrier concentration that is achievable in this way. It is also unclear whether the same effect would add to the 2DEG charge density at the interface if the starting system with compensated H and OH is already above the critical layer thickness. Our one calculation for a 4-LAO layer and full H coverage indicates the effects are accumulative.

D. Ti-Al interdiffusion effects

In this section, we consider various effects of interdiffusion. First we start with replacing one Al in the first LaO layer next to the interface by Ti in the 2 × 2 2D supercell. After relaxing the structure, we found that the Ti was slightly displaced away from the interface. This agrees with observations by Zaid *et al.* [2]. This can be seen in the structural panel (left) and buckling panel (middle) in Fig. 9.

The effect on the PDOS can be seen in the right panel of Fig. 9. The macroscopically averaged electrostatic potential is shown along with that of other cases, to be discussed in Fig. 10. The potential for the case of an added Ti_{Al} in the first AlO_2 layer is shown by the red-dotted curve, labeled Ti_{Al}. While potential slopes in this curve remain visible near the interface and near the surface, compared with the no interdiffusion case (solid line), the potential in the central region of the LAO layer now looks flat, whereas it had a monotonic slope toward the surface in the abrupt interface case without interdiffusion. One could conclude that the added Ti_{Al}, i.e., a 4-valent atom on a 3-valent site, had the effect of compensating the valence discontinuity at the interface. The remaining slopes near the surface are also clearly seen in the PDOS in Fig. 9. The Fermi level lies above the STO CBM. We can see that the Ti in the mixed layer however did not produce a defect level in that layer. The Ti-like PDOS in this layer lies well above the Fermi level with peaks at about 1 eV above the Fermi level and it has donated its electron to the interface. This implies that the

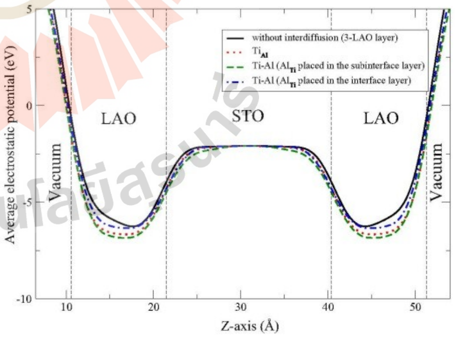

FIG. 10. (Color online) Macroscopically averaged electrostatic potentials for three Ti-Al interdiffusion models compared with the case of no interdiffusion. The vertical dashed lines show the position of the surface and interface layers.

Manuscript submitted in Physical Review B

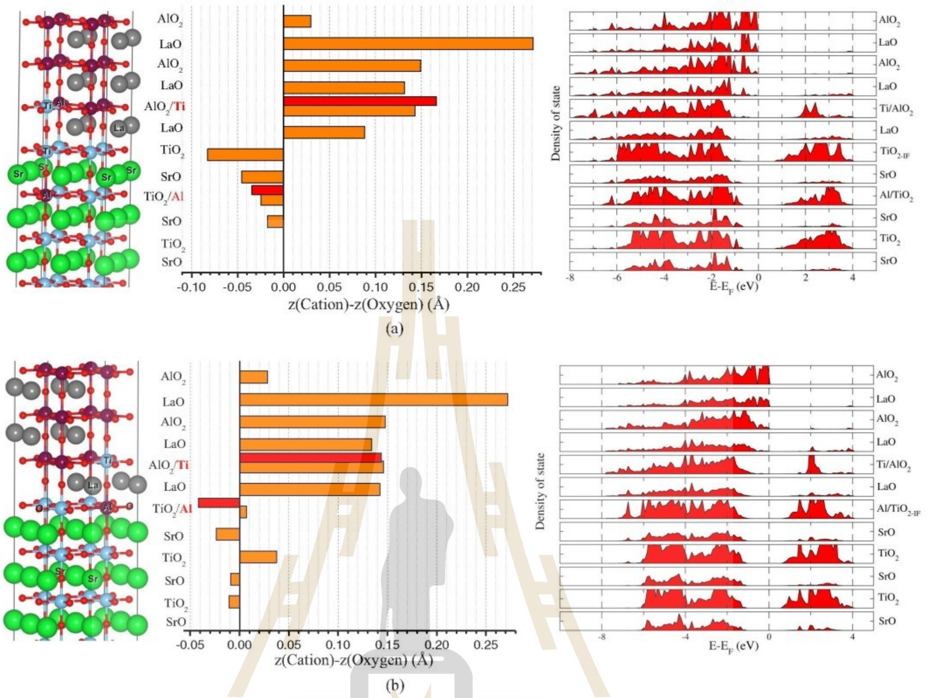

FIG. 11. (Color online) Structural model (left), buckling of layers (middle), and PDOS (right) for two Ti-Al intermixing models. The bar graphs show $\Delta z = z_{\text{oxygen}} - z_{\text{cation}}$ with z the distance normal to the interface. In (a) the Al$_{\text{Ti}}$ is placed in the subinterface TiO$_2$ layer; in (b) it is in the interface layer.

interdiffused Ti$_{\text{Al}}$ did not convert to Ti^{3+} as is often assumed. Instead because of the higher electrostatic potential of this layer, it turned out to be preferable to let this extra electron move to the interface. So, in some sense it contributes to the electronic reconstruction. Only, instead of the charge coming from a p-type surface it came from the Ti$_{\text{Al}}$ site in the mixed LaO interface layer. The sheet density of the 2DEG in the interface in this case is $1.1 \times 10^{13}\ e/\text{cm}^2$.

We now consider the PDOS in Fig. 9 in the four topmost layers starting from the surface. We here see a decreasing PDOS in the energy range −1 eV to −2 eV from the surface inward. These states persist all the way down to the first LaO layer above the mixed Ti-AlO$_2$ layer but are not present in the LaO layer near the interface. In that sense there is an abrupt change in the upper valence band state of the second and third LaO layer (counting down from the surface). It looks in other words like a localized surface state. This is similar to the models without interdiffusion discussed in Sec. III B. In some sense, what the added Ti did was shift the interface closer to the surface so it is now only two LAO layers below the surface instead of three. This slope in potential over the near-surface layers can also be seen in Fig. 10.

Next, instead of adding Ti, we studied swapping a Ti from the STO side with an Al in the LAO. The results are shown in Fig. 11. On the right of this figure, we show the model indicating in which layer the Ti$_{\text{Al}}$ and Al$_{\text{Ti}}$ are placed. In the middle we show the layer buckling after relaxation and on the right the PDOS. The corresponding electrostatic potential profiles are shown in Fig. 10. We considered two cases: in both the Ti$_{\text{Al}}$ occurs in the AlO$_2$ layer closest to the interface. In model (a), the Al$_{\text{Ti}}$ is placed deeper into the STO region, one TiO$_2$ layer removed from the interface layer; in model (b) it is placed in the interface TiO$_2$ layer. First we note that both the Al and Ti were displaced away from the interface. Their displacements relative to the O in their plane were 0.15 Å for the Ti$_{\text{Al}}$ compared to 0.14 Å for the Al in the same layer. For the Al$_{\text{Ti}}$ on the STO side, the displacement relative to the oxygen was −0.03 Å compared to −0.02 Å for Ti in that layer.

The results are similar to the previous case where we only added Ti. One can see that the Ti$_{\text{Al}}$ PDOS in the Al layer is located at about 2 eV above the Fermi level, well above the CBM of STO. Thus their electron is transferred to the STO. However, the TiO$_2$ layer on the STO now lacks an electron by having one Ti replaced by Al, and thus no electrons accumulate

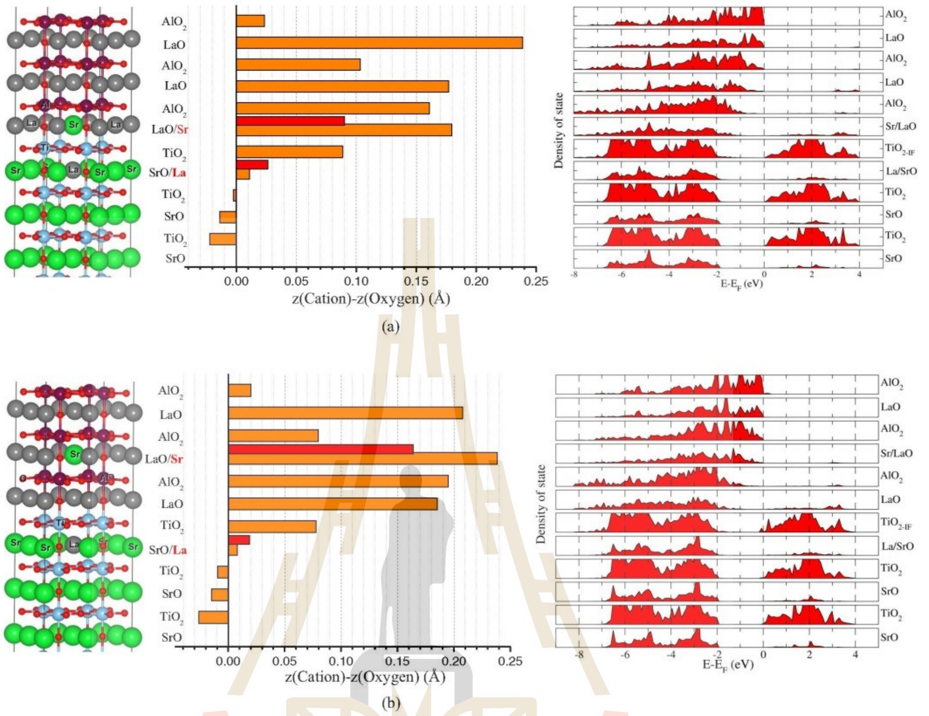

(a)

(b)

FIG. 12. (Color online) Structural model (left), buckling of layers (middle), and PDOS (right) for two Sr-La interdiffusion models. The bar graphs show $\Delta z = z_{\mathrm{oxygen}} - z_{\mathrm{cation}}$ with z the distance normal to the interface. In case (a) $\mathrm{Sr_{La}}$ occurs closer to the interface than in case (b).

in the STO. This is true in both models, neither of which show a 2DEG. In the case where the Al is placed deeper into the STO, one can see that the electrostatic potential is higher in that layer by the energy shift of the local PDOS.

The dipoles related to the swap and corresponding atomic displacements are such that the potential slope is reduced or taken care of within the near-interface region, as can be seen in Fig. 10. The three cases all show a more or less flat potential in the LAO region near the interface and a sloped potential near the surface. We can also see changes in the potential on the STO region of the interface. Depending on how deep the Al is placed, the potential slope in the interface region becomes more spread out. As expected the interdiffusion widens the interface region.

In summary, the $\mathrm{Ti_{Al}}$ in the LAO appears in each case to donate its electrons to the interface or STO region rather than forming $\mathrm{Ti^{3+}}$ in its own layer. However, if we also place Al on the STO side as would occur in actual interdiffusion without Ti enrichment, then the Al on the STO side compensates the added electrons and no 2DEG results. Nonetheless, the linear potential variation of the models without interdiffusion is no longer seen. The dipoles induced by the atomic displacements modify the potential profile and eliminate the overall slope in the near-interface region. However, a potential slope remains in the surface region and leads to a surface-state-like decay of the $\mathrm{AlO_2}$ PDOS. In other words, there is a surface band bending effect.

E. Sr-La interdiffusion effects

In this section, we present our results for Sr-La interdiffusion effects as studied in the same 3-LAO layer 2 × 2 2D supercell case. The results are shown in Fig. 12.

In the first example we place $\mathrm{Sr_{La}}$ in the LAO layer right next to the interface and $\mathrm{La_{Sr}}$ in the first SrO layer next to the $\mathrm{TiO_2}$ interface layer. In terms of the structure, we find that $\mathrm{Sr_{La}}$ moves less toward the surface from its oxygen layer than the La in the same layer. In other words, relative to the La, the Sr moves closer to the interface. This trend is opposite to that of $\mathrm{Ti_{Al}}$ in the previous section. The PDOS shows that no 2DEG forms.

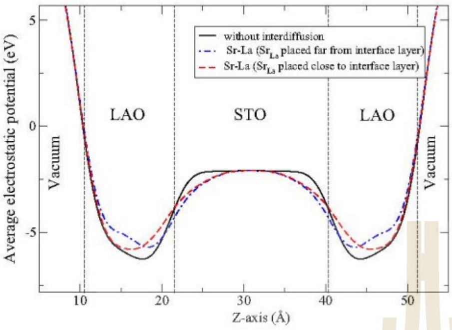

FIG. 13. (Color online) Macroscopically averaged electrostatic potentials for two cases of Sr-La interdiffusion compared with the case of no interdiffusion. The vertical dashed lines show the positions of the interface and surface layers.

As a second Sr-Al swap case we placed the Sr_{La} in the LaO layer farther away from the interface, in fact in the middle LaO layer, but kept the La_{Sr} in the SrO layer next to the TiO_2. The Sr_{La} was still found to move toward the interface relative to the La but slightly less so than in the near-surface layer, studied in the previous case. Remarkably in this case we do find an interface state in the TiO_2 interface layer and formation of a 2DEG. Apparently just shifting the Sr_{La} one layer farther away from the interface results in a somewhat different electrostatic potential profile which allows some of the surface charge to transfer to the TiO_2. It should be noted that in this case the Sr_{La} lies in the middle of the 3-layer LAO layer film and in some sense allows the surface to communicate with the interface, whereas in the previous case, the slope potential and any charge transfer were restricted to the near-interface region. The net sheet density in this case however is found to be only 6×10^{12} e/cm^2.

The potential profile for both Sr_{La} positions is shown in Fig. 13. For the case of Sr close to the interface, shown by the dashed red line, the profile is smooth and shows a flat region in the center of the LAO layer. For the Sr_{La} farther away form the interface, shown by the dashed-dotted blue line, the profile is more complex with a vanishing slope at about 49 Å and another one at about 44 Å. Overall the slopes in potential in the LAO region are reduced compared to the model without any interdiffusion (shown as solid black line) but the effect of the valence discontinuity is not entirely removed.

In summary of this section, the situation for a Sr-La swap is slightly more complex. Essentially the dipoles help adjust the potential slope in the near-interface region. However, the Sr_{La} may also contribute to the 2DEG formation if it lies in the middle of the LAO region. The variations in electrostatic potential layer by layer in that case seem to facilitate some charge transfer from surface to interface. The potential in the mixed Sr-La layer is raised and thereby the surface state extends deeper into the LAO region from the surface and allows charge to be transferred to the interface. However, the contribution to the sheet density was found to be smaller than for the other mechanisms discussed in the previous sections.

TABLE I. Summary of occurrence of 2DEG and its interface sheet density σ for various cases

System	2DEG	σ (10^{13} e/cm^2)
3-LAO layer	No	
4-LAO layer	Yes	1.43
5-LAO layer	Yes	2.14
3-LAO + $\frac{1}{8}$ H coverage	Yes	1.20
3-LAO + $\frac{1}{2}$ H coverage	Yes	2.88
3-LAO+ full H coverage	Yes	3.01[a]
4-LAO+ full H coverage	Yes	9.00
3-LAO + $\frac{1}{4}$ Ti_{Al}	Yes	1.10
3-LAO + $\frac{1}{4}$ Ti_{Al} + Al_{Ti}	No	
3-LAO + $\frac{1}{4}$ Sr_{La} at interface + La_{Sr}	No	
3-LAO + $\frac{1}{4}$ Sr_{La} in middle LAO + La_{Sr}	Yes	0.6

[a] In this case, a surface 2DEG of 6.2×10^{13} e/cm^2 is also present.

IV. CONCLUSIONS

In this paper we studied various models of LAO/STO interfaces with the goal of evaluating different possible mechanisms to avoid the polar discontinuity with or without formation of a 2DEG or electronic reconstruction. Our main conclusions can be summarized as follows.

First, we studied abrupt LAO/STO interface models with bare surfaces and without any interdiffusion. In agreement with previous work we find a critical layer thickness for formation of a 2DEG of 4 layers of LAO. We also determined quantitatively the electron density in the 2DEG and studied its spread over the STO layers. We find a 2DEG concentration on the order of 10^{13} e/cm^2 in qualitative agreement with experiment and also studied how this affects the slopes of the potential that remain near the interface. The 2DEG concentrations for the various cases studied are summarized in Table I.

We also analyzed the contributions of the lattice relaxation to this problem. The displacements are such as to reduce the potential slope. A larger sheet density is found for the 5-LAO layer case than the 4-LAO layer case and this results in a different orbital character of the states contributing to the 2DEG. In the 4-LAO layer case, only d_{xy}-like states are occupied while in the 5-LAO layer case, d_{xy}-like states are occupied near the interface but in addition d_{xz}- and d_{yz}-like states are also partially occupied in the deeper STO layers.

Next, we studied surface termination effects or surface passivation effects by water absorption. We did this for the situation of a below critical thickness LAO layer of only 3 unit cells thick. We find first that H_2O absorbed on Al prefers to split into OH on Al and H on surface O. We found that H on O donates its electrons to the interface rather than forming surface states in the AlO_2 layer. However, this is only true if the H concentration is not too high. Here we studied only two limiting cases, a low coverage of 1/8 H restricted by the size of cell we can deal with and a high coverage of 1 H per surface O. In the latter case, the potential slope problem is reversed and

Manuscript submitted in Physical Review B

a significant electron density is found in surface states below the LAO CBM.

Adsorption of OH on the Al on the other hand leads to a p-type surface and with acceptor-like surface states above the LAO VBM. This does not help to reduce the polar discontinuity potential and in fact compensates the H 2DEG if both are present simultaneously.

Finally we studied both Ti-Al and Sr-La interdiffusion effects. We found that Ti_{Al} and Al_{Ti} tend to be displaced away from the interface. These dipoles already would help reduce the potential slope resulting from the polar discontinuity. On the other hand, Ti_{Al} is found not to convert to Ti^{3+} but rather to donate its electrons to the STO. If there is excess Ti and the STO remains unmixed, the polar discontinuity is avoided and a sizable 2DEG concentration is achieved. On the other hand, if the Ti_{Al} is compensated by an Al_{Ti} in the STO TiO_2 interface layer, then the extra Al on the TiO_2 layer contributes a compensating hole so that no net 2DEG forms. A significant surface potential bending remains in the LAO layer leading to a surface-state-like decay of the LaO and AlO_2 layer PDOSs.

For Sr-La interdiffusion we found that both Sr_{La} and La_{Sr} tend to be displaced toward the interface. Both Sr and La are merely donors in their respective crystals and so do not contribute relevant energy levels near the VBM or CBM. The nuclear charge swaps simply compensate and no 2DEG forms if both are close to the interface. However, we found that they nonetheless affect the electrostatic potentials in the layers in which they reside. Thereby they can influence the potential profile and for example for Sr_{La} placed in the middle of the 3-layer LAO, we found that it helped transferring charge from the surface to the interface so that now a 2DEG formed even for a layer thickness below the normal critical layer thickness.

Although some interesting and unexpected effects of the interdiffusion were found here, we caution that a full study of this would require a statistical averaging and taking into account how much actual interdiffusion takes place and how the interdiffused atoms are distributed over the layers. Such information is recently becoming available from MEIS studies by Zaid *et al.* [2]. However, the gradual interdiffusion profile is too complex to treat directly with first-principles simulations. A small concentration in a any given layer would require a much larger 2D cell than we here can afford with present computational power. Second, some of the effects we found here could compensate each other. Therefore the value of the present results lies more in the qualitative findings. A fully quantitative treatment of these various effects on the 2DEG electron density requires probably a simpler modeling approach in which some of these qualitative aspects are incorporated.

Still, some of our predictions are worth further testing experimentally, in particular the prediction that Ti_{Al} on the LAO side after interdiffusion would stay Ti^{4+}. In both cases, of course it contributes to the overall 2DEG electron density but our calculation predicts the latter should stay confined to the STO rather than making the whole LAO film n-type doped.

ACKNOWLEDGMENTS

This work was supported by the US Air Force Office of Scientific Research under Grant No. FA9550-12-1-0441. One of the authors (I.F.) was supported by the Development and Promotion of Science and Technology Talents Project (DPST). S.L. and I.F. acknowledge support from the NANOTEC-SUT Center for Excellence on Advanced Functional Nanomaterials. The calculations used the High Performance Computing Resource in the Core Facility for Advanced Research Computing at Case Western Reserve University.

[1] A. Ohtomo and H. Y. Hwang, Nature **427**, 423 (2004).
[2] H. Zaid, M. Berger, D. Jalabert, M. Walls, N. G. R. Akrobetu, X. Gao, P. Berger, I. Fongkaew, W. R. L. Lambrecht, and A. Sehirlioglu, Atomic-resolved depth profile of strain and cation intermixing around $LaAlO_3/SrTiO_3$ interfaces (unpublished).
[3] R. Pentcheva and W. E. Pickett, Phys. Rev. B **78**, 205106 (2008).
[4] R. Pentcheva and W. E. Pickett, Phys. Rev. Lett. **102**, 107602 (2009).
[5] A. Janotti, L. Bjaalie, L. Gordon, and C. G. Van de Walle, Phys. Rev. B **86**, 241108 (2012).
[6] Z. S. Popović, S. Satpathy, and R. M. Martin, Phys. Rev. Lett. **101**, 256801 (2008).
[7] H. Chen, A. Kolpak, and S. Ismail-Beigi, Phys. Rev. B **82**, 085430 (2010).
[8] Z. Zhong, P. X. Xu, and P. J. Kelly, Phys. Rev. B **82**, 165127 (2010).
[9] R. Pentcheva and W. E. Pickett, Phys. Rev. B **74**, 035112 (2006).
[10] L. Yu and A. Zunger, Nat. Commun. **5**, 5118 (2014).
[11] Y. Li, S. N. Phattalung, S. Limpijumnong, J. Kim, and J. Yu, Phys. Rev. B **84**, 245307 (2011).
[12] L. Zhang, X.-F. Zhou, H.-T. Wang, J.-J. Xu, J. Li, E. G. Wang, and S.-H. Wei, Phys. Rev. B **82**, 125412 (2010).
[13] J. Lee and A. A. Demkov, Phys. Rev. B **78**, 193104 (2008).
[14] C. Cen, S. Thiel, G. Hammerl, C. W. Schneider, K. E. Andersen, C. S. Hellberg, J. Mannhart, and J. Levy, Nat. Mater. **7**, 298 (2008).
[15] C. Cen, S. Thiel, J. Mannhart, and J. Levy, Science **323**, 1026 (2009).
[16] G. Cheng, P. F. Siles, F. Bi, C. Cen, D. F. Bogorin, C. W. Bark, C. M. Folkman, J.-W. Park, C.-B. Eom, G. Medeiros-Ribeiro, and J. Levy, Nat. Nanotechnol. **6**, 343 (2011).
[17] G. Cheng, J. P. Veazey, P. Irvin, C. Cen, D. F. Bogorin, F. Bi, M. Huang, S. Lu, C.-W. Bark, S. Ryu, K.-H. Cho, C.-B. Eom, and J. Levy, Phys. Rev. X **3**, 011021 (2013).
[18] F. Bi, D. F. Bogorin, C. Cen, C. W. Bark, J.-W. Park, C.-B. Eom, and J. Levy, Appl. Phys. Lett. **97**, 173110 (2010).
[19] P. E. Blöchl, Phys. Rev. B **50**, 17953 (1994).
[20] G. Kresse and D. Joubert, Phys. Rev. B **59**, 1758 (1999).
[21] G. Kresse and J. Furthmüller, Comput. Mater. Sci. **6**, 15 (1996).
[22] G. Kresse and J. Hafner, J. Phys.: Condens. Matter **6**, 8245 (1994).

Manuscript submitted in Physical Review B

[23] J. P. Perdew, K. Burke, and M. Ernzerhof, Phys. Rev. Lett. **78**, 1396 (1997).

[24] J. P. Perdew, K. Burke, and M. Ernzerhof, Phys. Rev. Lett. **77**, 3865 (1996).

[25] D. Vanderbilt, Phys. Rev. B **41**, 7892 (1990).

[26] R. P. Feynman, Phys. Rev. **56**, 340 (1939).

[27] H. J. Monkhorst and J. D. Pack, Phys. Rev. B **13**, 5188 (1976).

[28] S. Thiel, G. Hammerl, A. Schmehl, C. W. Schneider, and J. Mannhart, Science **313**, 1942 (2006).

[29] M. Reinle-Schmitt, C. Cancellieri, D. Li, D. Fontaine, M. Medarde, E. Pomjakushina, C. Schneider, S. Gariglio, P. Ghosez, J.-M. Triscone, and P. Willmott, Nat. Commun. **3**, 932 (2012).

Manuscript submitted in Philosophical Magazine

Philosophical Magazine, 2015
Vol. 95, No. 33, 3785–3797, http://dx.doi.org/10.1080/14786435.2015.1099755

First principles study of Ca in $BaTiO_3$ and $Bi_{0.5}Na_{0.5}TiO_3$

Ittipon Fongkaew[a,b], Jiraroj T-Thienprasert[c,d] and Sukit Limpijumnong[a*]

[a]*School of Physics and NANOTEC-SUT Center of Excellence on Advanced Functional Nanomaterials, Suranaree University of Technology, Nakhon Ratchasima 30000, Thailand;* [b]*Department of Physics, Case Western Reserve University, Cleveland, OH 44106-7079, USA;* [c]*Thailand Center of Excellence in Physics (ThEP Center), Commission on Higher Education, Bangkok 10400, Thailand;* [d]*Faculty of Science, Department of Physics, Kasetsart University, Bangkok 10900, Thailand*

(*Received 5 July 2015; accepted 21 September 2015*)

$BaTiO_3$ $Bi_{0.5}Na_{0.5}TiO_3$ is one of the promising candidates as a high-temperature relaxor with a high Curie temperature and several preferred dielectric characteristics. It has been found experimentally for a long time that adding calcium to $BaTiO_3$ $Bi_{0.5}Na_{0.5}TiO_3$ improves its temperature characteristic of the capacitance [J. Electron. Mater. 39, 2471]. In this study, Calcium (Ca) defects in perovskite $BaTiO_3$ and $Bi_{0.5}Na_{0.5}TiO_3$ have been studied based on first-principles calculations. In both $BaTiO_3$ and $Bi_{0.5}Na_{0.5}TiO_3$, our calculations showed that Ca atom energetically prefers to substitute for the cations, that is Ba, Bi, Na and Ti, depending on the growth conditions. In most cases, Ca predominantly substitutes on the A-site without providing additional electrical carriers (serve as either neutral defects or self-compensating defects). The growth conditions where Ca can be forced to substitute for B-site (with limited amount) and the conditions where Ca can be forced to serve as an acceptor are identified. Details of the local structures, formation energies and electronic properties of these Ca defects are reported.

Keywords: $BaTiO_3$; $(Bi_{0.5}Na_{0.5})TiO_3$; perovskite oxides; first-principles calculations

1. Introduction

$BaTiO_3$ (henceforth, BT) and $Bi_{0.5}Na_{0.5}TiO_3$ (henceforth, BNT) are currently potential candidates to replace lead-containing ferroelectric materials, which are highly toxic. BT is a ferroelectric material with a tetragonal perovskite structure at room temperature. It has good piezoelectric and ferroelectric properties. However, it has a relatively low Curie temperature at T_c = 120 °C and a phase transition to the rhombohedral phase as the temperature is reduced below 5 °C [1,2]. It is necessary to increase both the T_c and the temperature of the secondary phase transition to make BT practical for real applications [3]. Adding Bi or other rare-earth elements with smaller ionic radius [4,5] to BT to form compounds, for example, $Bi_{0.5}Na_{0.5}TiO_3$ [6], and $Bi_4Ti_3O_{12}$ [7], has been reported to increase T_c, improve ferroelectric response and other properties [8–13]. BNT, by itself, is also a ferroelectric material. It has Bi^{3+} and Na^+ ions alternately

---

*Corresponding author. Email: sukit@sut.ac.th occupying A-site of ABO_3 perovskite structure with rhombohedral symmetry at room temperature. BNT has a rather high Curie temperature of $T_c = 320$ °C and a relative large remanent polarization at room temperature. It is expected that a mixture of BT and BNT (BT-BNT) is a ferroelectric material with properties superior to the parent materials. BNT-BT is highly attractive owing to the existence of a rhombohedral (F_α) – tetragonal (F_β) morphotropic-phase boundary. Takenaka et al. [4] reported that the BT-BNT at 6% BT composition, that is, $(Bi_{0.5}Na_{0.5})_{0.94}Ba_{0.06}TiO_3$, has good piezoelectric properties and high dielectric constant. However, the alloy has a stability problem at high temperatures. Yuan et al. [14] found that adding a small amount of calcium can effectively improve the temperature characteristic of capacitance (TCC) of the BNT-BT system. However, the role of Ca in BT-BNT system is currently unclear and its preferable site still also unknown. As a cation, Ca is expected to occupy either the A-site (Ba, Bi, or Na site) or B-site (Ti site). In order to gain a deeper understanding on the role of Ca, the preferable site of Ca in BT-BNT samples has to be identified.

In this study, we employed first-principles calculations to investigate Ca in BT and BNT. We focused our attentions on the identification of Ca's favourable sites and the resulting electronic properties. The outline of this article is as follows. In Section 2, the details of our theoretical and computational method are described. In Section 3, we present a detailed analysis of the possible equilibrium growth conditions of BT and BNT by introducing phase diagrams to show the possible range of chemical potentials of the starting elements. Different growth conditions lead to different form of Ca incorporation. Our main result of the formation energies and electronic properties of Ca substitution for different cation sites in BT and BNT are presented and discussed in Section 4. Finally, Section 5 contains the summary of our work.

2. Computational methods

In this work, we utilized first-principles calculations based on spin-polarized density functional theory (DFT) within the generalized gradient approximation with the functional introduced by Perdew, Burke and Ernzerhof [15,16]. To describe the electron-ion interactions, the projector-augmented wave method [17,18], as implemented in VASP code, was used [19–22]. The electron wave functions were described using a plane wave basis set with the energy cut-off of 500 eV. This energy cut-off is sufficient to provide a well-converged basis set to describe oxides when using ultrasoft pseudopotentials [23]. The calculated lattice parameters of tetragonal BT and BNT are in good agreement with the known experimental values as shown in Table 1. To study defects in BT and BNT, a supercell approach is used. For BT, we used a 135-atom cell, which is a 3 × 3 × 3 repetition of the conventional tetragonal-perovskite unit cell (5 atom/unit cell). For BNT, we used a 120-atom cell, which is a 2 × 2 × 3 repetition of the conventional tetragonal-perovskite unit cell (10 atom/unit cell) [24]. For *k*-space integrations, we used the Monkhorst–Pack scheme [25] with a shifted 2 × 2 × 2 *k*-point sampling. The calculated band gap of BT and BNT are smaller than the experimental values due to the well-known DFT problems. The calculated band gaps for BT and BNT at the special *k*-point are 1.68 and 2.19 eV, whereas the experimental band gaps are 3.2 [26] and 2.94 eV [27], respectively. All atoms in the supercell were allowed to relax until the residual Hellmann–Feynman forces [28] become less than 10^{-2} eV/Å.

Table 1. Lattice parameters of tetragonal $BaTiO_3$ and $Bi_{0.5}Na_{0.5}TiO_3$.

Lattice parameters	Present (calculation)	Experiment
$BaTiO_3$		
a (Å)	3.979	3.998[a]
c (Å)	4.078	4.018[a]
c/a	1.025	1.005[a]
$Bi_{0.5}Na_{0.5}TiO_3$		
a (Å)	5.561	5.519[b]
c (Å)	4.089	3.909[b]
c/a	0.728	0.708[b]

[a] Measurement by Electron diffraction from $BaTiO_3$ sample grown by flux-growth method [37].

[b] Measurement by Powder neutron diffraction from $Bi_{0.5}Na_{0.5}TiO_3$ sample grown by the flux; powder prepared from ground crystals [38].

3. Defect formation energies and crystal growth conditions

Under thermal equilibrium, the concentration of a defect D in a crystal can be written as [24,29,30]

$$c(D^q) = N_{\text{sites}} \exp\left[-\Delta E_f / k_B T\right] \tag{1}$$

where N_{sites} is the number of possible defect sites per unit volume and ΔE_{f} is the formation energy of the defect D defined as [31–33]

$$\Delta E_{\text{f}} = E_{\text{tot}}(D^q) - E_{\text{tot}}(\text{bulk}) + \sum \Delta n_X \mu_X + q(E_{\text{F}} + E_{\text{VBM}}) \tag{2}$$

where $E_{\text{tot}}(D^q)$ is the calculated total energy of a supercell containing a defect D in charge state q, E_{tot}(bulk) is the calculated total energy of a defect-free supercell, Δn_X is the number of atoms X being added to a defect-free supercell to create the supercell with the defect D, μ_X is the atomic chemical potential of atoms species X, E_{F} is the Fermi level of the system referenced to the valence band maximum (E_{VBM}). It is useful to explore the formation energy as the Fermi energy varied within the band gap of the host material. The stable charge state, that is, the charge state q that gives the minimum defect energy, could changes as the Fermi level varies and the defect levels can be estimated using the kink (the point where the slope changes) in a graph of defect formation energy versus E_{F}.

To use Equations (1) and (2) to determine the abundance of a defect, one needs to know the chemical potentials of all atomic species involved. The actual values of the chemical potentials depend on growth process. However, under suitable choices of thermodynamic equilibrium, the range of possible values of them can be determined by considering the requirements for controllable growth of the crystal as will be described in detail below.

To grow BT and BNT crystal under thermodynamic equilibrium, the following conditions must be satisfied [33,34]:

$$E_{\text{tot}}(BaTiO_3) = \mu_{\text{Ba}} + \mu_{\text{Ti}} + 3\mu_{\text{O}} \text{ and } E_{\text{tot}}(Bi_{0.5}Na_{0.5}TiO_3) = \frac{\mu_{\text{Bi}}}{2} + \frac{\mu_{\text{Na}}}{2} + \mu_{\text{Ti}} + 3\mu_{\text{O}} \tag{3}$$

where $E_{\mathrm{tot}}(\mathrm{BaTiO_3})$ and $E_{\mathrm{tot}}(\mathrm{Bi_{0.5}Na_{0.5}TiO_3})$ are the calculated total energy per molecular formula of BT and BNT, respectively, μ_X is the chemical potentials of atom species X referenced to their natural elementary forms. If the sum on the right-hand side of Equation (3) is larger than the left-hand side, then a rapid and uncontrolled growth of BT or BNT crystal takes place. On the other hand, if the sum on the right-hand side is smaller than the left-hand side, then the crystal disintegrates.

For BT, there are three chemical potentials to be considered. Therefore, the chemical potentials for a given growth condition can be presented as a point in the 3D chemical potential space, where each axis represents each of the three chemical potentials. Equation (3) is actually a plane in this 3D space. To make the plane symmetrically intercept the axes at 1, we can define a new set of normalized chemical potentials as follows:

$$\mu'_{\mathrm{Ba}} = \frac{\mu_{\mathrm{Ba}}}{E_{\mathrm{tot}}(\mathrm{BaTiO_3})},\ \mu'_{\mathrm{Ti}} = \frac{\mu_{\mathrm{Ti}}}{E_{\mathrm{tot}}(\mathrm{BaTiO_3})}\ \text{and}\ \mu'_{\mathrm{O}} = \frac{3\mu_{\mathrm{O}}}{E_{\mathrm{tot}}(\mathrm{BaTiO_3})} \tag{4}$$

This transforms the plane equation, Equation (3), to

$$1 = \mu'_{\mathrm{Ba}} + \mu'_{\mathrm{Ti}} + \mu'_{\mathrm{O}} \tag{5}$$

Similarly for BNT,

$$1 = \frac{\mu'_{\mathrm{Bi}}}{2} + \frac{\mu'_{\mathrm{Na}}}{2} + \mu'_{\mathrm{Ti}} + \mu'_{\mathrm{O}}, \tag{6}$$

where $\mu'_{\mathrm{Bi}} = \frac{\mu_{\mathrm{Bi}}}{E_{\mathrm{tot}}(\mathrm{Bi_{0.5}Na_{0.5}TiO_3})}$, $\mu'_{\mathrm{Na}} = \frac{\mu_{\mathrm{Na}}}{E_{\mathrm{tot}}(\mathrm{Bi_{0.5}Na_{0.5}TiO_3})}$, $\mu'_{\mathrm{Ti}} = \frac{\mu_{\mathrm{Ti}}}{E_{\mathrm{tot}}(\mathrm{Bi_{0.5}Na_{0.5}TiO_3})}$ and $\mu'_{\mathrm{O}} = \frac{3\mu_{\mathrm{O}}}{E_{\mathrm{tot}}(\mathrm{Bi_{0.5}Na_{0.5}TiO_3})}$ for Equation (6).

Additional limiting conditions have to be placed on the chemical potentials to prevent other low-energy phases of metal oxides, i.e. BaO, $\mathrm{BaO_2}$, $\mathrm{Bi_2O_3}$, $\mathrm{Na_2O}$, TiO, $\mathrm{TiO_2}$, and $\mathrm{Ti_2O_3}$ to form. These conditions can be written as:

$$\left.\begin{aligned} E_{\mathrm{tot}}(\mathrm{BaO}) &\geq \mu_{\mathrm{Ba}} + \mu_{\mathrm{O}}, \\ E_{\mathrm{tot}}(\mathrm{BaO_2}) &\geq \mu_{\mathrm{Ba}} + 2\mu_{\mathrm{O}}, \\ E_{\mathrm{tot}}(\mathrm{TiO}) &\geq \mu_{\mathrm{Ti}} + \mu_{\mathrm{O}}, \\ E_{\mathrm{tot}}(\mathrm{TiO_2}) &\geq \mu_{\mathrm{Ti}} + 2\mu_{\mathrm{O}}, \\ E_{\mathrm{tot}}(\mathrm{Ti_2O_3}) &\geq 2\mu_{\mathrm{Ti}} + 3\mu_{\mathrm{O}} \end{aligned}\right. \quad \text{for BaTiO}_3 \tag{7}$$

and

$$\left.\begin{aligned} E_{\mathrm{tot}}(\mathrm{Bi_2O_3}) &\geq 2\mu_{\mathrm{Bi}} + 3\mu_{\mathrm{O}}, \\ E_{\mathrm{tot}}(\mathrm{Na_2O}) &\geq 2\mu_{\mathrm{Na}} + \mu_{\mathrm{O}}, \\ E_{\mathrm{tot}}(\mathrm{TiO}) &\geq \mu_{\mathrm{Ti}} + \mu_{\mathrm{O}}, \\ E_{\mathrm{tot}}(\mathrm{TiO_2}) &\geq \mu_{\mathrm{Ti}} + 2\mu_{\mathrm{O}}, \\ E_{\mathrm{tot}}(\mathrm{Ti_2O_3}) &\geq 2\mu_{\mathrm{Ti}} + 3\mu_{\mathrm{O}} \end{aligned}\right. \quad \text{for Bi}_{0.5}\text{Na}_{0.5}\text{TiO}_3 \tag{8}$$

As a result, the possible chemical potentials of Ba, Na, Bi and Ti are further limited by their oxide phase according to Equations (7) and (8). To illustrate these limits, a triangular phase diagram can be used to represent the chemical potentials of Ba, Ti and O for BT (see Figure 1) and Bi, Na, Ti and O for BNT crystal (see Figure 2). In Figure 1, the black points and the shaded area on the diagram satisfied Equations (3–5), and (7). The chemical potentials of Ba, Ti, and O could be any values that lie within the shade

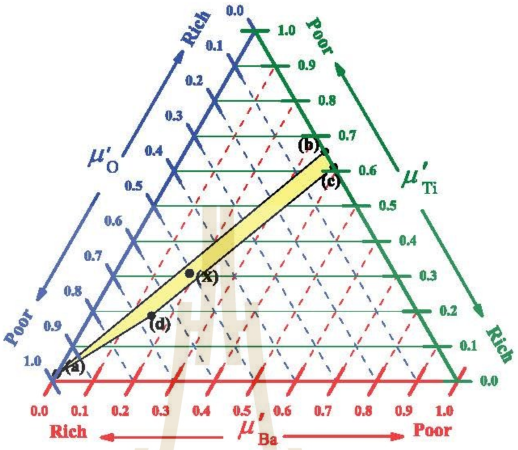

Figure 1. (colour online) Triangular phase diagram for representing the chemical potentials of Ba, Ti, and O according to Equations (3 5), and (7) (see text for details).

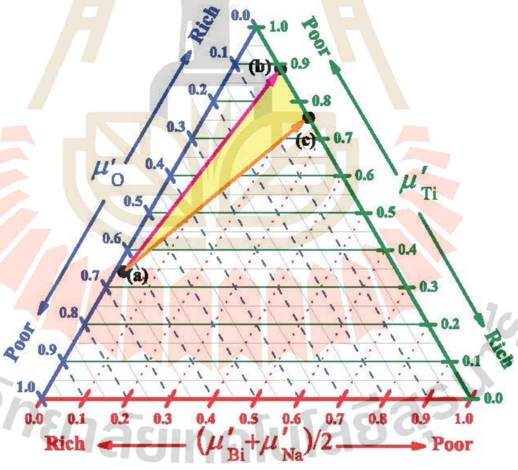

Figure 2. (colour online) Triangular phase diagram for representing the chemical potentials of Bi, Na, Ti, and O according to Equations (3), (6) and (8) (see text for details).

area. The black points connected with the black lines represent the solution to Equation (3) and the extreme points of Equation (7). Sets of chemical potentials along these lines are the result of the limits due to the possible oxide phases. These black points are marked as (a) to (d) in Figure 1. The values of the chemical potentials for Ba, Ti and O associated with the points (a)–(d) are tabulated in Table 1. At point ‘a’, the chemical potentials of Ba and Ti are at their maximum values and that of O is at its minimum value, that is, Ba-rich, Ta-rich and O-poor. At point ‘b’, the chemical potential of Ti is at its minimum value and O is at its maximum, that is, Ti-poor and O-rich. At point ‘c’, the chemical potential of Ba is at its minimum value and O is at its maximum value, that is, Ba-poor and O-rich. Note that points ‘b’ and ‘c’ are not much different. They both have O-rich and metal poor as the values of the chemical potentials of metal varied by only about 1 eV for the two conditions (see Table 2). Point ‘*x*’ represents a condition in the middle of the shaded area. Because these conditions cover the middle region and extrema of the growth conditions, the formation energies of Ca defects in BT will be presented using these conditions.

For BNT, there are four chemical potentials. To show the possible growth conditions of BNT in a 3D chemical potential space, we used the average value of μ'_{Bi} and μ'_{Na}, that is, $(\mu'_{\mathrm{Bi}} + \mu'_{\mathrm{Na}})/2$ to plot Figure 2. The black points and the shaded area on the diagram satisfied Equations (3), (6) and (8). The chemical potentials of Bi, Na, Ti and O could be of any value within the shade area. Similar to the case of BT, the black points connected with the black lines represent the solution between Equation (3) and the extreme points of Equation (8). Sets of chemical potentials along these lines are the result of the limits due to the possible oxide phases. These black points were marked by letters ‘a’–‘c’ in Figure 2. Note that only the average of the chemical potentials for Bi and Na is shown in Figure 2. To understand the possible growth range for each of them, additional chemical potential plots are needed. The possible chemical potentials for Bi and Na for the conditions along the line ‘a’ to ‘b’ and ‘a’ to ‘c’ in Figure 2 are shown in Figure 3(i) and (ii), respectively. In Figure 3(i) and (ii), we marked the chemical potential of O in the plots. At point ‘a’ in Figure 2, $\mu'_{\mathrm{O}} = 0.64$ and $(\mu'_{\mathrm{Bi}} + \mu'_{\mathrm{Na}})/2 = 0.01$, the line $(\mu'_{\mathrm{Bi}} + \mu'_{\mathrm{Na}})/2 = 0.01$ with the natural phase precipitate limits are shown in Figure 3(i) with a label $\mu'_{\mathrm{O}} = 0.64$. At point “b” in Figure 2, $\mu'_{\mathrm{O}} = 0$ and $(\mu'_{\mathrm{Bi}} + \mu'_{\mathrm{Na}})/2 = 0.11$, the line $(\mu'_{\mathrm{Bi}} + \mu'_{\mathrm{Na}})/2 = 0.11$ with the natural phase precipitate limits are shown in Figure 3(i) with a label $\mu'_{\mathrm{O}} = 0$. The lines for other oxygen chemical potentials in between are also shown. This plot (Figure 3(i)) allows us to show the possible range of the chemical potentials of Bi and Na for the conditions along the line ‘a’ to ‘b’ in Figure 2. Similarly, Figure 3(ii) shows the possible range of Bi and Na chemical potentials for the conditions along the line ‘a’ to ‘c’ in Figure 2. These black dots are used to mark the extreme points in Figure 3(i) and (ii) and labelled as $\boldsymbol{\mu}_{\mathbf{A}}$, $\boldsymbol{\mu}_{\mathbf{B1}}$, $\boldsymbol{\mu}_{\mathbf{B2}}$, $\boldsymbol{\mu}_{\mathbf{C1}}$ and $\boldsymbol{\mu}_{\mathbf{C2}}$. Note that for point ‘b’ in Figure 2, the chemical potentials of Bi and Na can be varied from condition B1 where Bi is rich and Na is poor to condition B2 where Bi is poorer and Na is richer. Similarly, for point ‘c’, the chemical potentials of Bi and Na can be varied from C1 to C2. For convenience, the values of chemical potentials for Bi, Na and O associated with the black dots are listed in Table 3.

Table 2. Chemical potentials of Ba, Ti, O and Ca for different growth conditions of BT.

Point	μ	μ_{Ba} (eV)	μ_{Ti} (eV)	μ_{O} (eV)	μ_{Ca} (eV)
a	$\boldsymbol{\mu}_{\mathbf{a}}$	0	−1.05	−4.97	−0.93
b	$\boldsymbol{\mu}_{\mathbf{b}}$	−5.01	−10.50	0	−5.91
c	$\boldsymbol{\mu}_{\mathbf{c}}$	−6.24	−10.12	0	−5.91
x	$\boldsymbol{\mu}_{\mathbf{x}}$	−3.13	−5.03	−2.62	−2.13

Table 3. Chemical potentials of Bi, Na, Ti, O and Ca for different growth conditions of BNT.

Point	μ	μ_{Bi}(eV)	μ_{Na}(eV)	μ_{Ti}(eV)	μ_{O}(eV)	μ_{Ca}(eV)
a	$\boldsymbol{\mu}_{\mathbf{A}}$	0	−0.52	−4.37	−2.75	−3.16
b	$\boldsymbol{\mu}_{\mathbf{B1}}$	−0.65	−2.19	−11.46	0	−5.91
	$\boldsymbol{\mu}_{\mathbf{B2}}$	−2.77	−0.06	−11.46	0	−5.91
c	$\boldsymbol{\mu}_{\mathbf{C1}}$	−3.94	−2.20	−9.77	0	−5.91
	$\boldsymbol{\mu}_{\mathbf{C2}}$	−6.20	0	−9.77	0	−5.91

For calcium defects, the formation energies depend on the chemical potential of Ca. The Ca-rich conditions give the lowest formation energies, that is, the richer Ca, the easier the formation of Ca defects. To properly investigate the plausible phase precipitate limits for Ca, common natural phases of Ca, that is, CaO, were considered and used to define the phase precipitate limits for Ca. The chemical potential of Ca, μ_{Ca}can be written as:

$$\mu_{\mathrm{Ca}} = E_{\mathrm{tot}}(\mathrm{CaO}) - \mu_{\mathrm{O}} \tag{9}$$

4. Results and discussions

In Figure 4, the formation energies of Ca substituting for Ba (denoted $\mathrm{Ca_{Ba}}$) and Ca substituting for Ti (denoted $\mathrm{Ca_{Ti}}$) defects in BT are plotted as functions of the Fermi energy, E_{F}. Only the lowest energy charge state of each defect at a given Fermi energy is shown in the plot. The charge state of each defect at each point can be identified from the slope of the plot. $\mathrm{Ca_{Ba}}$ is always neutral for the entire possible Fermi energy range. This is consistent with the fact that Ca and Ba are isovalent. $\mathrm{Ca_{Ti}}$ is a deep double acceptor with the calculated ionization energy of ~200 meV. This is also consistent with the fact that group-II Ca is substituted for Ti, which is 4+ in BT.

The plots in Figure 4 are for the three choices of growth conditions previously explained and shown in the chemical potential space in Figure 1. First, we can clearly see that the formation energy of $\mathrm{Ca_{Ba}}$ is always significantly lower than that of $\mathrm{Ca_{Ti}}$. Note that the formation energies of calcium interstitials and calcium antisite (not shown) are even higher than that of $\mathrm{Ca_{Ti}}$, making them unlikely to form. Under Ba-rich/O-poor growth condition ($\boldsymbol{\mu}_{\mathbf{a}}$), the formation energy of $\mathrm{Ca_{Ba}}$ is in the negative region, indicating that $\mathrm{Ca_{Ba}}$ can rapidly form spontaneously. In reality, under condition $\boldsymbol{\mu}_{\mathbf{a}}$, the chemical potential of Ca has to be lowered below the (precipitation limit) value used here in order to maintain a stable growth of BT and keep the level of Ca incorporation controllable. (Lowering the chemical potential of Ca directly increases the formation energy of Ca related defects.) For Ba-poor/O-rich growth condition $\boldsymbol{\mu}_{\mathbf{c}}$, the formation energy of $\mathrm{Ca_{Ba}}$ is slightly lower than that in the condition $\boldsymbol{\mu}_{\mathbf{a}}$. However, the formation energy of $\mathrm{Ca_{Ti}}$ is much reduced and turned negative. $\mathrm{Ca_{Ti}}$ is a deep double acceptor and the 2- charge state becomes lower in energy than $\mathrm{Ca_{Ba}}$ for $E_{\mathrm{F}} > 0.54$ eV (Figure 4, right panel). Even under this condition, the neutral charge state of $\mathrm{Ca_{Ti}}$ is still almost 1 eV higher in energy than $\mathrm{Ca_{Ba}}$. For the intermediate growth condition, at point "*x*" the formation energy of $\mathrm{Ca_{Ba}}$ is significantly lower than that of $\mathrm{Ca_{Ti}}$. Our results indicate that, for all possible growth conditions (shaded area in the chemical potential space in Figure 1), Ca prefer to substitute for Ba (or A-site of the perovskite lattice) in BT.

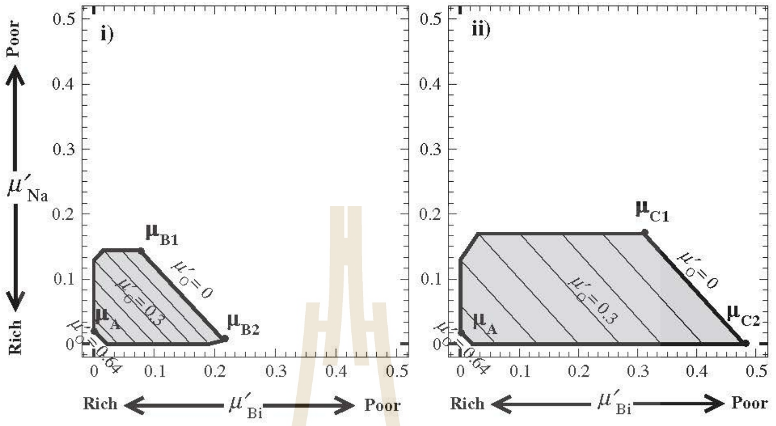

Figure 3. The possible chemical potentials of Bi and Na (shade area) that depend on chemical potential of O in each condition along the lines connecting (i) points (a) to (b) and (ii) points (a) to (c) in Figure 2.

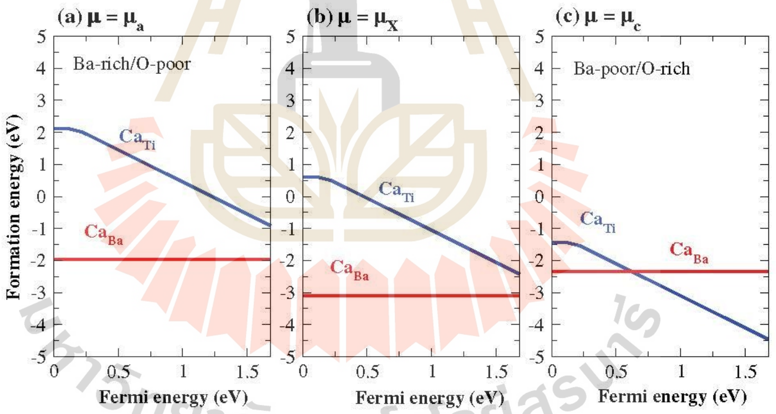

Figure 4. (colour online) The formation energies for Ca defects, that is, Ca substituting for Ba (denoted Ca_{Ba}) and Ca substituting for Ti (denoted Ca_{Ti}), in $BaTiO_3$ as functions of the Fermi level calculated under different growth conditions. Only the formation energies for the lowest energy charge states are shown. The charge state of each defect at each point can be identified from the slope of the plot.

For Ca in BNT, there are three types of cations. For the A-site of a perovskite lattice, there are two cations, Bi and Na. For B-site, there is only one type of cation (Ti). Therefore, we studied three substitutional defects, that is, Ca substituting for Ba

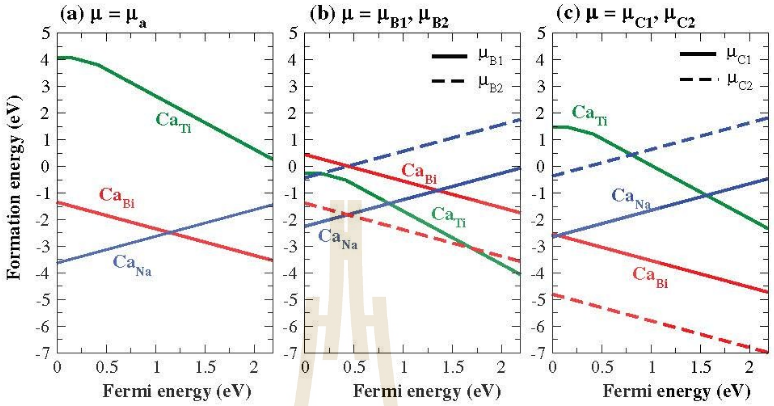

Figure 5. (colour online) The formation energies of Ca defects, that is, Ca substituting for Ba (denoted Ca_{Ba}), Ca substituting for Na (denoted Ca_{Na}) and Ca substituting for Ti (denoted Ca_{Ti}) in $Bi_{0.5}Na_{0.5}TiO_3$ as functions of Fermi level calculated under $\mathbf{\mu_A}$, $\mathbf{\mu_{B1}}$, $\mathbf{\mu_{B2}}$ (dash lines), $\mathbf{\mu_{C1}}$ and $\mathbf{\mu_{C2}}$ (dash lines) conditions. Only the formation energies for the lowest energy charge states are shown. The charge state of each defect at each point can be identified from the slope of the plot.

(denoted Ca_{Ba}), Ca substituting for Na (denoted Ca_{Na}) and Ca substituting for Ti (denoted Ca_{Ti}). In Figure 5, the formation energies of the three substitutional defects as functions of the Fermi energy are plotted. The plots are for the different choices of growth conditions previously discussed and shown in the chemical potential space in Figures 2 and 3. We found that Ca_{Ti} is a deep double acceptor with the calculated ionization energy 0/−1 of about 150 meV and −1/−2 of about 400 meV. Ca_{Bi} is a shallow single acceptor, while Ca_{Na} is a shallow single donor. These are consistent with what can be expected due to the electron counting. Calcium has two valence electrons therefore when it substitutes for Ti^{4+}, Bi^{3+}, and Na^{1+} it is expected to behave as a double acceptor, single acceptor and single donor, respectively. For the O-poor condition ($\mathbf{\mu_A}$), the formation energies are shown in the left panel of Figure 5. Under this condition, the formation energy of Ca_{Ti} is much higher than for Ca on A-site (Ca_{Bi} and Ca_{Na}). If the charge neutrality condition is required, the Fermi level is pinned at the crossing point between the Ca_{Bi} and Ca_{Na} line. At this crossing point, the formation energy of Ca_{Bi} and Ca_{Na} are equal and the two have the same concentration and fully charge compensate each other. It is noted, however, that the values of the formation energy shown are negative. In reality, the chemical potential of Ca has to be lowered to the point where the crossing point is in the positive region; leading to a low concentration of Ca and steady growth of BNT. For the O-rich conditions, one can vary the chemical potentials of Ti to its richest possible value and at the same time the average value of the chemical potentials of Bi and Na, that is, $(\mu_{Bi} + \mu_{Na})/2$, moves to its poor value. This is the condition $\mathbf{\mu_B}$. For this condition, the formation energies of Ca substitutional defects are shown in the middle panel of Figure 5. For a given average value of the chemical potentials of Bi and Na, the chemical potentials of Bi and Na can vary from Bi-rich Na-poor (B1) to Bi-poor Na-rich (B2). To present the formation energy in the same

Table 4. Calculated local structure around cations for pure and Ca-doped $BaTiO_3$ and $Bi_{0.5}Na_{0.5}TiO_3$.

Structure	Charge	Bond	Calculated distance (Å)	Coordination numbers
$BaTiO_3$	0	Ba-O	2.814	4
			2.850	4
			2.850	4
		Ti-O	1.990	4
			2.041	2
Ca_{Ba} in $BaTiO_3$	0	Ca-O	2.859	4
			2.902	4
			2.902	4
Ca_{Ti} in $BaTiO_3$	2−	Ca-O	2.049	4
			2.189	2
$Bi_{0.5}Na_{0.5}TiO_3$	0	Na-O	2.834	4
			2.505	4
			3.388	4
		Bi-O	2.838	4
			2.292	4
			3.263	4
		Ti-O	1.998	4
			2.258, 1.794	2
Ca_{Na} in $Bi_{0.5}Na_{0.5}TiO_3$	1+	Ca-O	2.833	4
			2.505	4
			3.382	4
Ca_{Bi} in $Bi_{0.5}Na_{0.5}TiO_3$	1−	Ca-O	2.831	4
			2.312	4
			3.257	4
Ca_{Ti} in $Bi_{0.5}Na_{0.5}TiO_3$	2−	Ca-O	2.054	4
			2.233, 2.021	2

plot, the formation energies of substitutional Ca corresponding to B1 are shown using solid lines and B2 using dashed lines. We can see that for B1 condition, Ca_{Na} is the most stable donor and it would compensate by Ca_{Ti} acceptor to maintain charge neutrality, the condition needed at a high Ca concentration. However, for B2 condition, Ca_{Bi} becomes the lowest formation energy acceptor; making Ca_{Ti} never stable. In an extreme n-type condition (when the Fermi level is near the conduction band minimum), the crossing of Ca_{Ti} below Ca_{Bi} is irrelevant because there is no compensating donor to pin down the Fermi energy in this region. Even if the Fermi level started in this region, as soon as the first few Ca_{Ti} acceptors started to form, the Fermi energy would immediately move lower toward the valence band – the region where Ca_{Bi} becomes more stable. Next, the O-rich conditions with the chemical potentials of Ti at its poorest possible value and at the same time the average value of the chemical potentials of Bi and Na, that is, $(\mu_{Bi} + \mu_{Na})/2$, moves to its highest possible value labelled by condition $\boldsymbol{\mu}_{\mathbf{C}}$ will be discussed. For this condition, the formation energies of Ca substitutional defects are shown in the right panel of Figure 5. While maintaining the average value, that is, $(\mu_{Bi} + \mu_{Na})/2$, the chemical potential of Bi and Na can vary from Bi-rich Na-poor (C1) to Bi-poor Na-rich (C2). For the C1 condition, the relevant compensating donor and acceptor are Ca_{Na} and Ca_{Bi} which cross near the valence band maximum Fermi energy. For the C2 condition, Ca_{Bi} is the only stable acceptor without a compensating donor. Similar to the case of B2, the Ca_{Bi} acceptor would be the only species that forms and the Fermi energy would move to the valence band maximum value (in the plot, the formation energy of Ca_{Na} is much higher and never crosses Ca_{Bi} at any point under B2 and C2 conditions). Our results indicate that, in BNT, Ca prefers to occupy the A-site, that is, substituting for Bi or Na for almost all growth conditions with the exception of condition B1 where Ca should substitute for both A-site and B-site with the concentration of Ca on B-site roughly half of Ca on A-site (Ca_{Ti} is a double acceptor while Ca_{Na} is a single donor).

The fact that Ca favours the A-site over B-site in perovskite BT and BNT is also consistent with the ionic radii. The ionic radii of 12-fold Ba^{2+}, Na^{1+} and 6-fold Ti^{4+} are 1.61, 1.39, and 0.605 Å, respectively. For Ca^{2+}, the 12-fold and 6-fold ionic radii are 1.34 and 1.0 Å, respectively [35]. We can see that the ionic radius of Ca^{2+} is a better fit with A-site ions (Ba^{2+} and Na^{1+}) than with the B-site ion (Ti^{4+}). The calculated relaxed bond distances of pure BT, BNT and Ca substitutional defects are summarized in Table 4. The local structure of Ca_{Ti} for both BT and BNT are similar. The same is also true for the Ca substitutional for the A-site (Ba in BT and Bi/Na in BNT). It is worth mentioning that, in the case of Ca_{Ba} in BT, Ca shifts off-centre along the *c*-axis by about 0.05 Å. This is consistent with the experimental observation that the T_c of the phase transformation of BT (from the low-temperature tetragonal phase to the cubic phase) shifts from the bulk value of $T_c = 403$ K to a higher value when the sample is doped with Ca [36]. Regarding the TCC of Ca-doped BNT-BT system, Ca substitutional on the A-site would have the local structure similar to that of $CaTiO_3$, which is known to be a very temperature stable (good TCC) material. Therefore, the improved TCC of BNT-BT system when doped by Ca observed by Yuan et al. [14] is consistent with our calculations that Ca prefers to substitute on the A-site.

5. Conclusions

Calcium defects in $BaTiO_3$ and $Bi_{0.5}Na_{0.5}TiO_3$ were studied by first principles calculations. Different growth conditions were investigated by introducing phase diagrams to show the possible range of chemical potentials of starting elements. It is found that Ca atoms prefer to substitute for cations. Calcium in the interstitial forms and antisite (substitute for oxygen) have high formation energies and are unlikely to form. Substitutional Ca in the A-site of the perovskite lattice, that is, Ca_{Ba} for $BaTiO_3$ and Ca_{Bi} and Ca_{Na} for $Bi_{0.5}Na_{0.5}TiO_3$, is the most favourable form of Ca incorporation in this class of materials and will predominantly form in all growth conditions. Only for the case of O-rich/Na-poor (condition B1) in $Bi_{0.5}Na_{0.5}TiO_3$, does Ca_{Ti} have a chance to form in a reasonable amount, that is, about half of the concentration of Ca_{Na}. In most cases, Ca does not lead to electrical doping in $BaTiO_3$ and $Bi_{0.5}Na_{0.5}TiO_3$. Ca is incorporated either as an electrical neutral defect (for the case of Ca_{Ba} in $BaTiO_3$) or self-compensating donor–acceptor pairs (for the cases of Ca_{Bi}/Ca_{Na} and Ca_{Ti}/Ca_{Na} pairs in $Bi_{0.5}Na_{0.5}TiO_3$). Only for the case of O-rich/Bi-poor in $Bi_{0.5}Na_{0.5}TiO_3$ (condition C2), do Ca_{Bi} acceptors have a chance to predominantly form without self-compensation by Ca donors.

Acknowledgements

Computations were carried out at the Synchrotron Light Research Institute (Public Organization), Thailand. We thank Prof. Walter R.L. Lambrecht for useful discussions and suggestions.

Manuscript submitted in Philosophical Magazine

Disclosure statement

No potential conflict of interest was reported by the authors.

Funding

This work was supported by NANOTEC-SUT Center of Excellence on Advanced Functional Nanomaterials. One of the authors (IF) was partially supported by the Development and Promotion of Science and Technology Talents Project (DPST, Thailand).

References

[1] S. Miyake and R. Ueda, J. Phys. Soc. Jpn. 3 (1948) p.177.
[2] W.J. Merz, Phys. Rev. 76 (1949) p.1221.
[3] L. Gao, Y. Huang, Y. Hu and H. Du, Ceram. Int. 33 (2007) p.1041.
[4] T. Takenaka, K. Maruyama and K. Sakata, Jpn. J. Appl. Phys. 30 (1991) p.2236.
[5] Y.-S. Jung, E.-S. Na, U. Paik, J. Lee and J. Kim, Mater. Res. Bull. 37 (2002) p.1633.
[6] Y. Yuan, S.R. Zhang, X.H. Zhou, B. Tang and B. Li, J. Electron. Mater. 38 (2009) p.706.
[7] T.A. Jain, C.C. Chen and K.Z. Fung, J. Eur. Ceram. Soc. 29 (2009) p.2595.
[8] K. Yoshii, Y. Hiruma, H. Nagata and T. Takenaka, Jpn. J. Appl. Phys. 45 (2006) p.4493.
[9] Y. Li, W. Chen, J. Zhou, Q. Xu, H. Sun and R. Xu, Mater. Sci. Eng., A 112 (2004) p.5.
[10] Z. Suchuan, L. Guorong, D. Aili, W. Tianbao and Y. Qingrui, J. Phys. D: Appl. Phys. 39 (2006) p.2277.
[11] D. Lin, D. Xiao, J. Zhu and P. Yu, J. Eur. Ceram. Soc. 26 (2006) p.3247.
[12] W. Ge, J. Li, D. Viehland and H. Luo, J. Am. Ceram. Soc. 93 (2010) p.1372.
[13] Q. Gou, J. Wu, A. Li, B. Wu, D. Xiao and J. Zhu, J. Alloys Compd. 521 (2012) p.4.
[14] Y. Yuan, X.H. Zhou, C.J. Zhao, B. Li and S.R. Zhang, J. Electron. Mater. 39 (2010) p.2471.
[15] J.P. Perdew, K. Burke and M. Ernzerhof, Phys. Rev. Lett. 77 (1996) p.3865.
[16] J.P. Perdew, K. Burke and M. Ernzerhof, Phys. Rev. Lett. 78 (1997) p.1396.
[17] P.E. Blöchl, Phys. Rev. B 50 (1994) p.17953.
[18] G. Kresse and D. Joubert, Phys. Rev. B 59 (1999) p.1758.
[19] G. Kresse and J. Hafner, Phys. Rev. B 47 (1993) p.558.
[20] G. Kresse and J. Hafner, Phys. Rev. B 49 (1994) p.14251.
[21] G. Kresse and J. Furthmüller, Comput. Mater. Sci. 6 (1996) p.15.
[22] G. Kresse and J. Furthmüller, Phys. Rev. B 54 (1996) p.11169.
[23] D. Vanderbilt, Phys. Rev. B 41 (1990) p.7892.
[24] C.G. Van de Walle and J. Neugebauer, J. Appl. Phys. 95 (2004) p.3851.
[25] H.J. Monkhorst and J.D. Pack, Phys. Rev. B 13 (1976) p.5188.
[26] S.H. Wemple, Phys. Rev. B 2 (1970) p.2679.
[27] B. Parija, T. Badapanda, V. Senthil, S.K. Rout and S. Panigrahi, Bull. Mater. Sci. 35 (2012) p.197.
[28] R.P. Feynman, Phys. Rev. 56 (1939) p.340.
[29] N.W. Ashcroftand and N.D. Mermin, *Solid State Physics*, Holt, Rinehart and Winston, 1976.
[30] J. Bass, Philos. Mag. 15 (1967) p.717.
[31] S.B. Zhang and J.E. Northrup, Phys. Rev. Lett. 67 (1991) p.2339.
[32] J.E. Northrup and S.B. Zhang, Phys. Rev. B 50 (1994) p.4962.
[33] F. Gupta, G. Brillant and A. Pasturel, Philos. Mag. 87 (2007) p.2561.
[34] Q. Li, B. Wang, C.H. Woo, H. Wang and R. Wang, J. Phys. Chem. Solids 68 (2007) p.1336.
[35] R. Shannon, Acta Crystallogr., Sect. A 32 (1976) p.751.

Manuscript submitted in Philosophical Magazine

[36] Y. Yamada, G. Shirane and A. Linz, Phys. Rev. 177 (1969) p.848.
[37] R.H. Buttner, E.N. Maslen, Acta Crystallogr., Sect. B: Struct. Sci. 48 (1992) p.764.
[38] G.O. Jones, P.A. Thomas, Acta Crystallogr., Sect. B 56 (2000) p.426.

Manuscript submitted in Journal of Applied Physics

JOURNAL OF APPLIED PHYSICS **115**, 203511 (2014)

Identification of oxygen defects in CdTe revisited: First-principles study

J. T-Thienprasert,[1,2,a)] T. Watcharatharapong,[1] I. Fongkaew,[2,3] M. H. Du,[4] D. J. Singh,[4] and S. Limpijumnong[3]
[1]*Department of Physics, Faculty of Science, Kasetsart University, Bangkok 10900, Thailand*
[2]*Thailand Center of Excellence in Physics (ThEP Center), Commission on Higher Education, Bangkok 10400, Thailand*
[3]*School of Physics and NANOTEC-SUT Center of Excellence on Advanced Functional Nanomaterials, Suranaree University of Technology, Nakhon Ratchasima 30000, Thailand*
[4]*Oak Ridge National Laboratory, Oak Ridge, Tennessee 37831, USA*

(Received 12 March 2014; accepted 14 May 2014; published online 28 May 2014)

By using first-principles calculations, several SO_2 complexes in CdTe were studied. Based on experimental observation, SO_2 complexes have been recently proposed by Lavrov *et al.* [Phys. Rev. B. **84**, 233201 (2011)] to be the cause of the observed IR absorption peaks at 1096.8 and 1108.4 cm^{-1} in O-doped CdTe. Chen *et al.* [Phys. Rev. Lett. **96**, 035508 (2006)] were originally proposed that the peaks come from O_{Te}-V_{Cd} complex. Our calculations indicate that the SO_2 molecule on the Te site $[(SO_2)_{Te}]$ has a low formation energy but its calculated vibration frequencies (~900 cm^{-1}) are lower than the observed IR modes. However, $(SO_2)_{Te}$ can form a complex with V_{Cd} with two possible configurations that give the vibration frequencies in a good agreement with the two observed IR peaks. The binding energies of the complex in these two configurations are about 1 eV under *p*-type conditions; indicating that the complex is quite stable. The two configurations are related to each other by a rotation of the SO_2 molecule with an energy barrier of ~0.4 eV. Therefore, the two configurations can co-exist at a low temperature and the high energy one gradually transforms to the low energy one as temperature increases. This agrees with the experimental observation that, at a high temperature, the two IR modes merged into one.
[http://dx.doi.org/10.1063/1.4880157]

INTRODUCTION

CdTe is recognized as an important semiconductor and used in many applications, such as x-ray and γ-ray detectors,[1,2] and solar panels.[3–5] The quality of such devices depends on the carrier lifetime, which is strongly affected by impurities and defects. The understanding of impurities and defects in CdTe is mandatory for improving such devices. The vibrational modes associated with light-atom impurities (compared to the host atoms) are generally distinct from the crystal phonon of the host atoms; leading to the localized vibrational modes (LVMs). Each impurity or defect has a unique LVM signature due to the distinction of the impurity mass and bonding character. Therefore, in many cases, LVMs can be used to characterize the local structure of light impurities in crystals.

Chen *et al.* experimentally studied the LVMs of oxygen-related impurities in CdTe using a Fourier transformed infrared (FTIR) spectroscopy technique.[6,7] In their work, CdTe samples were grown by using the vertical Bridgman technique and TeO_2 and CdO were intentionally added as a source of oxygen. The IR absorption peaks associated with oxygen impurity were found at two regions: (1) at low frequency with the LVM of 341 cm^{-1} and (2) at high frequency with the LVMs of 1096.8 (ν_1) and 1108.4 cm^{-1} (ν_2). They assigned the 341 cm^{-1} mode to a substitutional oxygen at Te site (O_{Te}), which is later confirmed by a vibrational calculations by first principles density functional calculations.[8,9]

For the two high LVMs at 1096.8 and 1108.4 cm^{-1}, Chen *et al.* assigned them to the O substitution Te–Cd vacancy defect complex (O_{Te}-V_{Cd}). They explained that the vibrational frequency of O_{Te} is increased when it formed a complex defect with Cd vacancy (O_{Te}-V_{Cd}) and because of V_{Cd} breaks the four-fold symmetry of O_{Te}, the frequency splits into two modes. However, for the frequency to be increased by 3 times, the bond strength of Cd-O has to be increased by 9 times, which is unlikely. Later, T-Thienprasert *et al.* have shown based on first principles density functional calculations that the O_{Te}-V_{Cd} model fails to explain the observed high LVMs and their calculated vibrational frequencies are only 197 and 467 cm^{-1}, which are far from the observed values but are considered to be a reasonable split of the 341 cm^{-1} mode as expected.[8]

More recently, Lavrov *et al.* have experimentally reexamined the LVMs of oxygen impurity in CdTe by using FTIR technique.[10] In their work, the sample was prepared by using single-crystal CdTe and $CdSO_4$ vapor as a source of sulfur and oxygen impurities. Surprisingly, the IR absorption lines at 1096.8 and 1108.4 cm^{-1} were reproduced. They reasoned that these LVMs are close to the vibrational mode of SO_2 molecule in the gas phase and assigned the two high LVMs at 1096.8 and 1108.4 cm^{-1} to the asymmetric stretching modes of a sulfur-dioxygen (SO_2^*) complex rather than O_{Te}-V_{Cd} complex. However, the detailed structure of SO_2^* complex in CdTe lattice is still unknown.

[a)] Author to whom correspondence should be addressed. Electronic mail: fscicwt@ku.ac.th

Here, by using first-principles density functional calculations, the structures of SO_2^*-related complexes in CdTe were investigated. The most probable structures that are responsible for the two IR observed absorption lines at 1096.8 and 1108.4 cm^{-1} are identified. The energetic and stability of SO_2^*-related complexes are also discussed.

COMPUTATIONAL METHOD

In this work, we performed first-principles calculations based on density functional theory (DFT) within the local density approximations (LDA). The projector augmented wave potentials,[11] as implemented in VASP code,[12,13] were used to describe the electron-ion interactions. The energy cutoff for the plane wave basis set was set at 500 eV. The calculated lattice constant of bulk CdTe is 6.42 Å, which is in a good agreement with the experimental value of 6.477 Å.[14]

To study the defects in CdTe, we used a supercell approach[15] with 64-atom supercell, which is a 2 × 2 × 2 repetition of the conventional zincblend cell. For each defect, all atoms in the supercell were fully allowed to relax until the Hellmann-Feynman forces[16] acting on each atom became less than 10^{-3} eV/Å. The Monkhorst-Pack scheme[17] with a sampling *k*-points mesh of 2 × 2 × 2 was used for *k*-space integrations. The stability and likelihood of forming each defect can be investigated by calculating the defect formation energy, defined by

$$\Delta H_f(D^q) = E_{\text{tot}}(D^q) - E_{\text{tot}}(\text{Bulk}) - \sum_X n_X\mu_X + q[E_F + E_{VBM}], \quad (1)$$

where $E_{\text{tot}}(D^q)$ is the total energy of a defect D in charge q, $E_{\text{tot}}(Bulk)$ is the total energy of a perfect supercell, n is the number of atom species X (here X can be Cd, Te, O, or S atoms) being added to (positive sign) or removed from (negative sign) the supercell to create the defect, μ_X is the atomic chemical potential of atom species X, which will be described below, q is the charge of the defect, and E_F is the Fermi-level which is referenced to the valence band maximum (E_{VBM}).

Under thermodynamic equilibrium growth condition, to steadily grow a single crystal CdTe, the following condition must be satisfied:

$$E_{\text{tot}}(\text{CdTe}) = \mu_{\text{Cd}} + \mu_{\text{Te}}, \quad (2)$$

where E_{tot}(CdTe) is the total energy of formula unit of pure zincblend CdTe crystal.

If μ_{Cd} is set to the total energy per formula of metallic-Cd, μ_{Te} can be directly obtained from Eq. (2). This growth condition is called Cd-rich condition. On the other hand, if μ_{Te} is set to the total energy per formula of metallic-Te, μ_{Cd} can be again obtained from Eq. (2). In this case, we call Te-rich growth condition.

When oxygen and sulfur are introduced to CdTe, we need to ensure that there is no precipitation of metal-oxide as well as metal-sulfate phases. This can be done by limiting the chemical potential of O to the value just below the formation of their plausible oxide and sulfate phases. The formation energy of CdS was used to determine the sulfur chemical potential based on the relationship $\mu_{\text{S}} = \mu_{\text{CdS}} - \mu_{\text{Cd}}$ for both Cd-rich and Te-rich growth conditions. For the oxygen chemical potential, μ_{O}, the formation energies of CdO and $CdSO_4$ were used based on the relationship $\mu_{\text{O}} = \mu_{\text{CdO}} - \mu_{\text{Cd}}$ and $\mu_{\text{O}} = (\mu_{\text{CdSO}_4} - \mu_{\text{Cd}} - \mu_{\text{S}})/4$ for Cd-rich and Te-rich growth conditions, respectively.

The LVMs of the defects were determined using the so-called frozen-phonon approach. Based on the harmonic approximation, a dynamical matrix could be constructed and the LVMs were obtained from the eigenvectors and eigenvalues of the dynamical matrix. The detail of LVM calculations used here has been previously described in Ref. 8. Based on previous results on similar systems, the accuracy of the frequencies obtained from this method is approximately ±10% when comparing with the experimental values.[8,18,19] This is considered very reliable and satisfactory since the approach takes no empirical parameters from experiments.

RESULTS AND DISCUSSIONS

In this paper, we focused our attentions on the study of oxygen O and sulfur S complex defects in CdTe based on the experimental results studied by Lavrov *et al.*[10] and Chen *et al.*[6] There are several plausible candidates of oxygen-sulfur complex defects in CdTe to be investigated. To gain a better understanding of the building block of these complexes, first, individual defects (O and S) were separately investigated.

For O defects in CdTe, we investigated two most probable forms, i.e., O substitution of Te (O_{Te}) and O interstitial (O_i). Results of O_{Te} have been previously reported along with O_{Te}-V_{Cd} defects by our group and would not be repeated here.[8] For O_i, among several possible configurations studied, the interstitial off-bonding (OB) center configuration turned out to be the lowest energy, i.e., the most stable one. The structure is shown in Fig. 1 and its formation energy is shown in Fig. 2. The local structure of O_i at the OB site is similar to the well-known O_i in Si.[20–22] However, here, the O atom at OB site is slightly closer to the Te atom than Cd atom with a Te-O and Cd-O bond length of 1.91 and 2.11 Å, respectively. The calculations showed that O_i is a charge neutral defect and does not introduce any electronic level in the bandgap of CdTe. In addition, the formation energy of O_i is rather high in Cd-rich growth conditions (see Fig. 2) indicating that they might be formed in a limited amount.

For S defects in CdTe, we found that the lowest energy form of S defect is S substitute for Te (S_{Te}). S_{Te} is neutral as expected, since S and Te are isovalent. The very low formation energy of S_{Te} under Cd-rich and Te-rich growth conditions can be clearly seen in the formation energy plot in Fig. 2. We also studied interstitial S (S_i) which has a much larger formation energy than that of S_{Te}. The formation energy of the neutral charge S_i is 2.2 eV larger than that of

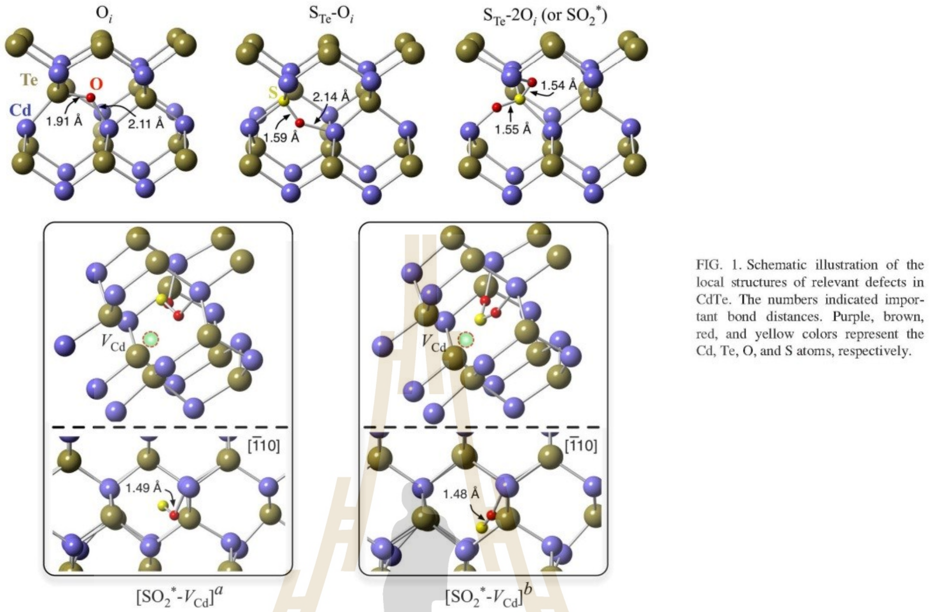

FIG. 1. Schematic illustration of the local structures of relevant defects in CdTe. The numbers indicated important bond distances. Purple, brown, red, and yellow colors represent the Cd, Te, O, and S atoms, respectively.

S_{Te} under Cd-rich growth condition (1.47 eV larger for the Te-rich condition).

For the complex defects between O and S, we found that O_i can bind with S_{Te}, forming a charge neutral S_{Te}-O_i complex with the binding energy of ~0.16 eV as shown in Fig. 1. The S-O bond length in S_{Te}-O_i complex is ~1.59 Å which is somewhat larger than that of SO_2 molecule (calculated value = 1.44 Å). Although, the binding energy of S_{Te}-O_i is quite small, the complex can bind another O becoming S_{Te}-$2O_i$ complex with a large binding energy of 1.68 eV. The complex is stable in a neutral charge state. The local structure of SO_2 in this complex defect is similar to the SO_2 molecule except that the S-O bonds are slightly larger than that in a free molecule as illustrated in Fig. 1. The large binding energy of the second O to the existing S_{Te}-O_i complex can be explained by the stability of the hybridized orbital of

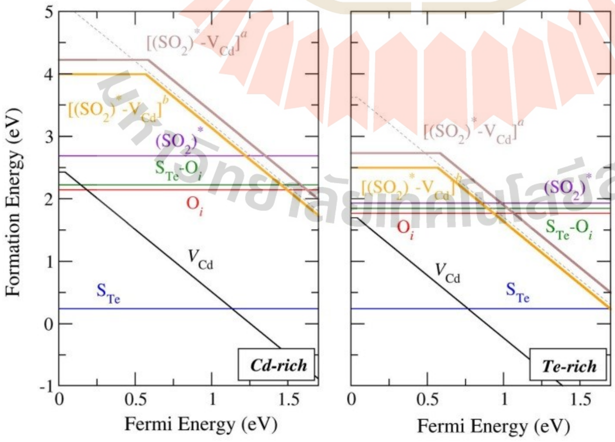

FIG. 2. The formation energies of defects in CdTe as a function of Fermi energy under Cd- and Te-rich growth conditions. The band gap range used for the plot is the calculated band gap at the special *k*-points. The slope of each line indicates the charge state of the defect. The dashed line is the sum of the formation energies of V_{Cd} and SO_2^* defects.

SO_2 molecule. Because of the similarity in the local structure with a SO_2 molecule, from this point on, we will abbreviate S_{Te}-$2O_i$ complex to SO_2^*. Our calculations showed that the formation energy of SO_2^* complex under Te-rich growth condition is quite lower than that under Te-rich growth conditions. This is mainly due to a large binding energy of a second oxygen atom to the S_{Te}-O_i complex to form SO_2^* (1.68 eV). Due to the larger S-O bond lengths in S_{Te}-O_i and SO_2^* complexes compared to a free SO_2 molecule, the vibrational frequencies associated with the S-O bond are expected to be lower than the corresponding ones of a free SO_2 molecule.

By using the frozen-phonon approach, we directly calculated the vibrational frequencies of S_{Te}-O_i and SO_2^* complexes to compare with the measured IR absorption lines.[6–8,10,19] To test the accuracy of this approach, the vibrational frequencies of the asymmetric stretching, symmetric stretching, and bending modes of a SO_2 molecule were calculated and tabulated in Table I. The calculated frequencies are satisfactorily in agreement with the known experimental values with the deviation of less than 4%. Based on this approach, the vibrational modes of S_{Te}-O_i and SO_2^* complexes in CdTe were calculated and the modes associated with the S-O bonds are also reported in Table I. The vibrational frequencies of S_{Te}-O_i and SO_2^* complexes are somewhat lower than those of SO_2 molecule, as expected, due to their larger S-O bond lengths. Compared with the targeted observed values of 1096.8 and 1108.4 cm^{-1}, the vibrational frequencies of these complexes are clearly lower with the highest one being only 926 cm^{-1} (a 16% smaller). Therefore, the S_{Te}-O_i and SO_2^* complexes, by themselves, do not fit with the observed IR lines. Next, we will show that the frequencies of SO_2^* complex depend somewhat on its neighbor such that if it binds with another common native defect of CdTe, i.e., Cd vacancy, the frequency could be in agreement with the observed IR absorption spectra.

By investigating several potential native defects that could bind with the SO_2^* complex, we found that cadmium vacancy, V_{Cd}, can bind with the SO_2^* and become SO_2^*-V_{Cd} complex. There are two stable structures for SO_2^*-V_{Cd} complex: (1) meta-stable configuration; $[SO_2^*\text{-}V_{Cd}]^a$ and (2) stable configuration; $[SO_2^*\text{-}V_{Cd}]^b$ (Fig. 1); related to each other by a simple rotation of the SO_2. These complexes are deep double acceptors with the transition levels $\varepsilon(0/-2) = 0.58$ and 0.57 eV for $[SO_2^*\text{-}V_{Cd}]^a$ and $[SO_2^*\text{-}V_{Cd}]^b$, respectively, as can be seen in the formation energy plot (Fig. 2). Because undoped CdTe samples are naturally *p*-type, we focus our attentions on the cases where the Fermi level is near the VBM. Under such condition, the SO_2^*-V_{Cd} complexes are stable in the neutral charge state. To determine the stability of these complexes, we calculated the sum of the formation energies of SO_2^* complex and V_{Cd} (dashed line in Fig. 2). The $[SO_2^*\text{-}V_{Cd}]^a$ and $[SO_2^*\text{-}V_{Cd}]^b$ complexes are bound if their formation energies are lower than the dashed line. From Fig. 2, the binding energy between the SO_2^* and the V_{cd} to form a complex in charge neutral is quite large, i.e., about 1 eV but that in 2-charge state is very low. This indicates that the $[SO_2^*\text{-}V_{Cd}]^a$ and $[SO_2^*\text{-}V_{Cd}]^b$ complexes should be stable in charge neutral. The metastable form of the complex, i.e., $[SO_2^*\text{-}V_{Cd}]^a$, is only 0.23 eV higher than that of the stable form, i.e., $[SO_2^*\text{-}V_{Cd}]^b$. Note, however that, the actual energy difference between the two configurations might be even smaller than 0.23 eV because the computation carries a small error bar.

Because the two forms of the complex are related to each other by a simple rotation of the SO_2, we used the so-called nudged elastic band (NEB) method[23–26] on top of the first principles total energy calculations to investigate the energy topology along the rotation path between these two configurations. We obtained the energy topology along the rotation path as shown in Fig. 3. There are clear two local energy minima corresponding to the configurations $[SO_2^*\text{-}V_{Cd}]^a$ and $[SO_2^*\text{-}V_{Cd}]^b$ with the barrier of about 0.4 eV between them. Actually, there is another meta-stable structures, labeled as $[SO_2^*\text{-}V_{Cd}]^c$ in the figure. However, because this structure has a much higher energy (about 0.73 eV above $[SO_2^*\text{-}V_{Cd}]^b$) with a very small barrier (only 0.04 eV) to rotate back to $[SO_2^*\text{-}V_{Cd}]^b$, $[SO_2^*\text{-}V_{Cd}]^c$ is unlikely to exist. Based on these results, we can predict that at sufficiently low temperature ($kT \ll 0.4$ eV) both $[SO_2^*\text{-}V_{Cd}]^a$ and $[SO_2^*\text{-}V_{Cd}]^b$ can

TABLE I. Calculated LVMs associated with the S-O bonds of defects in CdTe as well as a free SO_2 molecule. The calculated S-O bond lengths are also given. The experimental values of the free SO_2 molecule are given for comparison and the targeted frequencies observed in O-doped CdTe samples are also shown. The vibrational frequencies associated with the symmetric stretching mode correspond to much smaller dipole changes so their signals may be too low to be detected by IR.

Type	Charge state	S-O bond length (Å)	Vibrational mode	Calculated value (cm^{-1})	Experimental value (cm^{-1})
SO_2 molecule	0	1.44	Asymmetric stretching	1312.9	1361.8 (Ref. 27)
			Symmetric stretching	1122.6	1151.4 (Ref. 27)
			Bending	499.5	517.7 (Ref. 27)
S_{Te}-O_i	0	1.59	Stretching	863.6	
SO_2^*	0	1.54 and 1.55	Asymmetric stretching	926.2	
			Symmetric stretching	886.0	
$[SO_2^*\text{-}V_{Cd}]^a$	0	1.49	Asymmetric stretching	1094.9 (ν_1)	1096.8 (ν_1) and 1108.4 (ν_2)[6,7,10]
			Symmetric stretching	972.1	
$[SO_2^*\text{-}V_{Cd}]^b$	0	1.48	Asymmetric stretching	1097.4 (ν_2)	
			Symmetric stretching	994.8	
$[SO_2^*\text{-}V_{Cd}]^c$	0	1.48	Asymmetric stretching	1135.5	
			Symmetric stretching	923.4	

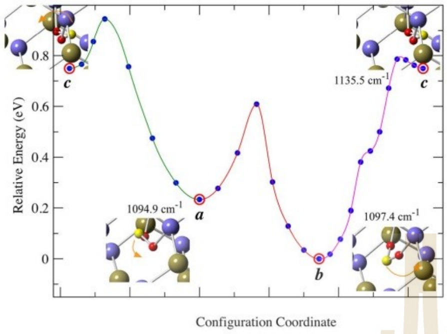

FIG. 3. Calculated energy of the SO_2^*-V_{Cd} complex as the SO_2 molecule rotates to form three different configurations, i.e., $[\mathrm{SO}_2^*\text{-}V_{\mathrm{Cd}}]^a$ (metastable), $[\mathrm{SO}_2^*\text{-}V_{\mathrm{Cd}}]^b$ (stable), and $[\mathrm{SO}_2^*\text{-}V_{\mathrm{Cd}}]^c$ (unstable). The energy is referenced to that of the $[\mathrm{SO}_2^*\text{-}V_{\mathrm{Cd}}]^b$ configuration.

co-existed. The population of $[\mathrm{SO}_2^*\text{-}V_{\mathrm{Cd}}]^b$ is always higher than that of $[\mathrm{SO}_2^*\text{-}V_{\mathrm{Cd}}]^a$ due to the lower formation energy.

After V_{Cd} is introduced to SO_2^*, the S-O bond lengths of SO_2^* are slightly reduced, i.e., reduced to 1.48 Å and 1.49 Å for $[\mathrm{SO}_2^*\text{-}V_{\mathrm{Cd}}]^b$ and $[\mathrm{SO}_2^*\text{-}V_{\mathrm{Cd}}]^a$ complex, respectively. As a result, the vibrational frequencies associated with the stretch mode of these bonds are expected to increase compared to the SO_2^* complex. The calculated vibrational modes associated with the stretch modes of S-O bonds of $[\mathrm{SO}_2^*\text{-}V_{\mathrm{Cd}}]^a$ and $[\mathrm{SO}_2^*\text{-}V_{\mathrm{Cd}}]^b$ complex defects are shown in Table I. The vibrational frequency of $[\mathrm{SO}_2^*\text{-}V_{\mathrm{Cd}}]^a$ complex is slightly lower than that of $[\mathrm{SO}_2^*\text{-}V_{\mathrm{Cd}}]^b$ complex, in agreement with the slightly longer S-O bond lengths. The vibrational frequencies of the asymmetric modes (1094.9 and 1097.4 cm^{-1}) are close to the observed low temperature IR absorption lines at 1096.8 and 1108.4 cm^{-1}. Therefore, we assign the observed 1096.8 cm^{-1} mode to $[\mathrm{SO}_2^*\text{-}V_{\mathrm{Cd}}]^a$ complex and the 1108.4 cm^{-1} mode to $[\mathrm{SO}_2^*\text{-}V_{\mathrm{Cd}}]^b$ complex. The smaller splitting between the two calculated vibrational frequencies (2.5 cm^{-1}) compared to the experimental one (11.6 cm^{-1}) might be due to the anharmonic effects that were not included in our calculations. At a higher temperature, the fact that the two observed IR lines merged into one is consistent with our assignment because at a high temperature the defect moves nearly freely between the ground state $[\mathrm{SO}_2^*\text{-}V_{\mathrm{Cd}}]^b$ and the metastable state $[\mathrm{SO}_2^*\text{-}V_{\mathrm{Cd}}]^a$. Therefore, the two IR peaks significantly broaden and merge into one. Regarding the IR line intensities, the higher frequency mode (1108.4 cm^{-1}) is observed to have a stronger intensity, I(ν_2), than that of the lower frequency (1096.8 cm^{-1}) one, I(ν_1).[6,7,10] Because I(ν_2) is about twice of I(ν_1), Chen *et al.*[7] assigned ν_2 to a doubly degenerate mode and ν_1 to a singlet mode of the same defect (O_{Te}-V_{Cd}). If the two modes are from the same defect as Chen *et al.* proposed, the I(ν_2)/I(ν_1) ratio should always close to two (assuming that the oscillator strength is comparable) and remain constant not depending on temperature because it is the signature of that single defect. However, they found that the ratio varied from 1.6 at very low temperature to about 2.0 at 100 K and handwavingly assigned this effect to the dynamic of O_{Te}-V_{Cd} defects at higher temperature. Here, both $[\mathrm{SO}_2^*\text{-}V_{\mathrm{Cd}}]^a$ and $[\mathrm{SO}_2^*\text{-}V_{\mathrm{Cd}}]^b$, that we assigned to be the source of ν_1 and ν_2, respectively, have the same configuration degeneracy. However, their formation energies are different with $[\mathrm{SO}_2^*\text{-}V_{\mathrm{Cd}}]^b$ being slightly lower. Therefore, the $[\mathrm{SO}_2^*\text{-}V_{\mathrm{Cd}}]^b$ complex should exist in a larger concentration than the $[\mathrm{SO}_2^*\text{-}V_{\mathrm{Cd}}]^a$ complex; making I(ν_2) larger than I(ν_1) in agreement with the measurement. For the increase of the ratio with temperature, we can explain it as the switching from the trapped metastable $[\mathrm{SO}_2^*\text{-}V_{\mathrm{Cd}}]^a$ to the ground state $[\mathrm{SO}_2^*\text{-}V_{\mathrm{Cd}}]^b$. In addition, the binding between SO_2^* and V_{Cd} defects is consistent with the Chen's work[6,7] reporting that the intensities of the observed IR absorption lines at 1096.8 and 1108.4 cm^{-1} are associated with the concentration of V_{Cd} and O defects which is intentionally introduced by adding TeO during the crystal growth process. Therefore, our proposed models are in good agreement with the experimental work.

CONCLUSION

Based on first-principles density functional calculations, several SO_2 defects in CdTe have been studied; following recent experimental work that suggested them to be the cause of the observed IR absorption peaks at 1096.8 and 1108.4 cm^{-1}. We assigned the observed IR modes at 1096.8 and 1108.4 cm^{-1} to the asymmetric stretching vibrational modes of $[\mathrm{SO}_2^*\text{-}V_{\mathrm{Cd}}]^a$ and $[\mathrm{SO}_2^*\text{-}V_{\mathrm{Cd}}]^b$ complexes, respectively. This assignment is supported by the calculations of the complex formation energies and the vibrational frequency calculations. Our assignment also explains the merging of the two IR absorption peaks at high temperatures.

ACKNOWLEDGMENTS

The work at Suranaree University of Technology was supported by NANOTEC, NSTDA (Thailand) through its Center of Excellence Network program. T. Watcharatarapong and I. Fongkaew acknowledge the scholarship from the Development and Promotion of Science and Technology (DPST). The work at Oak Ridge National Laboratory is supported by the U.S. Department of Energy, Basic Energy Sciences, Materials Sciences and Engineering Division. J. T-Thienprasert is funded by TRF 2014 and KURDI.

[1] T. E. Schlesinger, J. E. Toney, H. Yoon, E. Y. Lee, B. A. Brunett, L. Franks, and R. B. James, Mater. Sci. Eng. **32**, 103 (2001).
[2] C. Szeles, Phys. Status Solidi B **241**, 783 (2004).
[3] S. P. Albright, J. F. Jordan, B. Ackerman, and R. R. Chamberlin, Sol. Cells **27**, 77 (1989).
[4] N. Amin, K. Sopian, and M. Konagai, Sol. Energy Mater. Sol. Cells **91**, 1202 (2007).
[5] A. Morales-Acevedo, Sol. Energy Mater. Sol. Cells **90**, 2213 (2006).
[6] G. Chen, I. Miotkowski, S. Rodriguez, and A. K. Ramdas, Phys. Rev. Lett. **96**, 035508 (2006).
[7] G. Chen, I. Miotkowski, S. Rodriguez, and A. K. Ramdas, Phys. Rev. B **75**, 125204 (2007).
[8] J. T-Thienprasert, S. Limpijumnong, A. Janotti, C. G. Van de Walle, L. Zhang, M. H. Du, and D. J. Singh, Comput. Mater. Sci. **49**, S242 (2010).
[9] L. Zhang, J. T-Thienprasert, M. H. Du, D. J. Singh, and S. Limpijumnong, Phys. Rev. Lett. **102**, 209601 (2009).
[10] E. V. Lavrov, D. Bastin, J. Weber, J. Schneider, A. Fauler, and M. Fiederle, Phys. Rev. B **84**, 233201 (2011).

Manuscript submitted in Journal of Applied Physics

[11] G. Kresse and D. Joubert, Phys. Rev. B **59**, 1758 (1999).
[12] G. Kresse and J. Hafner, J. Phys.: Condens. Matter **6**, 8245 (1994).
[13] G. Kresse and J. Furthmüller, Comput. Mater. Sci. **6**, 15 (1996).
[14] *CRC Handbook of Chemistry and Physics*, 88th ed., edited by D. R. Lide (CRC Press/Taylor and Francis, Boca Raton, FL, 2008).
[15] C. G. Van de Walle and J. Neugebauer, J. Appl. Phys. **95**, 3851 (2004).
[16] R. P. Feynman, Phys. Rev. **56**, 340 (1939).
[17] H. J. Monkhorst and J. D. Pack, Phys. Rev. B **13**, 5188 (1976).
[18] J. T-Thienprasert, I. Fongkaew, D. J. Singh, M. H. Du, and S. Limpijumnong, Phys. Rev. B **85**, 125205 (2012).
[19] J. T-Thienprasert, S. Limpijumnong, M. H. Du, and D. J. Singh, Physica B **407**, 2841 (2012).
[20] M. Pesola, J. von Boehm, and R. M. Nieminen, Phys. Rev. Lett. **82**, 4022 (1999).
[21] S. Öberg, C. P. Ewels, R. Jones, T. Hallberg, J. L. Lindström, L. I. Murin, and P. R. Briddon, Phys. Rev. Lett. **81**, 2930 (1998).
[22] M. Needels, J. D. Joannopoulos, Y. Bar-Yam, and S. T. Pantelides, Phys. Rev. B **43**, 4208 (1991).
[23] G. Mills, H. Jónsson, and G. K. Schenter, Surf. Sci. **324**, 305 (1995).
[24] G. Henkelman and H. Jonsson, J. Chem. Phys. **113**, 9978 (2000).
[25] G. Henkelman, B. P. Uberuaga, and H. Jonsson, J. Chem. Phys. **113**, 9901 (2000).
[26] D. Sheppard, R. Terrell, and G. Henkelman, J. Chem. Phys. **128**, 134106 (2008).
[27] W. B. Person and G. Zerbi, *Vibrational Intensities in Infrared and Raman Spectroscopy* (Elsevier, Amsterdam, 1982).

Manuscript submitted in Ceramics International

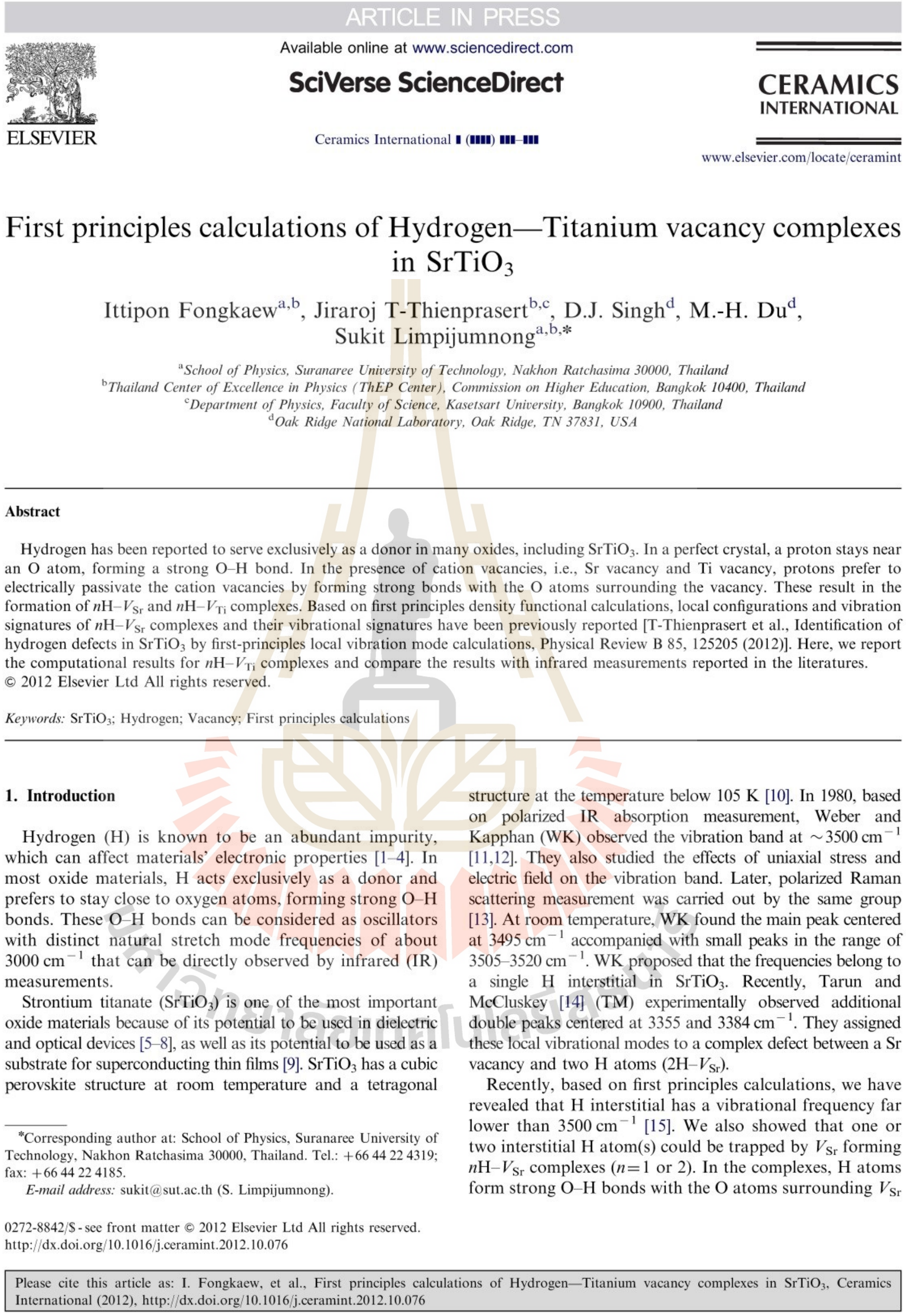

ARTICLE IN PRESS

Available online at www.sciencedirect.com

SciVerse ScienceDirect

ELSEVIER

Ceramics International ▮ (▮▮▮▮) ▮▮▮–▮▮▮

CERAMICS INTERNATIONAL

www.elsevier.com/locate/ceramint

First principles calculations of Hydrogen—Titanium vacancy complexes in $SrTiO_3$

Ittipon Fongkaew[a,b], Jiraroj T-Thienprasert[b,c], D.J. Singh[d], M.-H. Du[d],
Sukit Limpijumnong[a,b,*]

[a]*School of Physics, Suranaree University of Technology, Nakhon Ratchasima 30000, Thailand*
[b]*Thailand Center of Excellence in Physics (ThEP Center), Commission on Higher Education, Bangkok 10400, Thailand*
[c]*Department of Physics, Faculty of Science, Kasetsart University, Bangkok 10900, Thailand*
[d]*Oak Ridge National Laboratory, Oak Ridge, TN 37831, USA*

Abstract

Hydrogen has been reported to serve exclusively as a donor in many oxides, including $SrTiO_3$. In a perfect crystal, a proton stays near an O atom, forming a strong O–H bond. In the presence of cation vacancies, i.e., Sr vacancy and Ti vacancy, protons prefer to electrically passivate the cation vacancies by forming strong bonds with the O atoms surrounding the vacancy. These result in the formation of nH–V_{Sr} and nH–V_{Ti} complexes. Based on first principles density functional calculations, local configurations and vibration signatures of nH–V_{Sr} complexes and their vibrational signatures have been previously reported [T-Thienprasert et al., Identification of hydrogen defects in $SrTiO_3$ by first-principles local vibration mode calculations, Physical Review B 85, 125205 (2012)]. Here, we report the computational results for nH–V_{Ti} complexes and compare the results with infrared measurements reported in the literatures.

Keywords: $SrTiO_3$; Hydrogen; Vacancy; First principles calculations

---

1. Introduction

Hydrogen (H) is known to be an abundant impurity, which can affect materials' electronic properties [1–4]. In most oxide materials, H acts exclusively as a donor and prefers to stay close to oxygen atoms, forming strong O–H bonds. These O–H bonds can be considered as oscillators with distinct natural stretch mode frequencies of about 3000 cm^{-1} that can be directly observed by infrared (IR) measurements.

Strontium titanate ($SrTiO_3$) is one of the most important oxide materials because of its potential to be used in dielectric and optical devices [5–8], as well as its potential to be used as a substrate for superconducting thin films [9]. $SrTiO_3$ has a cubic perovskite structure at room temperature and a tetragonal structure at the temperature below 105 K [10]. In 1980, based on polarized IR absorption measurement, Weber and Kapphan (WK) observed the vibration band at ~3500 cm^{-1} [11,12]. They also studied the effects of uniaxial stress and electric field on the vibration band. Later, polarized Raman scattering measurement was carried out by the same group [13]. At room temperature, WK found the main peak centered at 3495 cm^{-1} accompanied with small peaks in the range of 3505–3520 cm^{-1}. WK proposed that the frequencies belong to a single H interstitial in $SrTiO_3$. Recently, Tarun and McCluskey [14] (TM) experimentally observed additional double peaks centered at 3355 and 3384 cm^{-1}. They assigned these local vibrational modes to a complex defect between a Sr vacancy and two H atoms (2H–V_{Sr}).

Recently, based on first principles calculations, we have revealed that H interstitial has a vibrational frequency far lower than 3500 cm^{-1} [15]. We also showed that one or two interstitial H atom(s) could be trapped by V_{Sr} forming nH–V_{Sr} complexes (n=1 or 2). In the complexes, H atoms form strong O–H bonds with the O atoms surrounding V_{Sr}

---

*Corresponding author at: School of Physics, Suranaree University of Technology, Nakhon Ratchasima 30000, Thailand. Tel.: +66 44 22 4319; fax: +66 44 22 4185.
E-mail address: sukit@sut.ac.th (S. Limpijumnong).

0272-8842/$ - see front matter © 2012 Elsevier Ltd All rights reserved.
http://dx.doi.org/10.1016/j.ceramint.2012.10.076

Please cite this article as: I. Fongkaew, et al., First principles calculations of Hydrogen—Titanium vacancy complexes in $SrTiO_3$, Ceramics International (2012), http://dx.doi.org/10.1016/j.ceramint.2012.10.076

Manuscript submitted in Ceramics International

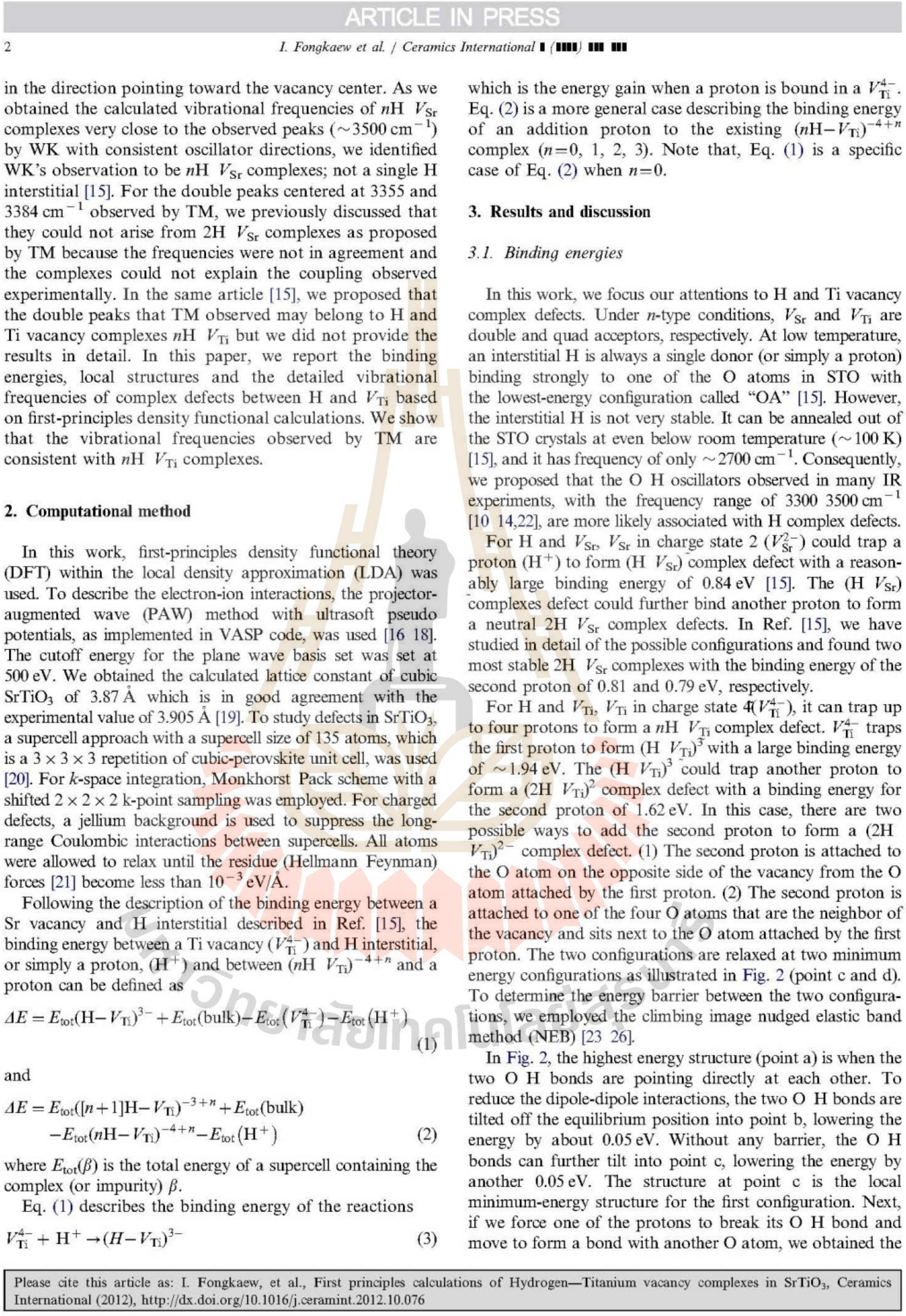

in the direction pointing toward the vacancy center. As we obtained the calculated vibrational frequencies of nH–V_{Sr} complexes very close to the observed peaks ($\sim 3500\ cm^{-1}$) by WK with consistent oscillator directions, we identified WK's observation to be nH–V_{Sr} complexes; not a single H interstitial [15]. For the double peaks centered at 3355 and 3384 cm^{-1} observed by TM, we previously discussed that they could not arise from 2H–V_{Sr} complexes as proposed by TM because the frequencies were not in agreement and the complexes could not explain the coupling observed experimentally. In the same article [15], we proposed that the double peaks that TM observed may belong to H and Ti vacancy complexes nH–V_{Ti} but we did not provide the results in detail. In this paper, we report the binding energies, local structures and the detailed vibrational frequencies of complex defects between H and V_{Ti} based on first-principles density functional calculations. We show that the vibrational frequencies observed by TM are consistent with nH–V_{Ti} complexes.

2. Computational method

In this work, first-principles density functional theory (DFT) within the local density approximation (LDA) was used. To describe the electron-ion interactions, the projector-augmented wave (PAW) method with ultrasoft pseudo potentials, as implemented in VASP code, was used [16–18]. The cutoff energy for the plane wave basis set was set at 500 eV. We obtained the calculated lattice constant of cubic $SrTiO_3$ of 3.87 Å which is in good agreement with the experimental value of 3.905 Å [19]. To study defects in $SrTiO_3$, a supercell approach with a supercell size of 135 atoms, which is a $3 \times 3 \times 3$ repetition of cubic-perovskite unit cell, was used [20]. For k-space integration, Monkhorst–Pack scheme with a shifted $2 \times 2 \times 2$ k-point sampling was employed. For charged defects, a jellium background is used to suppress the long-range Coulombic interactions between supercells. All atoms were allowed to relax until the residue (Hellmann–Feynman) forces [21] become less than 10^{-3} eV/Å.

Following the description of the binding energy between a Sr vacancy and H interstitial described in Ref. [15], the binding energy between a Ti vacancy (V_{Ti}^{4-}) and H interstitial, or simply a proton, (H^+) and between $(nH–V_{Ti})^{-4+n}$ and a proton can be defined as

$$\Delta E = E_{tot}(H-V_{Ti})^{3-} + E_{tot}(bulk) - E_{tot}(V_{Ti}^{4-}) - E_{tot}(H^{+}) \quad (1)$$

and

$$\Delta E = E_{tot}([n+1]H-V_{Ti})^{-3+n} + E_{tot}(bulk) - E_{tot}(nH-V_{Ti})^{-4+n} - E_{tot}(H^{+}) \quad (2)$$

where $E_{tot}(\beta)$ is the total energy of a supercell containing the complex (or impurity) β.

Eq. (1) describes the binding energy of the reactions

$$V_{Ti}^{4-} + H^{+} \rightarrow (H-V_{Ti})^{3-} \quad (3)$$

which is the energy gain when a proton is bound in a V_{Ti}^{4-}. Eq. (2) is a more general case describing the binding energy of an addition proton to the existing $(nH-V_{Ti})^{-4+n}$ complex ($n=0$, 1, 2, 3). Note that, Eq. (1) is a specific case of Eq. (2) when $n=0$.

3. Results and discussion

3.1. Binding energies

In this work, we focus our attentions to H and Ti vacancy complex defects. Under n-type conditions, V_{Sr} and V_{Ti} are double and quad acceptors, respectively. At low temperature, an interstitial H is always a single donor (or simply a proton) binding strongly to one of the O atoms in STO with the lowest-energy configuration called "OA" [15]. However, the interstitial H is not very stable. It can be annealed out of the STO crystals at even below room temperature ($\sim$100 K) [15], and it has frequency of only $\sim 2700\ cm^{-1}$. Consequently, we proposed that the O–H oscillators observed in many IR experiments, with the frequency range of 3300–3500 cm^{-1} [10–14,22], are more likely associated with H complex defects.

For H and V_{Sr}, V_{Sr} in charge state 2 (V_{Sr}^{2-}) could trap a proton (H^+) to form (H–V_{Sr}) complex defect with a reasonably large binding energy of 0.84 eV [15]. The (H–V_{Sr}) complexes defect could further bind another proton to form a neutral 2H–V_{Sr} complex defects. In Ref. [15], we have studied in detail of the possible configurations and found two most stable 2H–V_{Sr} complexes with the binding energy of the second proton of 0.81 and 0.79 eV, respectively.

For H and V_{Ti}, V_{Ti} in charge state 4 (V_{Ti}^{4-}), it can trap up to four protons to form a nH–V_{Ti} complex defect. V_{Ti}^{4-} traps the first proton to form $(H–V_{Ti})^{3}$ with a large binding energy of $\sim$1.94 eV. The $(H–V_{Ti})^{3}$ could trap another proton to form a $(2H–V_{Ti})^{2}$ complex defect with a binding energy for the second proton of 1.62 eV. In this case, there are two possible ways to add the second proton to form a $(2H–V_{Ti})^{2-}$ complex defect. (1) The second proton is attached to the O atom on the opposite side of the vacancy from the O atom attached by the first proton. (2) The second proton is attached to one of the four O atoms that are the neighbor of the vacancy and sits next to the O atom attached by the first proton. The two configurations are relaxed at two minimum energy configurations as illustrated in Fig. 2 (point c and d). To determine the energy barrier between the two configurations, we employed the climbing image nudged elastic band method (NEB) [23–26].

In Fig. 2, the highest energy structure (point a) is when the two O–H bonds are pointing directly at each other. To reduce the dipole-dipole interactions, the two O–H bonds are tilted off the equilibrium position into point b, lowering the energy by about 0.05 eV. Without any barrier, the O–H bonds can further tilt into point c, lowering the energy by another 0.05 eV. The structure at point c is the local minimum-energy structure for the first configuration. Next, if we force one of the protons to break its O–H bond and move to form a bond with another O atom, we obtained the

Please cite this article as: I. Fongkaew, et al., First principles calculations of Hydrogen—Titanium vacancy complexes in $SrTiO_3$, Ceramics International (2012), http://dx.doi.org/10.1016/j.ceramint.2012.10.076

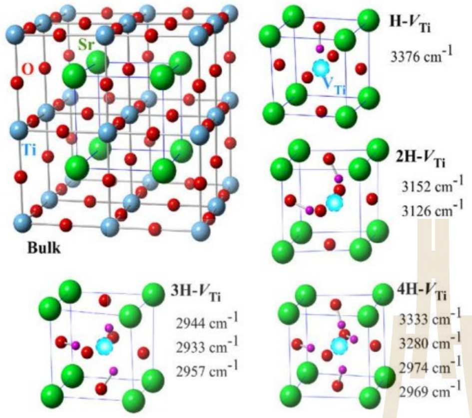

Fig. 1. The local structures of bulk $SrTiO_3$ and H–V_{Ti}, 2H–V_{Ti}, 3H–V_{Ti}, and 4H–V_{Ti} complexes. Green, blue, red, and pink spheres represent the Sr, Ti, O, and H atoms, respectively. The stretch vibrational frequencies for each configuration are also shown. (For interpretation of the references to color in this figure legend, the reader is reffered to the web version of this article.)

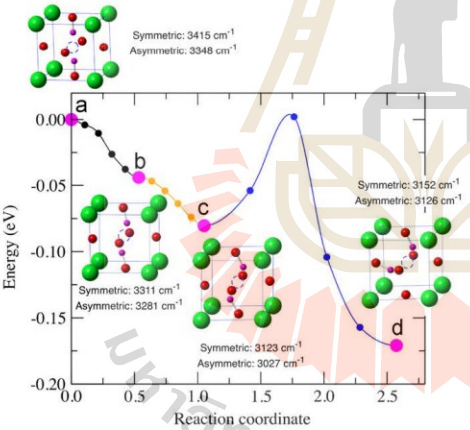

Fig. 2. Illustration of the energy path relating different configurations of $(2H–V_{Ti})^2$ complexes obtained from the nudged elastic band method. Points (a)–(d) indicate interesting configurations of which the configurations at (c) and (d) are the local minimum and global minimum energy configurations, respectively. The stretch vibrational frequencies are also listed for each configuration. (For interpretation of the references to color in this figure legend, the reader is reffered to the web version of this article.)

$c \rightarrow d$ path with a small energy barrier of ~0.1 eV for the proton to move from the first configuration to the lower energy (second) configuration, as shown in Fig. 2. This rather low energy barrier indicates that protons in the V_{Ti} could move rather freely to find their global minimum energy positions. Therefore, majority of the $(2H\ V_{Ti})^{2-}$ complexes should exist in their lowest energy configuration (point d) at reasonably low temperatures.

The $(2H\ V_{Ti})^{2-}$ complexes could trap another proton to form $(3H\ V_{Ti})^{-}$ complexes There are two possible configurations for the $(3H\ V_{Ti})^{-}$ complexes with the lower energy one shown in Fig. 1. The $(3H\ V_{Ti})^{-}$ complexes could further bind with another proton to form neutral 4H V_{Ti} complexes. Again, there are two possible configurations for the 4H V_{Ti} complexes with the lower energy one shown in Fig. 1. The formation of these complexes can be summarized in the following reaction equations.

$$\begin{aligned} &H^{1+} + V_{Ti}^{4-} \rightarrow (H\text{ - }V_{Ti})^{3-} + 1.94\ eV,\\ &H^{1+} + (H\text{ - }V_{Ti})^{3-} \rightarrow (2H\text{ - }V_{Ti})^{2-} + 1.62\ eV,\\ &H^{1+}(2H\text{ - }V_{Ti})^{2-} \rightarrow (3H\text{ - }V_{Ti})^{-} + 1.51\ eV,\\ &H^{1+} + (3H\text{ - }V_{Ti})^{-} \rightarrow (4H\text{ - }V_{Ti}) + 1.00\ eV \end{aligned} \tag{6}$$

3.2. Local vibrational frequencies of complex defects

The vibrational frequency associated with each defect was determined by calculating the dynamical matrix based on the harmonic approximations as described in Ref. [27] To test the reliability of the calculations, we first calculated the vibrational modes of a water molecule and obtained the vibrational frequencies of 3712, 3825, and 1533 cm^{-1} for symmetric stretching, asymmetric stretching, and bending modes, respectively. Comparing with the experimental values of 3657, 3756, and 1595 cm^{-1} [28,29] the computational values contain the error bar of ~70 cm^{-1}.

Next, we calculated the vibration signatures of nH V_{Ti} complex defects. We found that all nH V_{Ti} complexes give the vibrational frequency below 3400 cm^{-1} (see Fig. 1). The $(H\ V_{Ti})^{3-}$ complex has the calculated vibrational frequency of 3376 cm^{-1} in a reasonable agreement with the values observed by TM. When a second proton is added to form $(2H\ V_{Ti})^{2-}$ complex, the two O H bonds can vibrate as two oscillators. We found that, unlike the case of 2H V_{Sr} that the two oscillators have no coupling between them [15], here there is a coupling between the two oscillators. The reason can be attributed to the closer distance of the two oscillators in the case of the $(2H\ V_{Ti})^{2-}$ complex compared to the 2H V_{Sr} complex. The vibrational frequency of the $(2H\ V_{Ti})^{2-}$ complex is split into two values, as shown in Fig. 1. Interestingly, the two calculated frequencies are differed by 26 cm^{-1}, which is in a good agreement with the splitting of the two peaks of 29 cm^{-1} observed by TM [14]. This is the strongest indication that the observed IR absorption peaks by TM at 3355 and 3384 cm^{-1} should come from $(2H\ V_{Ti})^{2-}$ complex rather than 2H V_{Sr} complex. Note, however, that the absolute values of the calculated vibrational frequencies of the $(2H\ V_{Ti})^{2-}$ complex are only 3152 and 3126 cm^{-1}, somewhat lower than the values observed by TM (by about 7%). In addition to the vibrational frequencies of the lowest energy configuration, those of the higher energy configurations have also been

Please cite this article as: I. Fongkaew, et al., First principles calculations of Hydrogen—Titanium vacancy complexes in $SrTiO_3$, Ceramics International (2012), http://dx.doi.org/10.1016/j.ceramint.2012.10.076

Manuscript submitted in Ceramics International

calculated and are shown in Fig. 2. Beside the vibration frequencies of $(\mathrm{H}\ V_{\mathrm{Ti}})^{3-}$ and $(2\mathrm{H}\ V_{\mathrm{Ti}})^{2-}$ complexes, we further calculated the vibration of $(3\mathrm{H}\ V_{\mathrm{Ti}})^{-}$ and $4\mathrm{H}\ V_{\mathrm{Ti}}$ complexes in their lowest-energy configurations and showed their vibrational frequencies in Fig. 1. We found all calculated vibrational frequencies to be in the range of 2900 3400 cm^{-1}.

4. Conclusion

Based on first-principles density functional calculations, we reported the detailed study of complex defects between H and Ti vacancy ($n\mathrm{H}\ V_{\mathrm{Ti}}$ complexes) in $\mathrm{SrTiO_3}$. The lowest-energy configurations for $n\mathrm{H}\ V_{\mathrm{Ti}}$ complexes ($n=1$, 2, 3, 4) were identified and their vibrational frequencies were calculated. The calculated vibrational frequencies of $n\mathrm{H}\ V_{\mathrm{Ti}}$ complexes are in the range of 2900 3400 cm^{-1}. For the complexes containing more than one O H oscillator, there is some coupling between the stretch vibration modes. For $2\mathrm{H}\ V_{\mathrm{Ti}}$ complex, the coupling leads to the split in the two vibration frequencies of 26 cm^{-1}. This combined with our previous study of $n\mathrm{H}\ V_{\mathrm{Sr}}$complexes in $\mathrm{SrTiO_3}$, indicates that the twin IR absorption peaks at 3355 and 3384 cm^{-1} observed by Tarun and McCluskey [14] are associated with the complex defects between H and V_{Ti}. On the other hand, the higher IR absorption peaks at $\sim 3500\ \mathrm{cm}^{-1}$, observed much earlier by Weber and Kapphan, are associated with the complex defects between H and V_{Sr}.

Acknowledgements

Support from the Thailand Research Fund (Grant No. RTA5280009) and US Department of Energy, Division of Materials Sciences and Engineering are acknowledged. One of the authors (IF) acknowledges the scholarship from the Development and Promotion of Science and Technology Talents Project (DPST).

Reference

[1] M.-H. Du, K. Biswas, Anionic and hidden hydrogen in ZnO, Physical Review Letters 106 (2011) 115502.
[2] W.M. Hlaing, Oo, S. Tabatabaei, M.D. McCluskey, J.B. Varley, A. Janotti, C.G. Van de Walle, Hydrogen donors in $\mathrm{SnO_2}$ studied by infrared spectroscopy and first-principles calculations, Physical Review B 82 (2010) 193201.
[3] P.D.C. King, R.L. Lichti, Y.G. Celebi, J.M. Gil, R.C. Vilão, H.V. Alberto, J. Piroto Duarte, D.J. Payne, R.G. Egdell, I. McKenzie, C.F. McConville, S.F.J. Cox, T.D. Veal, Shallow donor state of hydrogen in $\mathrm{In2O_3}$ and $\mathrm{SnO_2}$: implications for conductivity in transparent conducting oxides, Physical Review B 80 (2009) 081201.
[4] S. Limpijumnong, P. Reunchan, A. Janotti, C.G. Van de Walle, Hydrogen doping in indium oxide: an ab initio study, Physical Review B 80 (2009) 193202.
[5] Z. Kun, J. Kui-juan, H. Yanhong, Z. Songqing, L. Huibin, H. Meng, C. Zhenghao, Z. Yueliang, Y. Guozhen, Ultraviolet fast-response photoelectric effect in tilted orientation $\mathrm{SrTiO_3}$ single crystals, Applied Physics Letters 89 (2006) 173507.
[6] G.M. Rao, S.B. Krupanidhi, Study of electrical properties of pulsed excimer laser deposited strontium titanate films, Journal of Applied Physics 75 (1994) 2604.
[7] N. Seung-Hee, K. Ho-Gi, The effect of heat treatment on the $\mathrm{SrTiO_3}$ thin films prepared by radio frequency magnetron sputtering, Journal of Applied Physics 72 (1992) 2895.
[8] F.J. Walker, R.A. McKee, Y. Huan-wun, D.E. Zelmon, Optical clarity and waveguide performance of thin film perovskites on MgO, Applied Physics Letters 65 (1994) 1495.
[9] X.D. Wu, D. Dijkkamp, S.B. Ogale, A. Inam, E.W. Chase, P.F. Miceli, C.C. Chang, J.M. Tarascon, T. Venkatesan, Epitaxial ordering of oxide superconductor thin films on (100) $\mathrm{SrTiO_3}$ prepared by pulsed laser evaporation, Applied Physics Letters 51 (1987) 861.
[10] D. Houde, Y. Lepine, C. Pepin, S. Jandl, J.L. Brebner, High-resolution infrared spectroscopy of hydrogen impurities in strontium titanate, Physical Review B 35 (1987) 4948.
[11] S. Kapphan, J. Koppitz, G. Weber, O–D and O–H stretching vibrations in monodomain $\mathrm{SrTiO_3}$, Ferroelectrics 25 (1980) 585.
[12] G. Weber, S. Kapphan, M. Wohlecke, Spectroscopy of the O–H and O–D stretching vibrations in $\mathrm{SrTiO_3}$ under applied electric field and uniaxial stress, Physical Review B 34 (1986) 8406.
[13] S. Klauer, M. Wohlecke, Local symmetry of hydrogen in cubic and tetragonal $\mathrm{SrTiO_3}$ and $\mathrm{KTaO_3}$: Li determined by polarized Raman scattering, Physical Review Letters 68 (1992) 3212.
[14] M.C. Tarun, M.D. McCluskey, Infrared absorption of hydrogen-related defects in strontium titanate, Journal of Applied Physics 109 (2011) 063706.
[15] J.T.- Thienprasert, I. Fongkaew, D.J. Singh, M.H. Du, S. Limpijumnong, Identification of hydrogen defects in $\mathrm{SrTiO_3}$ by first-principles local vibration mode calculations, Physical Review B 85 (2012) 125205.
[16] G. Kresse, J. Furthmüller, Efficiency of ab-initio total energy calculations for metals and semiconductors using a plane-wave basis set, Computational Materials Science 6 (1996) 15.
[17] G. Kresse, J. Hafner, Norm-conserving and ultrasoft pseudopotentials for first-row and transition-elements, Journal of Physics: Condensed Matter 6 (1994) 8245.
[18] G. Kresse, D. Joubert, From ultrasoft pseudopotentials to the projector augmented-wave method, Physical Review B 59 (1999) 1758.
[19] F.W. Lytle, X-ray diffractometry of low-temperature phase transformations in strontium titanate, Journal of Applied Physics 35 (1964) 2212.
[20] C.G. Van de Walle, J. Neugebauer, First-principles calculations for defects and impurities: applications to III-nitrides, Journal of Applied Physics 95 (2004) 3851.
[21] R.P. Feynman, Forces in molecules, Physical Review 56 (1939) 340.
[22] H. Hesse, S. Kapphan, Doping of $\mathrm{SrTiO_3}$ with hydrogen and deuterium, Physica Status Solidi A Applications and Material Science 50 (1978) K243.
[23] S. Daniel, T. Rye, H. Graeme, Optimization methods for finding minimum energy paths, Journal of Chemical Physics 128 (2008) 134106.
[24] H. Graeme, P.U. Blas, J. Hannes, A climbing image nudged elastic band method for finding saddle points and minimum energy paths, Journal of Chemical Physics 113 (2000) 9901.
[25] H. Graeme, J. Hannes, Improved tangent estimate in the nudged elastic band method for finding minimum energy paths and saddle points, Journal of Chemical Physics 113 (2000) 9978.
[26] G. Mills, H. Jonsson, G.K. Schenter, Reversible work transition state theory: application to dissociative adsorption of hydrogen, Surface Science 324 (1995) 305.
[27] J.T.- Thienprasert, S. Limpijumnong, A. Janotti, C.G. Van de Walle, L. Zhang, M.H. Du, D.J. Singh, Vibrational signatures of OTe and OTe-VCd in CdTe: a first-principles study, Computational Materials Science 49 (2010) S242.
[28] K.P. Huber, G. Herzberg, Molecular Spectra and Molecular Structure. IV. Constants of Diatomic Molecules, Van Nostrand Reinhold Co., 1979.
[29] T. Shimanouchi, Tables of Molecular Vibrational Frequencies, Consolidated Volume 1, NSRDS NBS-39.

Please cite this article as: I. Fongkaew, et al., First principles calculations of Hydrogen—Titanium vacancy complexes in $\mathrm{SrTiO_3}$, Ceramics International (2012), http://dx.doi.org/10.1016/j.ceramint.2012.10.076

Manuscript submitted in Physical Review B

PHYSICAL REVIEW B **85**, 125205 (2012)

Identification of hydrogen defects in $SrTiO_3$ by first-principles local vibration mode calculations

Jiraroj T-Thienprasert,[1,2] Ittipon Fongkaew,[2,3] D. J. Singh,[4] M.-H. Du,[4] and Sukit Limpijumnong[3,4]
[1]*Department of Physics, Faculty of Science, Kasetsart University, Bangkok 10900, Thailand*
[2]*Thailand Center of Excellence in Physics (ThEP Center), Commission on Higher Education, Bangkok 10400, Thailand*
[3]*School of Physics, Suranaree University of Technology and Synchrotron Light Research Institute, Nakhon Ratchasima 30000, Thailand*
[4]*Oak Ridge National Laboratory, Oak Ridge, Tennessee 37831, USA*

(Received 13 August 2011; revised manuscript received 3 March 2012; published 26 March 2012)

For over three decades, the infrared spectroscopy peaks of around 3500 cm^{-1} observed in hydrogen-doped $SrTiO_3$ samples have been assigned to an interstitial hydrogen (H_i) attached to a lattice oxygen with two possible configuration models: the octahedral edge (OE) and the cubic face (CF) models. Based on our first-principles calculations of H_i around O, both OE and CF configurations are not energetically stable. Starting from either configuration, the H_i would spontaneously relax into an off axis (OA) site; lowering the energy by 0.25 eV or more. The calculated vibrational frequency of 2745 cm^{-1} for OA invalidates the assignment of H_i to the observed 3500 cm^{-1} peak. In addition, the calculated diffusion barrier is low, suggesting that H_i can be easily annealed out. We propose that the observed peaks around 3500 cm^{-1} are associated with defect complexes. A Sr vacancy (V_{Sr}) can trap H_i and form a H-V_{Sr} complex which is both stable and has the frequency in agreement with the observed main peak. The complex can also trap another H_i and form 2H-V_{Sr}; consistent with the observed additional peaks at slightly higher frequencies (3510–3530 cm^{-1}).

DOI: 10.1103/PhysRevB.85.125205 PACS number(s): 61.72.Bb, 63.20.Pw

I. INTRODUCTION

Hydrogen is known to be ubiquitous in oxide materials and greatly impact their electronic properties.[1–4] A thorough understanding of local configurations of H is deemed essential for understanding energetics and kinetics of H in oxides. Infrared (IR) spectroscopy has proven to be a powerful tool to experimentally probe H structures. Based on known IR absorption peaks for molecules containing hydroxyl groups, absorption peaks around 3000 cm^{-1} are usually associated to O-H bonds. However, to identify actual local structures responsible for the observed peaks, first-principles calculations are generally needed. Many computational studies have been dedicated to the identification of proton sites in the crystal structures with fourfold coordinated O, for example, zincblende, wurtzite, rutile, and bixbyite.[2,3,5,6] For the perovskite structure, there are computational results on proton sites in some compounds, for example, $BaTiO_3$[7] and $BaZrO_3$.[8] However, the direct calculation details of H site in $SrTiO_3$ are limited which impedes further study of H migration. It is very difficult to understand proton migration mechanisms without knowing its ground state site first.[9]

Strontium titanate ($SrTiO_3$) is an important oxide material due to a rich variety of industrial applications, for examples, in dielectric and optical devices[10–13] and as a substrate for superconducting thin films.[14] Discovery of high mobility 2D electron gas at interfaces between $SrTiO_3$ and other oxides[15] further opened up new opportunities in oxide electronics. $SrTiO_3$ has a cubic perovskite structure at room temperature and exhibits an antiferrodistortive phase transition to tetragonal at 105 K.[16] Several infrared spectroscopy experiments have been performed to study hydrogen in $SrTiO_3$.[16–18] Depending on the sample conditions, O-H absorption bands have been observed around 3500 and 3300 cm^{-1}. The band around 3500 cm^{-1} has been studied in detail since 1980 by the group of Weber and Kapphan (WK) using polarized IR absorption spectroscopy[18,19] combined with the applications of uniaxial stress as well as electric field. Polarized Raman scattering measurement was later performed by the same group to confirm the IR results.[17] At room temperature they observed a main peak centered at 3495 cm^{-1} accompanied by a small hump consisting of several peaks in the range of 3505–3520 cm^{-1}. The main peak blue shifts to 3510 cm^{-1} at low temperature and subsequently splits into three lines ($\nu_A < \nu_B < \nu_C$ with the spacing of $\sim$2.5 cm^{-1}) as the crystal transforms into the tetragonal phase at temperature below 105 K. Polarizations of the split lines showed that the central line (ν_B) corresponds to dipoles lying in xy plane (the plane perpendicular to the tetragonal axis) while the outer lines (ν_A and ν_C) correspond to dipoles that have components both parallel and perpendicular to the tetragonal axis. By selectively applying uniaxial stress or electric field, the modes further split allowing WK to gain additional information on the stress and field dependencies of O-H dipoles in each direction. WK proposed two structural models for the proton in $SrTiO_3$, that is, octahedral edge (OE) and cube face (CF). Both models have various equivalent sites (24 for OE and 12 for CF[20]) in the cubic phase that would split into three unequivalent groups in the tetrahedral phase consistent with the measured results.

Recently, Tarun and McCluskey[21] observed twin peaks at 3355 and 3384 cm^{-1} and proposed that they are the local vibration modes (LVM) of a Sr vacancy decorated by two protons, that is, 2H-V_{Sr} complex, where the protons also form strong O-H bonds with the O atoms surrounding the V_{Sr}.

For semiconductors with sp^3 (fourfold) coordination, such as Si, Ge, GaAs, or even ZnO, a proton generally prefers to stay along the bonds; allowing the O-H bond to point along one of the sp^3 bonding directions. However, for $SrTiO_3$, a much more ionic compound with little directional bonding, the O-H direction is dictated by the overall Coulombic repulsions (to Ti^{4+} and Sr^{2+}) and attractions (to O^{2-}) with the neighboring atoms. An O-H pointing to a cation such as the CF configuration is usually unstable in a closely packed

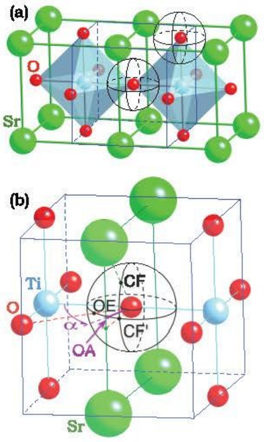

FIG. 1. (Color online) Schematic of low energy surface for a proton and four proton sites in $SrTiO_3$.

ionic crystal due to the strong Coulomb repulsion and limited space to relax.

In this paper we report our detailed first-principles computational results of a proton (H^+) in cubic perovskite $SrTiO_3$. The topology of low-energy proton sites around an O atom is thoroughly studied and the local vibrational mode of the stable site is calculated. We show that previous proposed structural models for H^+, that is, CF and OE,[18,19] are not stable and the calculated LVM of a single H^+ do not agree with the observed IR peak. We propose a new model based on a complex of V_{Sr} and H, which is energetically stable and can satisfactorily explain the observed IR peak.

II. HYDROGEN SITES IN $SrTiO_3$

Figure 1 shows the local structure around an O atom in $SrTiO_3$. In Fig. 1(a) two conventional unit cells of cubic $SrTiO_3$ are shown to clearly illustrate all neighbors of the middle O atom (all O atoms in the crystal are equivalent by symmetry) with the detail in Fig. 1(b). Each O atom has two Ti, four Sr, and eight O neighbors. It is known that, in oxides, a proton prefers to bind strongly with an O with a distance of ~1 Å; the region represented by a low energy surface (LES) which has the shape of a distorted sphere centered on the O [in Fig. 1(b) we show a perfect sphere for an illustration purpose]. On this LES, a proton has a chance to bind strongly with the O atom and the differences in the formation energy of the proton on different points on the surface arise from the interaction with neighbors. The OE site is on the line connecting an O atom to its O neighbor. This is the line defining the octahedral edge in Fig. 1(a). The CF site is on the cubic face and on the line connecting between an O and its Sr neighbor. There is another high symmetry site on the cubic face [labeled CF′ in Fig. 1(b)] which is on the line connecting an O atom and the midpoint of two adjacent Sr atoms on the same side of the cube. This site has been identified to be the minimum energy site for a proton in $BaZrO_3$.[8] On the LES, there are eight equivalent sites for OE and four equivalent sites for CF as well as CF′. In a cubic perovskite unit cell, which consists of three O atoms, the numbers of the equivalent sites are three times more, that is, 24 and 12, respectively.

TABLE I. Calculated energy, O-H bond length, and stretch frequency for proton in $SrTiO_3$ with and without V_{Sr}. For a proton without V_{Sr}, ΔE is the relative energy referenced to the OA. For the complex defects, ΔE is the binding energy of the last proton according to Eqs. (1) and (2). Note that the OE, CF, and CF′ configurations are not stable, the proton spontaneously relaxes to OA configuration. Rows highlighted in boldface are the ground state configurations.

Sites	(α,θ)	ΔE (eV)	$d_{\text{O-H}}$ (Å)	ω (cm^{-1})
OE	(45,90)	2.29	–	–
CF	(90,45)	0.25	–	–
CF′	(90,90)	0.01	0.992	3225
OA	(76,90)	**0.00**	**1.011**	**2745**
H-V_{Sr}		**– 0.84**	**0.985**	**3505**
2H-V_{Sr}^{I}		– 0.81	0.984	3523
2H-V_{Sr}^{II}		– 0.79	0.984	3527
2H-V_{Sr}^{III}		– 0.75	0.986	3489
2H-V_{Sr}^{IV}		– 0.64	0.986	3458

III. COMPUTATION METHOD

We used first-principles density functional theory within the local density approximation (LDA) and projector-augmented wave (PAW) method[22] as implemented in VASP code.[23,24] The cutoff energy for the plane wave basis set was set at 500 eV. This gives the bulk lattice constant of 3.873 Å which is in agreement to within 1% with the experimental value (3.905 Å[25]). To study a proton in $SrTiO_3$ as well as other defects, a supercell with 135 atoms was used.[26] For charged defects we use a jellium background. All atoms in the cell were relaxed until Hellmann-Feynman forces[27] were reduced below 10^{-3} eV/Å. A shifted $2 \times 2 \times 2$ k-point sampling based on the Monkhorst-Pack scheme is employed for the Brillouin-zone integration.

IV. RESULTS AND DISCUSSIONS

Relative energies of a proton at OE, CF, and CF′ sites are listed in Table I. The effects from the neighboring atoms on the stability of proton on the LES sites can be understood using a simple Coulomb interaction picture. A proton prefers to stay close to anions, that is, O ions, and far from cations, that is, Ti and Sr ions. This explains why the site between an O and a Ti nearest neighbor (not labeled) has a high energy. Among the three high symmetry sites, OE is the least favorable site because it is still rather close to Ti. The CF site is also not the most favorable site because the site is rather close to Sr. The CF′ is further away from Sr, that is, it is at the middle point between two Sr atoms and also closer to two O atoms; making it more stable than CF by 0.25 eV. However, CF′ is an unstable equilibrium configuration. If we slightly break the

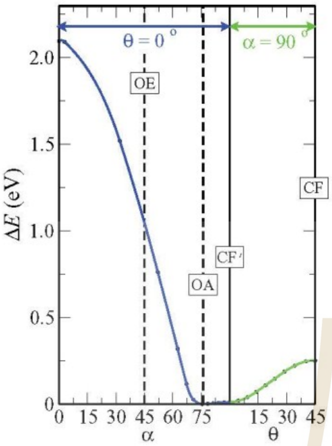

FIG. 2. (Color online) Calculated energy of a proton (referenced to the ground state configuration) on paths connection proton sites in Fig. 1. The azimuthal angle (α) is illustrated in Fig. 1 and θ is the angle between the O-H bond direction and the z axis. For the first section θ is fixed at 0° and for the second section α is fixed at 90°.

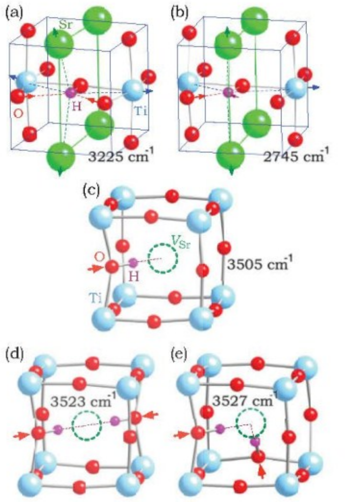

FIG. 3. (Color online) Local structures of H^+ (proton) defects in $SrTiO_3$. (a) and (b) Proton at CF′ and OA sites, (c) $(H\text{-}V_{Sr})^-$ complex, and (d) and (e) the two lowest energy $2H\text{-}V_{Sr}$ complexes. The arrows indicate the relaxation directions of the neighboring atoms. The frequencies shown are the calculated O-H stretch modes.

symmetry, the proton spontaneously moves away from the CF′ site to the off axis (OA) site. To describe the sites, we use an azimuthal angle (α) as defined in Fig. 1 and an angle deviated from the z axis (θ). In Table I only the angles related to the sites labeled in Fig. 1 are shown. The equivalent sites can be found by using the crystal symmetries. The global minimum energy site (OA) is significantly deviated from both CF and CF′, that is, by ∼30° and ∼15°, respectively.

To fully understand the energy landscape of an interstitial proton in cubic perovskite $SrTiO_3$, we employed the climbing image nudged elastic band method (NEB)[28–31] to calculate the total energy of the proton moving in the paths between important sites. On the basal plane ($\theta = 90°$) we studied the path that starts at the site between an O and a Ti ($\alpha = 0°$) (which is the highest energy point on the LES) passes through the OE and OA, and ends at the CF′ site ($\alpha = 90°$). The formation energy ΔE is calculated relative to the ground state configuration (OA). Along this path (Fig. 2) the energy drops by over 2 eV as the proton moves from the site between O and Ti to the OA site without any shoulder at the OE site, indicating that the OE site is not even a metastable site. As the proton passes the OA site, the energy increases but by a very small amount, that is, by only 0.01 eV, as the proton moves from OA to CF′. On the Sr plane ($\alpha = 90°$) we calculated a proton that travels on a path from CF′ ($\theta = 90°$) to CF ($\theta = 45°$). Along this path, the energy monotonically increases by ∼0.25 eV. Since CF is at the midpoint between two equivalent CF′ sites, it is a saddle point between minima on the LES. We have also calculated the barrier using NEB for a proton to hop from an OA site on one LES to an adjacent OA on a neighboring LES [two such LES are shown in Fig. 1(a)] and obtained a much smaller barrier (0.05 eV). Therefore the overall diffusion barrier of a proton in $SrTiO_3$ is set by the hopping between two OA sites in the same LES which is ∼0.25 eV. This means a proton is very mobile in $SrTiO_3$ even at temperature of ∼100 K[32] unless it is trapped by other defects.

The CF′ and OA configurations are shown in Figs. 3(a) and 3(b). The proton forms a strong bond with an oxygen with the bond lengths of 0.992 and 1.010 Å, respectively. Because of its positive charge, the proton repels cations (Ti^{4+} and Sr^{2+}) and attracts anions (O^{2-}). For the CF′ configuration, the proton is symmetrically placed with respect to the surrounding Ti, Sr, and O ions. This site minimized the Coulomb repulsion between H^+ and Ti^{4+}. Tilting away from the symmetric site (CF′ → OA) increases the Coulomb repulsions between H^+ and Ti^{4+} somewhat but decreases the H^+-Sr^{2+} Coulomb repulsions and increases the H^+-O^{2-} Coulomb attractions. The total energy decreases slightly (0.01 eV); rendering OA the lowest energy site. Note, however, that computational details can sometime affect the calculated energy difference in this scale. The O-H vibration frequencies for both OA and CF′ configurations were calculated using the approach described in Ref. 33 including anharmonic contributions which are important for the light H atom. To obtain the systematic errors of our calculations, we calculated the symmetric stretch frequency of a water molecule and obtained the value of 3515 cm^{-1} which is lower than the actual experimental value by 142 cm^{-1}. To correct this systematic error, all values of LVMs presented in this paper are corrected by adding this value. Even after the systematic error correction, we estimate the error bar on our calculated frequencies to be about 100 cm^{-1}. We obtained the vibration frequency of O-H in the ground state configuration (OA) of 2745 cm^{-1}.

From above detailed study we can see that a single proton in pure $SrTiO_3$ cannot explain the experimental observed IR mode around 3500 cm^{-1} for several reasons. (1) The most stable configuration for a proton in $SrTiO_3$ is OA and the previously proposed OE and CF configurations have considerably higher energies and are not even metastable. The OA configuration has an O-H dipole direction inconsistent with the measured polarized IR results. (2) The calculated stretch frequency of the O-H oscillator in the OA configuration is only 2745 cm^{-1} which is much lower than the observed 3500 cm^{-1} value. The difference of ~750 cm^{-1} is much larger than the typical computational error bar (about 100 cm^{-1}). (3) The vibration mode of a single proton in pure $SrTiO_3$ should be quickly broadened to the width of 500 cm^{-1} as the temperature goes from 0 to 100 K as the CF′ configuration being populated. However, the observed 3500 cm^{-1} mode remains rather sharp up to room temperature. (4) The diffusion barrier of a proton is very low such that a proton can diffuse even at room temperature. Thus, most of the interstitial protons should migrate out when the sample is cooled down.

Since a single proton cannot be the cause of the 3500 cm^{-1} mode, the outstanding question is "What O-H configuration could be the cause of it?" The obvious choice is H in cation vacancies. The complex of H and cation vacancies has been found in many oxides.[34] The observed twin peaks at 3355 and 3384 cm^{-1} in $SrTiO_3$ [21] have been suggested to originate from 2H-V_{Sr} complex. In $SrTiO_3$, there are two possible cation vacancies, V_{Sr} and V_{Ti}. Here we propose that the H in a Sr vacancy (H-V_{Sr}) is the cause of the 3500 cm^{-1} mode, and that the H in a Ti vacancy may explained the twin peaks reported in Ref. 21.

A $(\text{H-}V_{Sr})^-$ complex in $SrTiO_3$ has a fully relaxed O-H bond length of 0.985 Å (see Table I) and a calculated O-H vibration frequency of 3505 cm^{-1}, which is in excellent agreement with the experimentally observed mode. A V_{Sr}^{2-} has 12 O neighbors, all of which are equivalent by the cubic symmetry. A proton can bind to one of these O atoms, forming a $(\text{H-}V_{Sr})^-$ complex. There are 12 possible O-H oscillators pointing toward the vacancy center as shown in Fig. 3(c). Similarly, for a given Sr atom of a perfect crystal, there are also 12 possible CF sites for H to form O-H oscillators pointing toward it. It has been shown[16] that 12 CF sites in the cubic phase would split into three inequivalent groups in the tetragonal phase with polarization behaviors satisfied the observed mode. Therefore, the $(\text{H-}V_{Sr})^-$ model should also be equally consistent with the observed mode.

Actually, the double negative center V_{Sr}^{2-} could bind up to two protons in a similar way the V_{Zn}^{2-} binds protons in ZnO.[34] In the cases that the proton is abundant compared to the vacancy, the $(\text{H-}V_{Sr})^-$ could accept another proton forming a neutral charge 2H-V_{Sr}. There are four inequivalent ways to add the second proton to the existing $(\text{H-}V_{Sr})^-$ complex. The resulted 2H-V_{Sr} complexes are labeled with a superscript I to IV following the order of decreasing distances between the two O atoms that bind H. The two lowest energy configurations are 2H-V_{Sr}^{I} and 2H-V_{Sr}^{II} [Figs. 3(d) and 3(e)]. Since there are two O-H oscillators in each 2H-V_{Sr} complex, we first determined the coupling between the two oscillators by calculating the full dynamic matrix of the complex. Within our calculated force sensitivity (~0.001 eV/Å), we do not find any coupling between the two oscillators and thus obtained two degenerate modes. Small or no coupling is reasonable for this system because the two oscillators are attached to different O and are reasonably far apart. This allows us to separately calculate the frequency of each O-H oscillator including anharmonic effect in a systematic way. The calculated frequencies of all four complexes are shown in Table I. It can be seen that the vibrational frequencies of all seven configurations in Table I are nearly linearly correlated with the O-H bond length.

Next, we look into the energetic to evaluate the stability of these complexes. The binding energies between V_{Sr}^{2-} and H_{OA}^{+} and between $(\text{H-}V_{Sr})^-$ and H_{OA}^{+} are defined as

$$\Delta E = E_{\text{tot}}(\text{H-}V_{\text{Sr}})^- + E_{\text{tot}}(\text{bulk}) - E_{\text{tot}}\left(V_{\text{Sr}}^{2-}\right) - E_{\text{tot}}(\text{H}_{\text{OA}}^{+}), \tag{1}$$

and

$$\begin{aligned} \Delta E = {} & E_{\text{tot}}(2\text{H-}V_{\text{Sr}}) + E_{\text{tot}}(\text{bulk}) \\ & - E_{\text{tot}}(\text{H-}V_{\text{Sr}})^- - E_{\text{tot}}(\text{H}_{\text{OA}}^{+}), \end{aligned} \tag{2}$$

where $E_{\text{tot}}(\beta)$ is the total energy of a supercell containing the complex (or impurity) β.

We found that bringing the first H_{OA}^{+} to the V_{Sr}^{2-} is exothermic by 0.84 eV as shown in Table I. Bringing the second H_{OA}^{+} to $(\text{H-}V_{Sr})^-$ to form 2H-V_{Sr} complexes is also exothermic by 0.81, 0.79, 0.75, and 0.64 eV for the configurations I, II, III, and IV, respectively. The O-H vibrational frequency for $(\text{H-}V_{Sr})^-$ is in excellent agreement with the observed 3500 cm^{-1} peak and O-H LVMs for 2H-$V_{Sr}^{\text{I and II}}$ complexes are larger than that for the $(\text{H-}V_{Sr})^-$ complex by ~20 cm^{-1}, which may explain the experimentally observed higher frequency hump.

Recently, Tarun and McCluskey[21] observed twin peaks at 3355 and 3384 cm^{-1} and proposed that these IR peaks are originated from 2H-V_{Sr}^{IV}. Based on our results, this assignment has some problems. (1) The 2H-V_{Sr}^{IV} complex is the least stable among all four 2H-V_{Sr} complexes and has higher energy than 2H-V_{Sr}^{I} by 0.17 eV; rendering it unstable. (2) The 2H-V_{Sr} complexes have two O-H oscillators spatially well separated and do not couple with each other. Therefore, it cannot give the splitting of ~30 cm^{-1} (our calculations give doubly degenerated modes). (3) The calculated frequencies do not agree with the observed ones. Thus, the observed twin peaks are unlikely due to 2H-V_{Sr} complexes. They should originate from O-H in other configurations with stronger degree of coupling between two oscillators. One potential source is nH-V_{Ti} complexes where the two O-H oscillators reside closer to each other than 2H-V_{Sr}.

V. CONCLUSIONS

In summary, we have studied the stability and local vibration modes of a proton in cubic perovskite $SrTiO_3$ by first-principles calculations. In a perfect crystal, a proton has the lowest formation energy at a site with low symmetry [off-axis site (OA)]. The previously proposed center face (CF) and octahedral edge (OE) sites are 0.25 and 2.29 eV higher in energy than the OA site. While the proton at the OA site

Manuscript submitted in Physical Review B

forms a short O-H bond similar to a proton in other oxides, its calculated stretch vibration frequency is only 2745 cm^{-1} far lower than the observed absorption band at around 3500 cm^{-1} that was previously assigned to an interstitial proton. Not only the frequency does not match, but the OA configuration has an O-H dipole direction inconsistent with the measured polarized IR results. Moreover, our calculated diffusion barrier of an interstitial proton is only ~0.25 eV; indicating that a proton is very diffusive even at room temperature, and thus is likely to migrate out from the sample during the cooled down. We propose that the cause of the observed 3500 cm^{-1} band is a proton in a Sr vacancy $(\text{H-}V_{\text{Sr}})^-$ which has a strong binding energy of 0.84 eV and a calculated O-H vibrational frequency of 3505 cm^{-1} with the dipole orientations in agreement with the experimentally observed 3500 cm^{-1} band. The 2H-V_{Sr} complexes which can also form in samples with high H concentrations have the frequencies consistent with the observed hump ~20 cm^{-1} above the main 3500 band. We also propose that the distinct twin peaks at 3355 and 3384 cm^{-1} observed more recently should originate from O-H in other configurations such as protons decorating a Ti vacancy.

ACKNOWLEDGMENTS

Support from the US Department of Energy, Division of Materials Sciences and Engineering and Thailand Research Fund (Grant No. RTA5280009) are acknowledged.

---

[1] M.-H. Du and K. Biswas, Phys. Rev. Lett. **106**, 115502 (2011).
[2] S. Limpijumnong, P. Reunchan, A. Janotti, and C. G. Van de Walle, Phys. Rev. B **80**, 193202 (2009).
[3] W. M. HlaingOo, S. Tabatabaei, M. D. McCluskey, J. B. Varley, A. Janotti, and C. G. Van de Walle, Phys. Rev. B **82**, 193201 (2010).
[4] P. D. C. King *et al.*, Phys. Rev. B **80**, 081201 (2009).
[5] C. G. Van de Walle, Phys. Rev. Lett. **85**, 1012 (2000).
[6] X.-B. Li, S. Limpijumnong, W. Q. Tian, H. B. Sun, and S. B. Zhang, Phys. Rev. B **78**, 113203 (2008).
[7] Y. Iwazaki, T. Suzuki, and S. Tsuneyuki, J. Appl. Phys. **108**, 083705 (2010).
[8] P. G. Sundell, M. E. Bjorketun, and G. Wahnstrom, Phys. Rev. B **76**, 094301 (2007).
[9] N. Sata, K. Hiramoto, M. Ishigame, S. Hosoya, N. Niimura, and S. Shin, Phys. Rev. B **54**, 15795 (1996).
[10] G. M. Rao and S. B. Krupanidhi, J. Appl. Phys. **75**, 2604 (1994).
[11] N. Seung-Hee and K. Ho-Gi, J. Appl. Phys. **72**, 2895 (1992).
[12] Z. Kun *et al.*, Appl. Phys. Lett. **89**, 173507 (2006).
[13] F. J. Walker *et al.*, Appl. Phys. Lett. **65**, 1495 (1994).
[14] X. D. Wu *et al.*, Appl. Phys. Lett. **51**, 861 (1987).
[15] A. Ohtomo and H. Y. Hwang, Nature (London) **427**, 423 (2004).
[16] D. Houde, Y. Lepine, C. Pepin, S. Jandl, and J. L. Brebner, Phys. Rev. B **35**, 4948 (1987).
[17] S. Klauer and M. Wohlecke, Phys. Rev. Lett. **68**, 3212 (1992).
[18] G. Weber, S. Kapphan, and M. Wohlecke, Phys. Rev. B **34**, 8406 (1986).
[19] S. Kapphan, J. Koppitz, and G. Weber, Ferroelectrics **25**, 585 (1980).
[20] WK double counted the sites on the faces of the cubic and mentioned 24 equivalent sites for CF in their paper.
[21] M. C. Tarun and M. D. McCluskey, J. Appl. Phys. **109**, 063706 (2011).
[22] G. Kresse and D. Joubert, Phys. Rev. B **59**, 1758 (1999).
[23] G. Kresse and J. Furthmüller, Comput. Mat. Sci. **6**, 15 (1996).
[24] G. Kresse and J. Hafner, J. Phys. Condens. Matter **6**, 8245 (1994).
[25] F. W. Lytle, J. Appl. Phys. **35**, 2212 (1964).
[26] C. G. Van de Walle and J. Neugebauer, J. Appl. Phys. **95**, 3851 (2004).
[27] R. P. Feynman, Phys. Rev. **56**, 340 (1939).
[28] S. Daniel, T. Rye, and H. Graeme, J. Chem. Phys. **128**, 134106 (2008).
[29] H. Graeme, P. U. Blas, and J. Hannes, J. Chem. Phys. **113**, 9901 (2000).
[30] H. Graeme and J. Hannes, J Chem. Phys. **113**, 9978 (2000).
[31] G. Mills, H. Jonsson, and G. K. Schenter, Surf. Sci. **324**, 305 (1995).
[32] Estimation based on a hopping rate $\Gamma = \Gamma_0 \exp(-\beta E_a)$ of 1/min, and $\Gamma_0 = 100$ THz.
[33] S. Limpijumnong and S. B. Zhang, Appl. Phys. Lett. **86**, 151910 (2005).
[34] E. V. Lavrov, J. Weber, F. Borrnert, C. G. Van de Walle, and R. Helbig, Phys. Rev. B **66**, 165205 (2002).

Abstract submitted for The 10th Asian Meeting on Electroceramics (AMEC-2016), Taipei, Taiwan (2016).

AMEC-2016
The 10th Asian Meeting on Electroceramics
Dec. 04-07, 2016, Taipei, Taiwan

Local structure of Mn impurities in $SrTiO_3$: First principles study

Ittipon Fongkaew[1,2*], Jiraroj T-Thienprasert[3], and Sukit Limpijumnong[1]

[1]*School of Physics and NANOTEC-SUT Center of Excellence on Advanced Functional Nanomaterials, Suranaree University of Technology, Nakhon Ratchasima 30000, Thailand*
[2]*Synchrotron Light Research Institute, Nakhon Ratchasima 30000, Thailand.*
[3]*Department of Physics, Faculty of Science, Kasetsart University, Bangkok 10900, Thailand*

Mn-doped $SrTiO_3$ showed promising magnetic and electrical properties[1], but the doping mechanism remains unclear. In this work, a first principles study of Mn impurity in $SrTiO_3$ has been carried out to determine its favorable location and the associated electronic properties. We find that Mn is energetically favorable to substitute for Sr and Ti (as opposed to residing in an interstitial position) depending on equilibrium crystal growth conditions. Under oxygen-rich conditions, Mn predominantly occurs as a neutral-charge Mn substituting for Ti. However, under oxygen-poor conditions, Mn prefers to substitute for Sr. In addition, we find that Mn interstitial in highly positive charge can be stable in $SrTiO_3$ in some cases. Our finding showed that Mn is not really amphoteric as previously suggested[2]. Our work leads to a different viewpoint on defect mediated electrical and magnetic properties of transition metal-doped perovskites. Details of the local structures, formation energies, and electronic properties of these Mn defects and their possible complex defects are reported.

Keywords: $SrTiO_3$, First principles calculations, interstitial, equilibrium growth conditions.

*** Corresponding author's email:** ittipon @slri.or.th

[1] A. Tkach, P.M. Vilarinho, A. Kholkin, Structural and Dielectric Properties of Mn-Doped Strontium Titanate Ceramics, Ferroelectrics, 304 (2004) 87-90.

[2] M. Valant, T. Kolodiazhnyi, I. Arčon, F. Aguesse, A.-K. Axelsson, N.M. Alford, The Origin of Magnetism in Mn-Doped SrTiO3, Advanced Functional Materials, 22 (2012) 2114-2122.

Abstract submitted for The American Physical Society (APS) March meeting 2015. San Antonio, Texas, USA (2015).

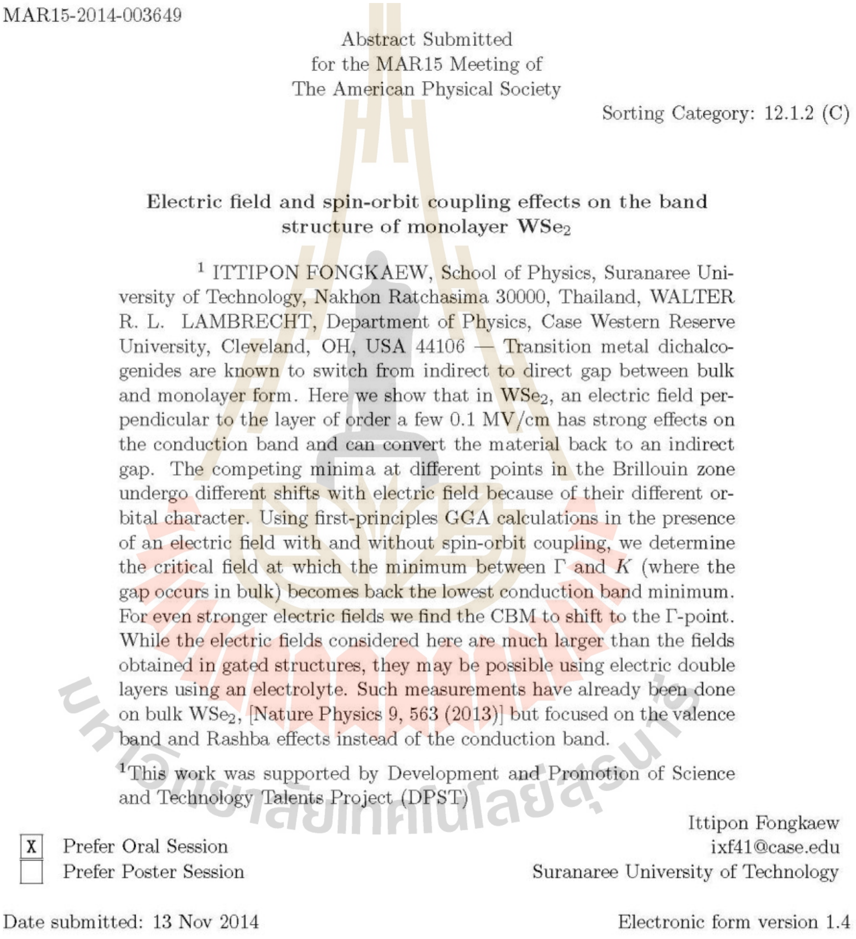

MAR15-2014-003649

Abstract Submitted
for the MAR15 Meeting of
The American Physical Society

Sorting Category: 12.1.2 (C)

Electric field and spin-orbit coupling effects on the band structure of monolayer WSe_2

[1] ITTIPON FONGKAEW, School of Physics, Suranaree University of Technology, Nakhon Ratchasima 30000, Thailand, WALTER R. L. LAMBRECHT, Department of Physics, Case Western Reserve University, Cleveland, OH, USA 44106 — Transition metal dichalcogenides are known to switch from indirect to direct gap between bulk and monolayer form. Here we show that in WSe_2, an electric field perpendicular to the layer of order a few 0.1 MV/cm has strong effects on the conduction band and can convert the material back to an indirect gap. The competing minima at different points in the Brillouin zone undergo different shifts with electric field because of their different orbital character. Using first-principles GGA calculations in the presence of an electric field with and without spin-orbit coupling, we determine the critical field at which the minimum between Γ and K (where the gap occurs in bulk) becomes back the lowest conduction band minimum. For even stronger electric fields we find the CBM to shift to the Γ-point. While the electric fields considered here are much larger than the fields obtained in gated structures, they may be possible using electric double layers using an electrolyte. Such measurements have already been done on bulk WSe_2, [Nature Physics 9, 563 (2013)] but focused on the valence band and Rashba effects instead of the conduction band.

[1] This work was supported by Development and Promotion of Science and Technology Talents Project (DPST)

☒ Prefer Oral Session
☐ Prefer Poster Session

Ittipon Fongkaew
ixf41@case.edu
Suranaree University of Technology

Date submitted: 13 Nov 2014

Electronic form version 1.4

Abstract submitted for Siam Physics Congress SPC 2012. Ayuttaya, Thailand, (2012).

Siam Physics Congress SPC2012
Past, Present and Future of Physics 9-12 May 2012

First Principles study of native defects and hydrogen impurities in SrTiO3

Ittipon Pongkaw[1*], Jiraroj T-Thienprasert[2] and S. Limpijumnong[1]

[1] *School of Physics, Suranaree University of Technology and Synchrotron Light Research Institute, Nakhon Ratchasima 30000, Thailand*

[2] *Department of Physics, Faculty of Science, Kasetsart University, Bangkok 10900, Thailand*

**Corresponding Ittipon Pongkaw. E-mail: ittipon_aof@yahoo.com*

Abstract

Native point defect in perovskite SrTiO (STO) are investigated by using first-principles pseudopotential calculations based on density-functional theory (DFT). Substitutional defects, Sr substituting on the Ti site (Sr_{Ti}) or Ti substituting on the Sr site (Ti_{Sr}) and O substituting on the Ti site (O_{Ti}) or Ti substituting on the O site (Ti_O) have high formation energies and are hence unstable. In contrast, Other fundamental native defect (V_{sr}, V_O, V_{Ti}, Ti_i, and O_i) have low formation energies. In particular, Oxygen vacancy (V_O) is a double donor defect with lowest formation energy in *p*-type samples, whereas Ti vacancy (V_{Ti}) is a quadruple acceptor defect with lowest formation energy in *n*-type samples. In addition, Based on first principles density functional calculations, local configurations and vibration signatures of a hydrogen impurities in STO with and without defects were studied. In a perfect crystal, a proton stays near an O atom, forming a strong O-H bond.

Keywords: SrTiO3, Hydrogen, Vacancy, First principles calculations

Abstract submitted for In The 3rd academic conference on natural science for master and Ph.D. students from asean countries (CASEAN 2013), Phnom Penh, Cambodia.

Local structure of Ca dopant in $BaTiO_3$ - $(Bi_{0.5}Na_{0.5})TiO_3$ system by Ca *K*-edge X-ray absorption near-edge structure and first-principles calculations

Ittipon Fongkaew[1,2,*], Sukit Limpijumnong,[1,2], Jiraroj T-Thienprasert[2,3]

[1] School of Physics, Suranaree University of Technology, NakhonRatchasima 30000, Thailand

[2] NANOTEC-SUT Center of Excellence on Advanced Functional Nanomaterials, Suranaree University of Technology, Nakhon Ratchasima 30000, Thailand

[3]Department of Physics, Faculty of Science, Kasetsart University, Bangkok 10900, Thailand

E-mial:ittipon_aof@yahoo.com

X-ray absorption near edge structure (XANES) experiment are performed on Ca-doped $BaTiO_3$ - $(Bi_{0.5}Na_{0.5})TiO_3$ (BT-BNT) samples and compared with first-principles XANES simulations. The feature of the measurement Ca *K*- edge XANES are consistent with the first-principles XANES of Ca on the Ba site and inconsistent with Ca on other sites. The clear agreement between and first-principles theoretical XANES spectra report here is by far the good evidence of Ca substituting for Ba in $0.9BaTiO_3 - 0.1(Bi_{0.5}Na_{0.5})TiO_3$. This work illustrates that a first-principle framework, which used to study impurities in crystal, can be used in conjunction with XANES measurement in order to identify an impurity structure with a high degree of confidence. This approach may thus be applicable to study impurities in other composite compound crystals.

Abstract submitted for Siam Physics Congress SPC 2013, Chiang mai, Thailand.

Siam Physics Congress SPC2013
Thai Physics Society on the Road to ASEAN Community 21-23 March 2013

First-principles study of Fe impurity in $BaTiO_3$

Ittipon Fongkaew[1,2,*], Sukit Limpijumnong,[1,2] Jiraroj T-Thienprasert[2,3]

[1] *School of Physics, Suranaree University of Technology, NakhonRatchasima 30000, Thailand*

[2] *Thailand Center of Excellence in Physics (ThEP Center), Commission on Higher Education, Bangkok 10400, Thailand*

[3] *Department of Physics, Faculty of Science, Kasetsart University, Bangkok 10900, Thailand*

**Corresponding author. E-mail: ittipon_aof@yahoo.com*

Abstract

Based on first principles calculations, various forms of Fe impurity in perovskite $BaTiO_3$ have been studied. The purpose is to determine the favorable locations, the possible complex defect structure and the resulting electronic properties. It is found that, Fe atom energetically prefers to substitute for the cations, namely Ba, and Ti, depending on the growth conditions. The complexes of Fe substitute for Ti (Fe_{Ti}) with native defects (O vacancy, Ba vacancy, and Ti vacancy) were studied. Our calculations showed the instability of the Fe_{Ti} complexes, in contrast to a general belief that the Fe_{Ti} complexes must exist by a virtue of the charge neutrality. Details of the local structures, formation energies, binding energy, charge analysis and related electronic levels were also studied.

Keywords: BaTiO3, Oxygen vacancy, First-principles calculations

Abstract submitted for The 8th Asian Meeting on Ferroelectrics (AMF-8). Ameri Hotel Pattaya, Thailand (2012).

First principles study of Ca in $BaTiO_3$ and $(Bi_{0.5}Na_{0.5})TiO_3$

Ittipon Fongkaew[1,2,*],**S. Limpijumnong,**[1,2] **Jiraroj T-Thienprasert**[2,3]

[1] *School of Physics, Suranaree University of Technology and Synchrotron Light Research Institute, NakhonRatchasima 30000, Thailand*

[2] *Thailand Center of Excellence in Physics (ThEP Center), Commission on Higher Education, Bangkok 10400, Thailand*

[3]*Department of Physics, Faculty of Science, Kasetsart University, Bangkok 10900, Thailand*

BNT-BT is one of the promising candidates as a high temperature relaxor with high Curie temperature and preferred dielectric constant characteristics. The addition of Ca has been shown experimentally to improve the temperature characteristic of capacitance for the BNT-BT system. In this work, Ca impurity in perovskite $BaTiO_3$ and $(Bi_{0.5}Na_{0.5})TiO_3$ have been studied based on first-principles calculations to determine their favorable location and thier electronic properties. In both BT and BNT, Ca atom energetically prefers to substitute for cations mainly Ba, Bi, Na, and Ti, depending on the growth conditions. Detail of local structure, formation energies, and related electronic levels will be presented.

***Presenting author's e-mail:** ittipon_aof@yahoo.com

CURRICULUM VITAE

Name	Mr. Ittipon Fongkaew
Date of Birth	31 August 1986
Place of Birth	Sakon nakhon, Thailand

Education:

2010 - Present.	Suranaree University of Technology (SUT), Nakhon Ratchasima, Thailand, Ph.D. candidate in Physics.
2006-2010	Khonkean University, Khonkean, Thailand. Bachelor of Science (First Class Honors in Physics)
2004-2006	Sakonraj Vittayanukul, Sakon nakhon, Thailand High school

Visiting research assistant and workshop:

- The 9th AOFSRR (Asia - Oceania Forum for Synchrotron Radiation Research) School Cheiron school 2015, September 10th - 19th, 2015, SPring-8, Hyogo, Japan.
- Department of Physics, Case Western Reserve University, Cleveland, Ohio. August, 1st 2014- August, 1st 2015. Supervisor: Prof. Dr. Walter R. L. Lambrecht
- Theory and Computation for Interface Science and Catalysis workshop.November 3-7, 2014, Brookhaven National Laboratory, New York.